

# The influence of visible-shortwave NIR spectroscopy hardware components on prediction of fruit attributes

Clinton John Hayes

A thesis submitted for the degree of Doctor of Philosophy

to the

School of Medical and Applied Sciences

and

School of Engineering and Technology

Central Queensland University, Rockhampton, Australia

March 2016

# Abstract

Overall performance of a visible-shortwave near infrared (NIR) spectroscopy system for a given application will be influenced by component performance, including optical geometry, lamp type and output stability in terms of aging and environmental conditions, detector wavelength range, signal to noise and stability to environmental conditions, model transfer across instruments and model robustness in terms of function in the face of varying temperature and ambient light levels. This thesis investigated the characteristics of individual components in context of their effect on performance of partial least squares (PLS) models of intact fruit total soluble solid content.

The requirement for a 'burn in' period (up to 2 h) before first use for quartz halogen lamps was characterised. Following this period, lamp output was spectrally stable for the purpose of predictive models based on second derivative of absorbance data until the last hours of lamp life. However, total lamp illumination was not constant until approximately 40 min from each start up event, and varied with ambient temperature. Temperature changes of the NIR spectrometric system components (lamp and front end electronics) affected signal level rather than quality, and thus did not affect the predictive performance of PLS models due to the second derivative absorbance pre-treatment.

Similar analysis of light emitting diodes (LED) demonstrated a requirement for a short (<24 h in all cases) 'burn in' period to stabilise output intensity. As expected, increase in ambient temperature produced a logarithmic decrease in overall intensity of the LEDs and a linear shift to longer wavelength of the peak emission. The effect of ambient temperature on performance of a commercially available instrument utilising LED illumination was documented, with a decrease observed in the measured  $I_{AD}$  Index ( $A_{670} - A_{720}$ ) with increased ambient temperature.

Spectroscopic assessment of intact fruit relies on collection of light that has passed into and out of the fruit, as opposed to specular reflection from the surface. The performance of a shadow probe interactance optical geometry was characterised in terms of the ratio of specular to diffuse radiation received by the detector using a technique based on polarisation of light. This ratio was less than 0.03 at probe to sample distances less than 30 mm but increased rapidly at greater distances due to loss of the shadowing effect.

Design features to increase the contribution of specular reflection to the detected signal are discussed.

The ability to transfer calibration models between instruments is imperative for the adoption and widespread use of an NIR spectrometric system. Pixel to wavelength assignments for a commercial Si diode array instrument showed errors of up to 2.3 nm. Improvement of wavelength assignment, particularly for the wavelength range used in the PLS regressions, was found to significantly decrease bias and standard error of prediction values. Several calibration transfer techniques were compared. It was found that a difference spectrum adjustment method, combined with new wavelength assignments and model updating, gave results comparable to the performance of the master instrument and to models directly developed on the slave instruments. Considering only 10 fruits were used, this is an easy method to transfer calibrations and allows for models to be updated for seasonal changes in samples.

NIR spectroscopy is being adopted in an increasing range of applications. The work of this thesis contributes to an understanding of the performance of a spectroscopic system for the application of fruit grading in context of illumination source, electronics and detector attributes.

# Acknowledgements

I would like to extend my sincerest thanks and appreciation to those patient people who helped me accomplish this study. I would like to express my sincere thanks and gratitude to Professor Kerry Walsh and Professor Colin Greensill for their patience, endurance, knowledge sharing, and guidance during research. Thanks for your time, encouragement, enthusiasm, and meticulous attention to detail during research and manuscript preparation. I would especially like to thank Col and Dr Richard Metcalfe for starting me on this path many years ago.

Thank you to the laboratory technicians who went out of their way to source, construct and fix equipment. The experiments would not have been possible without their assistance. Thank you to my research group team members, Bed Khatiwada, Umesh Acharya and Phul Subedi for their support. Thank you Phul, for allowing me to share your office.

I acknowledge the Commonwealth Government's Research Training Scheme for funding my doctoral studies.

Finally, special recognition goes to my family. Without their support, encouragement and patience during my pursuit, this educational journey would not have been possible.

# Declaration of Authorship and Originality

The work contained in this thesis has not been previously submitted either in whole or in part for a degree at CQUniversity or any other tertiary institution. To the best of my knowledge and belief, the material presented in this thesis is original except where due reference is made in text. I acknowledge input of my supervisors Kerry Walsh and Col Greensill in experimental design and interpretation, and also colleague Christo Leibenberg in these areas and data collection for Chapter 5. These people are (and will be) acknowledged as co-authors on journal publications arising from the thesis.

The following work has been published (to date):

Chapter 3 - C. Hayes, C. Greensill and K. Walsh, "Temporal and environmental sensitivity of a photodiode array spectrophometric system". *Journal of Near Infrared Spectroscopy*, **22**, 297 (2014)

Chapter 6 - C. Hayes, K. Walsh and C. Greensill, "Improving calibration transfer between shortwave near infrared silicon photodiode array instruments". *Journal of Near Infrared Spectroscopy*, **24**, 59 (2016).

Appendix A - C. Hayes, C. Greensill and K. Walsh, "The Impact of Lamp Environment on Prediction of Peach TSS Content" *Proceeding of The 29<sup>th</sup> International Horticultural Congress Symposia 2014, Brisbane*, In Press.

Name: Clinton John Hayes

Signature:

Date: 31<sup>st</sup> March 2016

# Copyright Statement

This thesis may be copied and distributed for private use and study, however, no chapter or materials of this thesis, in whole or in part, can be copied, cited or reprinted without the prior permission of the author and /or any reference fully acknowledged.

Name: Clinton John Hayes

Signature:

Date: 31<sup>st</sup> March 2016

# Table of Contents

Abstract.....	i
Acknowledgements.....	iii
Declaration of Authorship and Originality .....	iv
Copyright Statement .....	v
Table of Contents.....	vi
Table of Figures .....	ix
Table of Tables .....	xii
List of Abbreviations .....	xiii
1 Introduction.....	1
2 Underpinning Technology .....	3
2.1 NIR Spectroscopy .....	3
2.2 Vibrational Spectroscopy.....	3
2.2.1 Properties of light – polarisation.....	7
2.2.2 Optical geometry - Absorption .....	8
2.2.3 Optical geometry - Scattering and Reflection.....	9
2.3 Instrumentation .....	12
2.3.1 Light Sources .....	12
2.3.2 Gaining spectral information .....	17
2.3.3 Detectors .....	21
2.3.4 Spectrometer Specifications .....	23
2.3.5 Description of two common detectors .....	25
2.4 Chemometrics .....	30
2.4.1 Data Pre-treatment .....	30
2.4.2 Outliers.....	31
2.4.3 Models .....	31
2.4.4 Calibration Model Statistics/Testing/Assessment .....	33
2.4.5 Instrument Standardisation .....	34
2.5 Conclusion .....	45
3 Temporal and Environmental Sensitivity of a Photodiode Array Spectrophometric System .....	47
3.1 Introduction.....	48

3.2	Materials and Methods.....	51
3.2.1	Equipment.....	51
3.2.2	Experimental exercises: .....	53
3.2.3	Impact on predictive performance for a peach TSS model .....	53
3.2.4	Chemometrics .....	54
3.3	Results and Discussion .....	55
3.3.1	Stonefruit TSS PLS regression models.....	55
3.3.2	Spectral variation during lamp ‘warm-up’ .....	55
3.3.3	Spectral variation over lamp lifetime.....	59
3.3.4	Variation in components with environmental temperature.....	61
3.4	Conclusion .....	67
4	LEDs as light sources for spectroscopy of fruit - sensitivity to temperature .....	68
4.1	Introduction.....	69
4.2	Materials and Methods.....	74
4.2.1	Equipment.....	74
4.2.2	Experimental exercises: .....	75
4.3	Results and Discussion .....	76
4.3.1	Exercise 1 – Initial power up behaviour .....	76
4.3.2	Exercise 2 – Longer term power up behaviour .....	78
4.3.3	Exercise 3 – Response to temperature .....	80
4.3.4	Exercise 4 – Effect of environmental temperature on an LED based instrument (DA Meter) .....	83
4.4	Implications to instrument design.....	87
5	Characterisation of an interactance probe configuration in terms of the ratio of specular and diffusely reflected radiation .....	88
5.1	Introduction.....	89
5.2	Materials and Methods.....	92
5.2.1	Equipment.....	92
5.2.1	Experimental exercises: .....	93
5.3	Results and Discussion .....	93
5.3.1	Exercise 1 – MMS1 grating bias.....	93
5.3.2	Exercise 2 – Signal level with probe-sample distance.....	94
5.3.3	Exercise 3 – Polarised light characterisation of shadow probe.....	98
5.4	Conclusion .....	102

5.5	Acknowledgements.....	102
6	Improving calibration transfer between short wave near infrared silicon photodiode array instruments .....	104
6.1	Introduction.....	105
6.2	Materials and Methods.....	108
6.2.1	Instrumentation and fruit TSS.....	108
6.2.2	Experimental exercises .....	109
6.2.3	Chemometrics .....	112
6.3	Results and Discussion .....	114
6.3.1	Exercise 1. PDA response.....	114
6.3.2	Exercise 2. Impact of wavelength accuracy on PLS prediction of fruit TSS 118	
6.3.3	Exercise 3. Calibration transfer with on line unit .....	120
6.3.4	Exercise 4. Calibration transfer with handheld unit.....	123
6.4	Conclusion .....	124
6.5	Acknowledgements.....	125
7	Conclusion and future directions .....	126
8	References.....	130
9	Appendix A.....	143
10	Appendix B .....	153
11	Appendix C.....	170

# Table of Figures

Figure 1.1. Number of publications per annum .....	1
Figure 2.1. Calculated energy levels for (a) a simple harmonic oscillator and (b) an anharmonic oscillator. ....	5
Figure 2.2 Vibration modes of AX <sub>2</sub> group.....	6
Figure 2.3 Major analytical and relative peak positions for prominent NIR absorptions....	7
Figure 2.4 Scattering and polarisation of incident rays. ....	8
Figure 2.5 Specular reflectance .....	10
Figure 2.6 Comparison of the Kubelka-Munk (K) for given scattering coefficients and log(1/R) function. ....	11
Figure 2.7 Black-body emission spectrum at normal operating temperatures of QTH lamps.....	13
Figure 2.8 Illustrative representation of a blazed reflection grating.....	18
Figure 2.9 Graph of normalised black-body curve at 2900°C, actual and expected typical silicon detector response and diffraction grating efficiency.....	22
Figure 2.10 Spectral resolving power .....	23
Figure 2.11 Zeiss MMS1 and Ocean Optics USB2000+.....	25
Figure 2.12 Zeiss MMS1 schematic diagram .....	26
Figure 2.13. Ocean Optics USB2000+ .....	27
Figure 2.14 Signal transmission between two layers of neurons.....	43
Figure 2.15 Typical application of neural networks to calibration transfer.....	44
Figure 3.1. Spectral emittance as a function of temperature based on theoretical calculation (Planck's radiation law) .....	50
Figure 3.2. Graph of spectrometer output for three wavelengths .....	56
Figure 3.3. RMSEP variability, assessed as a SD (% TSS) (over the four hour trial), as a function of number of white reference spectra averaged before use in calculation of absorbance of the fruit data set. ....	56
Figure 3.4. PLS regression model prediction statistics (RMSEP, % TSS) based on use of white reference data collected at various times over 4 h from lamp power up .....	57

Figure 3.5. PLS regression model prediction statistics (RMSEP, % TSS) based on use of (average of ten) spectra collected at various times over 4 h from lamp power-up as white reference data .....	58
Figure 3.6. Spectral intensity of a lamp (OSRAM G) at 720 nm in the month ending in lamp failure.....	59
Figure 3.7. Spectral intensity (ADC) recorded of a white tile, with increasing lamp (OSRAM G) age, as a difference (top panel) and as percentage (bottom panel), recorded from spectra at 4 hours from power on.....	60
Figure 3.8. Plots showing model performance (as RMSEP, % TSS) using white references taken during lamp aging.....	61
Figure 3.9. Spectral intensity (ADC) recorded of a white tile, with increasing ambient temperature of the lamp .....	62
Figure 3.10. Spectral intensity (ADC) recorded of a white tile, with increasing ambient temperature of the FEE.....	65
Figure 3.11. Spectral intensity (ADC) recorded of a white tile, with increasing ambient temperature of the MMS1 spectrometer .....	66
Figure 4.1. Spectral output (ADCC) over the first second from power-on of a SMB880-1100-I LED operated at an ambient temperature of 23 °C.....	77
Figure 4.2. Intensity (ADCC) at 880 nm and maximum intensity at any wavelength (top panel) and the shift in peak wavelength emitted (bottom) of the SMB880-1100-I LED over a 6 min period from power-up. ....	78
Figure 4.3. The effect of environmental temperature (top panel) on SMB720R-1100 LED intensity (ADCC) (middle panel) and the wavelength of maximum intensity (bottom panel), monitored over a four hour period .....	79
Figure 4.4. Spectral output (ADCC) of a SMB720R-1100 LED with increase in environmental temperature from 10 to 60 °C.....	80
Figure 4.5. Wavelength of peak emission at a range of environmental temperatures for a SMB720R-1100 LED.....	81
Figure 4.6. Spectral intensity relative to that at 10 °C with change in environmental temperature, presented on a linear (top panel) and a logarithm (bottom panel) scale for intensity.....	82
Figure 4.7. Wavelength of peak emission at a range of environmental temperatures for the DA Meter.....	83

Figure 4.8. DA Meter $I_{AD}$ Index measurement of two mango fruits (1, 2) at two positions (A, B) with the instrument at various operating temperatures .....	84
Figure 4.9. Absorbance spectra of a mango fruit measured with an MMS1 spectrometer in an interactance mode. ....	85
Figure 4.10 Change in calculated $I_{AD}$ index of several mangos with shift in wavelength compared ( $A_{670+\lambda} - A_{720+\lambda}$ ), taken from full spectrum absorbance measurements. A 10°C increase in temperature gives approximately a 2 nm increase in peak wavelength. Results shown for a sample from 60 mango fruits.....	86
Figure 5.1. Shadow probe configuration, consisting of a parabolic reflector with lamp, projecting light past an optical probe which casts a shadow onto the sample (fruit).....	90
Figure 5.2. Ray tracing of shadow probe setup used (worst case scenario) .....	95
Figure 5.3. Detected light level (800 nm) for four shadow probe assemblies, for various probe-sample distances.....	97
Figure 5.4. Apple spectra at a probe-sample distance of 0 and 150 mm. ....	99
Figure 5.5. Ratio of specular to diffuse radiation at 800 nm, received at various probe-sample distances from an apple and a kiwi fruit. ....	102
Figure 6.1. Spectra of sample analogue to digital conversion count (ADCC) of a PFTE tile using the same light source but four different MMS1 spectrometers. .	115
Figure 6.2. Graph of PDA photometric response of different pixels within the same MMS1 unit.....	116
Figure 6.3. Graph of PDA photometric response of the same wavelength from different MMS1 units.....	117
Figure 6.4. Effect of a shift in wavelength scale by up to 5 nm on (top) RMSEP, (middle) SEP and (bottom) Bias for a PLSR regression model of total soluble solids (%TSS) of peach fruit created on the same data set (and original wavelength assignments). ....	119

# Table of Tables

Table 2.1. Commonly available wavelengths (nm) in LEDs, specified at 25 °C from Ushio Epitex Inc., Kyoto, Japan and Roithner LaserTechnik GmbH, Wien Austria. . 16	
Table 2.2 Photodiode Detector Characteristics .....	21
Table 2.3 Specifications of the Zeiss MMS1 NIR enhanced and Ocean Optics USB2000+ VIS-NIR-ES configured spectrometer .....	29
Table 3.1. Typical prediction statistics for a model based on reference spectra collected at 10 °C, used in prediction of a population with references at different temperatures, where temperature was varied of either (A) lamp, (B) FEE or (C) MMS1 ambient temperature.....	64
Table 4.1. LED (Epitex) specifications, for operation at 25 °C for each of peak wavelength and FWHM, at the stated forward current ( $I_F$ ) used for specifications, and typical driven current and forward voltage used in normal operation. ....	74
Table 4.2. Wavelength of peak emission and relative intensity of emission, for a 940 nm LED at a range of environmental temperatures.....	81
Table 4.3. Increase in peak wavelength position per degree environmental temperature increase with a linear fit for 9 LED types. ....	82
Table 5.1. Measurement of lamp and reflector characters .....	96
Table 5.2. MMS1 output (ADCC) at 800 nm assessed for different probe-fruit distances for an apple. ....	100
Table 5.3. MMS1 output (ADCC) at 800 nm assessed for different probe-fruit distances for a kiwi fruit. ....	101
Table 6.1. Apple total soluble solids (%TSS) for PLS regression model statistics for three different MMS1 units, for the manufacturer assigned wavelengths, new 4th order polynomial fit and a linear fit .....	120
Table 6.2. Apple total soluble solids (%TSS) prediction statistics for various master-slave combinations and transfer methods.....	121
Table 6.3. Apple total soluble solids (%TSS) model validation statistics for four handheld units, using pre-treatments of mean centring and autoscaling. ....	123
Table 6.4. Apple total soluble solids (%TSS) prediction statistics using unit A as the master, given use of several transfer methods.....	124

# List of Abbreviations

A	Absorbance
ADC	Analogue to digital conversion
ADCC	Analogue to digital conversion count
AlGaAs	Aluminium Gallium Arsenide
AlInGaP	Aluminium Gallium Indium Phosphide
ANN	Artificial neural network
AOTF	Acoustic optical tuneable filter
CCD	Charge coupled device
CLS	Classical least squares
DM	Dry matter
DS	Direct standardisation
DSA	Difference spectrum adjusted
DWPDS	Double window piecewise direct standardisation
FEE	Front end electronics
FFT	Fast Fourier transform
FIR	Finite impulse response filtering
FP	Fabry-Perot
FT	Fourier transform
FTNIR	Fourier transform near infrared
FWHM	Full width half maximum

GaAs	Gallium Arsenide
GLSW	Generalised least squares weighting
ILS	Inverse least square
InGaAs	Indium Gallium Arsenide
InGaAsP	Indium Gallium Arsenide Phosphide
InGaN	Indium Gallium Nitrogen
IR	Infrared
LED	Light emitting diode
MIR	Mid infrared
MLR	Multiple linear regression
MSC	Multiplicative scatter correction
MU	Model updating
NIR	Near infrared
NIRS	Near infrared spectroscopy
NN	Neural networks
OPLS	Orthogonal projection to latent structures
OSC	Orthogonal signal correction
PC	Principal component; synonymous to factor in multivariate analysis
PCA	Principal component analysis
PCR	Principal component regression
PDA	Photodiode array

PDS	Piecewise direct standardisation
PLS	Partial least squares
PLSR	Partial least squares regression
PTFE	Polytetrafluoroethylene (Teflon)
QTH	Quartz tungsten halogen
R	Correlation coefficient
$R^2$	Coefficient of determination
RMSEC	Root mean square error of calibration
RMSECV	Root mean square error of cross validation
RMSEP	Root mean square error of prediction
RPD	Ratio of standard error of prediction to standard deviation
SBC	Slope and bias correction
SD	Standard deviation
SDR	Ratio of standard deviation to standard error of prediction
SEC	Standard error of calibration
SEP	Standard error of prediction
SG	Savitzky Golay
Si	Silicon
SNR	Signal to noise ratio
SNV	Standard normal variate
SSBC	Spectral slope/bias correction

SSC	Soluble solid content
SWNIR	Short wave near infrared spectroscopy (700-1100 nm)
TA	Titrateable acidity
TOP	Transfer by orthogonal projection
TSS	Total soluble solids
UV	Ultraviolet
Vis-NIR	Visible near infrared spectroscopy
WT	Wavelet transform

# 1 Introduction

Near infrared (NIR) spectroscopic systems have been successfully utilised in non-invasive analysis of internal attributes of fresh horticultural produce over the last 25 years, with the first commercial use claimed by Mitsui (Japan) in 1988. The technology has been used in assessment of parameters such as total soluble solid content (TSS), dry matter (DM), acidity and other internal characteristics in real time, in both an in-line packhouse environment and in orchard. Instrument specifications for the required assessment of internal quality attributes, vary according to attribute and fruit type. This thesis focuses on the assessment of TSS or DM in fruit.

However, the technology is not yet fully mature in this application, as apparent in the number of publications per annum (Figure 1.1). Issues include sample geometry, lamp type, lamp and detector stability, model transfer across instruments and robustness in terms of function in the face of varying temperature and ambient light levels.

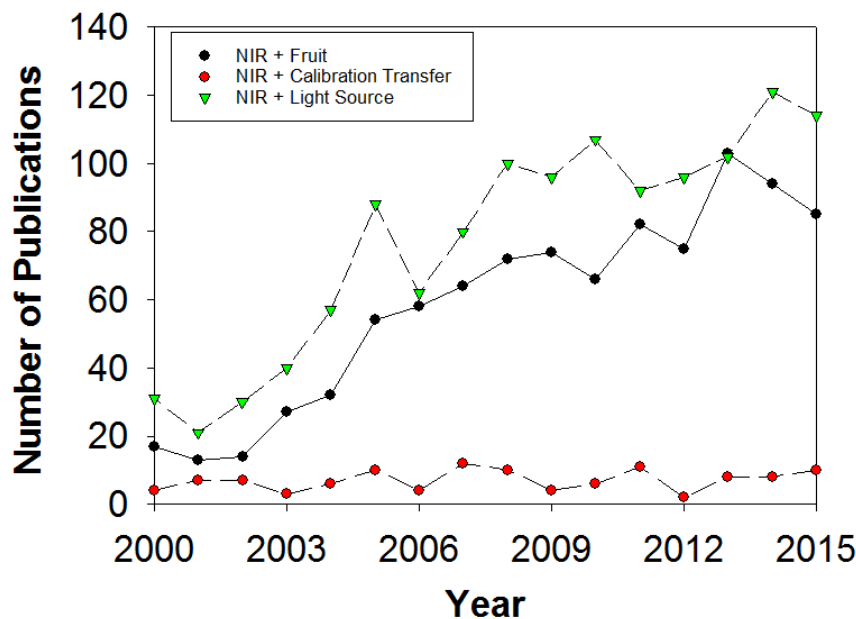


**Figure 1.1. Number of publications per annum, based on use of the keywords “Near Infrared + Fruit”, “Near Infrared + Fruit + Calibration Transfer” and “Near Infrared + Light Source” within Scopus database<sup>1</sup> as shown this figure (searched on 23 March 2016)**

Due to the popularity of fresh horticultural produce, and widespread awareness of internal quality issues, there has been an allure for many manufacturers attempt to enter the fruit assessment industry. The industry, however, is low cost, given the low cost product (fruit), non-technical and the market size is comparatively small. The harvest period is limited, and so equipment is not fully used, sitting idle for many months. The high moisture content, variable environmental conditions, limited attribute range, and sample matrix inconsistencies make it a demanding field, thus few manufacturers have survived or devices been widely adopted.

The following section reviews the science and technology underpinning the field of NIRS. Subsequent chapters present focussed literature reviews and experimental work on specific topics. Chapter 3 investigates quartz tungsten halogen lamp stability from power up and with temperature variations; and front end electronics and spectrometer readout with temperature variations. Chapter 4 assesses light emitting diode output with respect to elapsed time from power up and variation in environmental temperature. Chapter 5 deals with an optical geometry suited to non-contact assessment of fruit. Chapter 6 investigates transfer of calibration models for TSS of intact apple fruit between instrumentation based on silicon photodiode arrays.

## 2 Underpinning Technology

### 2.1 NIR Spectroscopy

In 1800, Sir William Herschel<sup>2</sup> investigated the amount of heat in each colour. Sunlight was directed through a prism to create a spectrum and made to fall on a thermometer. It was noted that the temperature of the colours increased from violet to the red part of the spectrum. The thermometer was moved to just beyond the visible (red) part of the spectrum and it was noted the temperature was highest in this region. He named this radiation “calorific rays” (derived from the Latin word for heat), later called infrared (IR) (the Latin prefix *infra* means “below”).

The near infrared region of the electromagnetic spectrum refers to the portion extending from the end of the visible range to the beginning of the IR spectral region. It is defined by the International Union of Pure Applied Chemistry (IUPAC) as the region 780 to 2500 nm.<sup>3</sup>

When electromagnetic radiation interacts with matter it may be absorbed, transmitted or reflected. The conservation of energy requires that the total incident radiant energy be equal to the sum of the radiant power absorbed, transmitted and reflected. For NIR spectroscopy, the specularly reflected data is rejected as non informational and the fraction of incident light subject to scattering or absorption is used. The measured deficiencies in the exiting electromagnetic energy can provide the identifying ‘fingerprint’ of the constituent molecules.

### 2.2 Vibrational Spectroscopy

The theory of vibrational spectroscopy is briefly reviewed in this section. For greater depth the reader is referred to Ciurczak<sup>4</sup>, Eisberg and Resnick<sup>5</sup>, Siebert and Hildebrandt<sup>6</sup> or Sathyanarayana<sup>7</sup>. The starting point for understanding vibrational spectroscopy is simple harmonic oscillation and Hooke’s Law. Hooke’s Law ( $F = -k_f x$ , where  $F$  is the force,  $k_f$  is the force constant and  $x$  is the distance travelled) can be combined with Newton’s Law ( $F = ma$ , where  $F$  is the force,  $m$  is the mass and  $a$  is the acceleration) to derive the classic equation for a simple harmonic oscillator (Eqn 2.1).

$$v = \frac{1}{2\pi} \sqrt{\frac{k_f(m_1 + m_2)}{m_1 m_2}} = \frac{1}{2\pi} \sqrt{\frac{k_f}{\mu}} \quad \text{Eqn 2.1}$$

where  $v$  is the vibrational frequency,  $k_f$  is the classical force constant and  $\mu$  is the reduced mass of the two atoms. The fundamental vibrations for diatomic molecules in the fundamental mid infrared (MIR) region of 2500 – 50000 nm can be derived from this equation. The NIR region contains combination bands and overtones of these fundamental frequencies.

In his studies of black body radiation in 1900, Max Planck proposed that the energy of an oscillator was discontinuous, and that changes in energy content (at a quantum level) could only occur between two discrete energy states. The discrete energy level steps were related to the frequency of the electromagnetic radiation,  $\nu$ , by the equation  $\Delta E = h\nu$ , where  $E$  is the energy and  $h$  is Planck's constant. Application of Schrödinger's equation yields solutions that are the quantum equivalent of a classical simple harmonic oscillator. This is given by

$$E_n = (n + 0.5)h\nu \quad (n = 0, 1, 2, \dots) \quad \text{Eqn 2.2}$$

where  $n$  is the vibrational quantum number.

The equation for a simple harmonic oscillator is only valid for ideal systems and, therefore, does not accurately describe the reality at a quantum level. In reality, molecules do not obey the laws of simple harmonic motion. Other inter-nuclear forces also contribute to the distribution of the molecular system. As two atoms approach each other, the potential energy, due to Coulomb repulsion, rises more rapidly than the harmonic model predicts. The equation to describe the anharmonic oscillator (Figure 2.1) is:

$$E_n = h\nu_0 \left[ \left( n + \frac{1}{2} \right) - x_e \left( n + \frac{1}{2} \right)^2 + y_e \left( n + \frac{1}{2} \right)^3 - \dots \right] \quad \text{Eqn 2.3}$$

where  $x_e$  and  $y_e$  are the anharmonic constants. For small values of  $n$  in Eqn 2.3, the third term and beyond can be ignored. The selection rules become  $\Delta n = \pm 1, \pm 2, \pm 3, \dots$

The transition from the ground state,  $n = 0$ , to the  $n = 1$  state produces the fundamental band. This transition has the highest probability and falls in the MIR region<sup>8</sup>. The

transitions from ground to higher states,  $n = 2, 3, 4, \dots$  produce overtones and occur within the NIR region. Combination bands, which also occur in the NIR region, emerge if two or more different vibrations interact to produce bands that are the sums (or differences) of multiples of fundamental frequencies. These overtones and combination bands characteristically have broad bandwidths (typically 30-40 nm FWHM)<sup>9</sup> and are extremely weak, typically about 100 times, compared to their corresponding mid IR counterparts<sup>10</sup>.

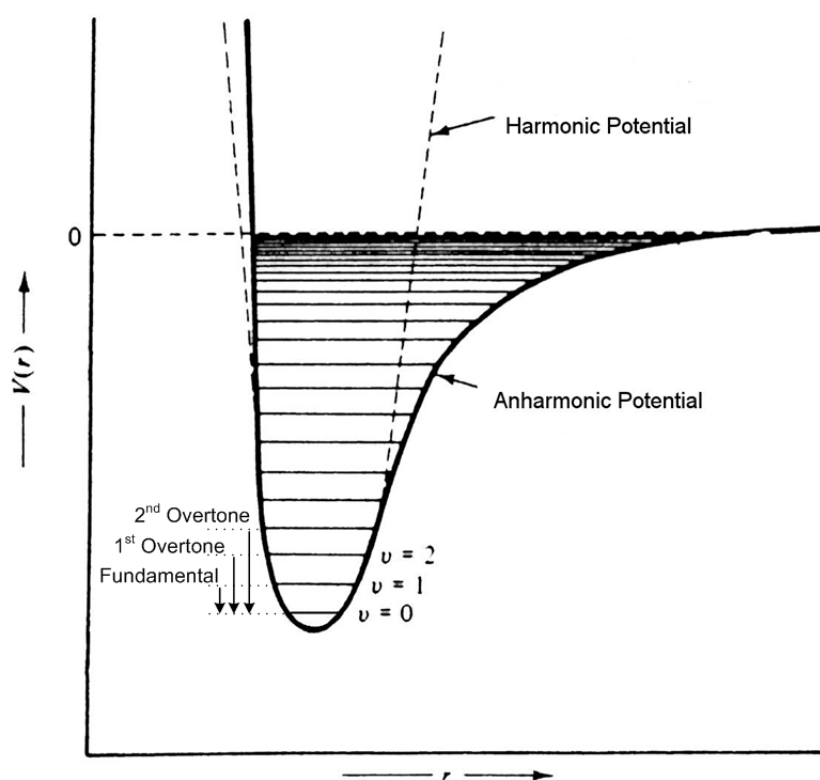


**Figure 2.1. Calculated energy levels for (a) a simple harmonic oscillator and (b) an anharmonic oscillator.  $V(r)$  is the potential (or energy),  $r$  is the interatomic distance and  $v$  is the vibrational quantum number<sup>4</sup>**

For a molecule to absorb electromagnetic energy in the infrared region (that is, for it to be IR active), the molecular vibration must cause a change in the dipole moment of the molecule. Spectral observations in the NIR region come principally from energy interactions from  $AX_2$  groups (triatomic molecules) and  $AX_3$  groups. Vibrations can include either stretching or bending movements, which involve changing of the interatomic distance or angle of the bonded atoms respectively (Figure 2.2).

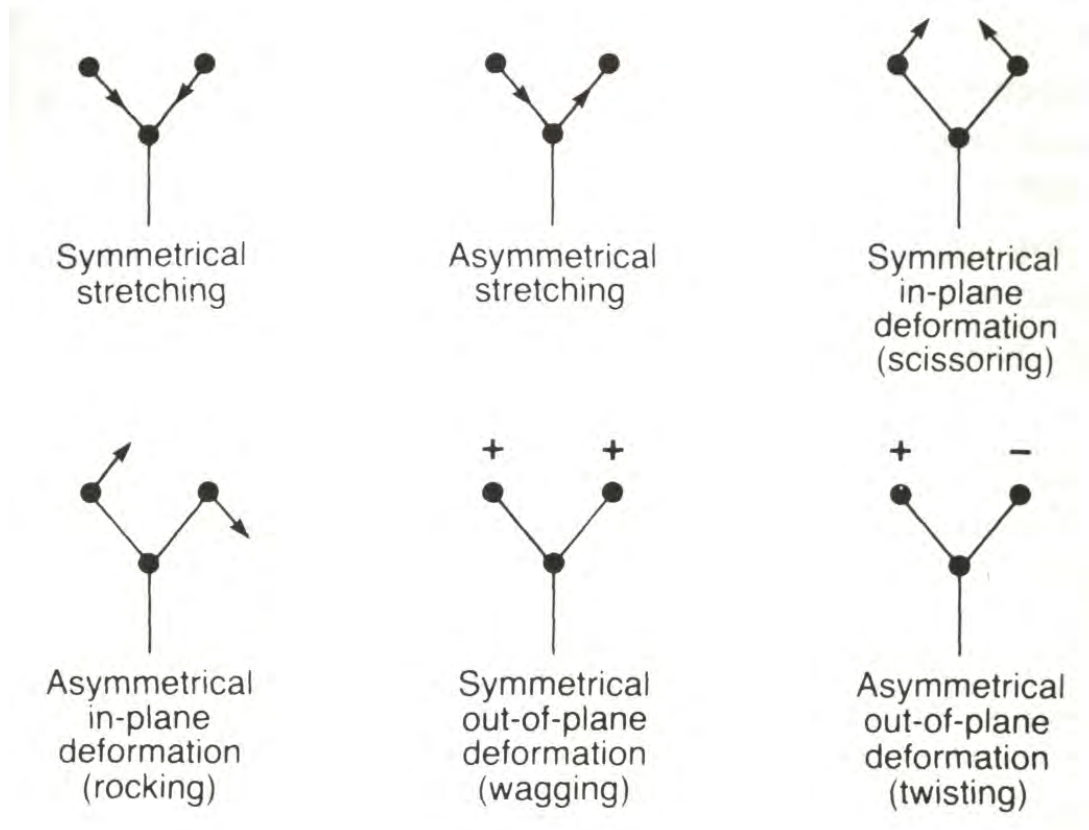


**Figure 2.2** Vibration modes of AX<sub>2</sub> group<sup>8</sup>

Each of these vibrational modes may yield overtones or combinations observable in the NIR. Eqn 2.4 and Eqn 2.5 define the energy levels for vibrational and rotational energy levels respectively.

$$E_{vib} = \hbar\omega \left( v + \frac{1}{2} \right) \quad v=1, 2, 3, \dots \quad \text{Eqn 2.4}$$

$$E_{rot} = \frac{\hbar^2}{2I_{cm}} j(j+1) \quad j=1, 2, 3, \dots \quad \text{Eqn 2.5}$$

where  $v$  is the vibrational quantum number,  $\omega$  is the classical frequency of vibration,  $j$  is the rotational quantum number and  $I_{cm}$  is the moment of inertia about the reduced mass. For combination band energy levels the relationship simply becomes:

$$\begin{aligned} E_{rot+vib} &= E_{rot} + E_{vib} \\ &= \frac{\hbar^2}{2I_{cm}} j(j+1) + (v + \frac{1}{2})\hbar\omega \end{aligned} \quad \text{Eqn 2.6}$$

The higher order overtones have lower absorption. Low absorptivity allows for the use of longer path lengths, allowing little or no sample preparation. The most prominent absorption bands in the NIR region are related to hydrogen bonds, for example, C-H, N-H and O-H molecular groups (Figure 2.3).<sup>11, 12</sup> For biological samples, the presence of water, a strong absorber, can limit effective path lengths.

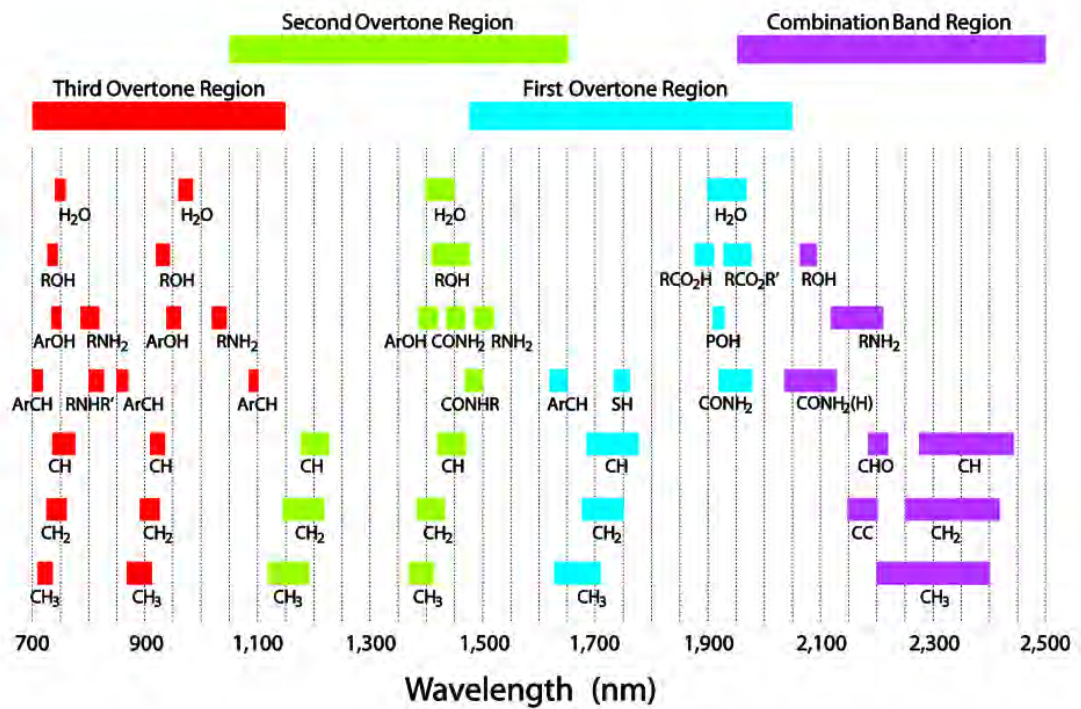
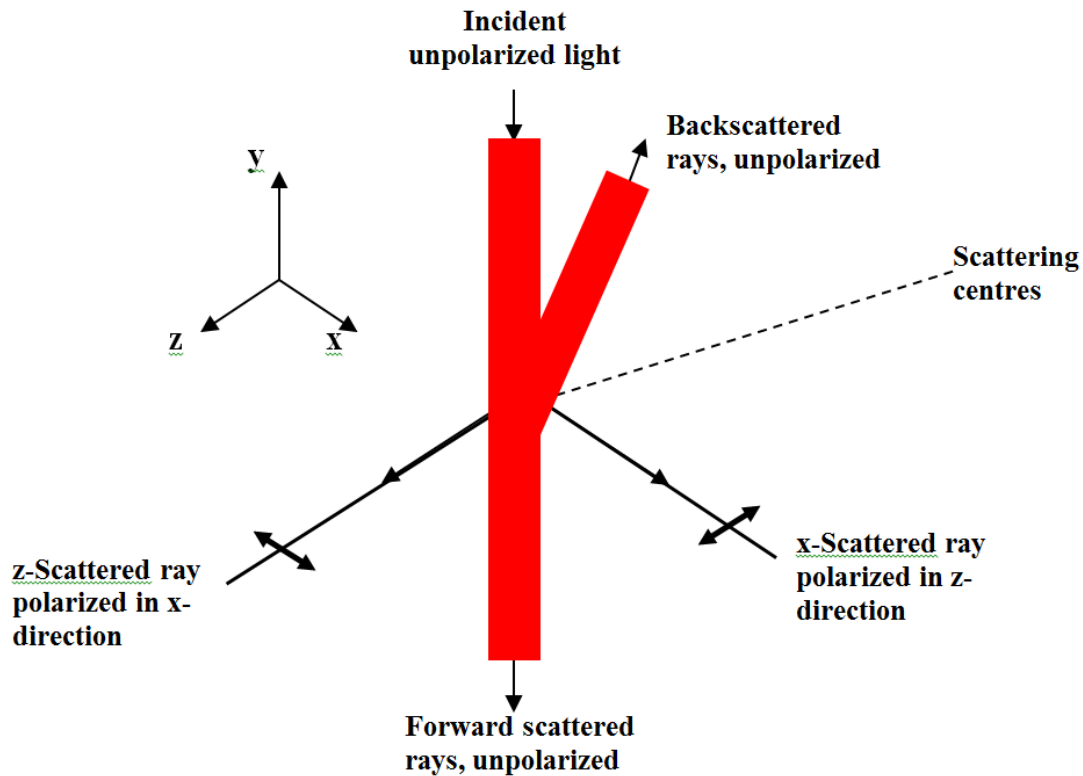


Figure 2.3 Major analytical and relative peak positions for prominent NIR absorptions<sup>13</sup>

### 2.2.1 Properties of light – polarisation

Back-scattered and forward-scattered rays are unpolarised (Figure 2.4), while rays scattered perpendicular to the incident rays are polarised. This is due to the fact that the vibrating electrons of particles in scattering centres absorb light and then re-emit it asymmetrically, with most light emitted perpendicular to the electronic vibration direction.



**Figure 2.4 Scattering and polarisation of incident rays.**

Once the source is polarised, a second linear polariser (polariser analyser) can be used to either transmit or absorb the light. When a second polariser is rotated, the vector component perpendicular to its transmission plane is absorbed, reducing its amplitude to<sup>14</sup>

$$E = E_0 \cos \theta \quad \text{Eqn 2.7}$$

Since the transmitted intensity is proportional to the amplitude squared, the intensity is given by the Law of Malus<sup>14</sup>

$$I = I_0 \cos^2 \theta \quad \text{Eqn 2.8}$$

### 2.2.2 Optical geometry - Absorption

NIR spectral analyses can be based on diffuse reflectance, or full or partial transmittance of the incident electromagnetic radiation through the object of interest. By considering light as an electromagnetic wave, in a three-dimensional space the electric field vector can oscillate up and down, side to side, or anywhere in between. Incandescent, fluorescent, light emitting diode (LED), and many laser light sources are randomly

polarised. Taken as a time average, therefore, randomly polarised light sources continuously output all angles of polarisation.

Quantitative absorption spectroscopy relies fundamentally on the Beer-Lambert Law. This law describes the relationship between absorbance and concentration of an absorbing species, stating that the fraction of radiant energy  $P$ , absorbed in an infinitesimal thick sample, is proportional to the number of molecules  $dn$ , in that sample:

$$\frac{-dP}{P} = k dn \quad \text{Eqn 2.9}$$

which gives

$$\log\left(\frac{1}{T}\right) = \log\left(\frac{P_0}{P_T}\right) = A = abc \quad \text{Eqn 2.10}$$

where  $T$  is the transmittance (ratio of transmitted energy  $P_T$  to incident energy  $P_0$ ),  $A$  is the absorbance,  $a$  is a wavelength-dependent absorptivity coefficient,  $b$  is the sample thickness, and  $c$  is the analyte concentration.

### 2.2.3 Optical geometry - Scattering and Reflection

The Beer-Lambert Law does not allow provision for other interactions, such as reflection or scattering. In practice some radiation will be transmitted through the first interface. If it undergoes absorption, it will be attenuated, according to the Beer-Lambert Law. At further interfaces inside the sample, random reflections, refractions and scattering may occur inside the sample to diffuse the radiation emerging from this first boundary. Scattering caused by radiation encountering discrete particles inside the sample that are much larger than the wavelength. The radiation can undergo further transmittance and absorption at other interfaces, or be re-emitted from the surface, producing diffuse body reflection (Figure 2.5). The phenomenon, known as scattering, was described by Tyndall in 1869<sup>8</sup>. When destructive interference becomes incomplete, the radiation propagates in all directions.

For most materials, except metals, at least 4 percent<sup>8</sup> of incident radiation undergoes specular reflectance and therefore a significant level of background specular reflectance is superimposed on the diffuse reflectance arising from internal effects. If the sample

surface is described as being ‘matt’, the boundary between the sample and the surrounding medium consists of a series of small edges, directed at all possible angles to the normal (Figure 2.5). The first consequence of this is to diffuse the specular component of reflectance<sup>8</sup>. NIR reflectance spectroscopy implements mathematical and physical techniques to minimise this surface specular reflectance component to use only the diffuse component originating from within the sample for analyses.

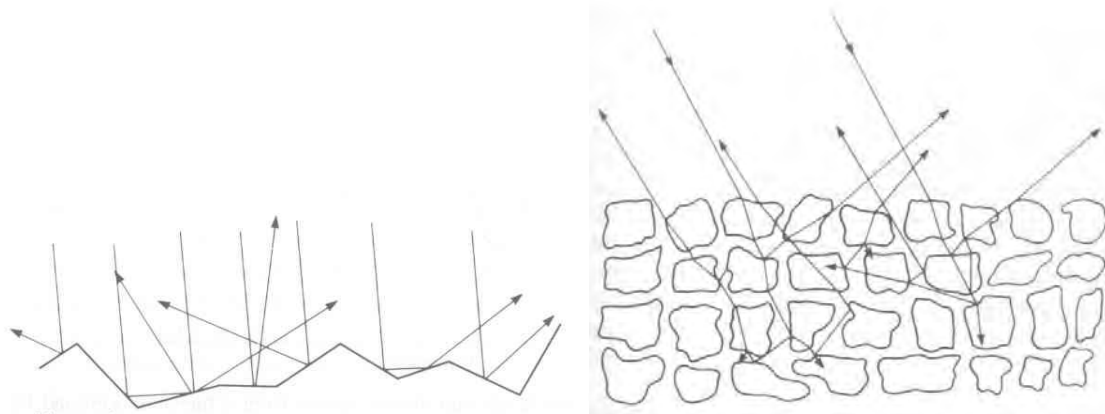


**Figure 2.5 Specular reflectance by a matt surface (left) and diffuse body reflectance (right)<sup>8</sup>**

It is extremely difficult to describe mathematically the exact path of the propagating radiation. The widely adopted method for describing the interaction of light with diffusing media is that formulated by Kubelka and Munk<sup>8</sup>. Their theory relates the total diffuse reflection from a sample to the scattering and absorption coefficients of that sample. The special case of a layer of infinite thickness that is completely opaque with a homogeneous distribution of absorbers and scatters can be described by the Kubelka-Munk function:

$$F(R) = \frac{(1-R)^2}{2R} = \frac{K}{S} \quad \text{Eqn 2.11}$$

where R is the observed diffuse reflectance, K and S are absorption and scattering coefficients respectively. F(R) is proportional to the absorber concentration.

Diffuse scattering from solids contain spectral information, and the Kubelka–Munk function is the theoretically preferred treatment<sup>8</sup>. However, it has found little favour with experimentalists in NIR spectroscopy, with preference given to use the function  $\log(1/R)$

to describe the absorbance. The most often quoted advantage for the Kubelka-Munk function is an improvement in linearity with concentration, which occurs when measurements are made over a wide range of reflection and concentration.

Both the Kubelka-Munk function and  $\log(1/R)$  are proportional to absorbance, and the interrelation with Reflectivity is shown in

Figure 2.6, for three scattering coefficients. Higher scattering results in higher reflectivity. As for the Kubelka-Munk function, the decline in absorbance at increasing reflectivities is much more rapid than that for the  $\log(1/R)$  function.

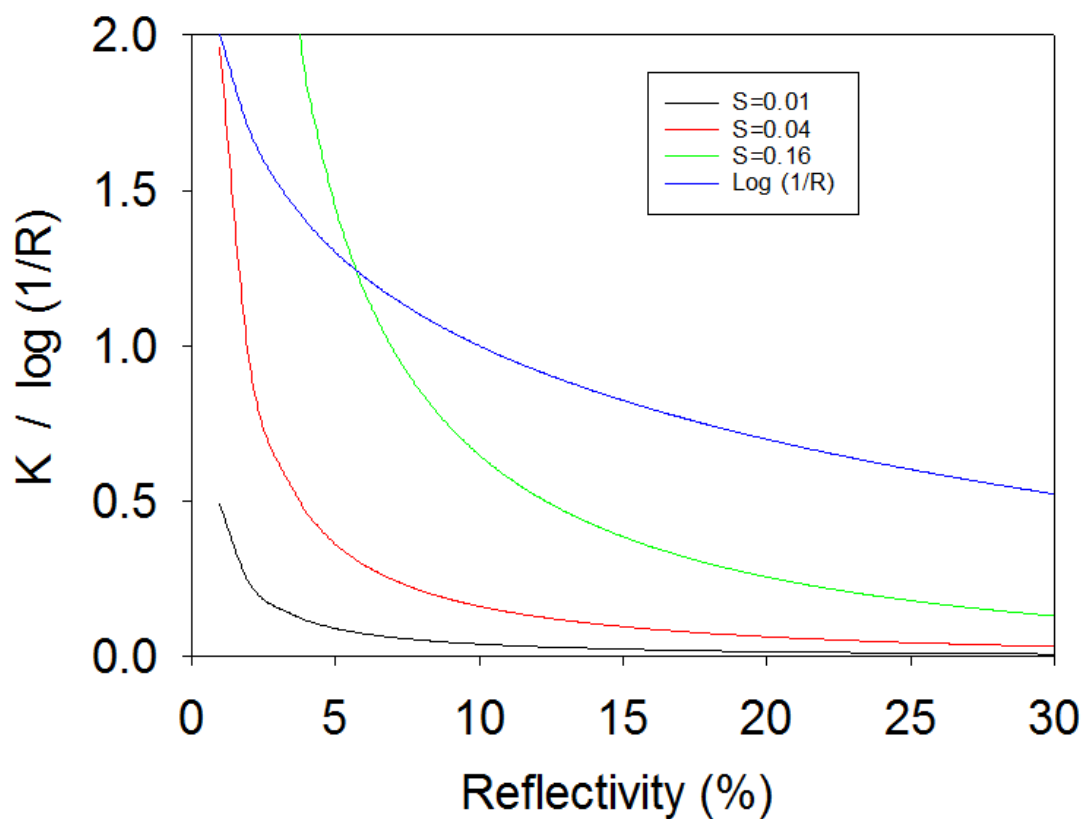


**Figure 2.6 Comparison of the Kubelka-Munk (K) for given scattering coefficients and  $\log(1/R)$  function.**

## 2.3 Instrumentation

The first instrument to automatically record NIR absorption spectra was developed by Kaye et al.<sup>15</sup> in 1951 using a lead sulphide detector to replace the photomultiplier tube of a Beckman Model DU spectrometer (Beckman Coulter Inc., Brea, CA, USA). Fourier Transform Near Infrared (FTNIR), Scanning Grating, Acousto-Optical Tuneable Filter (AOTF) and Photodiode Array (PDA) spectrometers are several different types of NIR spectrometers that are now commercially available. These instruments all use different principles to measure the NIR spectrum. It is generally accepted that the basic requirements of an NIR instrument are as follows<sup>8</sup>:

1. Detect within the NIR spectral window (700-2500 nm), depending on the application.
2. The instrument should be capable of resolving wavelength intervals that are narrow compared to an absorption feature, typically 0.1-2 percent of the measured wavelength.
3. For solid samples, an optical geometry suited to work with diffusely scattered radiation is required.
4. For liquid samples a transmission design may be required.
5. A wide photometric (or dynamic) range of  $10^4$ - $10^5$  may be required for weak or small absorption changes to be measured.
6. The instrument should be sufficiently luminous and efficient, to enable measurements to be acquired in real time.
7. The instrument should be robust and stable. It is also desirable for the equipment to be compact.

NIR spectrometers have three main components – light source, dispersion mechanism and detector. Each is discussed in the following sections.

### 2.3.1 Light Sources

#### 2.3.1.1 Thermal Sources

The quartz tungsten halogen (QTH) lamps, commonly referred to as quartz halogen lamps, are generally employed by dispersive and interferometric systems. The QTH lamp

is filled with halogen gas, which combines with the tungsten that has been sublimed from the filament. By dissociation the tungsten is deposited back on the hot filament. This procedure allows the lamp to run hotter and more efficiently. QTH lamps have running temperatures from 2600 to 3200 K<sup>8</sup>. The lamps have a finite life, due to the tungsten being randomly deposited on the filament, not necessarily the thinnest portion, which becomes coarsely crystalline, brittle and therefore prone to mechanical shock. Its life is highly dependent on its operating temperature. Typically QTH lamps have a life of 2000-3000 hours, with instrument grade lamps having a life of 10 000+ hours – operating at the lower end of the operating temperate range<sup>8</sup>.

Incandescent objects (such as tungsten) emit energy that approximates that of a blackbody. The spectral output of a QTH lamp is thus dependent on the operating temperature. At 3000K (the normal temperature of a QTH lamp) tungsten has a peak emission (Figure 2.7) of approximately 950 nm<sup>16</sup>, roughly coinciding with the peak efficiency of a silicon based detector, approximately 850 nm<sup>8</sup>. Their spectral output generally varies less than 2 percent until failure<sup>10</sup>. More detail of QTH lamp operation is covered in Chapter 3.

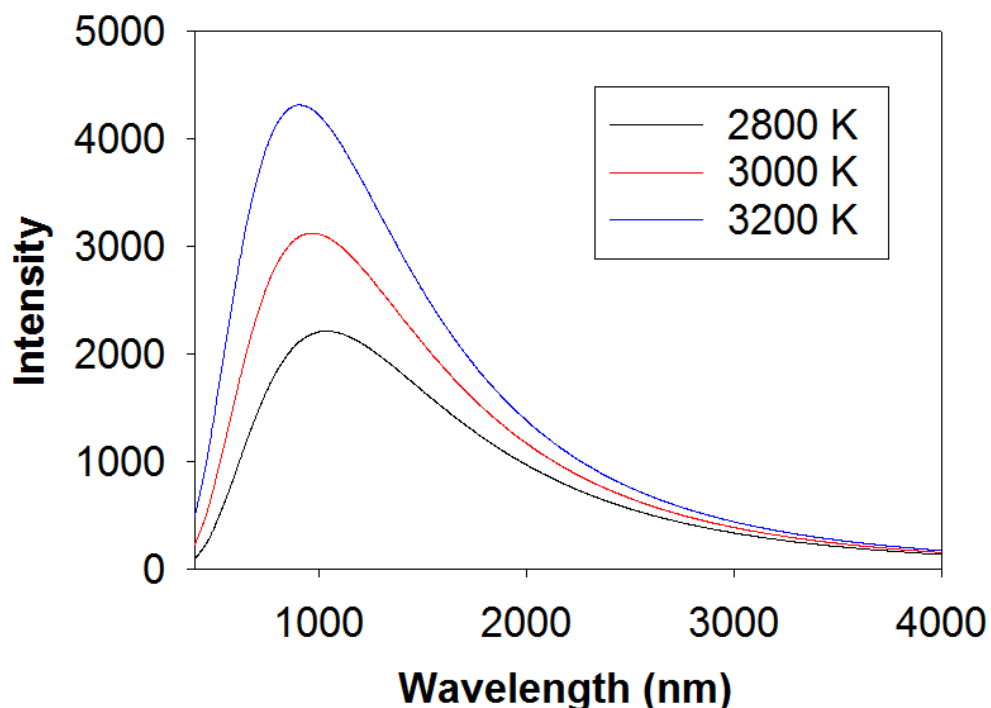


**Figure 2.7 Black-body emission spectrum at normal operating temperatures of QTH lamps**

### 2.3.1.2 Non-thermal Sources

Non-thermal sources emit radiation from a much narrower range of wavelengths, down to individual lines. These emitters are devices such as discharge lamps, LEDs, laser diodes and lasers. The advantage of non-thermal sources is their energy efficiency.

Due to their efficiency and now low cost, many instrument manufacturers are investigating the use of LEDs to replace QTH as light sources. An LED is an optoelectronic component, consisting of a chip of semiconducting material doped with impurities to create a p-n junction. In silicon or germanium diodes, p-n junctions, electrons and holes from n-type and p-type materials (the majority carriers), are injected across the junction to establish the flow of current. The electrons and holes usually recombine by a non-radiative transition, which produces no optical emission, because these are indirect band gap materials. Materials used in an LED have direct band gaps, with energies corresponding to bands in the near-infrared, visible, or near-ultraviolet. Light is produced from radiative recombination.

LEDs are considerably more efficient than QTH and arc-discharge lamps at converting electricity into visible light, often achieving outputs of up to 100 lumens per watt compared to the 22 lumens per watt for a 100 W arc-discharge lamp. LEDs are rugged and compact, and can survive for >100,000 hours<sup>17</sup> or approximately 500 times longer than a typical QTH lamp with life of 2000 hours<sup>18</sup>. Some manufacturers guarantee a lifetime of 100,000 hours before the source intensity drops to 70% of the initial value<sup>17</sup>. Under given conditions, LED spectral output remains stable throughout life. QTH lamps are also spectrally stable until close to their end of life<sup>19</sup>. However, due to low output power, a cluster of diodes is usually required to obtain an adequate signal-to-noise ratio (SNR), especially in diffuse reflection measurements.

LED light output is proportional to current flow, making LEDs particularly suitable to be driven by a microcontroller<sup>20</sup>. LEDs also have the advantage of being able to be “pulsed” for periods of milliseconds to higher voltages and/or currents to produce higher light output, whilst not burning out. Pulsing is more energy efficient and allow for greater heat dissipation relative to continuous current use. Instruments incorporating LEDs can have sub millisecond cycle times for pulse and detector readout. Indeed, information transfer is possible through such pulsing (so called ‘li-fi’).

Impurities, structural dislocations, and other crystalline defects in semiconductor materials can lead to non-radiative recombination events, which do not result in emission of a photon. A primary goal in LED design is to maximize the radiative recombination of charge carriers by careful selection of suitable semiconductor materials to provide the appropriate band structure in order to produce favourable quantum efficiency values.

Nearly all LED structures are composed of a layered configuration in which a series of lattice-matched materials are deposited on top of one another, with a transparent moulded plastic (polymer) to gather and focus the emitted light (lens). The amount of light escaping an LED is dependent upon the specific semiconductor materials, the p-n junction characteristics, and epoxy dome lens material and shape. The remaining light is absorbed within the semiconductor via total internal reflection. In a typical LED having a cubic geometry, only about 2 percent of the generated light is able to escape through the top surface, hence LEDs emit radiation in a narrow cone<sup>17, 21</sup>. When combined with the hemispherical epoxy dome, LED emission can typically range from  $\pm 7^\circ$  to  $\pm 62^\circ$  half viewing angle (50% intensity), depending on the dome/lens<sup>22</sup>. Due to low output power, a cluster of diodes is usually required to obtain an adequate illumination level, and thus signal-to-noise ratio (SNR).

There are few manufacturers of SWNIR wavelength LEDs. Commercially available LED visible-SWNIR wavelengths are given in Table 2.1 for two manufacturers.

**Table 2.1. Commonly available wavelengths (nm) in LEDs, specified at 25 °C from Ushio Epitex Inc., Kyoto, Japan and Roithner LaserTechnik GmbH, Wien Austria.**

Epitex			Roithner LaserTechnik		
365	620	800	365	620	810
375	630	810	375	630	820
385	660	830	385	635	830
395	680	850	395	650	850
405	690	870	405	660	870
415	700	880	410	670	880
420	720	910	420	680	940
430	735	940	435	690	970
450	740	970	450	700	980
470	750	980	470	720	1020
490	760	990	490	730	1030
520	770	1050	505	735	1050
525	780	1070	515	740	1300
		1200	520	750	1550
		1300	525	760	
		1450	590	770	
		1550		780	
		1600		780	

“White light” LEDs can be produced using two approaches. The first approach involves combination of the output of three monochromatic LEDs, red; green; and blue, in such a proportion that the output appears white, by either using different semiconductor materials in a common die, or by combining red, green, and blue diode dies into a single package, or in a lamp assembly housing a cluster of diodes. By employing circuitry that drives the three diodes independently, any combination of colours can be created, including white light. The second approach is to use an ultraviolet or violet (365 to 450 nm) LED to excite phosphor which then emits white light.<sup>17</sup>

Laser diodes and lasers emit over a narrow range of wavelengths, eliminating the need for pre-filtering for some applications. However, LEDs emit a wide range of wavelengths (typical FWHM 50 nm) and an interference filter is normally required so that radiation is limited to a suitable bandwidth.

There have been attempts to develop SWNIRS instrumentation based on LEDs as light sources, generally utilising one of two approaches : (i) sequential activation of LEDs at

discrete wavelengths, with use of a single detector; and (ii) use of a series of LEDs with overlapping emission or a white phosphor based LED that acts as a broadband source, with use of a grating to disperse light. However, given that the dependence of LED output on temperature is well known, surprisingly most reports fail to mention the effect of temperature. For example, temperature was not considered in the following reports:

Gaião et al.<sup>23</sup> constructed a portable instrument based on a 1550 nm LED (L1550-35k42 Eptitex Inc., Japan) and a PbSe photoresistor as detector, to detect adulterants (solvents and kerosene) in Brazilian blended gasoline.

Fonseca and Raimundo<sup>24</sup> developed an LED array based spectrometer for the determination of Zn and Cu in pharmaceutical and metallic alloy samples. Eight LEDs (Ultrabright, RS Components, UK, with wavelength maxima at 470, 500, 525, 562, 590, 612, 636 and 654 nm) were employed with a single photodiode detector (RS 308-067). Dependant on the application, either a single LED was continually driven, or when multiple wavelengths were required, the LEDs were sequentially pulsed. A 3-4% intensity decrease was noted after reaching maximum intensity from initial power on for all LEDs except the 500 and 525 nm units.

Veras et al.<sup>25</sup> employed a compact disc as a diffraction grid with a geared stepper motor to disperse the output of a white LED to produce a low cost spectrometer. This system was compared in performance to a HP 8453 diode array and a Micronal B34211 spectrophotometer for the determination of food colorants in synthetic samples and iron in solutions.

Further reports of LED based instrumentation development where temperature effects have been considered are presented in Chapter 4.

### **2.3.2 Gaining spectral information**

NIR spectrometers fall into one of three categories – discrete wavelength (usually non-thermal source), dispersive and interferometric. The dispersive element can be employed in the optical design of an instrument either before or after the sample, i.e. pre or post dispersive instrument.

### 2.3.2.1 Dispersive System

Dispersive systems are those where the wavelengths of light are separated spatially. Spectrometers commonly use diffraction gratings, with reflection gratings being simpler and much more efficient than standard transmission gratings. A reflection grating consists of a highly reflective surface, such as aluminium or gold, on which a large number of parallel grooves are created (sometimes as many as 2400 lines per mm<sup>10</sup>). The working faces may be specially shaped to create a blaze angle to optimise the efficiency of the grating (Figure 2.8). Incident light of wavelength  $\lambda$ , at an angle  $\alpha$ , on a diffraction grating of line spacing  $d$ , is reflected at an angle  $\beta$ , given by

$$d(\sin \alpha - \sin \beta) = m\lambda \quad \text{Eqn 2.12}$$

where  $m$  is the order of diffraction. If the grating has  $N$  lines, the intensity of the diffracted light  $I(\beta)$  is given by

$$I(\beta) = R(\theta, \beta) I_0 \frac{\sin^2(N\pi d \sin \beta / \lambda)}{\sin^2(\pi d \sin \beta / \lambda)} \quad \text{Eqn 2.13}$$

where  $I_0$  is the incident light intensity and  $R(\theta, \beta)$  defines the grating efficiency. Slits, mirrors and gratings all introduce an element of polarisation in a spectrometer, but the effect is dominated by the influence of the grating.<sup>26</sup>

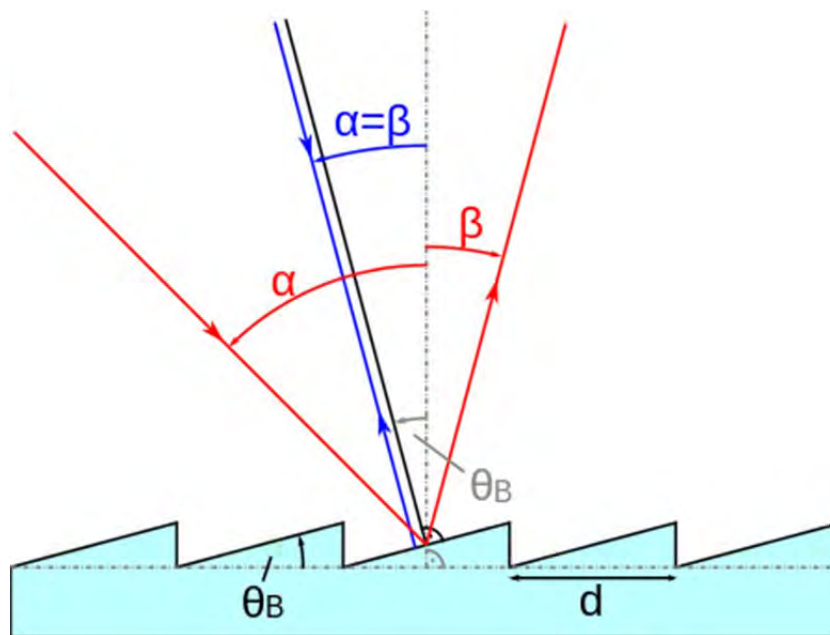


Figure 2.8 Illustrative representation of a blazed reflection grating<sup>27</sup>.

The efficiency of a grating also depends on the polarisation of the incident light (as well as blaze angle and grating period), although several design features can be used to minimise this effect<sup>28</sup>. S-polarised light, where the direction of the grating grooves and the oscillation direction of the electric field vectors is perpendicular, exhibits a higher diffraction efficiency at longer wavelengths than P-polarised light, where the direction of the grating grooves and the oscillation direction of the electric field vectors is parallel, for which diffraction efficiency peaks at the blaze wavelength and decreases with a smooth curve.<sup>29</sup> The efficiency difference between S and P polarised light thus depends upon a range of factors, and range from very little to over 80 %<sup>26</sup>. It is, however, easily experimentally determined.

A common type of grating in current use is the concave holographic grating. The gratings are created using the interference pattern of two intersecting lasers on a photosensitive material. This alleviates the imperfections and aberrations in mechanically ruled gratings. This design both disperses and focuses the light.

The classical dispersing instrument is the prism. Grating spectrometers achieve better resolution, but are more wasteful of light due to the production of many orders of diffraction. Prisms have a theoretical resolution limit of about  $0.3 \text{ nm}^{10}$ , but can be useful when high resolution is not a critical factor.

Another dispersive device is an acousto-optically tuneable filter. An AOTF is a solid-state device that is based on the grating. An anisotropic crystalline medium is specifically aligned, cut and polished. A piezo-electric transducer is attached to the side. When an electro radio frequency (RF) signal is applied, the wave produced in the crystal together with the spatial parameters of the crystal creates a standing wave, defining the parameters of the diffraction grating. The standing wave acts as a diffraction grating to the incident light. It separates the incident light into a non-deviating polychromatic beam and two monochromatic beams of the wavelength which interact with the spacing of the standing wave. Bragg's equation relates the wavelength and acoustic frequency via:

$$m\lambda = 2d \sin\theta \qquad \text{Eqn 2.14}$$

where  $d$  is the period of the standing wave in the crystal,  $m$  is the order of diffraction and  $\theta$  is the angle of the incident light.

### 2.3.2.2 Interferometric Systems (Non-dispersive)

Interferometers are modulators that do not produce angular dispersion. The basis for these systems is to split the beam of light into two or more beams. Their optical paths are then changed, by either lengthening the optical path distance or by slowing down the velocity of one ray over the same distance by using a material with a different refractive index.<sup>30</sup> The recombination of the beams is then observed, with interference created if a phase difference exists from the differences in optical path. A frequency decomposition, by taking the Fourier Transform (FT), is required to construct the spectrum. The construction and calculation of the spectra is rapid due to the use of Fast Fourier Transform (FFT) algorithms and microprocessors.

The Michelson interferometer is one such device. It divides light into two equal beams and coalesces them after a path difference has been introduced by use of a beam splitter (half silvered mirror) and two mirrors (one fixed, one adjustable). An interferogram is generated onto a single detector, by making measurements of the signal at many positions of the moving mirror. FT spectrometers use either a step scan approach, or modulate the incoming optical radiation by changing the optical path difference (mirror) in a smooth continuous fashion, thus each wavelength of the collected radiation is modulated at a unique frequency that is a function of the wavelength of the radiation and the velocity of the moving mirror.<sup>31</sup> When the mirror has travelled the required distance, governed by the required spectral resolution, it is rapidly returned to the start position to begin the next scan. The alignment of the mirrors to each other affects how the beams overlap as they recombine. Some systems incorporate a compensating mechanism that automatically adjusts the orientation of one mirror to maintain the precise alignment, while in other systems Michelson classical plane mirrors are replaced with cube corner reflectors that have the ability to always reflect the light in the parallel direction.<sup>31</sup> All fibre-optic FT spectrometers have been developed by precisely stretching the fibre optic in an instrument<sup>32</sup>, or by using the temperature dependency of refractive indices to alter the optical path sufficiently<sup>33</sup>.

Another type is the Fabry-Perot (FP) interferometer. Modern FP interferometers have the component plates measured and aligned piezo-electrically to a very high accuracy. They have a relatively rapid scan rate, with the ability to be scanned at 6  $\mu$ s intervals<sup>10</sup>. These

types of devices have practical limitations such as beam divergence, optical alignment and scanning, photometric range and phase errors.

### 2.3.3 Detectors

Infrared detectors can be classed as either photon or thermal detectors. The latter respond to total radiated energy, irrespective of wavelength, and are too inefficient for serious NIR spectroscopic use<sup>8</sup>. In a common system, a fibre optic cable collects light and delivers it onto a diffraction grating. The resultant spectrum is directed across two mirrors and onto an array, where it is converted into electrical output signals.

Low cost spectrometric designs operating in the SWNIR typically use a silicon based photodiode or linear charged coupled device (CCD). Photodiode cells consist of reverse-biased p-n junctions. A small potential is produced when sufficiently energised electrons create an electron-hole pair across the boundary. Silicon (Si) detectors respond throughout the visible part of the spectrum up to 1100 nm, peaking at 850 nm<sup>8</sup>. Photodiodes detectors can also be composed of germanium (Ge), indium gallium arsenide (InGaAs), lead sulphide (PbS) or lead selenide (PbSe). Ge and InGaAs have similar operating ranges of 800 – 1800 nm<sup>8</sup>. PbS and PbSe have operating ranges of 1000-2500 nm and 2500-3500 nm<sup>8, 34</sup> respectively. PbS is much more sensitive than PbSe, but has a much longer response time of 100-200  $\mu$ s compared to less than 1 $\mu$ s<sup>8</sup>. InGaAs has a response time of less than 1  $\mu$ s and has a higher SNR and sensitivity compared to PbS, but costs approximately 5 times more<sup>34</sup>. Detector characteristics are given in Table 2.2.

**Table 2.2 Photodiode Detector Characteristics**

Type	Range (nm)	Response time ( $\mu$ s)
Si	400 – 1100	< 1
Ge	800 – 1800	<1
InGaAs	800 – 1800	< 1
PbS	1000 – 2500	100 - 200
PbSe	2500 – 3500	< 1

Many NIR spectrometers utilise a linear array of individual photodiodes, called a photodiode array (PDA). The dispersed spectrum is incident on the PDA, thus a range of wavelengths are measured simultaneously. This results in PDAs having a much faster scan time for an entire spectrum than systems that select each wavelength and scan sequentially. However, each individual photodiode in the array has its own characteristics, and thus each array will have different characteristics. This results in less precision in measurements between instruments, affecting the transferability of measurements and calibration models between instruments. In order to accurately transfer calibrations between PDA based spectrometers, it is likely that the individual fingerprint (array of characteristics) for each array will be required.

Figure 2.9 shows the normalised efficiencies of a light source (blackbody), a dispersive mechanism (grating) and a detector (silicon photodiode).

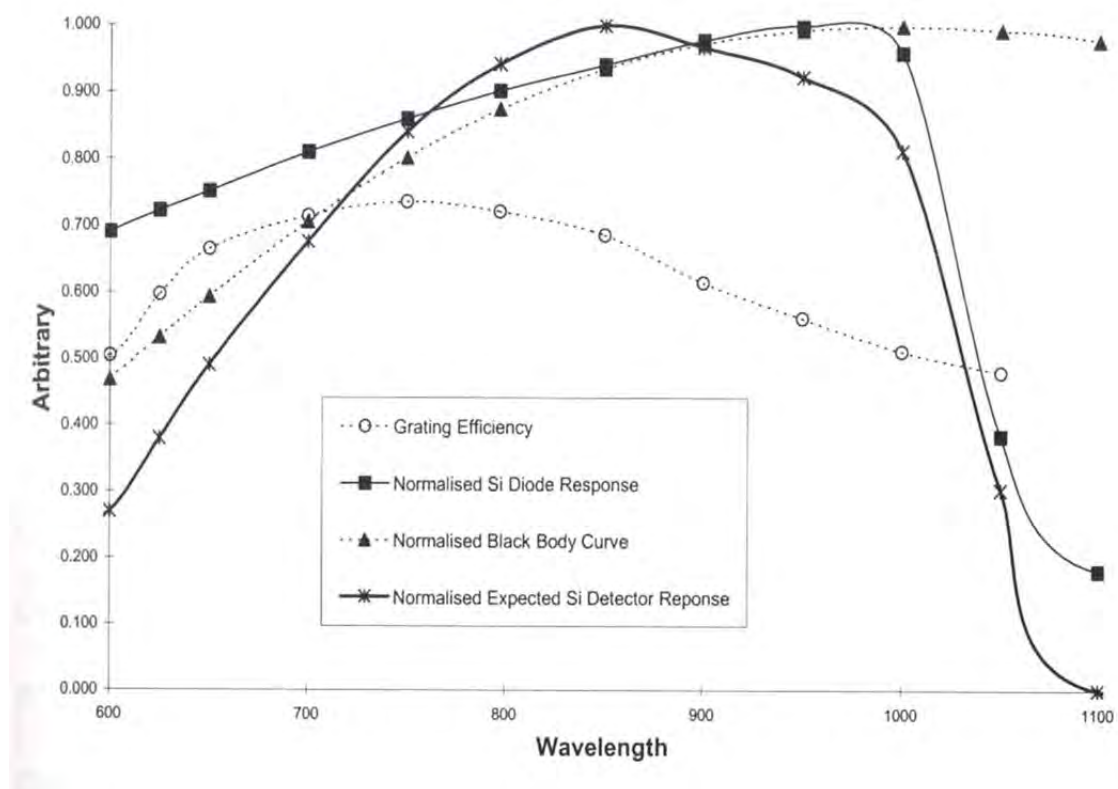


**Figure 2.9 Graph of normalised black-body curve at 2900°C, actual and expected typical silicon detector response and diffraction grating efficiency (flat, ruled, gold coated, blazed for 750 nm, 1200 grooves per mm)<sup>10</sup>**

Another highly sensitive photon detector commonly employed is the silicon based CCD. The CCD is divided up into a large number of light-sensitive small areas, known as pixels. Each of these is represented by p-doped metal oxide semiconductor capacitor. A photon of light which falls within the area defined by one of the pixels will be converted into one (or more) electrons and the number of electrons collected will be directly proportional to the intensity of the scene at each pixel. CCDs have a wavelength range the same Si photodiodes, peaking at approximately 700 nm<sup>35</sup>. A process known as backthinning makes it possible to extend the range to shorter wavelengths c.a. 200nm<sup>35</sup>.

### 2.3.4 Spectrometer Specifications

There are several specifications used for instrument comparisons. Spectral range, spectral resolution and intensity resolution are all important design parameters for application specific spectrometers. The spectral resolution of a spectrometer is described by several terms: Rayleigh criterion, Full Width at Half Maximum (FWHM), wavelength accuracy and pixel dispersion. The most significant is the Rayleigh criterion,  $\Delta\lambda_{\text{Rayleigh}}$ , which indicates the wavelength separation of two close peaks in the same spectrum of the same intensity. The decrease in intensity,  $\Delta I$ , between the peaks must be at least 19% from maximum for the lines to be individually recognised<sup>36</sup>. Another important property is the measured width of a spectral line. The Full Width at Half Maximum or measured bandwidth at 50% intensity  $\Delta\lambda_{\text{FWHM}}$  gives information about the broadening of the line.

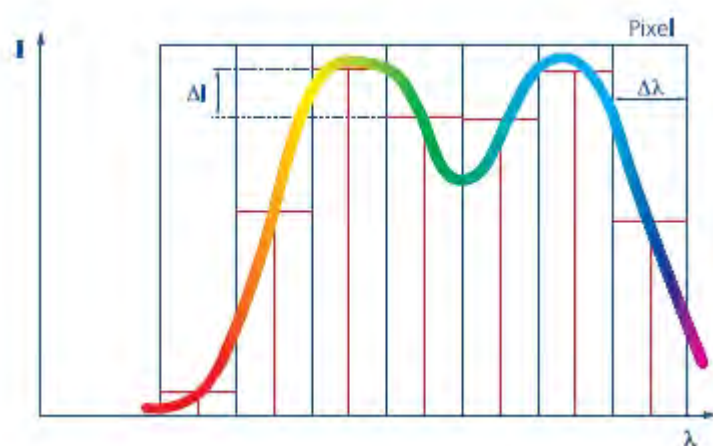


**Figure 2.10 Spectral resolving power:  $\Delta I$  must be 19% from maximum for lines to be individually recognised<sup>36</sup>**

Wavelength accuracy specifies that a measured wavelength will be within the specific accuracy  $\Delta\lambda_{\pm}$ , of the absolute spectral position  $\lambda$ . This is dependent on the stability and accuracy of the positions of the grating, optical bench and PDA, which are dependent on mechanical and thermal properties. Pixel dispersion refers to the linear dispersion of the PDA, i.e., the wavelength distance between consecutive pixels. Pixel dispersion and spectral resolution are related via the width of the slit and the imaging properties of the spectrometer.

Spectroscopy is based on measurement of ‘intensity’ changes at specific wavelengths. Thus ‘intensity’ resolution is an important factor. Intensity resolution is defined by the following related properties: smallest detectable change, signal stability, dynamic range of digital interface and linearity. The smallest detectable change and stability are dependent on each other. In most spectrometers the optical path is constant, thus the stability and smallest intensity step are limited by the electronic noise present and the analogue to digital conversion rate.

The dynamic range is the ratio of the intensity at saturation value and the noise, or the SNR. SNR depends upon both the detector and the electronics performing the digitalisation. These electronics determine the smallest step width of a measured signal. Linearity is significant in systems that require relative measurements of intensity to be made. For the instrument used in this study (Zeiss MMS1) it is claimed that behaviour of modern semiconductor detectors is almost perfectly linear within a wide range<sup>36</sup>, although it is also stated that before saturation, the increase of the current is not linear to the number of photons striking the photosensitive material and therefore the range of linearity is smaller than the dynamic range<sup>36</sup>. Changes in temperature can also affect the sensitivity of the detector by impacting on the detector quantum efficiency and the dark current (noise). This effect tends to be wavelength specific.

### 2.3.5 Description of two common detectors

A number of low cost SWNIR miniature spectrometers are marketed. Two units well established in the market are the Zeiss MMS1 (Carl Zeiss GmbH, Jena, Germany) and the Ocean Optics S2000+ (Ocean Optics Inc., Dunedin, USA) (Figure 2.11). A description of these two spectrometers is given below, with specification given in Table 2.3

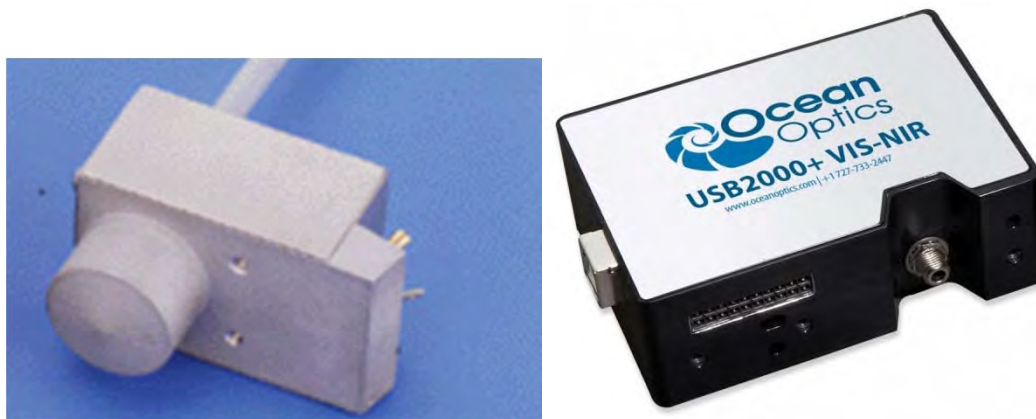


**Figure 2.11 Zeiss MMS1<sup>37</sup> (left) and Ocean Optics USB2000+<sup>38</sup> (right)**

#### 2.3.5.1 Zeiss MMS1: a Si photodiode array based spectrometer

The central body of the MMS1 is a lens-type device made of borosilicate crown glass (UBK 7, Schott AG, Mainz Germany). All components, including the grating, cross sectional converter and detector, are permanently connected to the quartz body (see Figure 2.12). This protects the components from environmental anomalies and makes the module exceptionally resistant to mechanical shock and temperature changes, thus ensuring wavelength accuracy. The use of an optically dense medium together with the resultant larger aperture allows the use of a smaller grating and thus fewer aberrations.

The grating is an aberration corrected concave, holographically blazed, efficiency optimised, flat-field grating. Produced using stationary wave techniques, it achieves higher efficiencies (for non-polarised light) than its sinusoidal counterpart. The grating images the entrance slit onto the diode array detector. Coma is minimised and the focal curve flattened (flat-field) by varying the groove density and using curved grooves. The flat-field effect ensures that the focal curve is optimally adapted to the flat detector structure, producing flat spectra over 6 mm long<sup>39</sup>.

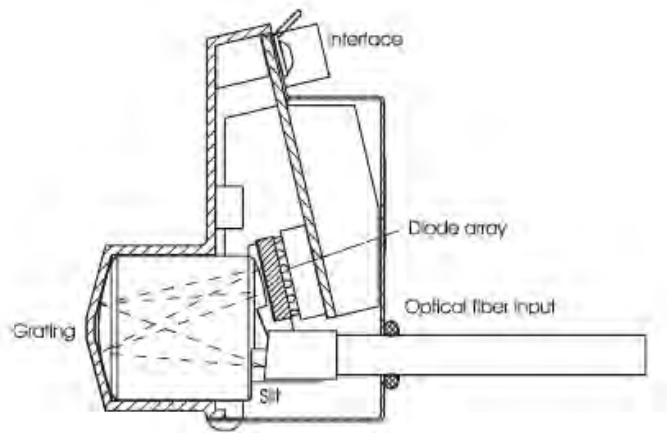


**Figure 2.12 Zeiss MMS1 schematic diagram<sup>37</sup>. The optical fibre input is converted to a linear configuration, forming the entrance slit, which is imaged via the grating onto the diode array.**

The light sensitivity of the device is further enhanced by the use of a fibre bundle cross-sectional converter. The fibre bundle consists of approximately 30 individual Infrasil-quartz glass fibres. The input bundle is 0.5 mm in diameter, which is converted into a linear configuration, forming the optical entrance slit. The output of the converter is approximately 2.5 mm high and 70  $\mu\text{m}$  wide (individual fibre diameter). The input diameter has been tailored to suit the pixel size of the diode array detector and the imaging and dispersive properties of the grating. This helps to achieve light intensities near the theoretical limit<sup>39</sup>.

The MMS1 NIR enhanced module employs a 256 pixel Hamamatsu S4874-256Q Silicon (Si) multiplexed linear diode array (Hamamatsu Photonics K.K., Hamamatsu City, Japan). This provides the module with a spectral range of 400 nm – 1100 nm. A special shorter housing allows the detector to be positioned closer to the optical input, resulting in a small split-off angle and increased grating efficiency. To suppress the second order diffraction, the diode array has been directly coated with a dielectric cut-off filter<sup>39</sup>. The specifications of the spectrometer are listed in Table 2.3.

### 2.3.5.2 Ocean Optics USB2000+: a Si CCD based spectrometer

All components of the USB2000+ are permanently connected to the body, as well as the electronic circuits for spectrometer operation. The user can select the entrance slit size, a long pass filter (optional), collimating mirror, grating and starting wavelength, focusing mirror, optional detector collection lens, optional longpass order-sorting filter and detector window. The user can customise each of these for the application.

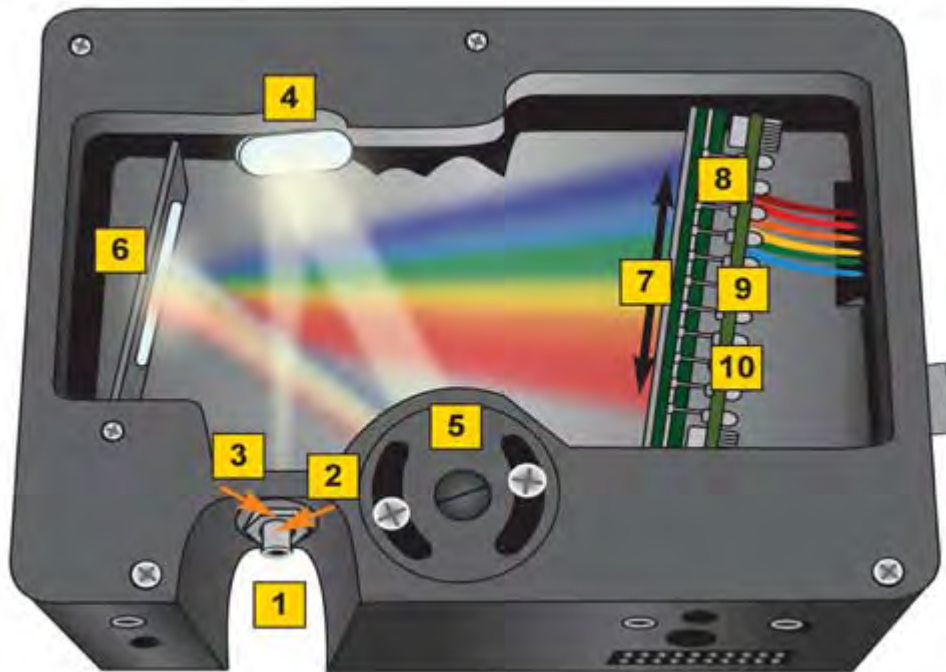


**Figure 2.13. Ocean Optics USB2000+<sup>38</sup>. The individual components are: (1) SMA 905 connector, (2) fixed entrance slit, (3) optional longpass absorbing filter, (4) collimation mirror, (5) grating (6) focusing mirror, (7) optional detector collection lens, (8) detector, (9) optional longpass order-sorting filter and (10) detector window.**

The entrance slit comes in six different sizes ranging from 5 to 200  $\mu\text{m}$ , giving pixel resolutions of  $\sim 3.0$  to 24 pixels. Seven optional longpass filters are available with cutoffs from 305 – 590 nm. The collimating mirror is matched to the 0.22 numerical aperture of the optical fibre, with either a standard or UV absorbing SAG+ mirror. The focussing mirror is also available in standard or SAG+.

Seven ruled gratings with blaze wavelengths of 250 to 1000 nm and grating densities of 500 to 1200 lines/mm are available. Also available are eight holographic gratings optimised for UV or visible, and grating densities of 1200 to 2400 lines/mm. Holographic gratings produce less stray light while ruled gratings are more reflective, resulting in higher sensitivity.<sup>40</sup>

The detector is a Sony ILX511B linear silicon CCD array. It has a range of 200-1100nm. It has 2048 pixels, each 14 x 200  $\mu\text{m}$  and a well depth of 62 500 electrons. It has an SNR of 250:1 and a dark noise of 50 RMS counts. The linearity is specified at 99.8 %. An optional cylindrical detector lens is available to increase collection efficiency and reduce stray light. An optional variable longpass order filter can be selected to block second and third order diffraction. The detector comes with a standard borosilicate crown glass (BK 7, Schott AG, Mainz Germany) window, although a quartz window is available to enhance application < 340 nm.

**Table 2.3 Specifications of the Zeiss MMS1 NIR enhanced and Ocean Optics USB2000+ VIS-NIR-ES configured spectrometer<sup>39</sup>**

<b>Spectrometer:</b>	Zeiss MMS1 NIR enhanced	Ocean Optics USB2000+ VIS-NIR-ES
<b>Optical entrance:</b>	Cross section converter - Fibre bundle consisting of approx. 30 Infrasil-quartz glass fibres. Dia. 0.5 mm, NA=2 Linear output: 70µm x 2.5mm	SMA 905 connector  Entrance slit – 1mm high 25 µm wide
<b>Grating:</b>	Holographically blazed, flat-field grating 366 lines/mm (centre); f-number 1.6; imaging ration 1:1	Ruled 600 lines/mm 500 nm blazed
<b>Diode array:</b>	Hamamatsu S4874-256Q Si PDA 256 pixels, 25x2500 µm each	Sony ILX511B Si CCD array, 2048 pixels, each 14 x 200 µm
<b>Spectral Range:</b>	400 - 1100nm	350 – 1000nm
<b>Spectral Resolution:</b> (Rayleigh-criterion)	≈10nm FWHM	≈1.5 nm FWHM
<b>Wavelength accuracy, absolute:</b>	0.3 nm	+/-0.0005
<b>Pixel dispersion:</b>	≈ 3.3 nm	≈0.33 nm
<b>SNR</b>	5000:1	250:1
<b>Dark Noise</b>	1.5 SD	50 RMS
<b>Dynamic Range</b>	2 <sup>14</sup>	8.5 x 10 <sup>7</sup> (system); 1300:1 for a single acquisition

## 2.4 Chemometrics

Chemometrics is defined as the application of mathematical, statistical, graphical or symbolic methods to process, evaluate and interpret the maximum chemical information that can be extracted from data<sup>34, 41</sup>. Chemometric methods are applied to find statistical correlations between spectral data and known properties of a sample<sup>34</sup>. The reduction of the number of elements needed to describe the characteristics of the data set, while still maintaining accuracy, is one of the primary goals of chemometrics. This can be achieved by numerous techniques, such as selecting a significant subset of the original variables, or by creating a set of new variables that are more effective.

### 2.4.1 Data Pre-treatment

Data pre-treatment procedures can assist in the extraction of information from the raw data, such as the distinguishing of overlapping spectral features or distinguishing between signal and noise and removing the latter. In the field of NIR spectroscopy, pre-processing is frequently, but not exclusively, performed to identify any baseline drift or slope in a spectrum, which tends to occur in diffuse-reflectance measurements due to significant light scattering by particulate matter<sup>34</sup>. This can be minimised by baseline subtraction and can entail a first and/or a second derivative transformation, the second being more common. It is advantageous to use the second derivative since, although positive peaks in raw spectrum are converted to negative peaks, enhanced resolution is achieved to allow separation of overlapping peaks and emphasis of small peaks and additive and multiplicative baseline shifts in a raw spectrum are removed<sup>34</sup>. There are, however, disadvantages to this approach. The SNR can be decreased with each successive derivative as two false valleys are generated in the positive ordinate scale for every band in a negative direction<sup>8</sup>. To combat this, various smoothing techniques are often used before and after differentiation. An alternative is to differentiate using the Savitzky-Golay<sup>42</sup> method, which effectively combines a smoothing step.

A number of other pre-treatments are commonly used, particularly with diffuse reflection data eg mean centering, auto scaling, standard normal variate, detrend, multiplicative scatter correction, orthogonal signal correction etc. For a summary and review see Martens and Næs<sup>43</sup> and Næs et al.<sup>44</sup>

### 2.4.2 Outliers

After corrections for baseline drift have been applied, outlying samples (those that fall considerably outside the trend of the main population) must be removed. These outlying samples may be the result of laboratory measurement error, or may be spectrally distinct. Of course, if the outlier is representative of samples to be predicted in the future, it should be retained in the model. A common method of outlier identification is based on Mahalanobis distance<sup>45, 46</sup>, calculated as the average distance of a sample from the population mean in multi-dimensional principle component (PC) space. Other common outlier identification methods include Hotelling's  $T^2$  test<sup>47, 48</sup>, X-residuals<sup>43</sup> and potential functions<sup>49</sup>, or use of robust regression methods.

Removing outliers from a calibration set will of course improve calibration statistics, but its effect on prediction of new data that is important. Note that outlier identification methods that are based on X (spectra) can be used to decide whether to implement a prediction or not. For a more comprehensive discussion of outliers see Cook and Weisberg<sup>50</sup> and Martens and Næs<sup>43</sup>.

### 2.4.3 Models

NIR analysis is dependent on the ability to develop a calibration model that relates the spectral intensities at different wavelengths to the chemical composition of the product. Numerous models have been employed in the development of a calibration model. These are briefly described below. For a more comprehensive discussion see Martens and Næs<sup>43</sup> and Næs et al.<sup>44</sup>

The classical least squares (CLS) model is basically a multiple linear regression (MLR) model that assumes the measurements are the weighted sum of linearly independent inputs.<sup>44</sup> When applied to spectroscopy, the CLS model deduces that measured spectra are the sum of spectra constituents from known pure component spectra, weighted by the concentration of the analytes. This model presents one major disadvantage in that the analyte concentrations must be known for all constituents or estimated from the data. This includes the spectra of minor components that are not necessarily of interest themselves, but may contribute to the measured signal. This problem can be avoided by using the inverse least square (ILS) method<sup>3</sup>.

One of the most versatile chemometric methods is principal components analysis (PCA). Its purpose is to maximise the variance information present in a data set in as few new dimensions as possible. It reduces the number of variables that need to be considered, yielding a new set of variables (principal components), which are orthogonal to each other. Mathematically it performs a simple linear transformation, achieving this by twisting the axes of the data to conform to new axes that contain a maximum amount of variance information.

A robust ILS calibration method is principal components regression (PCR). In this method the system properties are regressed on the principal component scores of the measured variables, instead of regressing the system properties on the original measured variables. The function of the regression model is to predict the properties of interest for new samples, thus a determination on the number of PCs that optimises the prognostic ability of the model must be made. This is achieved by cross-validation, where the available data is split between training and test sets.

Another chemometric method is partial least squares (PLS) regression. MLR seeks a single factor that best correlates predictor variables with concentrations of analyte, whereas PCR finds factors that capture the greatest amount of variance in the predictor variables. PLS goes further and endeavours to find factors that attain predictor variable variance and achieve predictor/predicted variable correlation.

Calibration models can be developed using pattern recognition methods (PRMs) to identify similarities and regularities in the data. There are two types of PRMs, clustering and supervised learning. Supervised methods entail the training of the system, using a set of objects belonging to specific previously known classes and a mathematical model to predict the class of a newly presented unknown object. Clustering methods engross the linking of all objects in a data set (one by one) by measuring their relative similarity.

After the calibration model has been developed, it must be tested to ensure its validity. In multivariate statistics, it is relatively easy to overfit data to a model. In this case, the model statistics (eg  $R^2$  and RMSEC) can look good, but as the model has effectively described some of the noise present in the calibration set, it will fail in prediction. Another major issue is that biological samples are variable, and one calibration set (eg 50

samples) will fail to represent the optical and chemical variation present in future samples.

#### 2.4.4 Calibration Model Statistics/Testing/Assessment

Several statistical parameters define the performance of a calibration model. Common parameters used are: the coefficient of determination ( $R^2$ ), standard deviation from the reference method values (SD), root mean standard error of calibration (RMSEC), root mean squared error of cross calibration (RMSECV), root mean squared error of prediction (RMSEP) and standard deviation residual (SDR).

RMSEP and RMSECV are both measures of model accuracy. For RMSEP, an independent validation set of samples (completely separate from the calibration samples) is used to provide a true estimate of the performance of the predictive model on unseen samples. RMSECV iteratively removes a subset of samples from the calibration set and calculates a new calibration model. The removed samples are then used for validation. The validation set is returned to the calibration set and the cycle is repeated for a specified number of validation samples. RMSECV is intended to avoid the need for a large separate validation set, but this depends on sound design in selection of cross validation groups. These statistics are calculated by:

$$RMSECV / RMSEP = \sqrt{\sum_{i=1}^N (\hat{c}_i - c_i)^2 / N} \quad \text{Eqn 2.15}$$

where  $\hat{c}_i$  and  $c_i$  are the reference and predicted values respectively of the  $i^{\text{th}}$  sample from the set of  $N$  validation samples. SDR is calculated as  $SD/RMSEP$  or  $RMSECV$ .

Another model statistic that can be employed to assess model performance is the standard error of prediction (SEP). This is calculated similarly to RMSEP, except it has been corrected for bias and with  $N-1$  as the denominator.

$$bias = \sum_{i=1}^N (\hat{c}_i - c_i) / N \quad \text{Eqn 2.16}$$

$$SEP = \sqrt{\sum_{i=1}^N (\hat{c}_i - c_i - bias)^2 / (N - 1)} \quad \text{Eqn 2.17}$$

### 2.4.5 Instrument Standardisation

A predictive model generated on spectra from one instrument generally gives poor results when used on spectra acquired from a different instrument. This is due to the small differences between detectors such as photometric response, wavelength accuracy, electronic noise, optical noise and temperature stability. These impact on the shape and position of the spectral characteristics. Generation of calibrations is labour and time intensive, thus expensive and impractical, due to the acquisition of large data sets over a broad range of samples.

A plethora of work on calibration transfer and instrument standardisation between NIR spectrometers has been published by Bergman et al.<sup>51</sup>, Blank et al.<sup>52</sup>, Blanco et al.<sup>53</sup>, Bouveresse et al.<sup>54-58</sup>, De Noord<sup>59</sup>, Despaigne et al.<sup>60, 61</sup>, Dresssi et al.<sup>62</sup>, Duponchel et al.<sup>63</sup>, Fearn<sup>64, 65</sup>, Geladi et al.<sup>66</sup>, Leion et al.<sup>67</sup>, Pérez-Marín et al.<sup>68</sup>, Shenk and Westerhaus<sup>69, 70</sup>, Sjöblom<sup>71</sup> and Wang<sup>72-76</sup>. The majority of published work focuses on the transfer of calibration models on scanning grating or Fourier transform near-infrared instruments. This has been successfully achieved on these instruments for relatively dry (< 10 %) samples, e.g. grain, pharmaceuticals and petroleum products<sup>77</sup>.

Instrument standardisation involves transfer of calibrations developed on one *master* spectrometer to the *slave* spectrometer(s), or by making the spectra on the slave instrument appear to originate from the master instrument, thus using the same calibration. This can be just as resource intensive as developing new calibration models for each spectrometer.

Common methods include:

- Slope and Bias Correction (SBC)
- Linear transforms
- Shenk and Westerhaus standardisation technique
- Direct Standardisation (DS)
- Piecewise Direct Standardisation (PDS)
- Double Window Piecewise Direct Standardisation (DWPDS)
- Orthogonal Signal Correction (OSC)
- Finite Impulse Response Filtering (FIR)

- Wavelet Transforms (WT)
- Neural Networks (NN)
- Model Updating (MU)

#### 2.4.5.1 Slope and Bias Correction

This method<sup>78, 79</sup> can work relatively well for instruments which are almost identical (light source, dispersion mechanism and detector) and where adjustments required are small<sup>8</sup>. Because only two constants are determined, only a small number of samples is required. Application of the method has to be repeated for each calibration model.

Spectra are acquired on both master and slave spectrometers and predictions are made using the predictive model generated on the master. Predicted values from master (old) instrument,  $\hat{Y}_m$ , are plotted against the predicted values from the slave (new) instrument,  $\hat{Y}_s$ . If a straight line can be fitted to the plot, the results are linearly regressed to give

$$\hat{Y}_m = slope \cdot \hat{Y}_s + bias \quad \text{Eqn 2.18}$$

Predictions made on the slave instrument are then altered using this equation, or alternatively, all the calibration constants (including the intercept) are multiplied by the slope and then the bias is added to the intercept. Bias correction is a simpler version that only corrects for the bias, not the slope.

#### 2.4.5.2 Linear transforms

Each wavelength in the spectra of the slave instrument is transformed by a linear function (which considers each constituent wavelength) and an offset.

The general formula is

$$\mathbf{x}^a = \mathbf{b} + \mathbf{x}\mathbf{F} \quad \text{Eqn 2.19}$$

where  $\mathbf{x}$  is a 1 x p row vector containing the raw spectra and  $\mathbf{x}^a$  is 1 x q row vector containing the adjusted spectra.  $\mathbf{b}$  is a 1 x q row vector of offsets and  $\mathbf{F}$  is a p x q transformation matrix.

The most common situation is where the instruments are of the same type and thus p = q. Spectra are acquired on both instruments and are used to calculate b and F. As this is

much like calibration itself, overfitting must be considered, where too many constants with too few data samples gives a perfect fit for the calibration data, but poor performance on unknown data.

The  $\mathbf{F}$  transformation matrix gives a set of weights which are applied to the raw spectra to give the corresponding adjusted wavelength. Depending on the values in this matrix, any or all of the wavelengths may contribute to the calculation of the new adjusted wavelength. Wavelength shift and multiplicative absorbance shift are correct by the  $\mathbf{F}$  matrix. The offset  $\mathbf{b}$  corrects for an additive absorbance shift.

#### 2.4.5.3 Shenk and Westerhaus standardisation technique

Shenk and Westerhaus<sup>80</sup> patented a standardisation technique in 1989. It is currently incorporated into their chemometric software WinISI (Infrasoft International, LLC, State College, U.S.A.). A detailed description is given by Bouveresse et al<sup>57</sup>. The two main steps of Shenk and Westerhaus's method are wavelength index correction and spectral intensity or photometric response correction.

Spectra from the standardisation sets acquired from both master and slave instruments are transformed by a first derivative. For each wavelength ( $i$ ) the absorbance on the master instrument ( $\mathbf{X}_m$ ) is linearly correlated to the absorbance on the slave instrument ( $\mathbf{X}_s$ ) at wavelengths in a spectral window ( $i \pm w$ ). The wavelengths with the highest correlation within the window are matched. A more precise wavelength correlation match is obtained by fitting a quadratic function to the matched wavelength ( $m$ ) and its two neighbours ( $m \pm 1$ ), giving new slave wavelengths

$$\hat{i} = a + bi + ci^2 \quad \text{Eqn 2.20}$$

where  $\hat{i}$  is the new (adjusted) slave wavelength,  $i$  is the master instrument wavelength and  $a$ ,  $b$  and  $c$  are regression constants.

Raw absorbance data is used for spectral intensity correction. Absorbance values for the new (adjusted) slave wavelengths ( $\mathbf{X}_s^\#$ ) are calculated using interpolation. The spectral intensity (absorbance) at each wavelength of the master and slave instruments are linearly regressed to identify correlation between them. The regression is given by

$$X_{m_i} = a(i) + b(i).X_{s_i}^{\#} \quad \text{Eqn 2.21}$$

This is then used to adjust the absorbance values to new values using

$$X_{STD_i} = a(i) + b(i).X_{s_i}^{\#} \quad \text{Eqn 2.22}$$

where  $\mathbf{X}_{STD}$  is the  $\mathbf{X}_s$  absorption matrix after standardisation and  $a(i)$  and  $b(i)$  are regression coefficients computed for each wavelength  $i$ . Each new spectrum obtained with the slave instrument is standardised using these wavelength and spectral intensity coefficients to correct for wavelength and absorbance values.

#### 2.4.5.4 Direct Standardisation

DS was proposed in 1991 by Wang et al.<sup>75</sup>. Samples are scanned on both master and slave instruments and used as training sets. Response matrices from both instruments are related to each other via

$$\bar{\mathbf{R}}_1 = \bar{\mathbf{R}}_2 \mathbf{F} \quad \text{Eqn 2.23}$$

where  $\mathbf{R}_1$  and  $\mathbf{R}_2$  are matrices of absorbance values for the same subset of standardisation samples measured of master and slave instruments respectively and  $\mathbf{F}$  is the standardisation transformation matrix. PCR or PLS is used to estimate the coefficient vector for predicting the absorbance at wavelength  $j$  on the master instrument from the full spectrum on the slave instrument. This forms the  $j$ th column of  $\mathbf{F}$  and the process is repeated for each wavelength. The response vector  $\mathbf{r}_{2,un}^T$  of an unknown sample measured on the slave instrument is standardised to appear as a response vector  $\hat{\mathbf{r}}_{1,un}^T$  originating from the master instrument using

$$\hat{\mathbf{r}}_{1,un}^T = \mathbf{r}_{2,un}^T \mathbf{F} \quad \text{Eqn 2.24}$$

The full spectrum acquired on the slave instrument is used to calculate each data point on the standardised new spectrum. As there are generally not many samples in the training set and numerous coefficients to be calculated in  $\mathbf{F}$ , overfitting is a very likely risk.

#### 2.4.5.5 Piecewise Direct Standardisation

This method was also developed by Wang et al.<sup>75</sup>. It is similar to DS, but reconstructs each spectral point from the measurements within a sliding window on the slave instrument, not the entire spectrum. Sample spectra are acquired on the master instrument  $\mathbf{X}_1$  and slave instrument  $\mathbf{X}_2$ . For each wavelength of a sample collected on the master, absorbances are regressed against the corresponding absorbances within a window of neighbouring wavelengths, of width  $2j + 1$ , from the slave instrument. The regression vector is calculated by

$$\mathbf{X}_1(:,i) = \mathbf{X}_2(:,i-j:i+j)\mathbf{b}_i \quad \text{Eqn 2.25}$$

where  $\mathbf{X}_1(:,i)$  and  $\mathbf{X}_2(:,i-j:i+j)$  are columns used in the calculation of  $\mathbf{b}_i$ . The regression is performed via numerous multivariate calibration methods such as PLS or PCR. The response vector of an unknown sample measured on the slave instrument is standardised using

$$\hat{\mathbf{r}}_{1,un,i} = \mathbf{r}_{2,un,i-j,\dots,i+j}\mathbf{b}_i \quad \text{Eqn 2.26}$$

An additive background correction for an intercept  $b$  was included by Wang et al. which was shown to give improvement over the purely multiplicative version.

#### 2.4.5.6 Double Window Piecewise Direction Standardisation

In some FTNIR spectra, spectral features are very narrow, with regions of only noise in between. PDS does not perform well in these cases. Wise<sup>81</sup> developed double windows PDS (DWPDS) to address this issue. DWPDS is very similar to PDS, but uses a sliding window on the slave instrument (width  $2[j + k] + 1$ ) and a (different) sliding window on the master instrument (width  $2k + 1$ ). The regression vector is identified by

$$b_i = X_{2DW} + X_{1DW} \quad \text{Eqn 2.27}$$

where

$$X_{2DW} = \begin{bmatrix} X_2(:, i-j-k : i+j-k) \\ X_2(:, i-j-k+1 : i+j-k+1) \\ X_2(:, i-j-k+2 : i+j-k+2) \\ \dots \\ X_2(:, i-j : i+j) \\ \dots \\ X_2(:, i-j+k : i+j+k) \end{bmatrix}$$

and

$$X_{1DW} = \begin{bmatrix} X_1(:, i-k) \\ X_1(:, i-k+1) \\ X_1(:, i-k+2) \\ \dots \\ X_1(:, i) \\ \dots \\ X_1(:, i+k) \end{bmatrix}$$

#### 2.4.5.7 Orthogonal Signal Correction

OSC was introduced by Wold et al.<sup>82</sup>. Use of OSC for instrument standardisation was investigated by Sjöblom et al.<sup>71</sup> as a technique for pre-processing NIR spectra before they are subjected to a multivariate calibration. Sjöblom claimed that OSC makes the spectra less dependent on instrument variation, by removing instrument specific features from the spectra before a calibration model is developed. The main principle of OSC is to reduce the largest features possible to model variation in  $\mathbf{X}$  (spectra) not correlated to analyte variation described by  $\mathbf{y}$  (concentration). This is achieved by correcting the  $\mathbf{X}$ -matrix by subtraction of variation that is orthogonal to the calibration  $\mathbf{Y}$ -matrix. Usually both spectral and analyte matrices are individually centred before orthogonalisation. A score vector is calculated using PCA, then orthogonalised to  $\mathbf{y}$ . This is repeated until stability is achieved. The spectral data is then PLS regressed against this score vector. B coefficients are employed to construct new scores and loading which transform the spectral data. This

correction is applied to new spectra which are going to be used in predictions. Several different algorithms have been developed for the calculation of the score vector by Wold et al.<sup>83</sup>, Fern<sup>84</sup>, direct orthogonalisation (DO) by Andersson<sup>85</sup>, direct OSC (DOSC) by Westerhaus et al.<sup>86</sup> and orthogonal projection to latent structures (OPLS) by Trygg and Wold<sup>87</sup>.

#### 2.4.5.8 Wavelet Transform

Transference of near-infrared spectra in the wavelet domain was proposed by Walczak et al.<sup>88</sup> in 1997. A WT involves the decomposition of a spectrum into simpler fixed building blocks at different scales and positions. It allows for the analysis of signals at different levels of resolution. WT has a similar mathematical basis to Fourier transforms in transforming a signal linearly from its domain to a different domain. WTs use a *scaling variable* and a *position variable* that closely resembles their Fourier transform time-frequency variable counterparts. This method can have the benefit of reducing spectral noise.

The signal of length  $N = 2^L$  can be divided into its low frequency components (approximation/average) and high-frequency components (details/difference) from 0 Hz to the Nyquist frequency (half the number of wavelengths) on the L different scales/levels of resolution. The data is transformed by the discrete wavelet transform (DWT)<sup>89</sup>. At each stage the sample signal is passed through a low-pass filter (scaling filter), denoted as **H**, and a high pass-filter (wavelet filter), denoted as **G**. These filters must satisfy the orthogonality conditions

$$\mathbf{HG}^* = \mathbf{GH}^* = \mathbf{0} \quad \text{Eqn 2.28}$$

and

$$\mathbf{H}^* \mathbf{H} + \mathbf{G}^* \mathbf{G} = \mathbf{I} \quad \text{Eqn 2.29}$$

where **I** is the identity operator

This produces a set of N/2 coefficients of approximations and N/2 coefficients of details. The decomposition is iterated on the low frequency components only (approximations). Each time this results in new sets of approximations and details and continues until the set

consists of a single unit. If  $\mathbf{a}$  and  $\mathbf{d}$  denote approximation and detail respectively and  $\mathbf{f}$  is initial signal, the decomposition and reconstruction can be represented by

*Decomposition:* Set  $\mathbf{a}^j = \mathbf{f}$ . Then for  $j = 0, 1, 2, \dots, L$

$$\mathbf{a}^{j+1} = \mathbf{H}\mathbf{a}^j \quad \text{Eqn 2.30}$$

and

$$\mathbf{d}^{j+1} = \mathbf{G}\mathbf{a}^j \quad \text{Eqn 2.31}$$

*Reconstruction:* Start with  $\mathbf{a}^L$  and  $\mathbf{d}^L$ . Then for  $j = L, L-1, \dots, 0$

$$\mathbf{a}^{j+1} = \mathbf{H}^* \mathbf{a}^j + \mathbf{G}^* \mathbf{d}^j \quad \text{Eqn 2.32}$$

For calibration transfer, a subset of spectra from the master ( $^m\mathbf{S}$ ) and slave ( $^s\mathbf{S}$ ) instruments are chosen and wavelet transforms are applied using the selected filter and resolution criteria. These yield the  $^m\mathbf{W}$  and  $^s\mathbf{W}$  matrices, containing the WT coefficients of the master and slave respectively. A univariate linear regression model is applied to the  $^m\mathbf{W}$  and  $^s\mathbf{W}$  matrices via

$$^m\mathbf{W}(:,i) = t(i)^s \mathbf{W}(:,i) \quad \text{Eqn 2.33}$$

where  $i=1, \dots$ , number of wavelet transform coefficients.

Each slave spectrum is then computed using the wavelet transform. The coefficients are transferred with the computed standardisation parameters  $t$ . The inverse WT (reconstruction) is performed to the transferred wavelet coefficients, giving standardised NIR spectra.

#### 2.4.5.9 Finite Impulse Response

This method proposed by Blank et al.<sup>52</sup> has the advantage that only one spectrum from the master instrument is required, not a complete set of spectra from standardisation samples. This approach involves the reduction of the instrument variation function in the presence of chemically relevant variation. A spectrum from the master instrument, denoted by  $\mathbf{r}$ , is used to filter the spectra to be transferred using a sliding processing

window of  $2p + 1$ . A spectrum acquired on the slave instrument, denoted by  $\mathbf{s}$ , and  $\mathbf{r}$ , are mean centred within the procession window by the relations

$$\bar{\mathbf{s}} = [s_{-p} - \text{mean}(\mathbf{s}), s_{1-p} - \text{mean}(\mathbf{s}), \dots, s_p - \text{mean}(\mathbf{s})] \quad \text{Eqn 2.34}$$

$$\bar{\mathbf{r}} = [r_{-p} - \text{mean}(\mathbf{r}), r_{1-p} - \text{mean}(\mathbf{r}), \dots, r_p - \text{mean}(\mathbf{r})] \quad \text{Eqn 2.35}$$

where the subscript on  $s$  and  $r$  refer to elements within the  $2p + 1$  window and

$$\text{mean}(x) = \sum_{k=-p}^p \frac{x_k}{2p+1} \quad \text{Eqn 2.36}$$

The mean centred spectra are regressed against each other using least squares (within the processing window), yielding a regression coefficient,  $b_i$ . This is iteratively repeated for each wavelength according to

$$\mathbf{b}_i = \left( \bar{\mathbf{r}}^T \bullet \bar{\mathbf{r}} \right)^{-1} \bullet \bar{\mathbf{r}}^T \bullet \bar{\mathbf{s}} \quad \text{Eqn 2.37}$$

The regression coefficient is then used to generate the transferred spectrum,  $\bar{\mathbf{s}}^*$ , by the relation

$$\bar{\mathbf{s}}_i^* = \frac{\bar{\mathbf{s}}_i}{\mathbf{b}_i} + \text{mean}(\mathbf{r}) \quad \text{Eqn 2.38}$$

End points of the slave spectra are processed using multiplicative scatter correction.

It is claimed that centring at each point reduces reliance on regression, improves the predictive power and makes the model more resistant to model errors, such as error caused by nonlinear effects<sup>52</sup>.

#### 2.4.5.10 Neural Networks

Artificial NN can be broadly classified as feed forward networks or recurrent networks. Recurrent networks model oscillating or dynamic systems, where the output is fed back into the network as input for the next cycle. Feed forward networks are purely functions of the current input, thus the most appropriate for spectroscopic data<sup>90</sup>.

A typical multilayer feed forward NN architecture consists of three layers: input, intermediate or hidden and finally the output. The inputs layer of neurons is simply input with no processing ability. The hidden (intermediate) layer of neurons is where the majority of the processing/calculation is performed. The output layer contains a single neuron unit for each response. All neurons in adjacent layers are connected by links, each having an associated weight. Neurons sum the weighted signals that are supplied to them, and then scale the signal via an activation/transfer function, before outputting to each driven connection (see Figure 2.14).

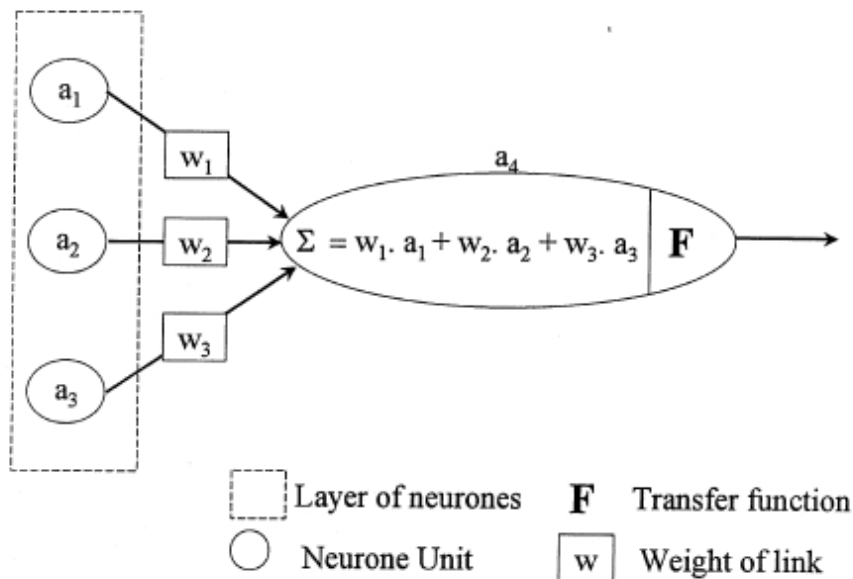


**Figure 2.14 Signal transmission between two layers of neurons<sup>63</sup>**

A NN is trained by iteratively adjusting the weightings on each of the links. This is achieved by inputting a training set, then noting the differences between the actual and desired output at each neuron. These differences, taken over the entire training set, are fed in reverse direction to signal flow (back-propagation of error) through the NN, modifying the weights. This process is repeated until a suitable error is achieved.

Goodacre et al.<sup>91</sup>, Duponchel et al.<sup>63</sup> and Despagne et al.<sup>61</sup> have all applied NN to calibration transfer. The framework for calibration transfer is based on PDS, but with the PLS or PCR replaced with artificial neural networks. Figure 2.15 shows a typical application of NN to calibration transfer.

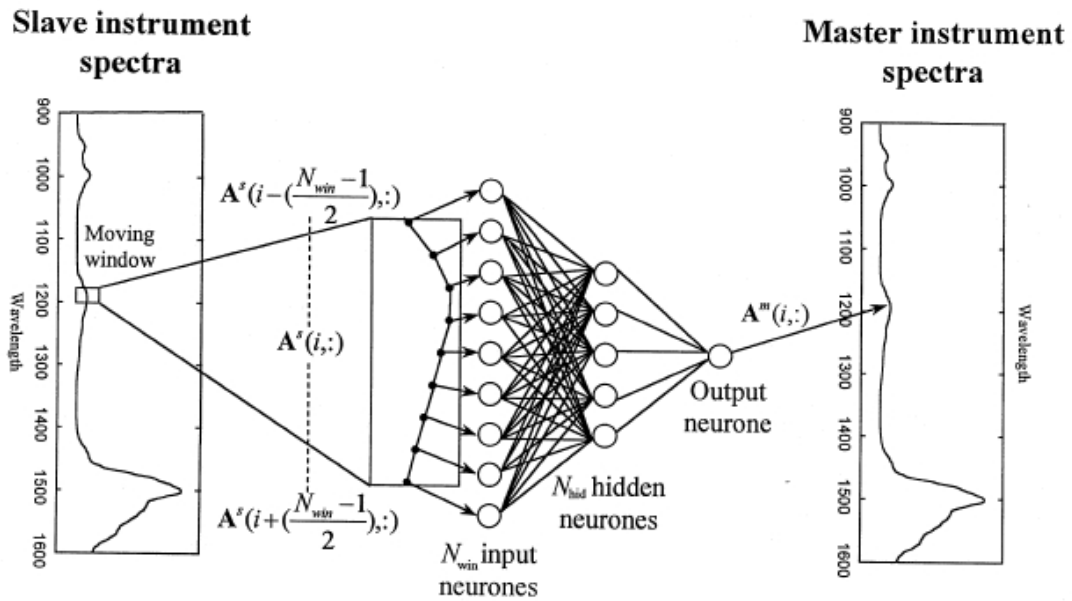


Figure 2.15 Typical application of neural networks to calibration transfer<sup>63</sup>

#### 2.4.5.11 Model Updating

MU provides an evolving model by where new spectra from the slave (new) instrument are added and old spectra from the master instrument are removed from the calibration model. Eventually the calibration model will contain only spectra from the slave (new) instrument. Samples are not required to be measured on both instruments, but a new predictive model for each instrument is required.

## 2.5 Conclusion

Individual visible-shortwave NIR spectroscopy hardware components influence the performance. Issues including lamp type, lamp and detector stability, model transfer across instruments and robustness in terms of varying temperature have been sparsely reported. The aim of this thesis is investigate the characteristics of individual components, particularly their effect on performance on PLS models. The following objectives were thus proposed

- Investigate light source stability from power-up and with temperature variations
- Investigate front end electronics and spectrometer readout with temperature variation
- Assess optical geometry suited to non-contact assessment of fruit
- Assess spectrometer linearity and wavelength accuracy.
- Transfer calibration models for TSS of intact apple fruit between instrumentation based on silicon photodiode arrays

**DECLARATION OF CO-AUTHORSHIP AND CONTRIBUTION**

Title of Paper	Temporal and Environmental Sensitivity of a Photodiode Array Spectrophometric System
Full bibliographic reference for Journal/Book in which the Paper appears	C. Hayes, C. Greensill and K. Walsh, "Temporal and environmental sensitivity of a photodiode array spectrophometric system". <i>Journal of Near Infrared Spectroscopy</i> , <b>22</b> , 297 (2014)
Status	Published

Nature of Candidate's Contribution

All experimental work and analysis

Nature of Co-Authors' Contributions

Supervision

Candidate's Declaration

*I declare that the publication above meets the requirements to be included in the thesis as outlined in the Publication of Research Higher Degree Work for Inclusion in the Thesis Procedures*

*Signature*

*Date* 31 March 2016

### 3 Temporal and Environmental Sensitivity of a Photodiode Array Spectrophometric System <sup>1</sup>

#### Abstract

The effect of the spectral variation in quartz tungsten lamp output with respect to elapsed time from power up and variation in environmental temperature, and the variation in readout in the front end electronics (FEE) and spectrometer with temperature, on predictive model performance of total soluble solids (TSS) in intact fruit was assessed for a silicon photodiode spectrometer based system. Lamp (10 each of OSRAM HLX64623 and Sylvania 521995 12 V 100 W GY6.35 QTH) output was assessed at 10 s intervals over a 4 h period, and 10 min intervals over approximately 3,000 h. Environmental temperature of each component in an NIRS system (lamp, FEE, spectrometer) was incrementally adjusted in 10°C intervals between 10 and 60 °C. Lamp output was spectrally stable within the time of the first measurement (10 s), although total illumination was not stable until approximately 40 min from start-up. Thus performance of the predictive models based on second derivative of absorbance data was not significantly impacted by lamp warm-up time. Noise on measurement associated with use of a single white reference resulted in a mean increase in RMSEP as high as 0.22% TSS and individual increases high as 0.82. Averages of white reference measurements significantly improved performance. When predictive models were developed using second derivative absorbance data and averaged (10) white references, there was no statistically significant impact in RMSEPs on time of lamp warm up (after 10 s), even during the last hours of lamp life. Spectral variation resulting from temperature changes of NIRS system components (lamp & FEE) also affected output quantity rather than quality and thus did not affect the predictive performance due to the second derivative absorbance pre-treatment. Some lamps displayed start-up output characteristics on their first use, which were not repeated in subsequent trials. This result indicates the need for a short lamp ‘burn in’ period.

---

<sup>1</sup> This chapter has been published under this title in the Journal of Near Infrared Spectroscopy 2014. A shortened version was presented at the International Horticultural Congress 2014 (Appendix A), which includes additional work on QTH lamp stability during warm up, to sub second time frames during the first few seconds of power on, and statistical analysis comparing performance of lamps from two manufacturers.

### 3.1 Introduction

The repeatability of a NIR measurement is linked to the stability of the illumination source and the detector system. This stability can be impacted by several factors, including power stability and ambient temperature. Typical NIR equipment protocols require halogen lamps to be stabilised for a period (e.g., 1 h) before use, and ideally a reference measurement would be taken before every sample measurement. In portable instrumentation, however, power demands may mean it is impractical to allow such lengthy warm up periods, and in other instruments, references are often taken at long intervals.

Changes in ambient temperature can affect both lamp output (intensity and quality) and detector response (wavelength sensitivity), as well as electronic noise<sup>10</sup>. For example, for a silicon photodiode array based shortwave NIR (Zeiss MMS1) detector and halogen lamp assembly, Walsh et al.<sup>92</sup> reported a small change in detector output, and an order of magnitude larger change in lamp output from time of power on. Lamp output (irradiance) was effectively stable within 30 min of activation. The ‘dark’ count from the detector increased with temperature by a count of  $0.33\text{ }^{\circ}\text{C}^{-1}$  from a count of 29 at  $0\text{ }^{\circ}\text{C}^{-1}$  (i.e.  $0.1\%\text{ }^{\circ}\text{C}^{-1}$ ) while a 912 nm peak count increased by  $0.40\%\text{ }^{\circ}\text{C}^{-1}$ , consistent with Zeiss Spectral Sensor product information (79-802e)<sup>37</sup> which reports a sensitivity increase of 0, 0.18, 0.47 and  $0.69\%\text{ }^{\circ}\text{C}^{-1}$  at 500, 735, 912 and 1000 nm, respectively.

Quartz tungsten halogen (QTH) lamps are commonly employed by dispersive and interferometric spectroscopic systems. QTH lamps consist of a quartz glass envelope holding a low pressure halogen gas and a tungsten filament through which a current is passed. Halogen gas combines with tungsten that has been sublimed from the filament and deposits the tungsten, by dissociation, back on the filament once the correct filament temperature has been reached. This process allows the lamp to run hotter, longer and more efficiently, with lamp filaments typically reaching from 2600 to  $3200\text{ }^{\circ}\text{C}$ .<sup>93</sup> The lamps have a finite life because as the tungsten is deposited on the filament, it becomes coarsely crystalline, brittle and therefore prone to mechanical shock. ‘Typical’ QTH lamps have a life of 2000 - 3000 h, while instrument grade lamps<sup>8</sup> have a life of more than 10,000 hours, with lifespan dependent on the operating temperature.

Incandescent objects (such as a heated tungsten filament) emit energy over a broad range of wavelengths, approximating that of a blackbody. The intensity distribution is dependent on the object temperature. The intensity per wavelength,  $I$ , for blackbody radiation is given by the Planck radiation law<sup>94</sup>

$$I(\lambda) = \frac{2\pi hc^2}{\lambda^5 (e^{hc/\lambda kT} - 1)} \quad \text{Eqn 3.1}$$

where  $h$  is Planck's constant,  $c$  is the speed of light,  $k$  is Boltzmann's Constant,  $\lambda$  is the wavelength and  $T$  is the absolute temperature. Thus as object temperature increases, intensity is expected to increase, and increase more at shorter wavelengths, giving a non-correlating curvilinear trend in spectral intensity variation between wavelengths as ambient temperature varies. Assuming a filament temperature of 2900 °C, the effect of a temperature increase of 20 – 60 °C (representing expected change in ambient temperature) might be assumed to have minimal effect on blackbody output, but, from eqn. 1, intensity at 1000 nm is expected to increase by 10.7% with a 60 °C increase (Figure 3.1). Note that at an operating temperature of 2900 °C, a tungsten filament is expected to have a peak emission of approximately 1000 nm, roughly coinciding with the peak efficiency of a silicon based detector, approximately 900 nm.<sup>16, 95</sup> However, grating efficiency, typically varying from 0.9 at the blaze wavelength to 0.4 or lower at other wavelengths, impacts on overall spectrometer sensitivity. For example, the peak count of a Zeiss MMS1 (NIR enhanced)-halogen lamp based system is seen at approximately 800 nm.

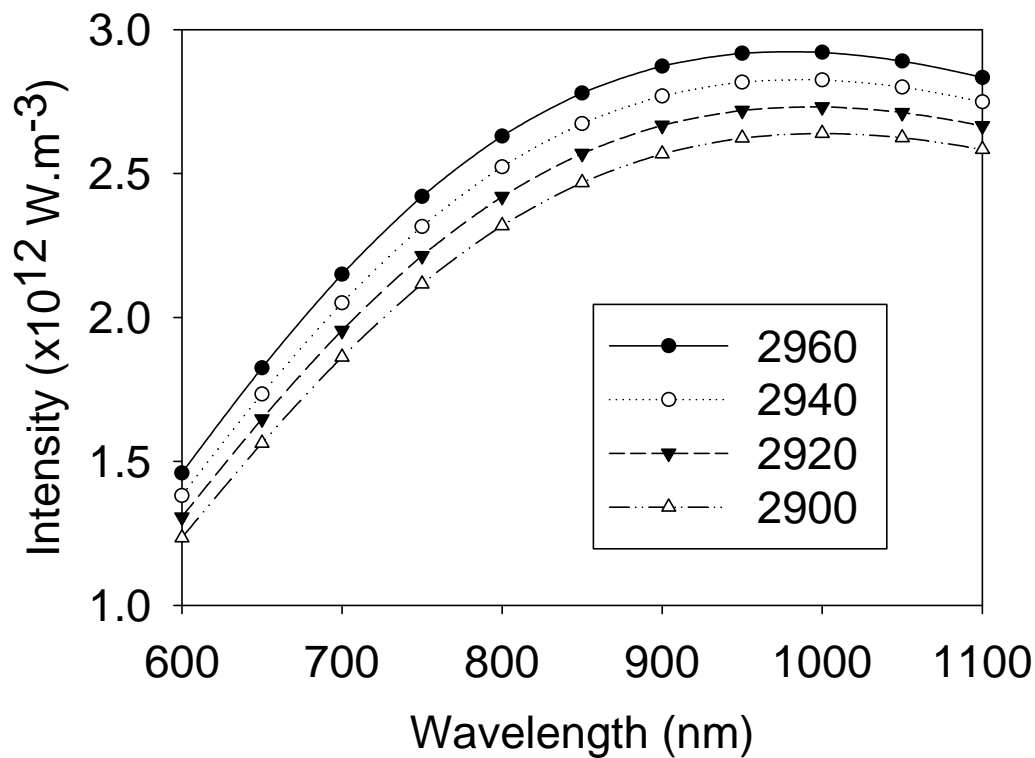


**Figure 3.1. Spectral emittance as a function of temperature based on theoretical calculation (Planck's radiation law)**

Another potential effect of ambient temperature increase is through its effect on expansion of the different components of a spectrometer optical bench, resulting in changes in wavelength calibration to detector pixels (or wavelength accuracy). Wavelength drift of  $0.012 \text{ nm}/^\circ\text{K}$  is reported for the Zeiss MMS1 (NIR enhanced) unit<sup>37</sup>. Martinsen and coworkers<sup>96</sup> considered the effect of drift in wavelength calibration over a 12 month period. Although the drift was small ( $<0.1 \text{ nm}$ ), they noted that partial least squares (PLS) regression models based on short wavelength NIR could be very sensitive to such changes, e.g. a kiwifruit dry matter (DM) model demonstrated a bias shift of 7% DM for a 1 nm perturbation.

Additional to effect on lamp spectral output, detector spectral sensitivity and wavelength accuracy, increasing temperature will also increase electronic noise (detector dark current). Poor power supplies or poor grounding can also contribute to such detector noise.

In summary, lamp and detector behaviour can be expected to change with time, and with changes in environmental conditions, principally temperature. In implementing NIR solutions into field based applications, ambient temperature variations of 50 °C or more may be experienced, and a past reference measurement may no longer be representative of the current condition, with surprisingly small changes capable of causing large bias effects on PLS model predictions. Such impacts can be minimised by reducing temperature change and/or by collecting reference spectra under the same conditions experienced in collection of sample spectra. Thus guidelines on frequency of reference measurements need to be established for a given instrument/application/environment to ensure and maintain optimal system performance.

The objective of the current study was to document the spectral variation of quartz halogen lamps with respect to elapsed time from power up and to environmental temperature, and the effect of environmental temperature on front end electronics (FEE) and detector in terms of readout, to aid in the development of guidelines to enhance predictive model performance. Our work is focussed on the application of SWNIRS to internal quality of fruit, so this study is framed by work with a spectrometer system and data set relevant to that application.

## **3.2 Materials and Methods**

### **3.2.1 Equipment**

The spectrometric system comprised a light source constructed from a 100 W quartz tungsten halogen lamp with the filament at the focal point of a parabolic reflector to produce a collimated beam of light, and an optical probe accepting light to the detector, located in the centre of this light beam and thus creating a shadow on the viewed sample<sup>97</sup>. This configuration enforces an interactance optical geometry. Zeiss MMS1 NIR Enhanced (Carl Zeiss GmbH, Jena, Germany) spectrometers were interfaced with computers via 16-bit tec5 PD-PCI01V1 A/D card (Tec5 AG Sensorik und Systemtechnik, Oberursel, Germany) and front end electronics box (Tec5 AG Sensorik und Systemtechnik, Oberursel, Germany), and used to acquire spectral data of light interacting with a white teflon tile which was illuminated by the light source. Spectral data were acquired using software incorporating LabView (National Instruments

Corporation, Austin, TX, USA) drivers supplied and developed specifically for this project. A stabilised 12V power supply (MAF Oceania, Bacchus Marsh, Vic., Australia) was used to minimise current fluctuations to the halogen lamps. A Contherm 5200HS environmental chamber (Contherm Scientific Limited, Petone, New Zealand) was used to control the environmental temperature of the components under assessment. Temperature inside the environmental box was monitored using a TSI TH-Calc 7425 Thermohygrometer (TSI Inc, Shoreview, MN, USA) whilst the temperature outside was monitored using a Vaisala HMI 31 Thermohygrometer (Vaisala, Helsinki, Finland). The relative humidity level of the enclosure was maintained at 50% for all experiments.

This study assessed the performance of:

- (i) Twenty 12 V 100 W GY6.35 QTH Lamps, of which ten were Osram HLX64623 (Osram A.G., Munich Germany) and ten were Sylvania 521995 (Sylvania Lighting Australasia Pty Ltd, Macquarie Park NSW, Australia.) with rated lifespans of 1500 and 3000 hours respectively<sup>18,98</sup>;
- (ii) 3 FEE devices manufactured by tec5 (Oberursel, Germany), serial numbers (SN) 023, 026 and 029,
- (iii) 6 Zeiss MMS1 NIR Enhanced (Carl Zeiss GmbH, Jena, Germany), SN 301726, 301729, 023104, 023126, 053009 and 055074.

Interactance spectra of peaches were collected using an in-line system ('InSight' MAF Oceania) operating at 7 fruit per second, in a commercial packhouse employing the optical configuration we described previously<sup>97</sup>. White and dark references were collected once only, at the beginning of the day. Fruit total soluble solids (TSS) was assessed using an Atago digital refractometer of juice squeezed from a 2 cm diameter, 1 cm deep core of fruit taken at the point of spectral acquisition.

### **3.2.2 Experimental exercises:**

#### **3.2.2.1 Exercise 1: Spectral variation during lamp ‘warm-up’**

To assess spectral variation from ‘cold’ power up, spectral measurements were automatically acquired at ten second intervals over a period of 4 h after initial power up. The light source, parabolic reflector and Teflon tile were housed within an environmental chamber, at a temperature of 30 °C. The spectrometer (SN 301726), FEE (SN 023) and associated computer were located outside the environmental box, in an air conditioned laboratory at  $22.5 \pm 1$  °C. This procedure was repeated three times for each of the 20 lamps used in this study (60 trials in total).

#### **3.2.2.2 Exercise 2: Spectral variation over lamp lifetime**

To assess spectral variation over the life of the lamps, spectral measurements were automatically acquired at 10 min intervals over a period of 8 months of continual use, or until failure. Seven lamps were so monitored (3 Sylvania and 4 Osram). All components were housed within a laboratory under the same temperature conditions ( $22.5 \pm 3$  °C) during the working day, when the building air conditioning system was operating.

#### **3.2.2.3 Variation in components with environmental temperature**

To assess the effect of variation in environmental temperature on the NIRS system, each of the components being tested, lamp (including parabolic reflector), FEE or MMS1, was housed in the environmental chamber whilst the other components and computer were located outside the environmental box, in an air conditioned laboratory at  $22.5 \pm 1$  °C . The temperature in the enclosure was incrementally increased in 10 °C intervals between 10 and 60 °C. The system was initially stabilised over 3 h, with a 1 h stabilisation between temperature intervals.

### **3.2.3 Impact on predictive performance for a peach TSS model**

The impact of spectral variation recorded in the above the exercises were assessed in the context of effect on predictive performance measures. PLS predictive models for fruit

TSS were developed using a system employing MMS1 SN301738 and a population of 101 peaches.

For Exercise 1, the white reference spectra used in the calculation of (fruit) absorbance spectra was replaced with white reference data acquired during lamp testing. The average of the last ten white reference measurements collected over the four hour period was used (lamp output was considered stable at this extended time point), and a PLS model on fruit TSS developed. The model was used to predict TSS of data sets in which, iteratively, each white tile measurement taken over the 4 h period was used as the white reference for calculation of the 101 fruit absorbance spectra. This exercise was repeated using white reference spectra calculated as the average of three, six, ten and twenty sequential measurements.

This analysis was repeated for the Exercise 2, using white tile measurements taken at 10 minute intervals over the life of the lamp (approx. 3000 h) as white references. The analysis was again repeated for the third exercise, using an average of 10 white tile measurements acquired at a range of temperatures (10 to 60 °C at 10 °C intervals). The PLS predictive models were redeveloped using the white reference acquired with the lamp ambient temperature of 10 °C, and used for prediction on spectra redeveloped using as a reference the average of ten white tile measurements at each lamp ambient temperature setting.

### 3.2.4 Chemometrics

PLS regression models were developed using MATLAB R2012b (MathWorks Inc., Natick, USA) with PLS toolbox 6.7 (Eigenvector Research Inc., Wenatchee, USA). The wavelength range used was 730-930 nm. Model performance was assessed in terms of calibration  $R^2$ , root mean square error of cross validation (RMSECV) based on full cross validation, and the ratio of SD to RMSECV (SDR). Prediction performance was assessed in terms of root mean square error of prediction (RMSEP) and bias corrected RMSEP ( $SEP_{-b}$ ).

Bias can be calculated as:

$$bias = \sqrt{RMSEP^2 - SEP_{-b}^2} \quad \text{Eqn 3.2}$$

When the white reference used for calculation of absorbance for a set of spectra is changed, the effect on a PLS regression model prediction will be to change the bias of the model, with no effect on SEP<sub>b</sub>. This bias could be calculated by multiplying the second derivative of the absorbance spectrum of the new white tile measurement (using the original white measurement as reference) by the coefficients of the model. However, RMSEP data is presented, with the minimum RMSEP in the plots being equivalent to that of the original model, to illustrate the importance of the error to the model prediction.

### 3.3 Results and Discussion

#### 3.3.1 Stonefruit TSS PLS regression models

The population (n=101) of fruit used had a mean TSS of 9.71 and SD 0.619 %w/v. The PLS regression models developed on the spectra as received from the in-line grading unit achieved a root mean square error of calibration (RMSEC) of 0.347, RMSECV of 0.423 %TSS and  $R_{cv}^2$  of 0.966.

#### 3.3.2 Spectral variation during lamp ‘warm-up’

Following lamp power-up, spectral intensity decreased across all wavelengths, entering a plateau phase after approximately 40 min (Figure 3.2).

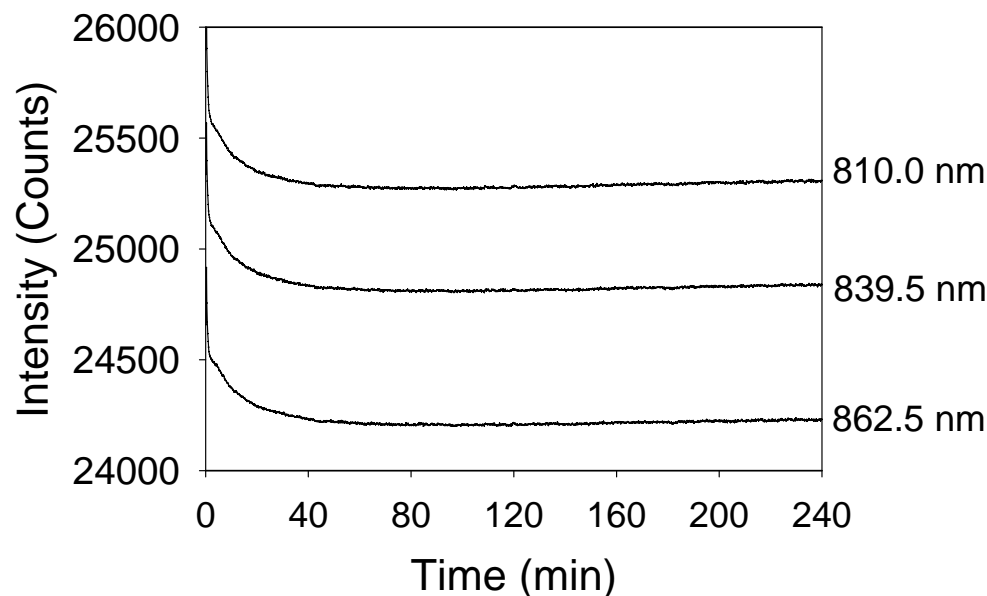


**Figure 3.2. Graph of spectrometer output for three wavelengths (810, 840, 863 nm represented by upper, middle and lower lines, respectively) for a QTH lamp output over a four hour period from cold start-up (data shown for an example lamp, of 20 lamps trialled).**

To test the impact of reference averaging on the predictive performance, white references were averaged over three, six, ten and twenty sequential measurements. The variation in RMSEP values with use of a single white reference were well above the RMSECV for the model (Figure 3.3 and Figure 3.4). For all subsequent analysis, an average of 10 white references was used (conforming to the protocol used in the InSight on-line grading system).

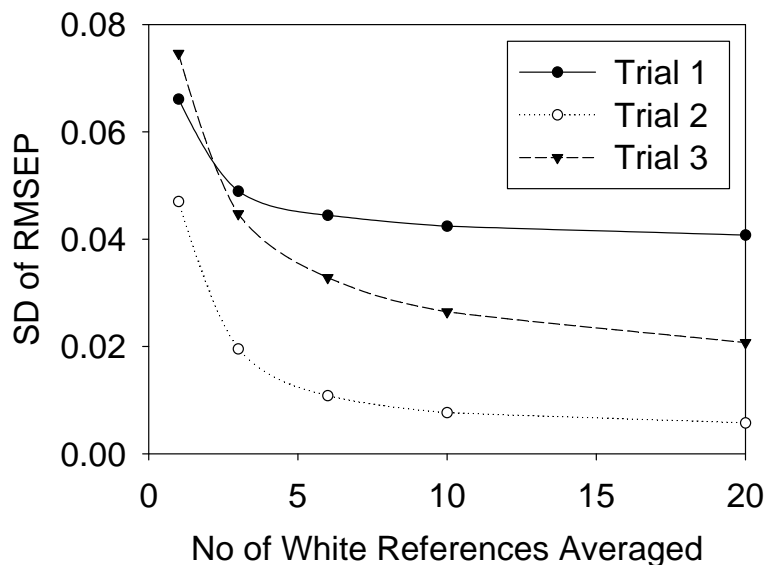


**Figure 3.3. RMSEP variability, assessed as a SD (% TSS) (over the four hour trial), as a function of number of white reference spectra averaged before use in calculation of absorbance of the fruit data set.**

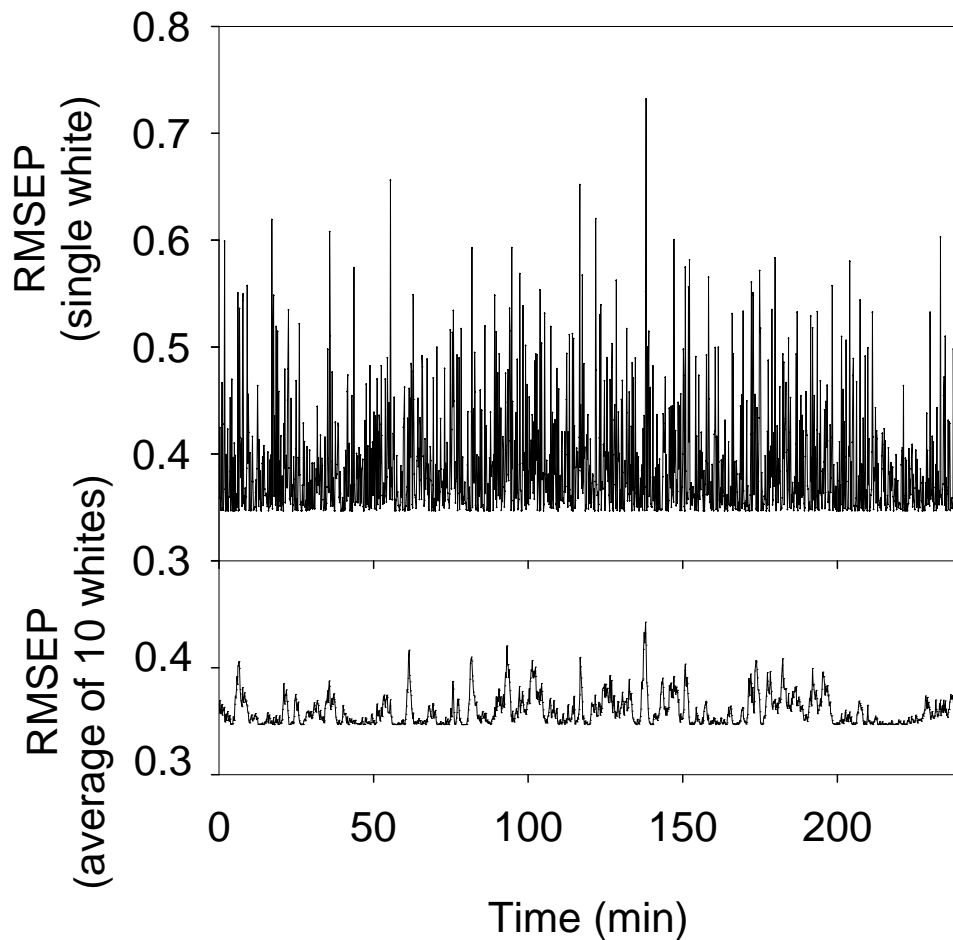


**Figure 3.4. PLS regression model prediction statistics (RMSEP, % TSS) based on use of white reference data collected at various times over 4 h from lamp power up for the representative case of data from Osram Lamp J Trial 1. The top panel represents use of individual spectra in the absorbance calculation, while the bottom panel represents use of a running average of 10 spectra.**

The effect of the change in lamp spectral quality in terms of predictive performances of the calibration models were assessed for the 60 trials. In most cases, there was no improvement in RMSEP after the initial 10 s measurement following start up (example Sylvania lamp, Figure 3.4 and example used Osram lamp, Figure 3.5). The exceptions were four of the Osram lamps and three of the Sylvania lamps, which displayed improvements in RMSEP after an initial warm up period, but only on their first trial (Figure 3.5). This result was interpreted as evidence of lamps requiring an initial “burn in” period to achieve to achieve the same spectral quality. The length of the “burn in” period was not consistent across the seven lamps, varying from 20 to 220 min.

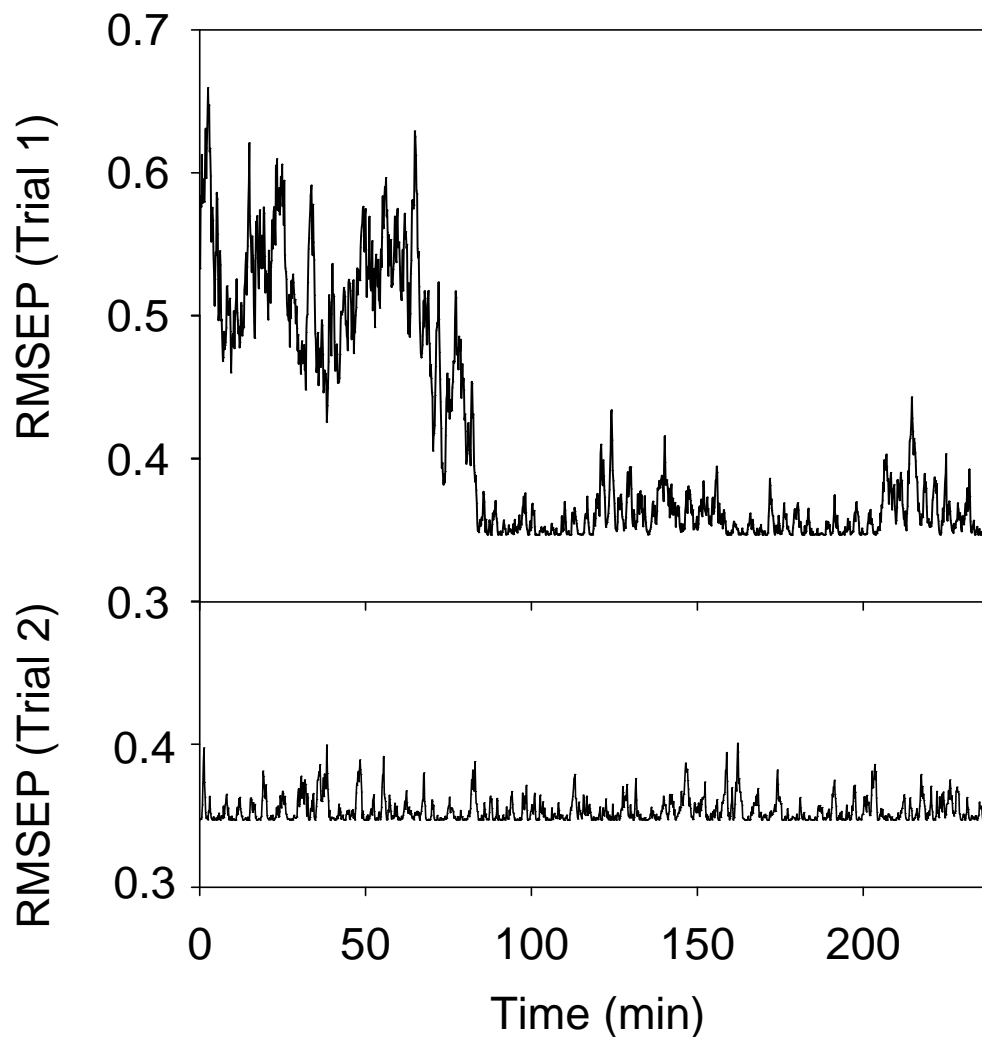


**Figure 3.5. PLS regression model prediction statistics (RMSEP, % TSS) based on use of (average of ten) spectra collected at various times over 4 h from lamp power-up as white reference data. Data from Sylvania lamp G is displayed. The top panel represents a 4 h period involving power up of the unused bulb, while the bottom panel represents a 4 h period after 4 h of lamp use.**

The performance of each lamp and manufacturer was compared using the mean RMSEP of relative reconstructed prediction sets. There was no statistically significant difference (at  $\alpha=0.10$ ) between lamps of a given type, or between lamp types (analysis of variance, data not shown).

### 3.3.3 Spectral variation over lamp lifetime

Lamp output was remarkably stable until filament breakage, although a clear diurnal cycle linked to the building's air-conditioning was obvious (Figure 3.6). Some lamps showed no ageing apparent in spectra through to filament breakage, while others demonstrated change in the last minutes to hours of lamp life (as in the example shown in Figure 3.6). During this end-of-life period, the increase in lamp intensity was greater at shorter wavelengths (Figure 3.7), but there was no effect on RMSEP values. Of the seven lamps trialled, one lamp lasted only for approximately 520 h, while all others outlasted the manufacturers' specifications of 1500 and 3000 h (Osram and Sylvania, respectively).

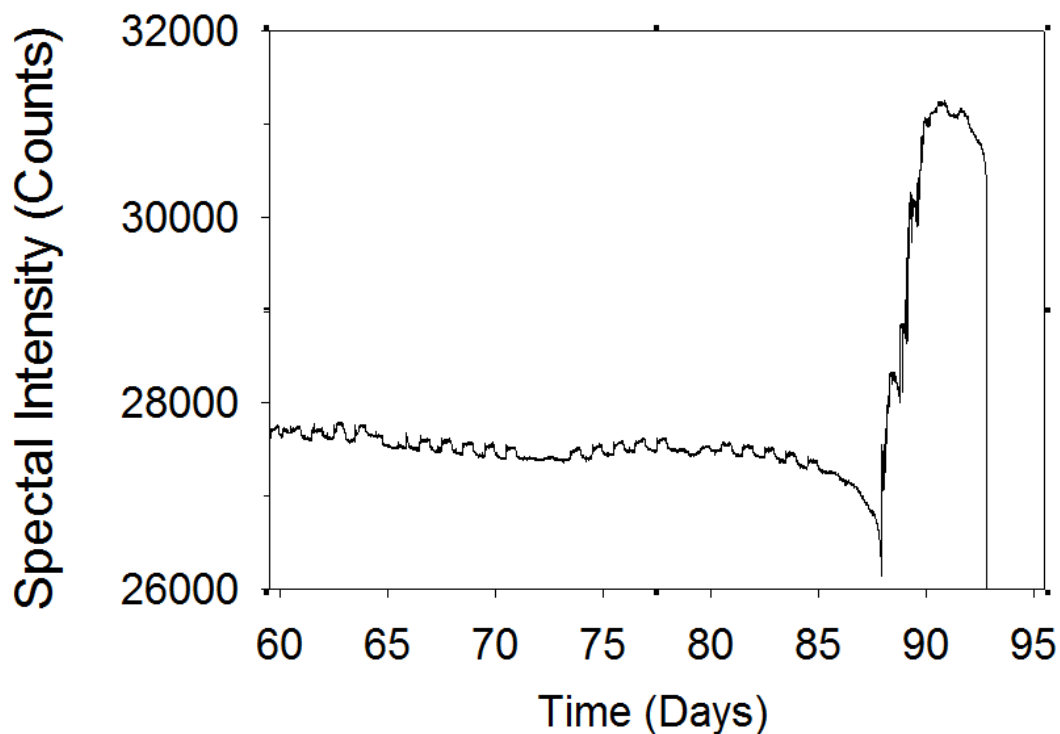


**Figure 3.6. Spectral intensity of a lamp (OSRAM G) at 720 nm in the month ending in lamp failure, showing the diurnal cycle of the laboratory airconditioning (note weekend periods are not airconditioned) and the increase in spectral intensity before the filament breaks.**

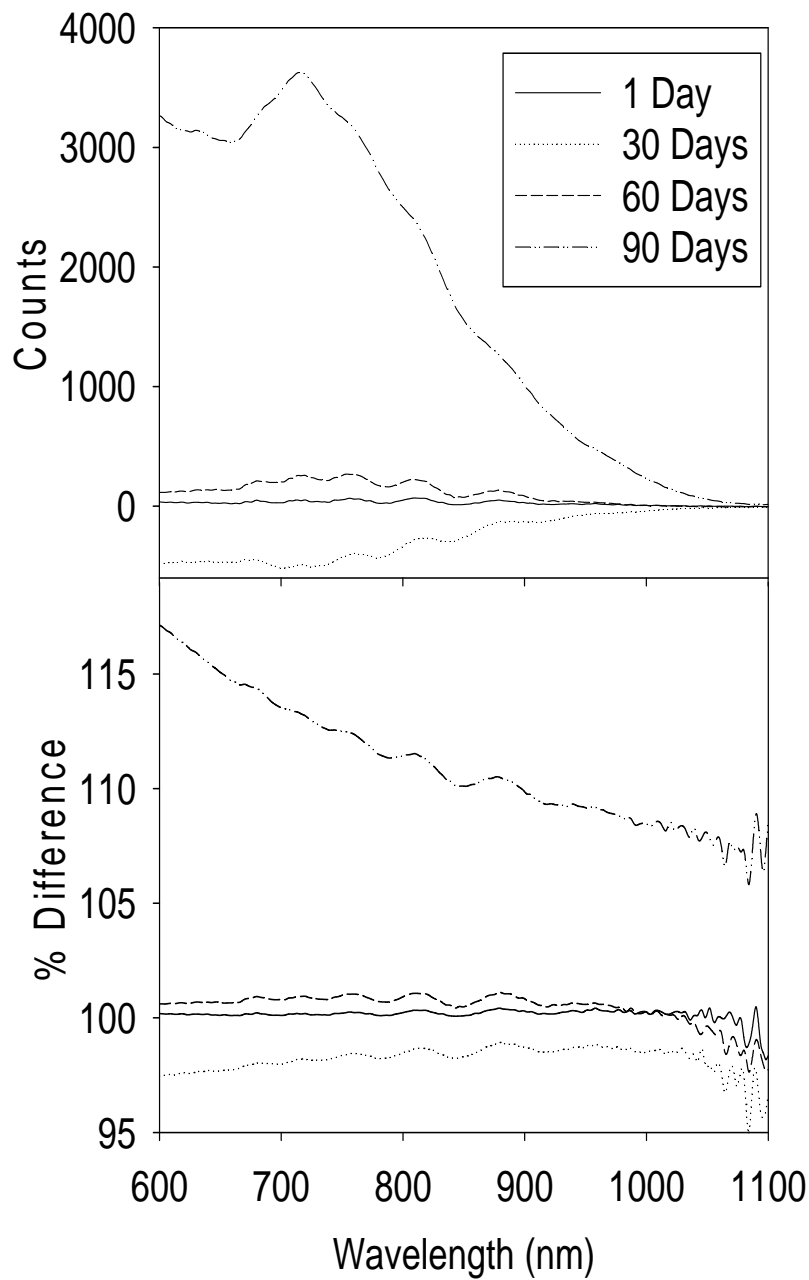


**Figure 3.7. Spectral intensity (ADC) recorded of a white tile, with increasing lamp (OSRAM G) age, as a difference (top panel) and as percentage (bottom panel), recorded from spectra at 4 hours from power on.**

The effect of lamp age across 90 days (2000 h) on regression model prediction varied greatly across the 60 trials, demonstrating lamp individuality (Figure 3.8). Some lamps were quite stable over the period, others showed instability.

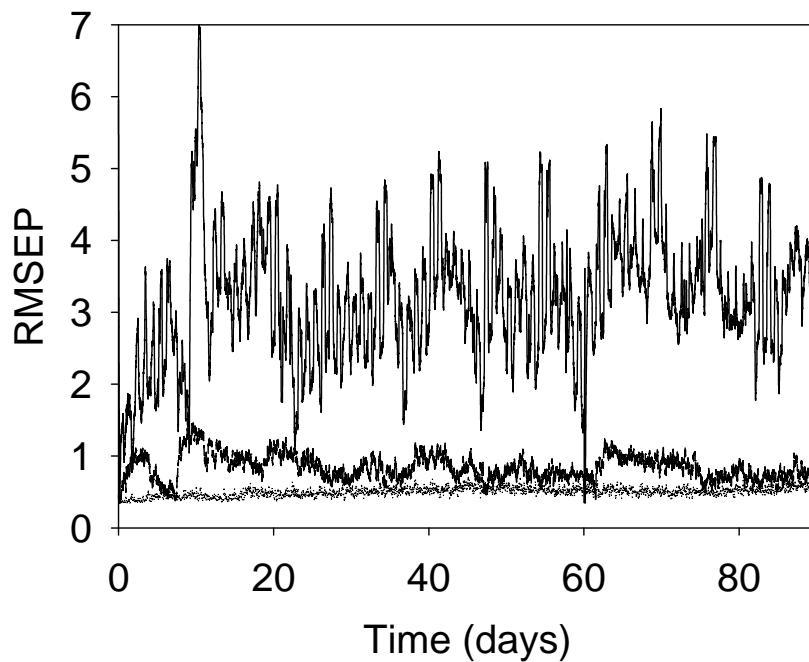


**Figure 3.8. Plots showing model performance (as RMSEP, % TSS) using white references taken during lamp aging for Osram Lamp J (bottom) and G (top) and Sylvania Lamp A (middle).**

### **3.3.4 Variation in components with environmental temperature**

#### **3.3.4.1 Lamp variation**

The spectral output of the QTH lamps decreased as ambient temperature increased, consistent with the observed diurnal cycle of but with little differential variation over the wavelength range 720 - 970 nm (the range used in the Brix PLS model) (Figure 3.9). At 800 nm, a 4% decrease in spectral emittance was observed over the 50°C temperature range.

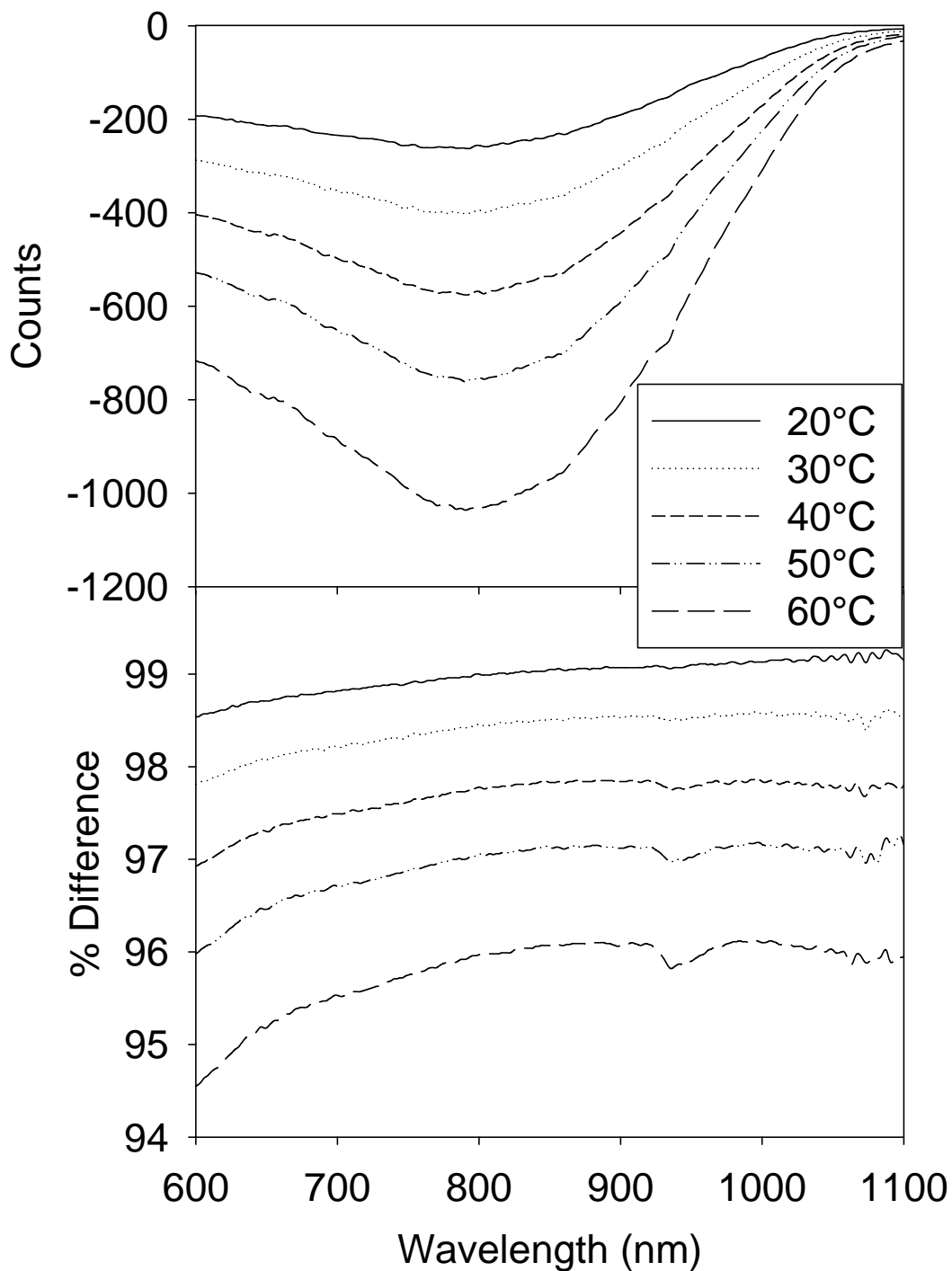


**Figure 3.9.** Spectral intensity (ADC) recorded of a white tile, with increasing ambient temperature of the lamp, presented as a difference spectrum from spectra recorded at an ambient temperature of 10 °C (A) and as percentage of spectra recorded at an ambient temperature of 10 °C (B). Results are shown for a single lamp (Osram E), but were typical of 60 trials.

In contrast, a 11.1% increase in spectral emittance at 800 nm is expected from a 50°C temperature increase based on blackbody behaviour (from Eqn 3.1). From Plank's radiation law (Eqn 3.1), the change in spectral intensity at 2900K for 800 nm is calculated to be 0.22% K<sup>-1</sup>. However, an increase in filament temperature would also cause an increase in resistivity of the filament, which varies via a resistivity coefficient,  $\alpha$ , for the given conductor<sup>94</sup> given by.

$$\frac{\Delta R}{R} = \alpha \Delta T \quad \text{Eqn 3.3}$$

where  $R$  is the resistivity and  $\Delta T$  is the change in temperature. For tungsten,  $\alpha$  is 0.0045  $\Omega\text{K}^{-1}$ .<sup>94</sup> Thus a 50K increase would result in a 22.5% increase in resistivity, which gives a corresponding drop in power output.

It cannot, however, be assumed that the filament temperature and ambient temperature are linearly correlated during lamp operation. Solving for a 4% decrease in counts given both the change in resistivity and blackbody behaviour gives an estimate of lamp filament temperature - approximately an 18 °K increase in filament temperature for the 50 °K ambient temperature increase.

As ambient temperature was increased, an absorption feature at 940 nm, also increased (Figure 3.9). This feature is interpreted as a water vapour absorption feature. Relative humidity was held constant at 50% across the temperature conditions, such that water vapour pressure will have increased from 4.69 to 60.68 g/m<sup>3</sup> at 10 to 60°C, respectively<sup>99</sup>, throughout the 15 cm pathlength of the experimental set up. Pure water has many absorption peaks in the 934-952 nm range<sup>100</sup>, due to the rotational-vibrational transitions of the hydrogen bonds, but the spectrometer wavelength resolution (FWHM of approx. 10 nm) results in an apparent single peak centred at 940 nm.

To assess the impact of change in lamp ambient temperature on in-line assessment of fruit, TSS model predictions were calculated by replacing white tile reference measurements, as in the previous exercises. The PLS predictive models were redeveloped using the new white reference acquired with the lamp ambient temperature of 10 °C, and used for prediction on spectra redeveloped using the white reference at each lamp ambient temperature setting. The average of ten measurements taken at each temperature setting was used.

Change in lamp temperature had little effect on RMSEP or bias values (Table 3.1) and indeed the observed variation in RMSEP and bias values was within that observed associated with lamp variation with time (Exercise 2). The lack of an effect resulting from changes in lamp spectral output with ambient temperature is ascribed to the second derivative absorbance pre-treatment, and a temperature impact on spectral intensity, but not quality.

**Table 3.1. Typical prediction statistics for a model based on reference spectra collected at 10 °C, used in prediction of a population with references at different temperatures, where temperature was varied of either (A) lamp, (B) FEE or (C) MMS1 ambient temperature. The calibration model possessed an RMSEC of 0.347 %TSS.**

	<b>Lamp ambient temperature increase (°C)</b>				
	<b>10</b>	<b>20</b>	<b>30</b>	<b>40</b>	<b>50</b>
<b>RMSEP</b>	0.350	0.347	0.375	0.415	0.362
<b>Bias</b>	0.048	0.000	-0.143	-0.227	-0.103
	<b>FEE ambient temperature increase (°C)</b>				
	<b>10</b>	<b>20</b>	<b>30</b>	<b>40</b>	<b>50</b>
<b>RMSEP</b>	0.368	0.383	0.373	0.367	0.363
<b>Bias</b>	0.124	0.162	0.137	0.120	0.106
	<b>MMS1 ambient temperature Increase (°C)</b>				
	<b>10</b>	<b>20</b>	<b>30</b>	<b>40</b>	<b>50</b>
<b>RMSEP</b>	0.415	0.674	0.969	1.581	2.467
<b>Bias</b>	0.228	0.578	0.904	1.54	2.44

#### **3.3.4.2 FEE and spectrometer temperature variation**

The same procedure was repeated for variation in readout with changes in FEE temperature (Figure 3.10). Again, variation in RMSEP values was consistent with that observed associated with lamp variation with time, and the lack of impact was ascribed to the use of a second derivative absorbance pre-treatment, and impact on spectral intensity, but not quality.

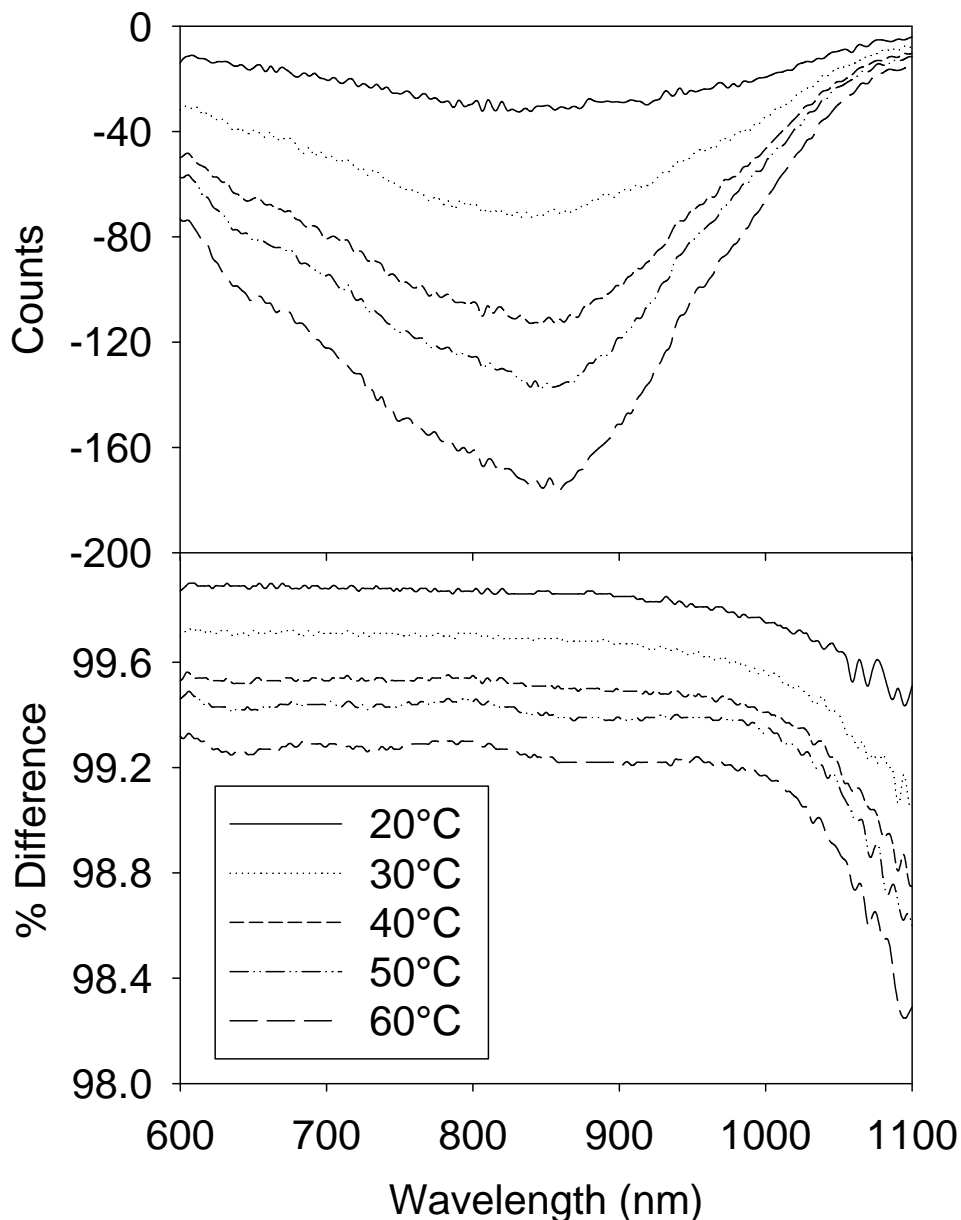


**Figure 3.10. Spectral intensity (ADC) recorded of a white tile, with increasing ambient temperature of the FEE, as a difference spectrum from spectra recorded at an ambient temperature of 10 °C (A) and as percentage of spectra recorded at an ambient temperature of 10 °C (B). Results are shown for a single lamp, but were typical of 9 trials.**

The procedure was repeated for variation in readout with changes in MMS1 temperature. In all trials of all MMS1 units, RMSEP increased with temperature of spectrometer, albeit by differing amounts. For reasons that require further investigation, the bias and thus RMSEP values for some units became significantly higher after only a 10 °C increase,

whilst for other units the change was minimal for the first 30 °C increase. In the example given (Figure 3.11), change in the 730 – 930 nm region used in the Brix model was relatively small. Thus the temperature at which a model fails (e.g. RMSEP > 1% TSS) is unit dependent, for reasons that require further investigation.

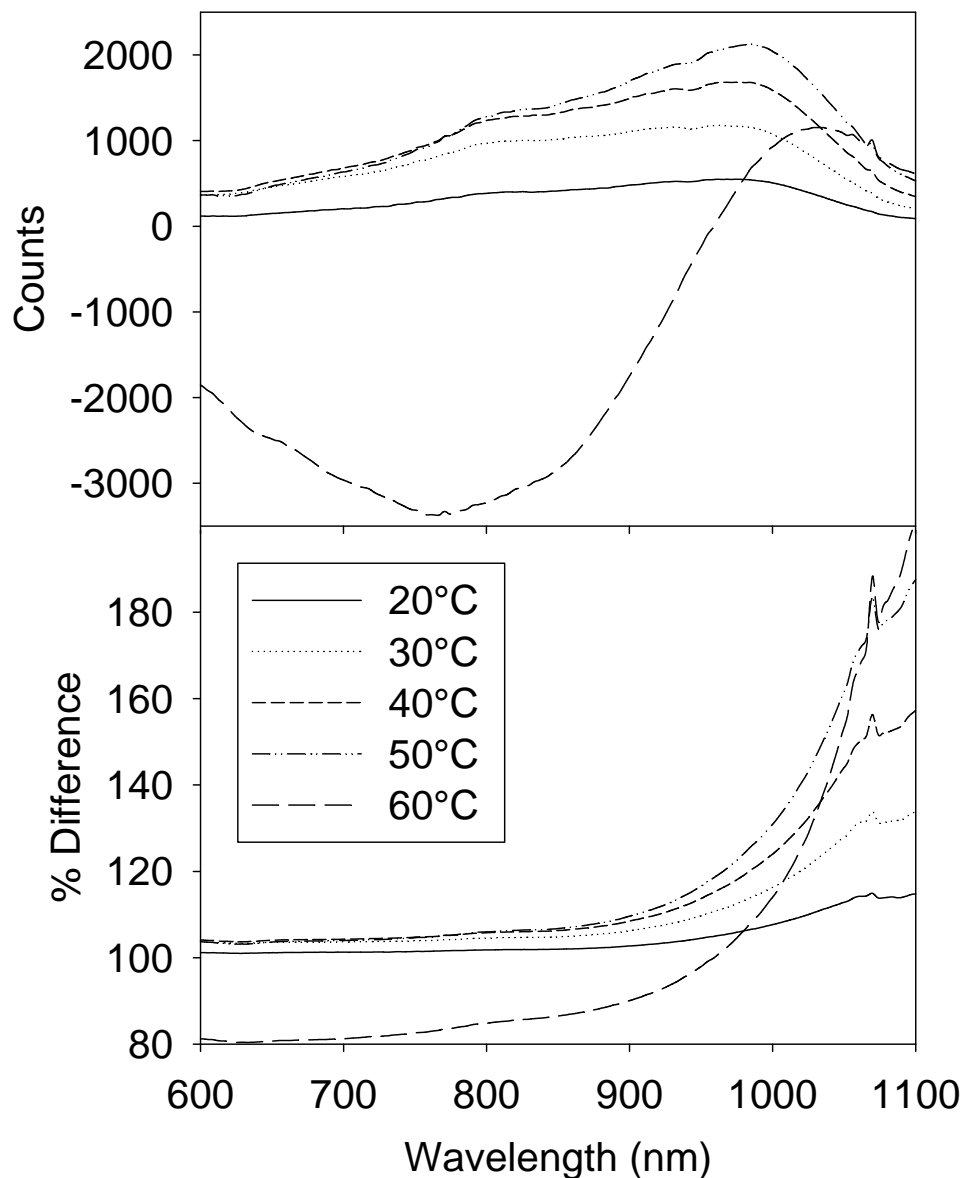


**Figure 3.11. Spectral intensity (ADC) recorded of a white tile, with increasing ambient temperature of the MMS1 spectrometer, as a difference spectrum from spectra recorded at an ambient temperature of 10 °C (A) and as percentage of spectra recorded at an ambient temperature of 10 °C (B). Results are shown for a single spectrometer, but were typical of 18 trials.**

### 3.4 Conclusion

Lamp output was spectrally stable within the time of the first measurement (10 s), although total illumination was not stable until approximately 40 min from start-up. Thus performance of the predictive models based on second derivative of absorbance data was not impacted by lamp warm-up time. Noise on measurement associated with use of a single white reference resulted in a mean increase in RMSEP as high as 0.22 and individual increases high as 0.82. Averages of white reference measurements significantly improved performance. When predictive models were developed using second derivative absorbance data and averaged (10) white references, there was no statistically significant impact in RMSEPs on time of lamp warm up (after 10s), even during the last hours of lamp life.

Spectral variation resulting from changes of NIRS system components (lamp and FEE) also affected lamp output quantity rather than quality and thus did not affect the predictive performance due to the second derivative absorbance pre-treatment.

Some lamps displayed start-up output characteristics on their first use, which were not repeated in subsequent trials. This result indicates the need for a short lamp 'burn in' period.

## 4 LEDs as light sources for spectroscopy of fruit - sensitivity to temperature <sup>2</sup>

### Abstract

Understanding of LED lamp behaviour is essential to support the use of these devices as illumination sources in NIR spectroscopy. Spectral variation in LED (of each of 9 peak wavelengths : 680, 700, 720, 735, 760, 780, 850, 880 and 940 nm) output was assessed with respect to elapsed time from power up and variation in environmental temperature from 0 to 60 °C, in 10°C intervals. Initial LED power-up to full intensity occurred within a measurement cycle (12 ms), then decreased exponentially over approximately 6 min, a result ascribed to an increase in junction temperature as current is passed through the LED. Some LEDs displayed start-up output characteristics on their first use, which were not repeated in subsequent trials. This result indicates the need for a short lamp ‘burn in’ period, which was less than 24 h in all cases. Increase in ambient temperature produced a logarithmic decrease in overall intensity of the LEDs and a linear shift to longer wavelength of the peak emission. This behaviour is consistent with the observed decrease in the I<sub>AD</sub> Index ( $A_{670} - A_{720}$ ) with increased ambient temperature, as measured by an instrument based on LED illumination (DA Meter). With the shift in wavelength with temperature being predictable, instruments should be designed to accommodate for the effect of temperature.

---

<sup>2</sup> This chapter has been submitted under this title to the Journal of Near infrared Spectroscopy, March 2016

## 4.1 Introduction

The non-invasive assessment of parameters relevant to fruit quality typically involves use of visible wavelengths pertinent to the assessment of pigment (e.g. chlorophyll, carotenoid, anthocyanin) levels, and SWNIR wavelengths which allow for relatively long path-lengths through fruit while carrying information on attributes such as total soluble solid content (TSS) and dry matter content (DM). The repeatability of a NIR measurement is impacted by the stability of the illumination source and the detector system, which are in turn impacted by factors such as power stability and ambient temperature.

Light sources for NIRS can be divided into two groups, broadband (thermal) and narrowband (non-thermal)<sup>8</sup>. Quartz tungsten halogen (QTH) lamps are excellent thermal broadband excitation light sources in terms of their lifetime and stability<sup>19, 101</sup>. Unfortunately, they can lead to strong heating of the sample, affecting both NIR spectra and the physico-chemical stability of the sample material<sup>102</sup>. Ambient temperature also impacts QTH lamp output<sup>19</sup>. Non-thermal sources emit radiation over a much narrower range of wavelengths, down to individual lines, and thus consume far less power than a QTH for a given intensity of a specified wavelength. These emitters include discharge lamps, light-emitting diodes (LEDs), laser diodes and lasers, and can have a feedback loop on current/voltage, under photodetector control. Laser diodes and lasers emit over a range of wavelengths as narrow as 0.18 nm FWHM<sup>103</sup>, eliminating the need for pre-filtering for most applications. LEDs emit a wider range of wavelengths, typically 20-50 nm FWHM, and an interference filter can be used to limit radiation to a suitable bandwidth. Alternatively, LEDs of different wavelength maxima can be combined to make a broadband source over a given wavelength range (e.g. at equal 50 nm steps, 8 emitters would be required to cover the SWNIR, 700-1100 nm). LEDs can achieve outputs of up to 100 lumens per watt and can survive for >100,000 hours<sup>17</sup>. LEDs can also be pulsed for milliseconds to produce higher light output, which is more energy efficient and allow for greater heat dissipation.

Materials used in LED production have direct band gaps, with energy levels corresponding to bands in the near-infrared, visible, or near-ultraviolet, with light produced from radiative recombination. The band gap energy depends on the materials

forming the p-n junction, i.e. the semiconductor material and the doping elements. The approximate energies of the carriers correspond to the upper energy level of the valence band and the lowest energy of the conduction band. The wavelength ( $\lambda$ ) of the light emitted from an LED is approximated according to<sup>17</sup>

$$\lambda \approx \frac{hc}{E_{bg}} \quad \text{Eqn 4.1}$$

where  $h$  is Plank's constant,  $c$  is the velocity of light and  $E_{bg}$  is the band gap energy.

Semiconductor materials commonly used in LEDs include AlInGaP (Aluminium–Gallium–Indium–Phosphide), AlGaAs (Aluminium–Gallium–Arsenide), GaAs (Gallium–Arsenide), InGaN (Indium–Gallium–Nitrogen) and InGaAsP (Indium–Gallium–Arsenide–Phosphide). There are few manufacturers of SWNIR wavelength LEDs, but these manufacturers offer LEDs with peak wavelength outputs available at approximately every 10 nm from 700 – 830, then 850, 870, 880, 910, 940, 970, 980, 990, 1020, 1030, 1050, 1070, 1200, 1300, 1450, 1550, and 1600 nm.

LEDs, however, have the disadvantage of being sensitive to ambient temperature in terms of intensity and peak emission. With any LED, temperature increases give relative intensity decreases and shifts to longer wavelengths (“red-shifts”) in peak emission. Near room temperature, LED emission intensity,  $I$ , is frequently described as<sup>104</sup>

$$I = I_{300K} e^{\frac{T-300}{-T_1}} \quad \text{Eqn 4.2}$$

where  $I_{300K}$  is the intensity at 300 K,  $T$  is the ambient temperature (in kelvin) and  $T_1$  is the characteristic temperature specific to each LED. The temperature dependence of the energy gap is expressed by the Varshni formula<sup>105</sup>

$$E_{bg} = E_{g0} - \frac{\alpha T^2}{(T + \beta)} \quad \text{Eqn 4.3}$$

where  $E_{g0}$  is the band gap energy at  $T=0$  K,  $\alpha$  and  $\beta$  are fitting parameters characteristic of a given material, frequently called the Varshni parameters. Thus a change in band gap energy produces a change in peak emission according to Eqn 4.1, and therefore a change in temperature produces a change in the wavelength of peak emission.

For example, Ushio Epitex (Kyoto, Japan) specifications indicate ambient temperature changes between 20-60 °C will cause variations of LED intensity of between 10-28%, and shifts in peak wavelength of 8-10 nm, dependant on the band gap material<sup>22</sup>. Consistent with these specifications, Yu et al.<sup>106</sup> reported an intensity decrease of approximately 10% as the ambient temperature was increased from 20 to 60 °C for a 1 W blue LED and Guo et al.<sup>107</sup> reported an intensity decrease of 6 and 10-14% for blue and red LEDs, respectively, and an almost linear increase in peak wavelength emission. In these cases, the LEDs were driven at 350 mA and the increase in temperature was associated with a decrease in forward voltage. Chhajed et al.<sup>108</sup> reported peak wavelength increases of approximately 0.05, 0.04, 0.03 and 0.16 nm/°C in UV, blue, green (all GaInN), and red (AlGaInP) LEDs respectively, when changing ambient temperature between 23 and 120 °C.

Other factors in quality control of LEDs include batch variation at manufacture and burn in period.<sup>109</sup> The final product step in LED manufacture involves optical characterisation (with these values often reported on manufacturer specification sheets), followed by sorting to 'bins'. This measurement is typically undertaken approximately 20 ms after the LED is switched on, although the LED will not be thermally stabilised or fully 'burnt in'.<sup>110</sup>

'Burn in' refers to a period of instability in peak emission wavelength and intensity in the first period of use after manufacture. Modern high power LEDs have a relatively lengthy stabilisation period. Nägele<sup>110</sup> documented an increase in intensity of approximately 10% over the first 1000 h, while most others, such as Chen et al.<sup>111</sup>, Narendran and Gu<sup>112</sup> and Meneghesso et al.<sup>113</sup> report decreases in intensity over time, with the amount dependant on the operating current. Variation between individual LEDs is also expected, even with units from the same manufacturer's flux bin. Therefore users of these products are advised to perform their own characterisation under stable conditions appropriate for the intended use.

There have been attempts to develop SWNIRS instrumentation based on LEDs as light sources, generally utilising one of two approaches: (i) use as a monochromatic source, with sequential activation of LEDs at discrete wavelengths and use of a single detector; and (ii) use as a broadband source, employing a series of LEDs with overlapping emission spectra, with use of a grating or other means to obtain monochromatic light.

However, given that the dependence of LED output on temperature is well known, surprisingly most reports fail to mention the effect of LED temperature on a spectroscopic application. For example, temperature was not considered in the reports by Gaião et al.<sup>23</sup>, Fonseca and Raimundo<sup>24</sup> or Veras et al.<sup>25</sup>.

Other developers have documented attempts to minimise temperature change. Malenin et al.<sup>114</sup> developed a 32 wavelength NIR LED-array comprised of surface-emitting LEDs centred at 850, 900, 935, 950 and 1020 nm, temperature stabilised with a Peltier element and thermistor. Control electronics sequentially drive the LED array, with light directed to a fixed grating monochromator positioned to give the required wavelength scale. The narrow band spectrum was then transmitted and detected by a single Si diode. As the unit aged, optical output decreased from 0 to 10% depending on the wavelength, but changes in wavelength scale were limited to  $\pm 0.05$  nm.

Dasgupta et al.<sup>115</sup> reviewed the use of LED based instruments for absorbance, fluorescence and spectrochemical measurements in planar flow-through cells, and suggested that thermal stability of the light output could be achieved using a resistor in combination with a negative temperature coefficient thermistor. To combat long-term output instability, it was suggested that the LED be driven with photometric feedback while maintaining the photosensor at constant temperature (e.g. using a temperature sensor and Peltier heating). The commercial Methanalyzer (Alpha-Omega Power Technologies LLC, Albuquerque, NM, USA) uses such a circuit.

Many researches have attempted assessment of TSS or DM of fruit using measurement at only a few SWNIR wavelengths. Early work includes that of Norris<sup>116</sup> and Kawano<sup>117</sup>. Long et al.<sup>118</sup> reported  $R^2$  values of 0.91 %TSS for PLS (720-930 nm) and 0.52 %TSS for MLR models (at 869, 882, 905 and 915 nm) for assessment of melon tissue TSS. More recently, Shafie et al.<sup>119</sup> optimised a six-wavelength (650, 800, 815, 885, 920 and 930 nm) MLR model for predicting kiwifruit dry matter, with results at least as accurate as PLS models ( $R^2$  value of 0.94 and RMSEP of 1.22 %TSS). MLR and PLS models were based on the same Zeiss MMS1 spectra. The temperature related drifts expected of LED sources were also simulated, with wavelength perturbations of up to  $\pm 5$  nm investigated. Fixed drift of as little as  $\pm 1$  nm or random drift of 0.25 nm caused a relative percentage increase of approximately 3% in RMSEP values. This result is consistent with that of Hayes et al.<sup>19</sup>, who noted a wavelength shift of 1 nm resulted in an increase in bias

corrected SEP from 0.64 to 0.85 and a bias change of 4.2 %TSS for a PLS model prediction of stonefruit.

Several instruments targeting fruit assessment have used LEDs as their light source, as follows, although no documentation of the effect of temperature on performance was found:

Giovenzana et al.<sup>20</sup> reported on an optical prototype system for rapid estimation of the ripening parameters (soluble sugar content, TSS, and titratable acidity) of white grape in the field. Reflectance measurements were made at four wavelengths (630, 690, 750 and 850 nm) using AlInGaP and AlGaAs based LEDs (ELJseries, Roithner Lasertechnik GmbH, Austria). Silicon based photodiode detectors (IQ800 series, Roithner Lasertechnik GmbH, Austria) were used, one for each LED. Each LED was paired with a filter at the same wavelength to further improve SNR. The filter would act to maintain wavelength maximum of light reaching the sample, despite drift in LED spectral output with temperature. This system was reported to be only slightly less accurate in estimation of grape TSS and titratable acidity (TA) than that of a PLSR model developed using spectra collected with a vis/NIR spectrometer (QTH source and a CCD 2048 pixel detector ; Jazz, OceanOptics, USA operating over the range 400-1000 nm).

The CP Pigment Analyzer 1101 (Control in applied Physiology, GbR, Falkensee, Brandenburg, Germany) is a commercially available instrument intended for use with fruit. It has an LED broadband light source and a Zeiss MMS1 unit as the dispersive element and detector, and has been used in assessment of fruit pigment content and TSS<sup>120</sup> by researchers such as Praeger et al.<sup>121</sup>, Seifert et al.<sup>122</sup> and Rutkowski et al.<sup>123</sup>. The DA Meter (Turoni, Italy) uses LEDs to produce light at 680 and 720 nm, sequentially activated. The difference in absorbance at the two wavelengths is used as an index of chlorophyll content, and thus fruit maturity. An LED based handheld unit ('Spectron') was developed by Pellenc P/L (France) for assessment of grape bunch TSS, however the unit has not been commercially released.<sup>124</sup>

The objective of the current study was to document the spectral variation of LEDs with respect to ambient temperature and to elapsed time from power up, to aid in the development of instrumentation based on use of LEDs. This study characterises the

temperature and power up response of LEDs appropriate for use in a fruit spectroscopic system.

## 4.2 Materials and Methods

### 4.2.1 Equipment

Three SMB series High Power Top LEDs (Eptitex Inc. Japan) each of 9 peak wavelengths (680, 700, 720, 735, 760, 780, 850, 880 and 940 nm) were used. The 940 nm LED is GaAs based, whilst the rest are AlGaAs based. The units were powered by a Powertech MP-3086 Regulated Variable DC Laboratory Power Supply (Jaycar Electronics, Sydney, NSW, Australia), used to minimise current fluctuations to the LEDs. The current and voltage for each LED is given in Table 4.1, and was based on specification sheet information.

**Table 4.1. LED (Epitex) specifications, for operation at 25 °C for each of peak wavelength and FWHM, at the stated forward current ( $I_F$ ) used for specifications, and typical driven current and forward voltage used in normal operation.**

Model	Peak Wavelength (nm) @ $I_F$ (mA)	FWHM (nm) @ $I_F$ (mA)	Typical driving	
			$I_F$ (mA)	V (V)
SMB680-1100-I	680 (20)	25 (100)	500	2.4
SMB700-1100	700 (20)	25 (500)	500	2.4
SMB720R-1100	720 (100)	25 (100)	600	2.1
SMB735-1100	735 (50)	25 (100)	600	1.9
SMB760-1100	760 (50)	25 (100)	800	2.0
SMB780-1100-I	780 (50)	25 (100)	800	2.0
SMB850D-1100-02	850 (100)	20 (100)	1000	2.1
SMB880-1100-I	880 (800)	50 (800)	800	1.7
SMB940-1100-02-I	940 (50)	60 (100)	500	1.4

A Contherm 5200HS environmental chamber (Contherm Scientific Limited, Petone, New Zealand) was used to control the environmental temperature of the components under assessment. Temperature inside the environmental box was monitored using a TSI TH-Calc 7425 Thermohygrometer (TSI Inc, Shoreview, MN, USA), while the temperature outside was monitored using a Vaisala HMI 31 Thermohygrometer (Vaisala, Helsinki,

Finland). The relative humidity level of the enclosure was maintained at 50% for all experiments.

Zeiss MMS1 NIR Enhanced (Carl Zeiss GmbH, Jena, Germany) spectrometers were interfaced with computers via 16-bit tec5 PD-PCI01V1 A/D card (Tec5 AG Sensorik und Systemtechnik, Oberursel, Germany) and front end electronics box (Tec5 AG Sensorik und Systemtechnik, Oberursel, Germany) to acquire spectral data of a Teflon<sup>TM</sup> (PFTE) tile illuminated by an LED. Spectral data were acquired using software incorporating LabView (National Instruments Corporation, Austin, TX, USA) drivers developed in-house.

## **4.2.2 Experimental exercises:**

### **4.2.2.1 Exercise 1 – Initial power up behaviour**

To assess spectral variation from ‘cold’ power up over a short period, spectral measurements were acquired at 12 ms intervals over a period of 6 min after initial power up. All components were maintained in an air conditioned laboratory at  $23 \pm 1$  °C.

### **4.2.2.2 Exercise 2 – Longer term power up behaviour**

To assess spectral variation from ‘cold’ power up over a longer period, spectral measurements were acquired at one second intervals over a period of 4 h after initial power up. LEDs were housed within an environmental chamber at 10 °C while the power supply, spectrometer (SN 301726), front end electronics (SN 023) and associated computer were located outside the environmental box in an air conditioned laboratory at  $23 \pm 1$  °C.

### **4.2.2.3 Exercise 3 – Response to temperature**

To assess the effect of variation in environmental temperature on the LEDs, the temperature in the enclosure was incrementally increased in 10 °C intervals between 10 and 60 °C, with a 1 h stabilisation between increments after the initial start-up period of 4 h. These procedures were repeated three times for each of the LEDs used in this study (81 trials in total).

#### **4.2.2.4 Exercise 4 – Effect of environmental temperature on an LED based instrument (DA Meter)**

The  $I_{AD}$  index of fruit maturation involves measurement of the absorbance difference between 670 and 720 nm.<sup>125</sup> This is achieved in the 53500 DA Meter (T.R. Turoni srl, Forlì, Italy) utilising LED illumination. The DA Meter has a stated operating temperature range of 0 to 70 °C.<sup>126</sup> To demonstrate the effect of temperature on LED output in context of a specific application, a DA Meter was housed within the environmental chamber, with temperature incrementally increased in 10 °C intervals between 0 and 60 °C as in Exercise 3. Spectra of LED output reflecting from a Teflon<sup>TM</sup> tile were acquired using a MMS1 spectrometer located outside the chamber. DA Meter readings were acquired of two mango fruit at two locations as the instrument temperature was increased, with the fruit maintained and the meter referenced at  $23 \pm 1$  °C.

### **4.3 Results and Discussion**

#### **4.3.1 Exercise 1 – Initial power up behaviour**

Initial LED power-up to full intensity occurred within a measurement cycle (12 ms). Spectral intensity then decreased exponentially over 6 min, but did not stabilise during this period (Figure 4.1 and Figure 4.2). This behaviour is ascribed to an increase in junction temperature as current is passed through the LED. A shift in peak intensity to longer wavelengths also occurred (Figure 4.1 and Figure 4.2), varying from 10 - 27 nm depending on the LED wavelength rating (data not shown). The time taken for junction temperature equilibration will depend on the forward current driving the LED, and thus the maximum temperature reached. The spectral change did not stabilise during the 6 min period, suggesting junction temperature was not equilibrated in this period.

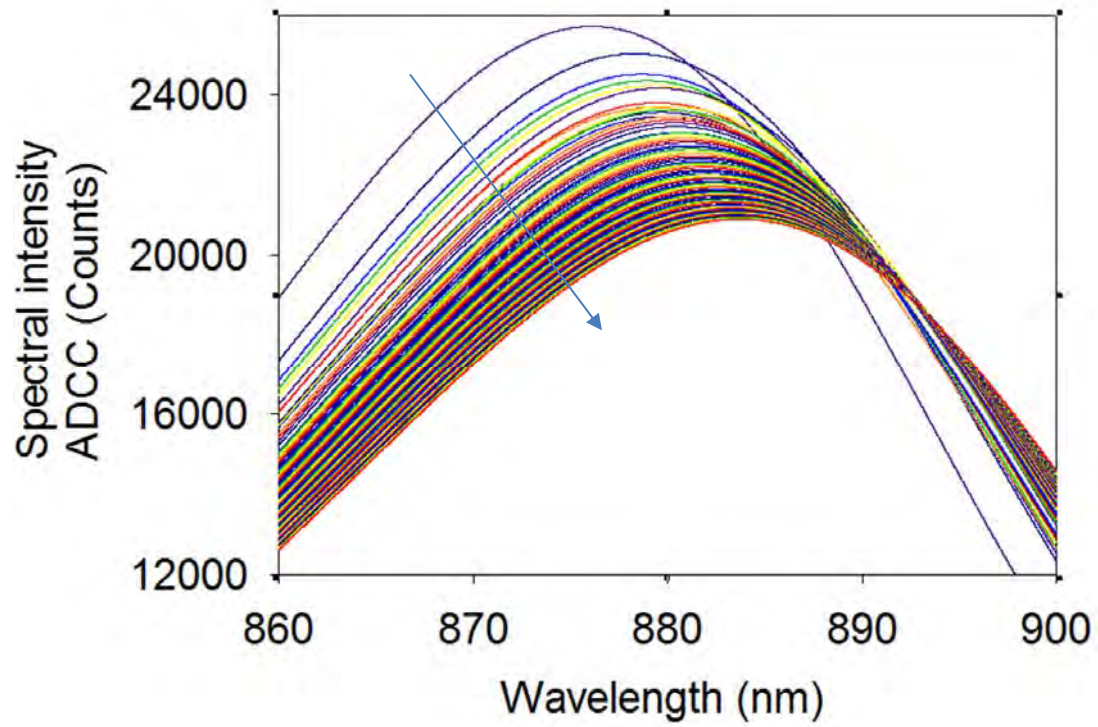


**Figure 4.1.** Spectral output (ADCC) over the first second from power-on of a SMB880-1100-I LED (representative of three replicate trials of three LEDs) operated at an ambient temperature of 23 °C. Spectra were acquired at 12 ms intervals. Arrow represents direction of time.

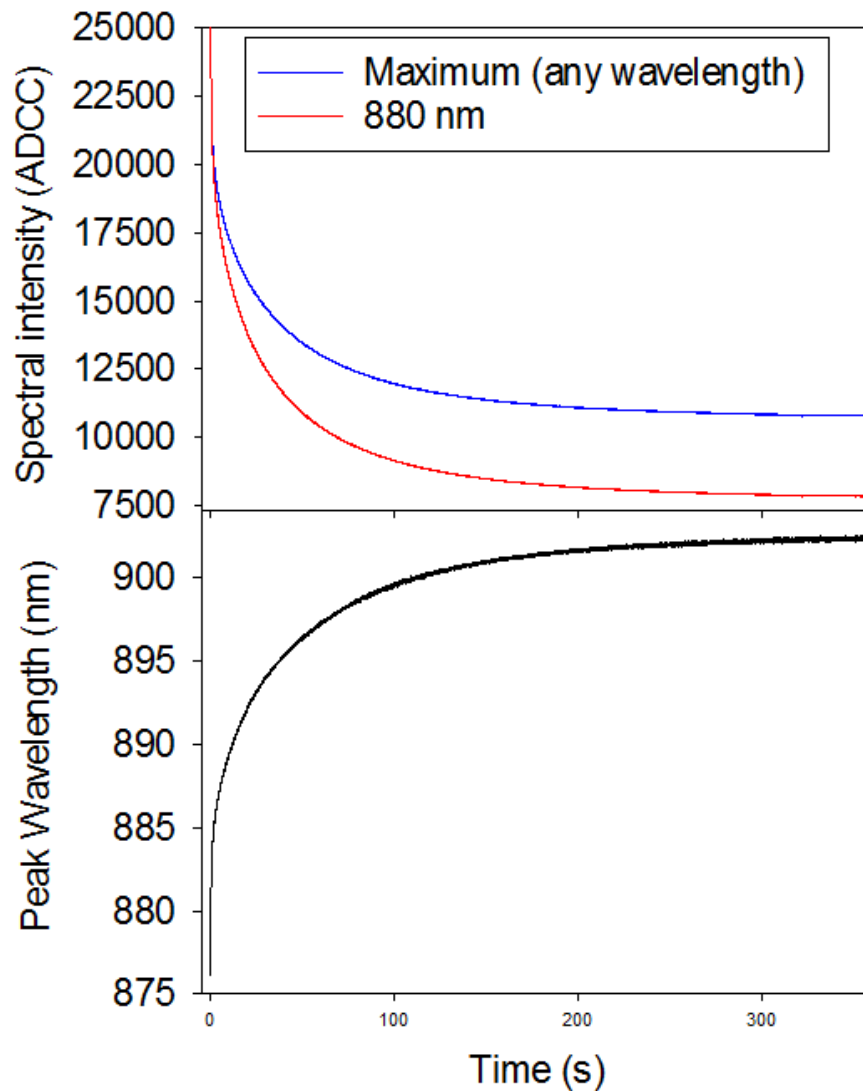


**Figure 4.2. Intensity (ADCC) at 880 nm and maximum intensity at any wavelength (top panel) and the shift in peak wavelength emitted (bottom) of the SMB880-1100-I LED over a 6 min period from power-up (representative of three replicate trials of three LEDs). Power was turned on at  $t = 0$ .**

### 4.3.2 Exercise 2 – Longer term power up behaviour

In the initial minutes following LED power-up, intensity decreased and the wavelength of peak intensity was red-shifted (Figure 4.3, bottom panel), as seen with the shorter trials in Exercise 1. This shift is consistent with an increase in junction temperature during operation. The peak wavelength stabilised at approximately this time (6 min) in all trials involving previously used LEDs, varying by less than 0.5 nm thereafter, if environmental temperature was constant (e.g. variation was noted during cabinet defrost cycles).

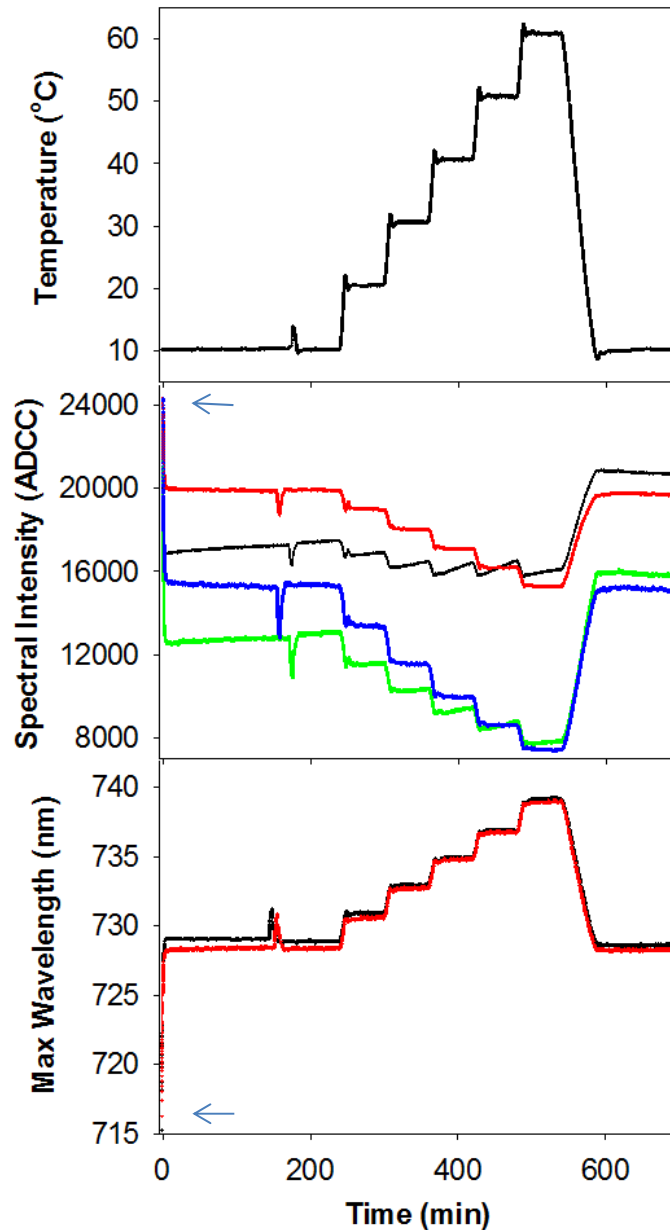


**Figure 4.3.** The effect of environmental temperature (top panel) on SMB720R-1100 LED intensity (ADCC) (middle panel) and the wavelength of maximum intensity (bottom panel), monitored over a four hour period. Black and red lines represent sequential trials of one LED, being the maximum intensity at any wavelength. Green and blue lines are intensity at 720 nm for the same two trials. This was the first use (power-up) of these units. Arrows mark initial readings ( $t = 0$ , ie at power up). The sharp feature (at approx. 180 min) was associated with a cabinet defrost cycle event. The intensity difference between the two trials was due to slight differences in the LED to fibre optic input alignment.

However of the 27 LEDs used, 13 demonstrated a ‘burn in’ behaviour on their first use. In these cases emission intensity was not stabilised within 240 min of initial power up, and five did not reach a stable emission over this period in their second use, although the intensity difference was much smaller ( $<2.5\%$ ). In the example provided (Figure 4.3, first trial), emission intensity increase was superimposed on the shifts due to change in environmental temperature (ie. intensity was higher on return to environmental temperature, post 240 min from power on; black and green lines on Figure 4.3). The ‘burn in’ period required to achieve output stability varied between individual LEDs but was less than 24 h in all cases.

### 4.3.3 Exercise 3 – Response to temperature

An increase in environmental temperature produced a decrease in overall intensity of the LEDs and a shift to longer wavelength of the peak emission (Table 4.2, Figure 4.3, Figure 4.4, Figure 4.5), ranging from 0.20 to 0.33 nm depending on LED type (Table 4.3). This shift was consistent with the Epitex LED specification for temperature response of approximately  $0.2\text{ nm}/^{\circ}\text{C}$ .

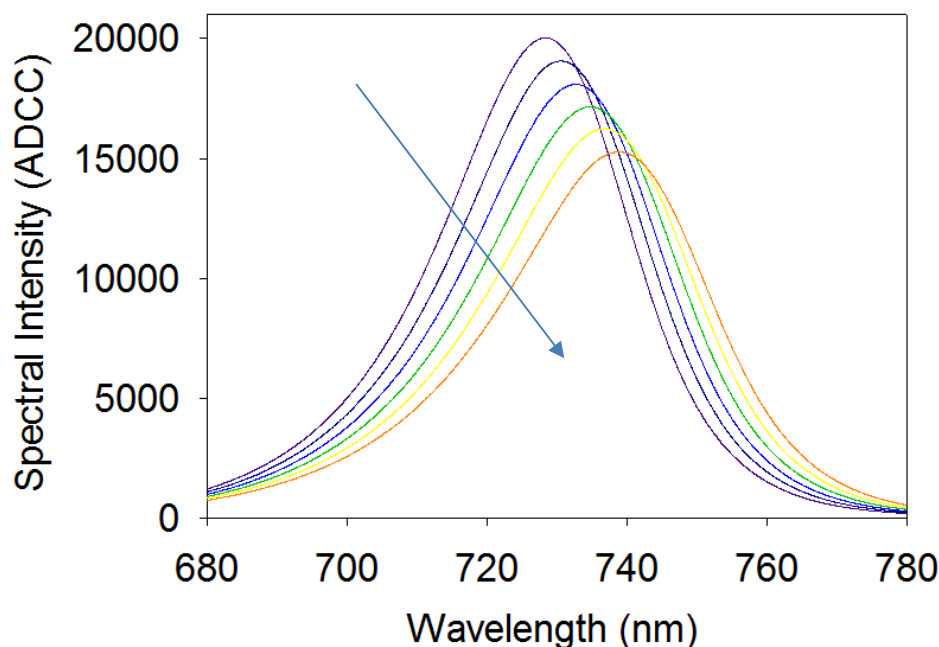


**Figure 4.4. Spectral output (ADCC) of a SMB720R-1100 LED with increase in environmental temperature from 10 to 60 °C. Arrow indicates direction of increasing temperature.**

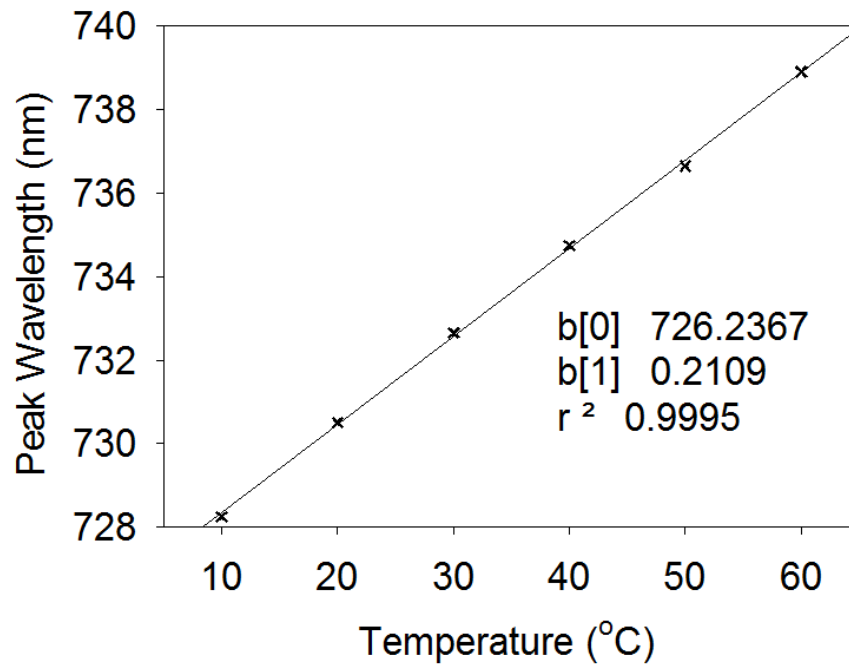


**Figure 4.5. Wavelength of peak emission at a range of environmental temperatures for a SMB720R-1100 LED.**

LED output intensity decreased with increase in temperature (Table 4.2), with the relationship described slightly better by a logarithmic than a linear relationship (Figure 4.6).

**Table 4.2. Wavelength of peak emission and relative intensity of emission, for a 940 nm LED at a range of environmental temperatures. Mean and standard deviation of three repeated trials is presented.**

Temperature (°C)	Wavelength (nm)	$\sigma$	Relative Intensity (%)	$\sigma$
10	938.9	0.25	100.0	0
20	942.7	0.35	90.7	0.08
30	946.5	0.25	81.6	0.18
40	950.3	0.25	74.1	0.21
50	952.7	0.30	67.3	0.17
60	955.6	0.35	61.1	0.02

**Table 4.3. Increase in peak wavelength position per degree environmental temperature increase with a linear fit for 9 LED types.**

LED Peak Wavelength (nm)	Peak shift (nm/°C)
680	0.206
700	0.204
720	0.210
735	0.242
760	0.234
780	0.253
850	0.265
880	0.259
940	0.333

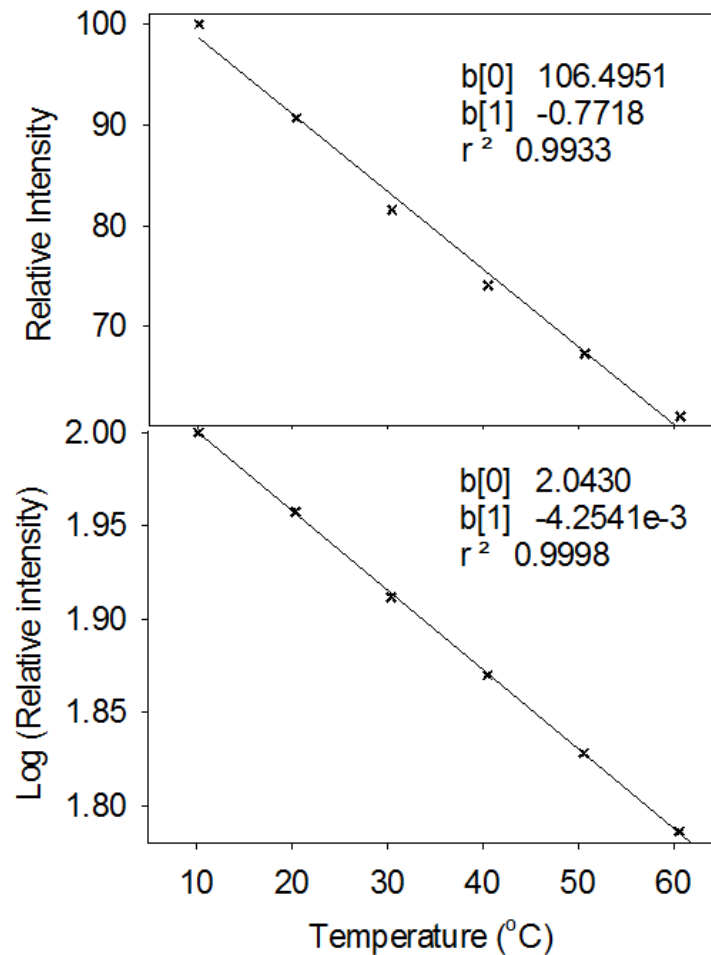


**Figure 4.6. Spectral intensity relative to that at 10 °C with change in environmental temperature, presented on a linear (top panel) and a logarithm (bottom panel) scale for intensity. Data presented for a SMB940-1100-02-I LED.**

#### 4.3.4 Exercise 4 – Effect of environmental temperature on an LED based instrument (DA Meter)

The DA instrument has three LEDs each of two wavelengths. The two sets pulse alternately, each for a period of approximately 115 ms, during which time a slight increase in the peak wavelength  $\sim 0.5$  nm occurred as the LED warmed up (data not shown). There was 2 - 3 nm difference in peak wavelength between the individual LEDs of each set (data not shown). As expected, as instrument temperature was increased, the peak wavelength shifted to longer wavelengths (Figure 4.7), although the shift was slightly smaller  $\sim 0.18$  nm/ $^{\circ}\text{C}$  than noted in Exercise 3. Temperature increase was also associated with a decrease in the  $I_{AD}$  Index readings of the instrument (Figure 4.8).

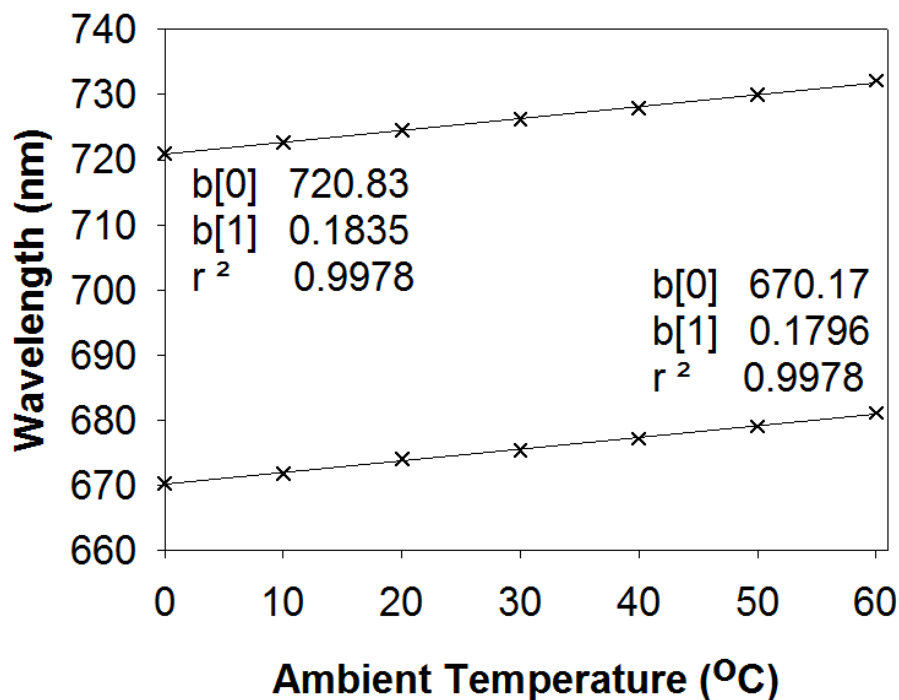


**Figure 4.7.** Wavelength of peak emission at a range of environmental temperatures for the DA Meter. Mean standard deviation at each wavelength was 0.27 and 0.21 for the 670 and 720 nm wavelengths respectively.

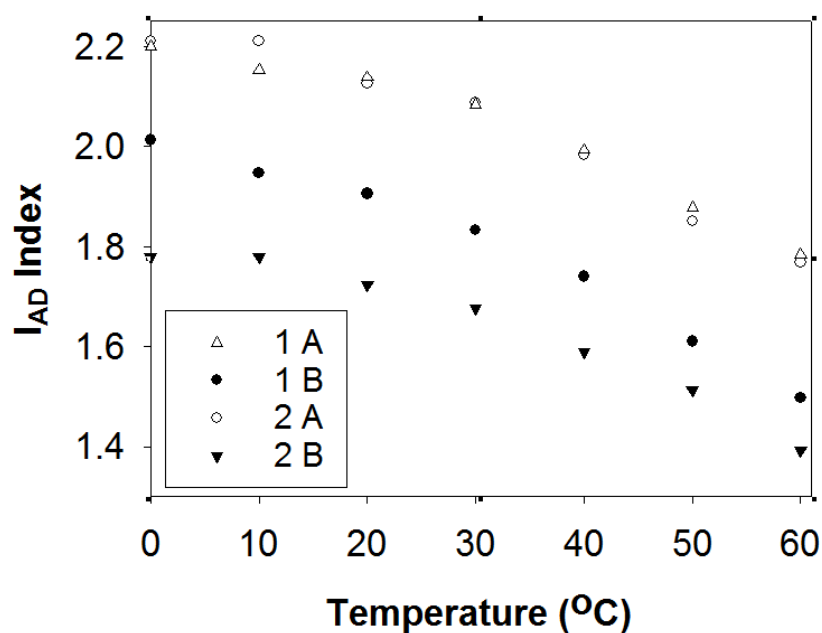


**Figure 4.8.** DA Meter  $I_{AD}$  Index measurement of two mango fruits (1, 2) at two positions (A, B) with the instrument at various operating temperatures. Fruit temperature was constant at 23 °C.

In the  $I_{AD}$  index, the 670 nm reading is associated with chlorophyll while 720 nm is used for normalisation. In an interactance spectra of mango fruit, the chlorophyll peak can be centred at between 668 and 676 nm, dependent on sample (example spectrum given, Figure 4.9). The peak is narrow, with 16 – 31 nm between peak maximum and the red edge, that is, maximum derivative of right shoulder of peak, at 691 – 701 (Figure 4.9).

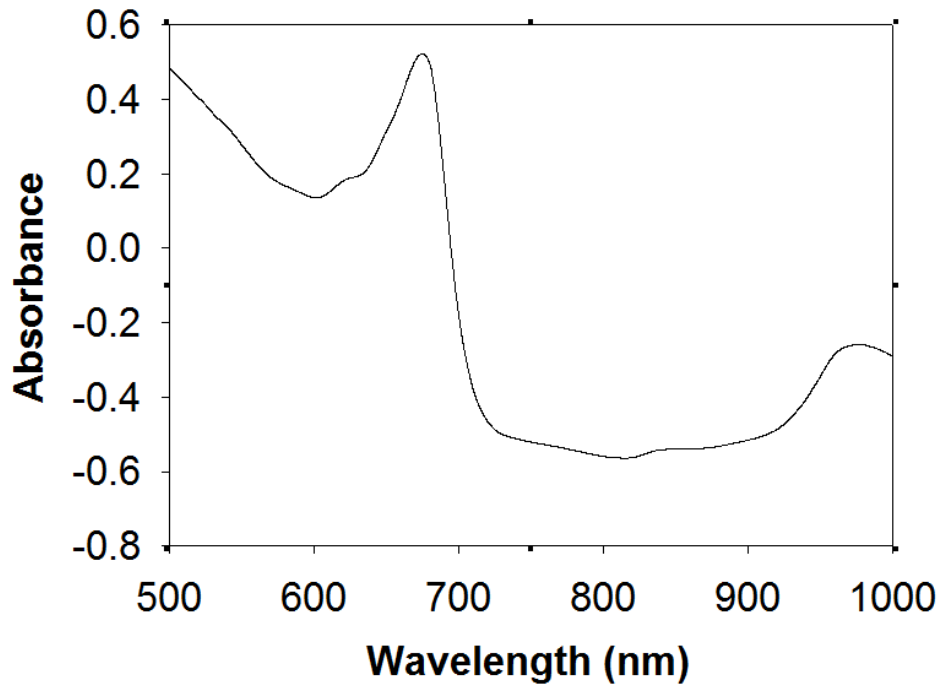


**Figure 4.9. Absorbance spectra of a mango fruit measured with an MMS1 spectrometer in an interactance mode.**

The  $I_{AD}$  index can be calculated from the interactance spectra of mango fruit (as in Figure 4.9), based on apparent absorbance at 670 and 720 nm. A shift in of LED operating temperature of 10 °C invokes a shift of approximately 2 nm in peak wavelength, e.g. from 670 to 672 nm and 720 to 722 nm. The effect of such a shift on the  $I_{AD}$  index was calculated based on spectra of 60 mango fruits, incrementing the wavelengths used for the index from 670 and 720 nm by up to 12 nm (representing approximately a 0 - 60 °C change in LED temperature). Under these conditions, the calculated index changed by 0.02 to 0.16 units (Figure 4.10).

The pattern of change of the calculated  $I_{AD}$  index with increased temperature/wavelength was different to that observed with the DA Meter. Of course the calculated index is based only on the difference between  $A_{670}$  and  $A_{720}$  using the Zeiss MMS1 spectrometer, which has a FWHM of approximately 10 nm. The DA Meter LEDs have approximately 50 nm FWHM wide peaks and thus in practice,  $I_{AD}$  measurements for 670 and 720 nm will be based on overlapping wavelengths. Intensity change with temperature will also impact the estimation of  $I_{AD}$ , unless the unit is referenced at the temperature prevailing during the sample scan.

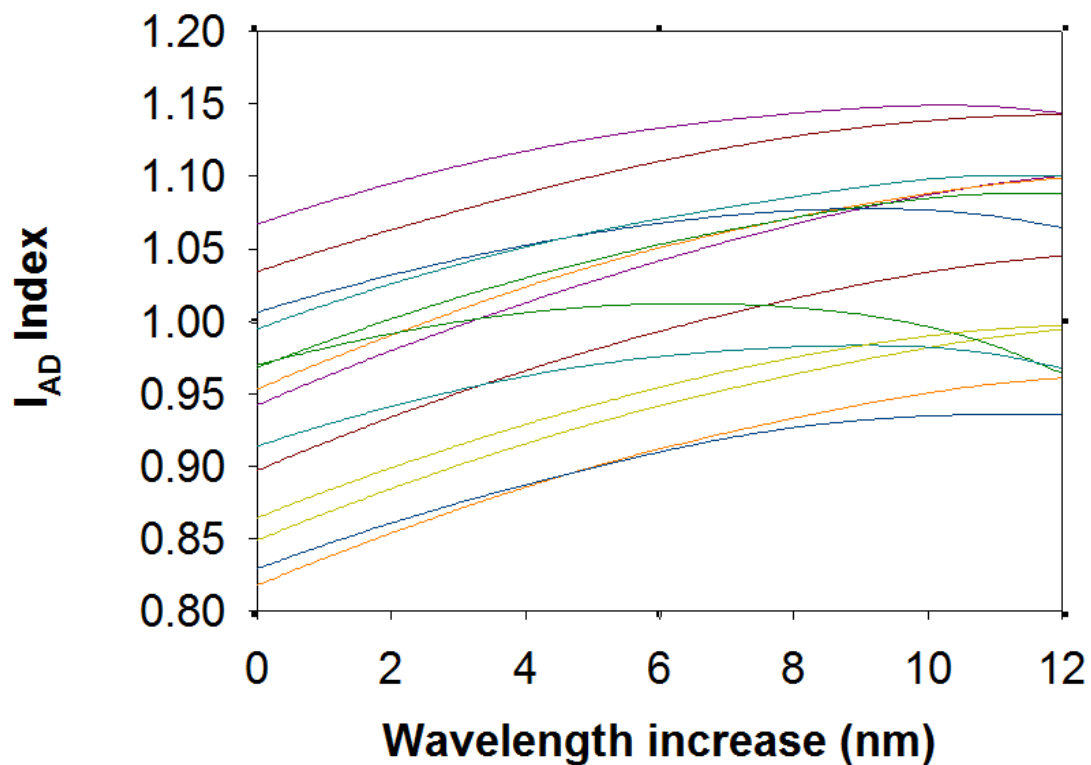


**Figure 4.10** Change in calculated  $I_{AD}$  index of several mangos with shift in wavelength compared ( $A_{670+\lambda} - A_{720+\lambda}$ ), taken from full spectrum absorbance measurements. A  $10^{\circ}\text{C}$  increase in temperature gives approximately a 2 nm increase in peak wavelength. Results shown for a sample from 60 mango fruits.

## 4.4 Implications to instrument design

LEDs that are pulsed rather than operated constantly will also show spectral intensity and wavelength shifts similar to the above exercise in start up and as ambient temperature changes. The time taken for temperature equilibration will depend on the forward current, pulsing cycle and duration time. Change in LED intensity and spectral profile, as caused by changes in temperature due to LED warm up or environmental temperature, will obviously impact the performance of a spectroscopic system employing these units as an illumination source.

Several measures could be implemented to mitigate such effects. In an ‘avoidance’ strategy, as Dasgupta et al.<sup>115</sup> suggested, stability of the light output could be achieved using a resistor in combination with a negative temperature coefficient thermistor, with photometric feedback. For continuously operating instruments, a warm-up time should be established to ensure wavelength and intensity stability. An alternate avoidance strategy involves the use of interference filters to maintain spectral bandwidth, however intensity changes would still need to be accommodated, either mathematically or via re-referencing. In an ‘adaptation’ strategy, change in illumination intensity and spectral quality could be mitigated by re-referencing. Alternately, the observed changes in peak wavelength and relative intensity are explicable in terms of forward current and temperature and thus predictable if current and temperature are known. Change in illumination intensity and spectral quality could thus be addressed by modelling, given knowledge of current and temperature.

## 5 Characterisation of an interactance probe configuration in terms of the ratio of specular and diffusely reflected radiation <sup>3</sup>

### Abstract

The polarisation properties of light were used to determine the effect of light polarisation on detector response, and quantify the ratio of specular to diffuse radiation of the light collected by a 'shadow probe' geometry. The spectrometer in use was demonstrated to possess a grating bias of 1.85% at 800 nm, for vertically polarised light relative to horizontally polarised light.

Using a polariser on the light source as well on the detector input, spectra of an apple, and subsequently a kiwi fruit, were acquired with the sample incrementally moved to 150 mm from the probe. At probe to sample distances < 30 mm, the ratio of specular to diffuse radiation was < 3%, with slightly higher values noted for kiwifruit compared to apple. This is consistent with an effect of kiwi skin hairs on light scattering. The specular component increased rapidly at greater distances due to loss of the shadowing effect. At probe-sample distances >70 mm, a reduced specular component was demonstrated in apple fruit compared to kiwi fruit. This result is consistent with a higher component of diffuse reflection for apple than for kiwi fruit.

---

<sup>3</sup> This chapter has been submitted under this title to the Journal of Near infrared Spectroscopy, March 2016

## 5.1 Introduction

The use of near infrared spectroscopy with solids involves either diffuse reflectance, partial transmission (interactance) or full transmission geometries. For determination of the properties of a solid sample it is desirable to minimise the contribution of specular reflection compared to diffusely scattered light to the determinate. For example, for determination of total soluble solids (TSS) of intact fruit using near infrared spectroscopy (NIRS), a partial transmission system yields a better result than a reflectance system. The so-called ‘shadow probe’ interactance geometry as described by Greensill *et al.*<sup>97</sup> consists of a light collection assembly connected to a VIS-NIR spectrometer, situated directly in front of a parabolic lamp reflector (Figure 5.1), resulting in a well-defined shadow just in front of the probe. Light incident on the sample is diffusely scattered, with a portion of the radiation re-emerging in the probe shadow collected for measurement. The probe contains a convex lens, such that only parallel rays emerging from the sample at normal to the lens diameter will be focussed to the detector fibre optic, thus the observation area of the probe is constant for different probe-fruit distances. The InSight I, InSight II-RH (MAF Oceania, Bacchus Marsh, Vic, Australia), Nirvana (Integrated Spectronics, Sydney, Australia) and F750 (Felix Instruments, Camas, WA, USA) employ this configuration in measurement of internal attributes of intact fruit (e.g. as described by Walsh *et al.*<sup>127</sup>).

Ideally a parabolic lamp reflector is used, although a true collimated beam is not achievable due to the non-point source, that is, the finite dimensions of the QTH filament (Figure 5.1). Thus, as the image plane moves away from the probe, the projected shadow deteriorates and this area is filled with light directly from the lamp source. The scattered light measured by the probe is therefore a convolution of directly reflected light (specular reflection) from the sample’s surface, and diffusely scattered light from scattering centres from within the sample, and emitted within the observation area of the probe. The specular component should be minimised with respect to the diffusely scattered component, since only the latter component contains spectral information about the internal composition of the sample. This aim is true for any optical geometry employed in a spectroscopic system. For example, in a typical reflectance geometry, the incident light beam is positioned at a 45° angle to the detector and the sample, to minimise specular reflection reaching the detector. In another approach, a fluid of a refractive index

matching human tissue is used to couple the tissue to the analyser, resulting in less internal reflection and a greater contribution of diffuse than specular reflection to the detected signal<sup>128</sup>.

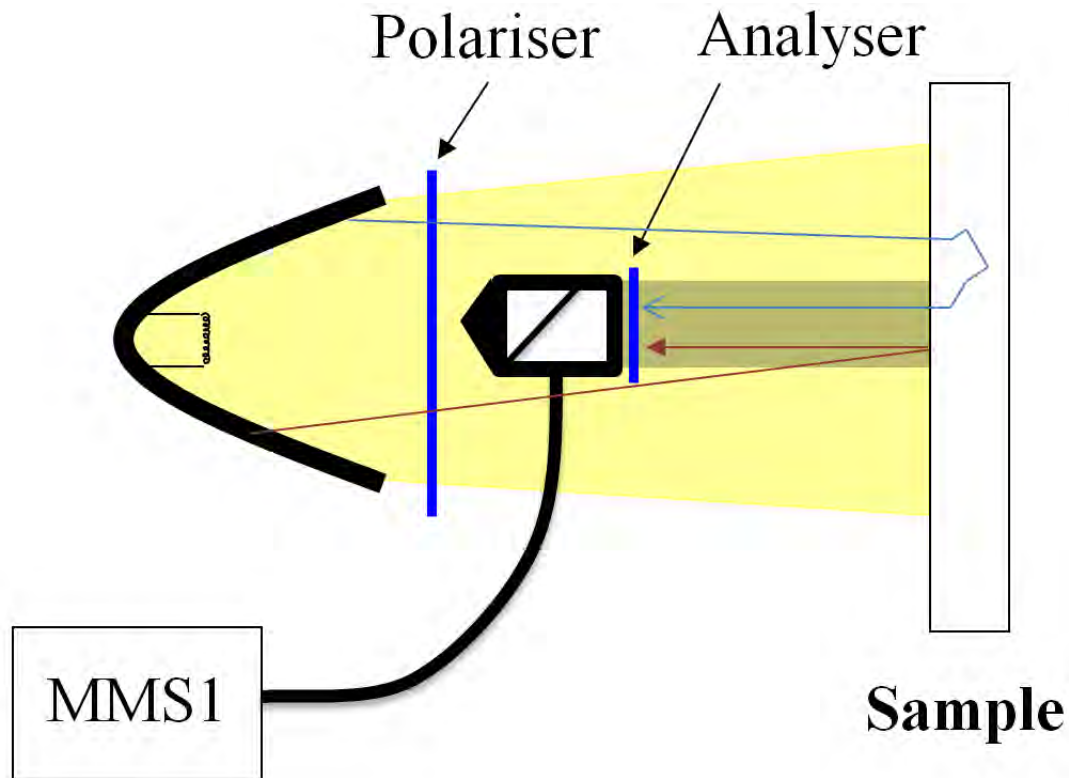


**Figure 5.1. Shadow probe configuration, consisting of a parabolic reflector with lamp, projecting light past an optical probe which casts a shadow onto the sample (fruit). Light received by the optical probe, be that specular reflection or diffusely scattered light emerging from the sample, is passed to the spectrometer. The probe entrance contains a double convex lens and the probe body contains a mirror to direct parallel incident light onto the detector fibre optic. For this experiment (exercise 3), polariser and analyser elements were added.**

Transmission spectroscopy systems are routinely characterised in terms of stray light detected, which is effectively a measure of light that has not interacted with the sample<sup>129</sup>. However, spectroscopic systems employing reflectance and interactance optical geometries are rarely characterised in terms of the proportion of specular reflection detected, although attempts are made to reduce the contribution of specular relative to diffuse. Specular reflections also degrade image quality and considerable knowledge exists on methods to physically (e.g. using polarising filters<sup>130</sup>) or mathematically<sup>131</sup>

remove its influence. Incandescent, fluorescent, LED, and many laser light sources are randomly polarised.

A linear polariser will allow only a linearly polarised component of such radiation to pass, and a polariser analyser (a second linear polariser) can then be used to either transmit or absorb this light. The fraction of incident polarised light transmitted through a polariser analyser equates to  $\cos^2\theta$ , where  $\theta$  is the angle between the polarised light and the transmission axis of the polariser analyser (Law of Malus)<sup>14</sup>.

When a sample is illuminated with polarised light, specular reflection from the sample will maintain its polarisation, while diffusely reflected light will lose its polarisation. Thus if an analyser is placed in front of the shadow probe optic, and the polariser-analyser combination appropriately aligned, specular reflection together with a component of diffuse reflection will pass through the analyser. If the analyser is crossed with respect to the polariser, the specular reflection will be absorbed and a small component of diffuse reflection will pass. Measurements using this optical filtering system allow estimation of the ratio of specular and diffusely reflected light received. In a parallel exercise, but without estimation of relative specular and diffuse components, Backman et al.<sup>132</sup> report on the use of polarising filters to restrict measurement to diffuse reflections on measurement of a highly scattering medium (human tissue).

One further consideration is the effect of light polarisation on spectrometer response. Slits, mirrors and gratings all introduce an element of polarisation in a spectrometer, but the effect is dominated by the influence of the grating.<sup>26</sup> Further, the efficiency of a grating also depends on the polarisation of the incident light (as well as blaze angle and grating period), although several design features can be used to minimise this effect<sup>28</sup>. S-polarised light, where the direction of the grating grooves and the oscillation direction of the electric field vectors is perpendicular, exhibits a higher diffraction efficiency at longer wavelengths than P-polarised light, where the direction of the grating grooves and the oscillation direction of the electric field vectors is parallel, for which diffraction efficiency peaks at the blaze wavelength and decreases with a smooth curve.<sup>29</sup> The efficiency difference between S and P polarised light thus depends upon a range of factors, and range from very little to over 80%<sup>26</sup>. It is, however, easily determined experimentally.

In this study, the polarisation properties of light were used to quantify the ratio of specular to diffuse radiation of the light collected by a shadow probe geometry with increase in distance between probe and sample surface.

## 5.2 Materials and Methods

### 5.2.1 Equipment

The shadow probe assembly from an InSight I, InSight II-RH (MAF Oceania, Bacchus Marsh, Vic, Australia) and F750 (Felix Instruments, Camas, WA, USA), henceforth referred to as probes A, B and C respectively, were comprised of a light source (quartz tungsten halogen lamp, QTH) and reflector to produce a collimated beam of light, and an optical probe, accepting light to the detector, located in the centre of this light beam and thus creating a shadow on the viewed sample<sup>97</sup>, of dimensions as shown in Table 1. For the InSight assemblies, Zeiss MMS1 NIR Enhanced (Carl Zeiss GmbH, Jena, Germany) spectrometers were interfaced with computers via 16-bit tec5 PD-PCI01V1 A/D card (Tec5 AG Sensorik und Systemtechnik, Oberursel, Germany) and front end electronics box (Tec5 AG Sensorik und Systemtechnik, Oberursel, Germany), and used to acquire spectral data of light interacting with the sample. Spectral data were acquired using software incorporating LabView (National Instruments Corporation, Austin, TX, USA) drivers. A stabilised 12 V power supply (MAF Oceania, Bacchus Marsh, Vic, Australia) was used to minimise current fluctuations to the halogen lamp. For the F750 unit, in built electronics and power supply were used, again with an MMS1 spectrometer.

Probe A assembly employed a 100 W QTH bulb positioned with the filament at the focal point of a parabolic reflector. Probe B assembly employed a 150 W lamp with an inbuilt gold coated reflector. Probe C assembly employed a 5 W lamp, again with an inbuilt reflector, with a cylindrical barrel between lamp and sample. In this case, the internal surface of the cylindrical barrel was polished (ie. reflective). The last 36 mm of the barrel is blackened, however it is not a perfect absorber and a small component of light is still reflected from this surface.

## **5.2.1 Experimental exercises:**

### **5.2.1.1 Exercise 1 – MMS1 grating bias**

The effect of light polarisation on detector response was considered using probe A. The Zeiss MMS1 diode array spectrometer used in this study contains a 366 line/mm holographic blazed flat-field grating, with a standing wave technique used in its manufacture, which is reported to maximise the average reflectivity and minimise the grating bias<sup>36</sup>. Spectra were acquired at a probe-sample distance of approximately 100 mm. At this distance the shadow was lost with the detected field of view fully illuminated by the lamp. A 20 mm diameter polariser analyser was placed directly in front of the probe, and the analyser rotated. Maximum and minimum signals (analogue to digital conversion count, ADCC) at 800 nm were recorded. The experimental setup was as shown in Figure 5.1, but with the polariser in front of the lamp removed.

### **5.2.1.2 Exercise 2 – Signal level with probe-sample distance**

Spectra of a white PFTE tile was acquired using probe A, B, and C assemblies, with the tile incrementally moved in approximately 2 mm increments from the probe.

### **5.2.1.3 Exercise 3 – Specular-diffuse ratio**

Using the probe A assembly, random polarised light from the parabolic reflector was converted to a linear polarisation using a 3M NIR polarising film (75 x 75 mm), and a 20 mm diameter polariser analyser placed directly in front of the probe to discriminate between specular and diffuse components (Figure 5.1). Spectra of an apple, and subsequently a kiwi fruit, were acquired with the sample incrementally moved in 10 mm increments to 150 mm from the probe.

## **5.3 Results and Discussion**

### **5.3.1 Exercise 1 – MMS1 grating bias**

Both specular and diffuse light from a sample illuminated from a QTH lamp is expected to be randomly polarised. A polarising analyser was used to transmit either a vertical or horizontal polarisation into the probe, connected to the MMS1 spectrometer. The peak

signal count measured at 800 nm demonstrated a grating bias of only 1.85% for vertically polarised light relative to horizontally polarised light (e.g. maximum and minimum ADCC of 27090 and 26598, respectively). The result was highly reproducible and was wavelength dependent<sup>26, 28</sup> (data not shown).

### 5.3.2 Exercise 2 – Signal level with probe-sample distance

A point source placed at the focal point of a parabolic reflector will produce a collimated output. However, lamp filaments have finite dimensions and reflectors are rarely perfect parabolas, such that the resulting lamp output contains diverging and converging light rays. The full divergence angle of a parabolic lamp reflector depends on its design specifications, but it can be as low as  $9^\circ$  (~150 mrad) (compared to laser beams with divergence angles less than 0.5 mrad).

In a shadow probe configuration, the converging rays from the outer perimeter of a lamp reflector will be the first direct rays to illuminate the observation area of the probe as probe-sample distance increases. This illumination can result in unwanted specular reflection from the area of detection. Specular reflection from the observed area is expected to rapidly increase as the sample moves away from the probe, as the observed area moves out of the umbra of the detector, causing an increase in detected light level. However, as the lamp does not project parallel light only, the sample will receive decreasing irradiance (radiant flux per unit area) at larger distances from the lamp.

The geometric parameters involved are illustrated in Figure 5.2, with the “worst-case” rays converging from the perimeter of the parabolic reflector (of diameter A).

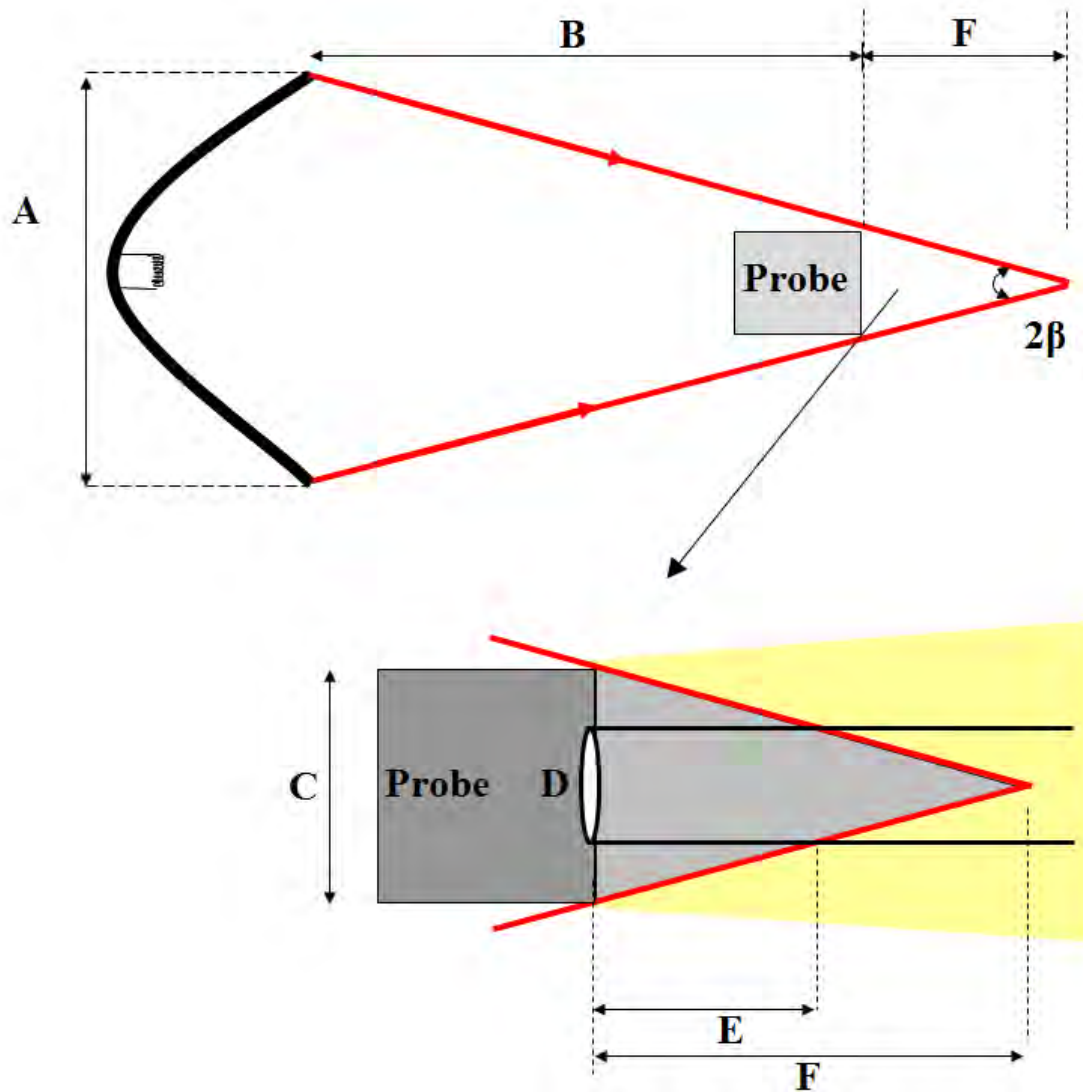


**Figure 5.2.** Ray tracing of shadow probe setup used (worst case scenario). The parabolic reflector has an outside diameter of  $A$  and distance to probe end of  $B$ . Bottom figure illustrates an enlarged version of the permanently shadowed area (umbra). The probe has an outside diameter of  $C$  and an optical entrance diameter of  $D$ . When the probe-sample surface distance is  $E$ , the area of detection is matched by the probe. Position  $F$  indicates the onset for full illumination of the observation area.

The converging light rays converge to a point (distance F from the probe), resulting in a characteristic (dark) full angle of  $2\beta$ . From basic trigonometry it follows that:

$$E = \frac{B(C-D)}{A-C} \quad \text{Eqn 5.1}$$

$$F = \frac{BC}{A-C} \quad \text{Eqn 5.2}$$

$$\beta = \arctan\left(\frac{A-C}{2B}\right) \quad \text{Eqn 5.3}$$

Dimensions and calculations using equations 1, 2 and 3 are given in Table 5.1. With the analyser filter in place (Exercise 3), the measurements for the Probe A become  $C = 20$  mm,  $E = 13$  mm,  $F = 37.3$  mm and  $2\beta = 33^\circ$

**Table 5.1. Measurement of lamp and reflector characters. All measurements are in mm. Legend refers to Figure 2.**

Character	Figure legend	Probe assembly		
		A	B	C
Lamp diameter	A	72	45	28.2
Lamp-probe distance	B	97	127	27.6 (blackened)
Outside diameter of probe	C	18	15.5	11.8
Inside diameter of probe	D	13	9.0	7.3
Probe-sample distance	E	9.0	28.0	7.6
Probe-sample distance	F	32.3	66.7	19.9
Angle of umbra	$2\beta$	$31.1^\circ$	$13.2^\circ$	$33.1^\circ$

Therefore, as a first approximation, reflected light from the perimeter of the parabolic reflector will just start to fall inside the observation areas of probes A, B and C at probe-sample distances of 9, 28 and 8 mm respectively, and thus result in collection of specular reflected light. As the probe-sample distance is increased, the irradiance in the observation area will increase sharply because this area will be exposed to an increasing area of the parabolic lamp reflector. At a distances of 32, 67 and 20 mm respectively, the

complete observation areas will be irradiated, with intensity increasing with increasing distance.

In practice, measured signal intensity level (ADCC) increased as a function of probe-sample distance (Figure 5.3). For probes A and B, probe geometry maintained a low ADCC (i.e. a clear shadow, with minimal specular reflection expected) for probe-sample distances of up to approximately 25 mm, while at greater distances, detected (specular) light rapidly increased (Figure 5.3). There were slight differences between two units of the one model (probe A). With probe B, a slight increase in ADCC was measured at distances up to 40 mm, consistent with the use of a less collimated lamp, although at greater distances the increase in ADCC was not as pronounced as for probe A. Probe C demonstrated a poorer collimation of light associated with the reflective cylinder used between lamp perimeter and sample.

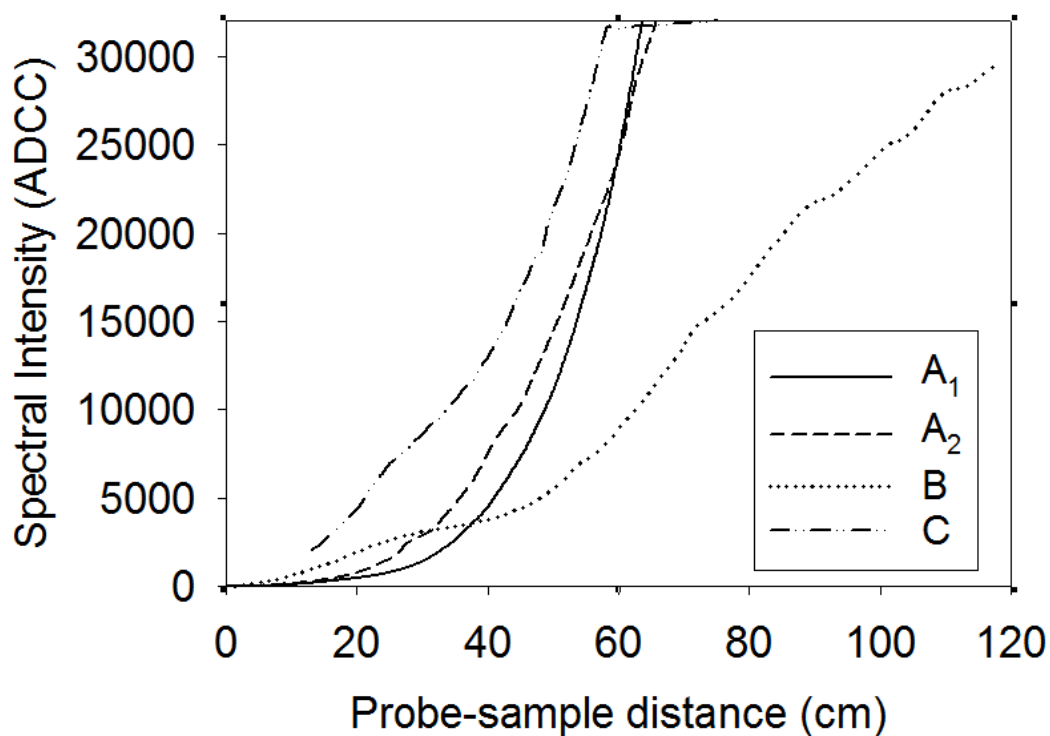


**Figure 5.3. Detected light level (800 nm) for four shadow probe assemblies, for various probe-sample distances.**

### 5.3.3 Exercise 3 – Polarised light characterisation of shadow probe

With both polarisers in the vertical position, the amount of light transmitted through the analyser consists of:

$$I_{Total} = I_S + I_D \quad \text{Eqn 5.4}$$

where  $I_S$  is the specular intensity and  $I_D$  the vertical component of the total diffuse intensity. With the analyser crossed with respect to the polariser, the light transmitted to the probe is:

$$I_{Total*} = I_{D*} \quad \text{Eqn 5.5}$$

where  $I_{D*}$  is the horizontal component of the total diffuse intensity, assuming that all of the specular intensity is absorbed.  $I_{D*}$  will equal the product of  $I_D$  and a grating bias factor.

With the apple at 0 mm from the probe, spectra were similar when the polariser-pair was either parallel or crossed (Figure 4). This condition represents detection of “pure” diffuse spectra, with maximum spectral information derived from the fruit sample.

With the apple at 150 mm from the probe, crossing of the polariser-pair will eliminate the specular component of radiation received by the probe, resulting in only a component of diffusely scattered light from the apple and no specular light (Figure 5.4).

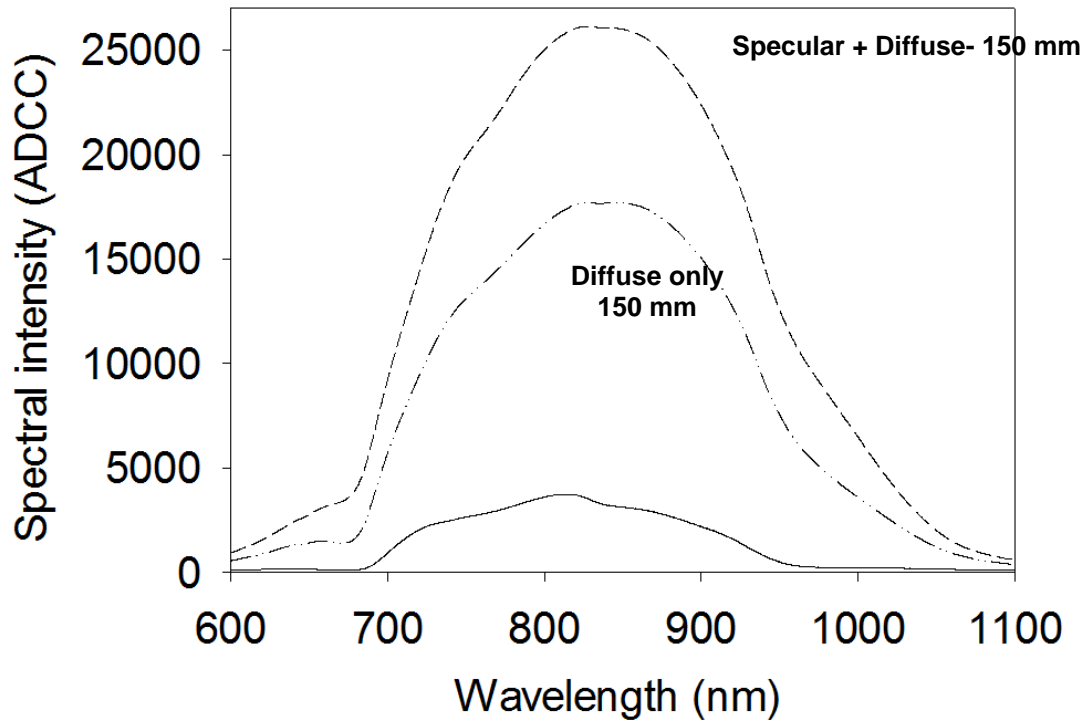


**Figure 5.4. Apple spectra at a probe-sample distance of 0 and 150 mm. The top dotted lines are with the polarised filters parallel (top most) and perpendicular (crossed) respectively. The solid line at bottom is with the apple spectra at a probe-sample distance of 0 mm, for both polariser positions (i.e. indistinguishable results).**

MMS1 ADCC output at 800 nm was assessed for different probe-fruit distances for both apple (Table 5.2) and kiwifruit (Table 5.3). A dark count correction was performed on all values, and  $I_{D*}$  corrected using the grating polarisation factor 0.0185. These calculations assumed that the lamp illumination was perfectly linearly polarised by the film polariser, that all the specularly reflected light maintained its polarisation, and that all light diffusely reflected from the fruit was randomised.

**Table 5.2. MMS1 output (ADCC) at 800 nm assessed for different probe-fruit distances for an apple.**

<b>Apple</b> Probe-sample distance (mm)	$I_S + I_D$ ↑↑	$I_D^*$ ↑→*	$I_D^*$ Corrected (= $I_D$ ) ↑→	$I_S$ (= $I_S + I_D - I_D$ )	$I_S/I_D$ (%)
0	3600	3536	3601	-1	0.0
10	4587	4506	4589	-2	-0.1
20	4147	4030	4105	42	1.0
30	4065	3905	3977	88	2.2
40	4525	4210	4288	237	5.5
50	5755	4950	5042	713	14.2
60	7790	6030	6142	1648	26.8
70	10280	7330	7466	2814	37.7
80	13090	8770	8932	4158	46.5
90	16410	10255	10445	5965	57.1
100	19520	11655	11871	7649	64.4
110	22370	12933	13172	9198	69.8
120	25140	14075	14335	10805	75.4
130	27140	15050	15328	11812	77.1
140	28707	15825	16118	12589	78.1
150	29575	16420	16724	12851	76.8

**Table 5.3. MMS1 output (ADCC) at 800 nm assessed for different probe-fruit distances for a kiwi fruit.**

<b>Kiwi</b> Probe-sample distance (mm)	<b>I<sub>S</sub> + I<sub>D</sub></b> ↑↑	<b>I<sub>D</sub>*</b> ↑→*	<b>I<sub>D</sub>* Corrected</b> <b>(=I<sub>D</sub>)</b> ↑→	<b>I<sub>S</sub></b> <b>(= I<sub>S</sub> + I<sub>D</sub> -</b> <b>I<sub>D</sub>)</b>	<b>I<sub>S</sub>/I<sub>D</sub></b> <b>(%)</b>
0	3640	3573	3639	1	0.0
10	4175	4013	4087	86	2.1
20	3825	3662	3730	93	2.6
30	3750	3569	3635	112	3.2
40	4045	3761	3831	209	5.6
50	4920	4287	4366	541	12.7
60	6460	5070	5164	1271	25.1
70	8490	6014	6125	2326	38.6
80	10790	7023	7153	3586	50.8
90	13115	8020	8168	4886	60.6
100	15370	8960	9126	6176	68.4
110	17440	9844	10026	7340	73.9
120	19345	10617	10813	8453	78.9
130	21010	11250	11458	9469	83.4
140	22300	11781	11999	10215	85.8
150	23265	12180	12405	10772	87.5

The ratio of specular-diffuse light varied as a function of fruit-probe distance (Figure 5.5), with both apple and kiwi fruit giving similar results. The amount of specular light entering the probe was less than 3% of the diffusely reflected detector light at probe-sample distances less than 30 mm and less than 6% of the diffusely reflected detector light at probe-sample distances less than 40 mm, but specular light entry increases rapidly at greater distances due to the loss of the shadowing effect. The contribution of specular was slightly less for kiwifruit than for apple for probe-sample distances less than 30 mm, consistent with an effect of skin hairs on light scattering from outside. At probe-sample distances greater than 70 mm, a reduced specular component was demonstrated in apple fruit compared to kiwi fruit, presumably with full illumination specular hairs of kiwifruit less aligned.

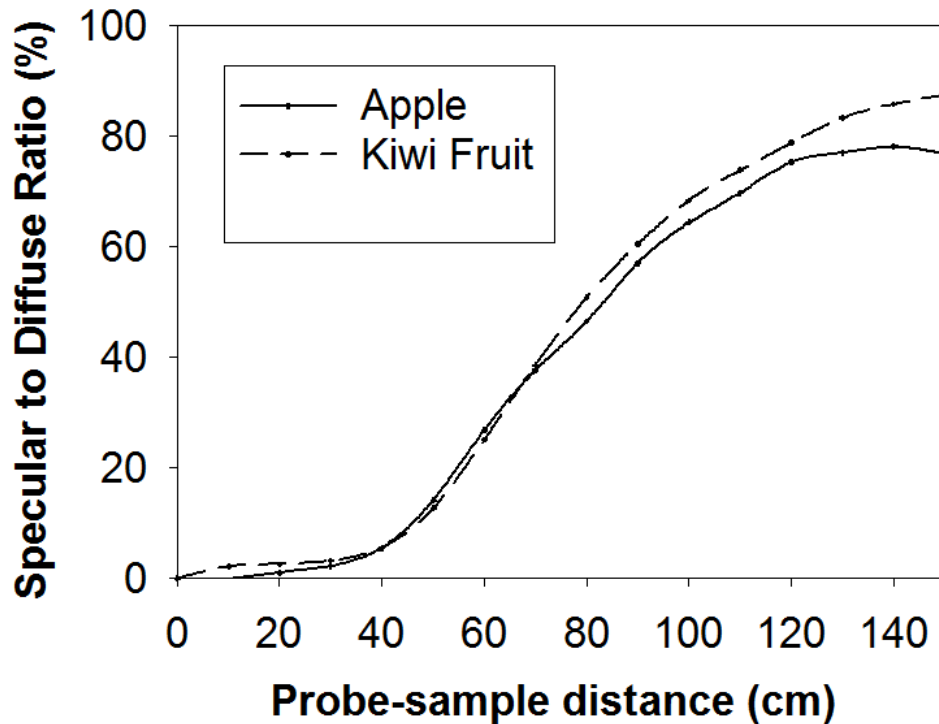


**Figure 5.5. Ratio of specular to diffuse radiation at 800 nm, received at various probe-sample distances from an apple and a kiwi fruit.**

## 5.4 Conclusion

Specular reflections contributed less than 3% of detected light at probe-sample distances up to 35 mm for the shadow probe assemblies. Designs with less collimation of the light source were associated with lamp converging rays impacting the shadow area, and thus a greater contribution of specular reflection to the detected signal. Any shadow probe design should seek to minimise specular reflection. Effectively, the umbra size is proportional to lamp-probe distance and shadow probe diameter, and inversely proportional to the lamp diameter. However, increasing lamp-probe distance reduces sample illumination intensity and thus increases noise. A more powerful light source adds heating effects.

## 5.5 Acknowledgements

Christo Liebenberg was involved in experimental design and data collection. Support from MAF Roda and Felix Instruments and advice from Zeiss GmbH is acknowledged.

## DECLARATION OF CO-AUTHORSHIP AND CONTRIBUTION

Title of Paper	Improving calibration transfer between short wave near infrared silicon photodiode array instruments
Full bibliographic reference for Journal/Book in which the Paper appears	C. Hayes, K. Walsh and C. Greensill, "Improving calibration transfer between shortwave near infrared silicon photodiode array instruments". <i>Journal of Near Infrared Spectroscopy</i> , <b>24</b> , 59 (2016).
Status	Published

Nature of Candidate's Contribution

All experimental work and analysis

Nature of Co-Authors' Contributions

Supervision

Candidate's Declaration

*I declare that the publication above meets the requirements to be included in the thesis as outlined in the Publication of Research Higher Degree Work for Inclusion in the Thesis Procedures*

*Signature*

*Date*

31 March 2016

## 6 Improving calibration transfer between short wave near infrared silicon photodiode array instruments <sup>4</sup>

### Abstract

The use of a model developed on spectra of one (master) instrument with spectra collected using another (slave) instrument requires differences in spectra of master and slave units to be orthogonal to the calibration model. The more spectral similarity is achieved in hardware, i.e. by matching the optical characteristics of the devices, the less chemometric correction is required. The transfer of partial least squares (PLS) models for total soluble solid (TSS) of intact apple fruit between instrumentation based on silicon photodiode arrays was improved by use of more accurate wavelength assignments over the wavelength range used in the model. Several transfer methodologies were trialled, including piecewise direct standardisation (PDS), transfer by orthogonal projection (TOP), model updating (MU) and difference spectrum adjustment. The difference spectrum method combined with new wavelength assignments and model updating gave results comparable to the performance of the master instrument and to models directly developed on the slave instruments ( $r^2 = 0.95$ ,  $SEP_b = 0.47$  and bias =  $-0.03$  %TSS, for a population of mean = 14.45 and SD = 1.64 % w/v). The use of average difference spectrum adjustment combined with model updating was preferred over PDS due to ease of implementation.

---

<sup>4</sup> This chapter has been published under this title in the Journal of Near Infrared Spectroscopy 2016. Techniques from this chapter also informed the publication “Spectrophotometer Aging and Prediction of Fruit Attributes” (Appendix B) and “Assessment of internal flesh browning in intact apple using visible-short wave near infrared spectroscopy” (Appendix C).

## 6.1 Introduction

Silicon photodiode array (PDA) detectors find use within spectrometers targeted to high speed, low cost applications that require use of the Herschel region (780-1000 nm, also known as short wave NIR) of the spectrum. Example applications include those involving transmission through biological material, given strong absorbance by water. Such spectrometers vary in both photometric response and wavelength accuracy, and thus calibration models tend to be spectrometer specific. Calibration models can be developed for each device, but this is inefficient. The transfer of calibration models between instruments has been reported to be possible even across categories of instruments (e.g. PDA, Fourier Transform (FT-NIR), scanning grating), however, hardware matched instrumentation will minimise the software correction required in the calibration transfer process.

As noted in the useful review on standardisation and calibration transfer for NIR instruments by Fearn<sup>64</sup>, the comparison of similar instruments can be simplified to a description of wavelength differences and absorbance differences. A small shift in wavelength scale may cause model prediction problems if high model weighting is given to parts of the spectrum with high slopes. Fearn<sup>64</sup> also noted that the transfer problem can be approached in three ways (i) by making of a model that transfers without requiring standardisation, e.g. using spectral pre-treatments, by selection of wavelengths in areas of spectra 'stability', or by including several instruments in the calibration set; (ii) adjusting the model output such that it works on other instruments, e.g. simple slope and bias correction; and (iii) adjusting spectra from slave instruments to appear as they were produced by the master instrument. A fourth approach was introduced by Andrew and Fearn<sup>133</sup> (and investigated by Soldado et al.<sup>134</sup> and Igne et al.<sup>135</sup>) was that of transfer by orthogonal projection (TOP), with removal of spectral differences orthogonal to the calibration model.

Simple slope and bias correction of model predictions can be effective, e.g. Roggo<sup>136</sup> recommended this procedure for the transfer of a model of total soluble solids (TSS) content in sugar beets between two Foss NIRSystems 6500 scanning grating spectrometers (FOSS, Silver Springs, U.S.A.) over the methods of spectral correction

methods of spectral slope/bias correction (SSBC) and spectral bias correction (i.e. spectra modification).

A range of techniques have been used to address the third approach in calibration transfer, that of adjusting spectra from slave instruments to appear as master instrument spectra. The methods of SSBC and spectral bias correction<sup>136</sup> involve wavelength by wavelength simple linear regressions of spectra from each instrument. Other techniques include direct standardisation (DS), piecewise direct standardisation (PDS), double window piecewise direction standardisation (DWPDS), orthogonal signal correction (OSC), finite impulse response (FIR) and wavelet transform (WT), as reviewed by Fearn<sup>1</sup>.

For example, Almar et al.<sup>137</sup> investigated the use of the PDS method to transfer calibrations of models of apple TSS from an FTNIR (InfraProver, Bran & Luebbe, Norderstedt, Germany) to PDA based spectrometers (Corona, Carl Zeiss GbmH, Jena, Germany) and between two PDA based spectrometers for the common wavelength range of 1020 to 1690 nm. The use of PDS decreased the root mean square error of prediction (RMSEP) from 17.69 to 0.56 % TSS. Salguero-Chaparro et al.<sup>138</sup> investigated PDS, SBC and TOP algorithms for transferring olive quality (fat, free acidity and moisture content) databases between a Foss NIRSystems 6500 scanning grating spectrometer and a PDA based Corona 45 vis NIR system (Carl Zeiss GbmH, Jena, Germany). All three transfer methods were reported to work well.

Other approaches achieve an 'implicit' orthogonalisation, such as the 'repeatability file' concept<sup>139</sup>, in which difference spectra (e.g. of the same sample scanned on multiple instruments) is assigned an attribute value of zero and included in the calibration set with a weighting factor proportional to the ratio of the number of samples in the repeatability file and calibration set. In a similar vein, Saranwong and Kawano<sup>140</sup> proposed a method using the difference in the average (second derivative absorbance) spectra of a group of samples to adjust the spectra of a slave instrument by simple subtraction, for transfer of a calibration on apple TSS between two Foss NIRSystems 6500 spectrometers. The method was quite effective, with the resulting bias at the same level as the validation results on the master instrument, and a 95% confidence pair t-test indicated no significant difference between the actual and predicted TSS values after spectral adjustment.

There are few reports on calibration transfer work involving the silicon PDA based spectrometers used with sorting of fruit. For applications involving melon and mandarin TSS assessment, Greensill et al.<sup>77, 141</sup> compared the performance of the seven techniques mentioned above and a model updating (MU) technique based on use of Kennard-Stone selected representative spectra. WT and MU proved to be the best methods, decreasing the RMSEP from 7.03 to 0.21 % TSS, with very little difference in the RMSEP of the two techniques, although PDS and DWPDS methods also performed well.

However, before attempting a chemometric correction of spectra from slave units, it is logical to first maximise matching of instrument optics, and in particular, wavelength accuracy. A 'selling' point of FTNIR instruments is the ease of model transfer between units, based on the superior wavelength resolution and accuracy of these units (e.g. FT instruments have manufacturer claims of reproducibility corresponding to 0.002 nm at 1369.9 nm<sup>142</sup>). Leion et al.<sup>67</sup> found that differences between scanning grating instruments of  $>\pm 0.3$  nm increased RMSEP of transferred models. Similarly, Shenk and Westerhaus<sup>70</sup> reported that a wavelength alignment of  $\pm 0.25$  nm is sufficient for most food and agricultural products. Brimmer and DeThomas<sup>143</sup> found differences in wavelength value for an absorbance peak of polystyrene at 1676 nm varied by only 0.1 nm between several scanning grating units (Foss NIRSystems, model 6500) and this indicated that, providing scanning grating instruments meet manufacturer specifications, wavelength alignment issues in calibration transfer should be minimal for these instruments.

For PDA units, wavelength to pixel assignments are typically based on a third order polynomial fit to the peaks of spectral output from a mercury/argon (HgAr) lamp, with inaccuracies in peak assignment of up to 0.26 nm for a Si PDA with approximately 3.3 nm pixel dispersion, such as the Zeiss MMS1<sup>144</sup>. Given that such instruments typically have a wavelength resolution (full width half maximum) around 10 nm and that the spectral features of the SWNIR are broad and overlapped, the wavelength accuracy attained in the current calibration process would appear adequate to the task of matching instruments. However, the issue of wavelength differences between units is of more importance than that of absorbance differences for diode array UV-Vis spectrometers (Blanco et al.<sup>53</sup>), in contrast to the situation for scanning monochromator NIR spectrometers.

The objective of the current study was therefore to document the impact of wavelength accuracy on predictive model performance for a SWNIR instrument, and the benefit of improvement in wavelength calibration in concert with transfer routines for the porting of models between instruments. We were encouraged in this endeavour by Fearn's<sup>64</sup> observation that 'there are surprisingly few comparative studies (of transfer methods) in the literature'. Our work is focussed on the application of SWNIRS to internal quality of fruit, so this study was framed by work with a spectrometer system and data set relevant to that application.

## **6.2 Materials and Methods**

### **6.2.1 Instrumentation and fruit TSS**

Four exercises were undertaken, using procedures documented in later sections. In Exercises 1 and 2, Zeiss MMS1 NIR enhanced (Carl Zeiss GmbH, Jena, Germany) spectrometers were interfaced with computers via a 16-bit tec5 PD-PCI01V1 analogue to digital converter card (Tec5 AG Sensorik und Systemtechnik, Oberursel, Germany) and a front end electronics box (Tec5 AG Sensorik und Systemtechnik, Oberursel, Germany). Spectral data were acquired using software incorporating a LabView (National Instruments Corporation, Austin, TX, USA) program developed specifically for this project.

The four MMS1 units used were from two different manufacturing batches, with difference in the PDA used. Older MMS1 units (part number 224001-9001-000; serial number 3017XX) use a S4874 detector (Hamamatsu Photonics K.K., Hamamatsu City, Shizuoka, Japan). Newer MMS1 units (000000-1233-038; serial number 0231XX) have a S8381 detector (Hamamatsu Photonics K.K., Hamamatsu City, Shizuoka, Japan). The older units suffered a "ghost" effect, with charge being carried over between read out cycles. The new units have a faster removal time of electrons from each well, but less sensitivity past 800 nm. Calibration transfer between units from different manufacturing lots is therefore expected to be more problematic than between units of the same batch.

In exercise 3, spectra of fruit were acquired using a stationary system employing an interactance optical configuration<sup>97</sup> ('InSight1', MAF Oceania, Bacchus Marsh, Vic., Australia). A stabilised 12V power supply (MAF Oceania) was used to minimise current

fluctuations to the halogen lamps. White and dark references were collected once only, at the beginning of each day. For exercise 4, spectra of fruit were collected on each of four handheld units (Nirvana, Integrated Spectronics, Sydney, Australia). These units were equivalent to the F750 from Felix Instruments, Camas, WA, USA, with serial numbers A001, A002, A003 and A015, in which a reference is taken associated with every sample. Both instruments employ the MMS1 spectrometer.

Fruit TSS was assessed using an Atago digital refractometer of juice squeezed from a 2 cm diameter, 1 cm deep core of fruit taken at the point of spectral acquisition.

## **6.2.2 Experimental exercises**

### **6.2.2.1 Exercise 1. PDA response**

The photometric response of the four MMS1 spectrometers (serial numbers 301726, 301729, 023104, 023126) was assessed using combinations of eight optical crown glass metallic neutral density filters (Newport Corporation, Irvine, CA, U.S.A.) and bandpass spectral filters (Andover Corporation, Salem, NH, U.S.A.). A halogen light source (HL-2000-HP; Mikropack GmbH., Ostfildern, Germany; serial number 200332) was connected to a stabilised power supply (EA1050B-240, CUI Inc, Tualatin, OR, U.S.A.) and allowed two hours to stabilise before measurements were taken. The fibre optic output of the light source was directly aligned with the MMS1 fibre optic input, and the filters placed in the optical path between. For each bandpass filter, MMS 1 integration time was set to approximately 75% of saturation level for the instrument, without a neutral density filter, and then combinations of neutral density filters giving optical densities between 0.04 and 1.5 (i.e. between 91.2 and 3.2 % transmittance) were placed in the optical path and spectra acquired. This procedure was repeated for each spectrometer, using the same integration time.

### **6.2.2.2 Exercise 2. Impact of wavelength accuracy on PLS prediction of fruit**

#### **TSS**

The MMS1 PDA spectrometers are supplied with a pixel to wavelength third order polynomial relationship calculated from the fit of 11 peaks from a HgAr lamp from across the wavelength range 300-1100 nm. Spectra were acquired from a HgAr

Calibration Source (HG-1, Ocean Optics Inc, Dunedin, FL, U.S.A.) using five Zeiss MMS1 spectrometers (serial numbers 301726, 301729, 023103, 023104, 023126). The HG-1 source was given 30 min to stabilise before spectra were acquired. Using inbuilt Matlab functions, spectra were interpolated to 0.0001 nm steps, based on a cubic spline fit, and the wavelengths of the HgAr peaks compared to NIST values<sup>145</sup>.

The impact of wavelength inaccuracy on predictive performance was then assessed. A PLS regression model for apple TSS was developed using the spectra acquired for exercise 3, on MMS1 023103. The wavelength scale of the spectra were then shifted by 0.01 to 5 nm in 0.01 nm steps, and the PLS model used to predict TSS using the modified spectra.

### **6.2.2.3 Exercise 3. Calibration transfer between on line units**

Spectra were acquired of 88 apples using an InSight unit, with two spectra acquired from each of two sides of the fruit (i.e. 352 spectra), using three MMS1 units (023103, 023126 and 301729, hereby designated by the last three digits). Subsets of these spectra were used for calibration (spectra of 53 fruit, mean TSS of 12.60 and SD of 1.95 % w/v), validation (spectra of 20 fruit, mean TSS of 12.83 and SD of 1.56 % w/v) and transfer (spectra of 15 fruit, mean TSS of 12.68 and SD of 2.34 % w/v). Fruit were randomly assigned to the three groups. PLS regression models for fruit TSS were developed on each unit, based on interpolated second derivative absorbance spectra.

Each instrument was treated as a master unit, with performance of the PLS model for each unit tested against the unaltered and transformed spectra of the other units. The transformation techniques of PDS and DSA, which act to modify slave spectra to appear to be from the master instrument, the technique of model updating (MU) using the slave instrument fruit spectra from the PDS subset, and the combination of the transfer methods with MU were compared. The spectral pre-treatments of mean centring (MC), standard normal variate (SNV), multiplicative scatter correction (MSC) and/or autoscaling were also compared.

The comparisons described above were then repeated using new wavelength to pixel assignments for each spectrometer. Pixel wavelength assignments for the 695 – 1014 nm range were generated for each spectrometer from a linear fit between adjacent peaks and a fourth order polynomial fit to wavelength peaks, using the HgAr data from Exercise 2.

PLS models for fruit TSS were then re-developed for each unit, and, as above, tested in terms of use with other spectrometers.

#### **6.2.2.4 Exercise 4. Calibration transfer between handheld units**

Spectra of 59 apples were collected on each of four handheld units. Four spectra were collected from two locations on each of 29 fruit and, at a later date an independent apple population, five spectra at two different sites on a group of 30 apples. Subsets of the spectra were used for calibration (spectra of 39 fruit, mean TSS of 14.45 and SD of 1.64 % w/v), validation (spectra of 10 fruit, mean TSS of 14.35 and SD of 1.76 % w/v) and transfer (spectra of 10 fruit, mean TSS of 14.68 and SD of 1.93 % w/v). All fruit from the first group were assigned to the calibration set, with the second group randomly assigned into calibration, validation and transfer groups. To compensate the influence of measurement condition, particularly the position of the fruit relative to the instrument optics, interpolated second derivative absorbance spectra were averaged for spectra collected from a given position on the fruit for the samples used in PLS calibration and transfer. The validation sets were of individual spectra.

PLS regression models for fruit TSS were developed for each unit. The PLS TSS model developed for the master unit was used in prediction of TSS using unaltered spectra of other units, as well as using instrument standardisation techniques of MU, PDS and DSA. The technique of model updating (MU), and the combination of transfer methods with MU were also tested, and the spectral pre-treatments of MC, SNV, MSC and/or autoscaling were compared.

As the HgAr lamp spectra could not be collected without disassembly of the instruments, the master instrument was arbitrarily defined as having “correct” pixel wavelength assignments. The average of interpolated second derivative absorbance spectra in the set of spectra allocated to PDS development was used to generate new pixel wavelength assignments across the 695 – 1014 nm range from fourth order polynomial fits to spectra peaks in the slave units. PLS models for fruit TSS were then redeveloped on each unit, and, as above, tested in terms of use with other spectrometers.

### 6.2.3 Chemometrics

PLS regression models were developed using MATLAB R2014a (MathWorks Inc., Natick, MA, USA) with PLS Toolbox 7.3 (Eigenvector Research Inc., Wenatchee, WA, USA), using mean centred second derivative absorbance data interpolated to 3 nm steps, and the wavelength range 732-936 nm. The optimal number of principal components was chosen using software package The Unscrambler 10.3 (CAMO Software AS, Oslo Norway), however all other calculations were performed in MATLAB. Model performance was assessed in terms of validation  $r^2$  and prediction performance was assessed in terms RMSEP and bias corrected RMSEP (SEP<sub>b</sub>).

PDS, as developed by Wang et al.<sup>75</sup>, reconstructs each spectral point from the measurements within a sliding window on the slave instrument. Sample spectra are acquired on the master instrument  $\mathbf{X}_1$  and slave instrument  $\mathbf{X}_2$ . For each wavelength  $i$  of a sample collected on the master, spectra were regressed against the corresponding spectra within a window of neighbouring wavelengths, of width  $2j + 1$ , from the slave instrument. In this study,  $j$  was assigned a value of 1 (given superior results for a width of 3 compared to 5 and 7, data not shown). The regression vector is calculated by

$$\mathbf{X}_1(:, i) = \mathbf{X}_2(:, i - j : i + j) \mathbf{b}_i \quad \text{Eqn 6.1}$$

where  $\mathbf{X}_1(:, i)$  and  $\mathbf{X}_2(:, i - j : i + j)$  are columns used in the calculation of  $\mathbf{b}_i$ . The response vector of an unknown sample measured on the slave instrument is standardised using

$$\hat{\mathbf{r}}_{1,un,i} = \mathbf{r}_{2,un,i-j,\dots,i+j} \mathbf{b}_i \quad \text{Eqn 6.2}$$

The difference spectrum adjusted (DSA) method of Saranwong and Kawano<sup>140</sup> requires calculation of a difference spectrum of the average of the second derivative absorbance spectra of a set of samples acquired on each instrument according to

$$a_i = y_i - x_i \quad \text{Eqn 6.3}$$

where  $a_i$  is the value for the difference spectrum at wavelength  $i$ ,  $x_i$  and  $y_i$  are the average second derivative absorbance value of calibration sample at wavelength  $i$ , measured with the master and slave instruments respectively.

Spectral correction is then performed via

$$\hat{y}_{ki} = y_{ki} - a_i \quad \text{Eqn 6.4}$$

where  $y_{ki}$  is the second derivative absorbance value of sample  $k$  at wavelength  $i$  measured by the slave instrument, and  $\hat{y}_{ki}$  is the corrected second derivative absorbance value of sample  $i$  at wavelength  $i$  for the slave instrument.

The ‘repeatability file’ concept of Westerhaus<sup>139</sup>, takes difference spectra of the same samples scanned on multiple instruments, and is assigned an attribute value of zero. These are included in the calibration set with the spectra multiplied by a weighting factor,  $W$ , given by

$$W = \sqrt{\frac{cal\ n}{rep\ n}} \quad \text{Eqn 6.5}$$

where  $cal\ n$  is number of samples in the calibration set and  $rep\ n$  is the number of samples used in the repeatability file.

The TOP method introduced by Andrew and Fearn<sup>133</sup> removes spectral differences orthogonal to the calibration model. Spectra from a small number of samples scanned on each of  $m$  instruments, are averaged to produce one spectrum for each instrument. A resulting  $m \times p$  matrix  $R$  of mean spectra is formed, where  $p$  is the number of wavelengths. A principal component analysis is performed on  $R$  giving  $m - 1$  components representing the main directions of instrument variation in spectral space. This gives a  $p \times d$  matrix  $P$  whose columns are the orthonormal eigenvector of  $R$ , where  $d \leq m - 1$ . The required calculation is

$$\tilde{X} = X - XPP^T \quad \text{Eqn 6.6}$$

where  $\tilde{X}$  is the projection of calibration set matrix  $X$  onto the space orthogonal to the columns  $P$ .  $\tilde{X}$  is used for the PLS regression model, with  $d$  being the maximum for this study (given superior results, data not shown).

## 6.3 Results and Discussion

### 6.3.1 Exercise 1. PDA response

The four MMS1 units demonstrated differences in photometric response consistent with a change in the type of Hamamatsu PDA used in these units. The units with 3017xx serial numbers displayed greater sensitivity from 820 to 970 nm (Figure 6.1). Calibration transfer between units from different manufacturing lots is therefore expected to be more problematic than between units of the same batch. Of course, the absorbance calculation given by

$$A = -\log\left(\frac{S - D}{W - D}\right) \quad \text{Eqn 6.7}$$

(where  $S$  is the sample analogue to digital conversion count (ADCC),  $D$  is the dark reference ADCC and  $W$  is the white reference ADCC) accommodates such differences, but differences in sensitivity and thus signal to noise remains, which may impact model performance.

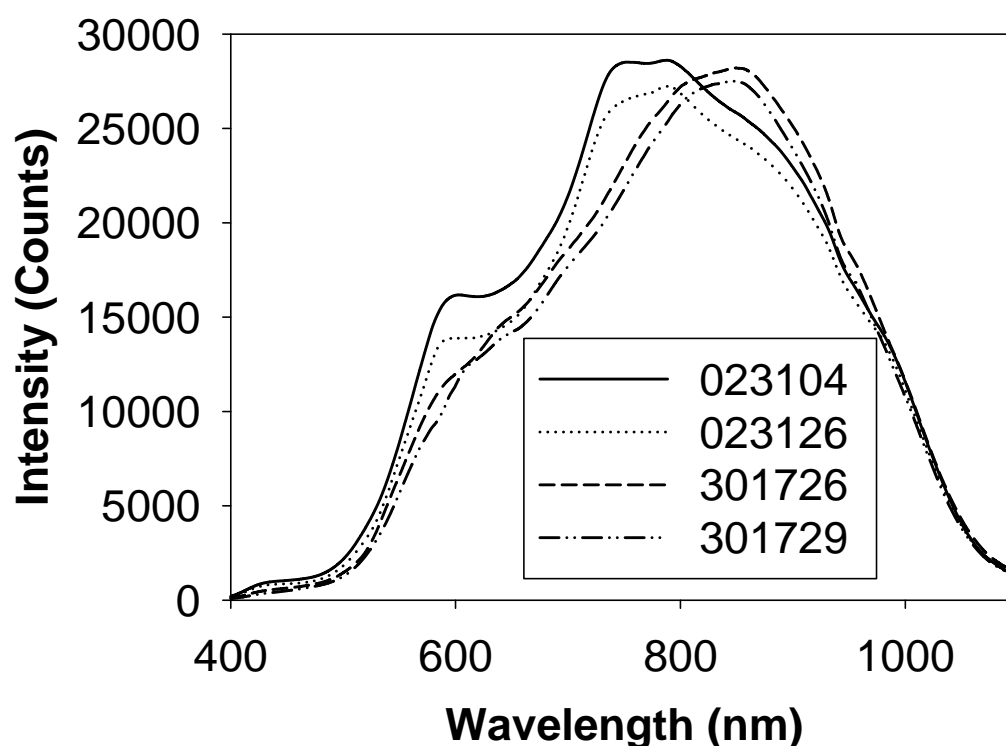


**Figure 6.1. Spectra of sample analogue to digital conversion count (ADCC) of a PFTE tile using the same light source but four different MMS1 spectrometers.**

There was a linear response by the sensors to increasing illumination over the ADCC range considered (0 to 75% of maximum ADCC; data not shown). There was also a high correlation between the photometric response of pixels of a given PDA with increasing illumination. As expected, conversion to absorbance values normalised the slope of the relationship between different pixel of an array to unity (Figure 6.2). When corresponding pixels of different MMS1 were compared (Figure 6.3), similar relationships for ADCC and absorbance were evident. Thus the use of absorbance data should correct for photometric response differences between instruments, allowing for calibration transfer. Sensor response differences that result in a marked increase in signal to noise ratio for data within the wavelength region used in a PLS model may result in a decreased  $SEP_b$  for a transferred model, although bias should be unaffected.

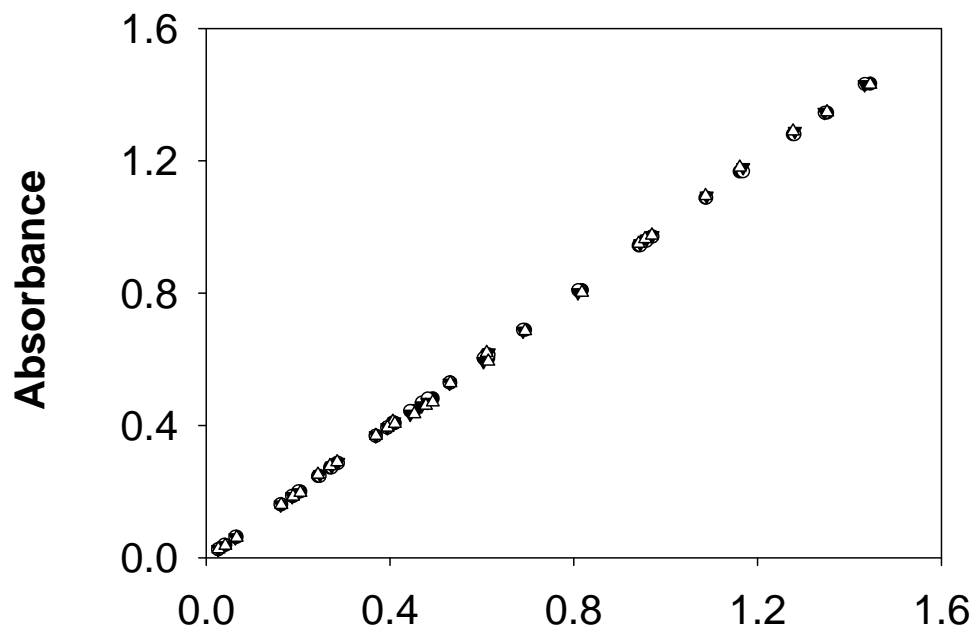
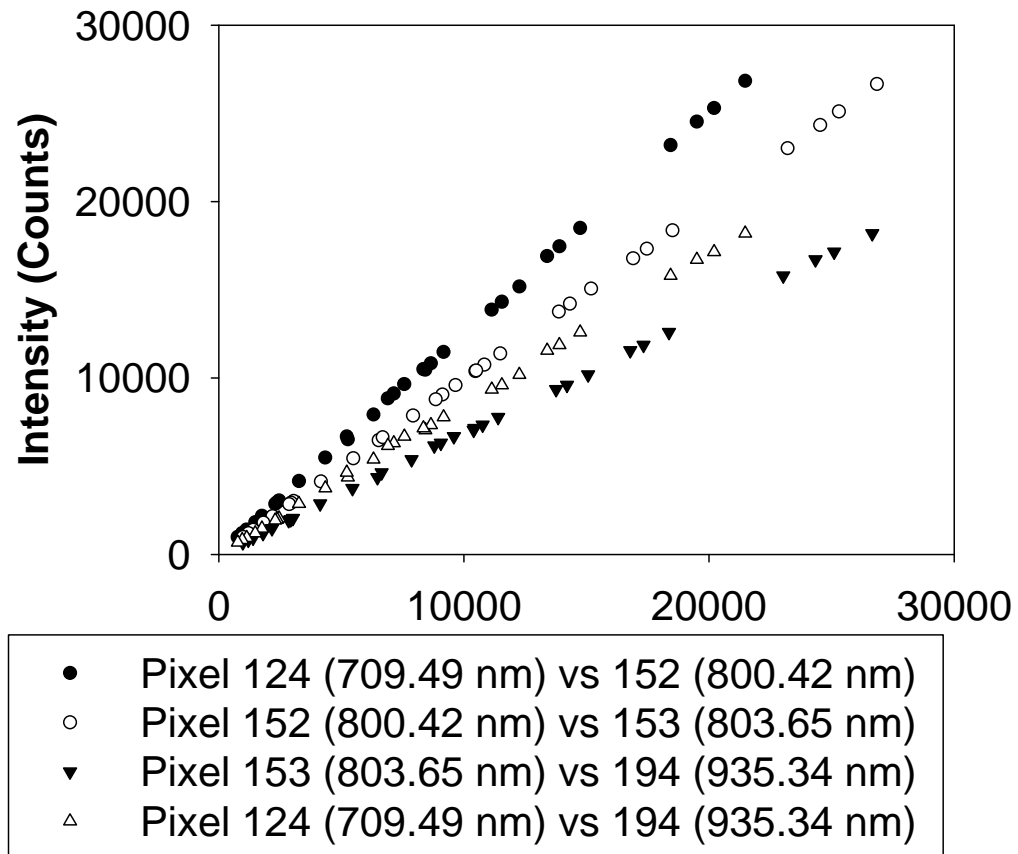
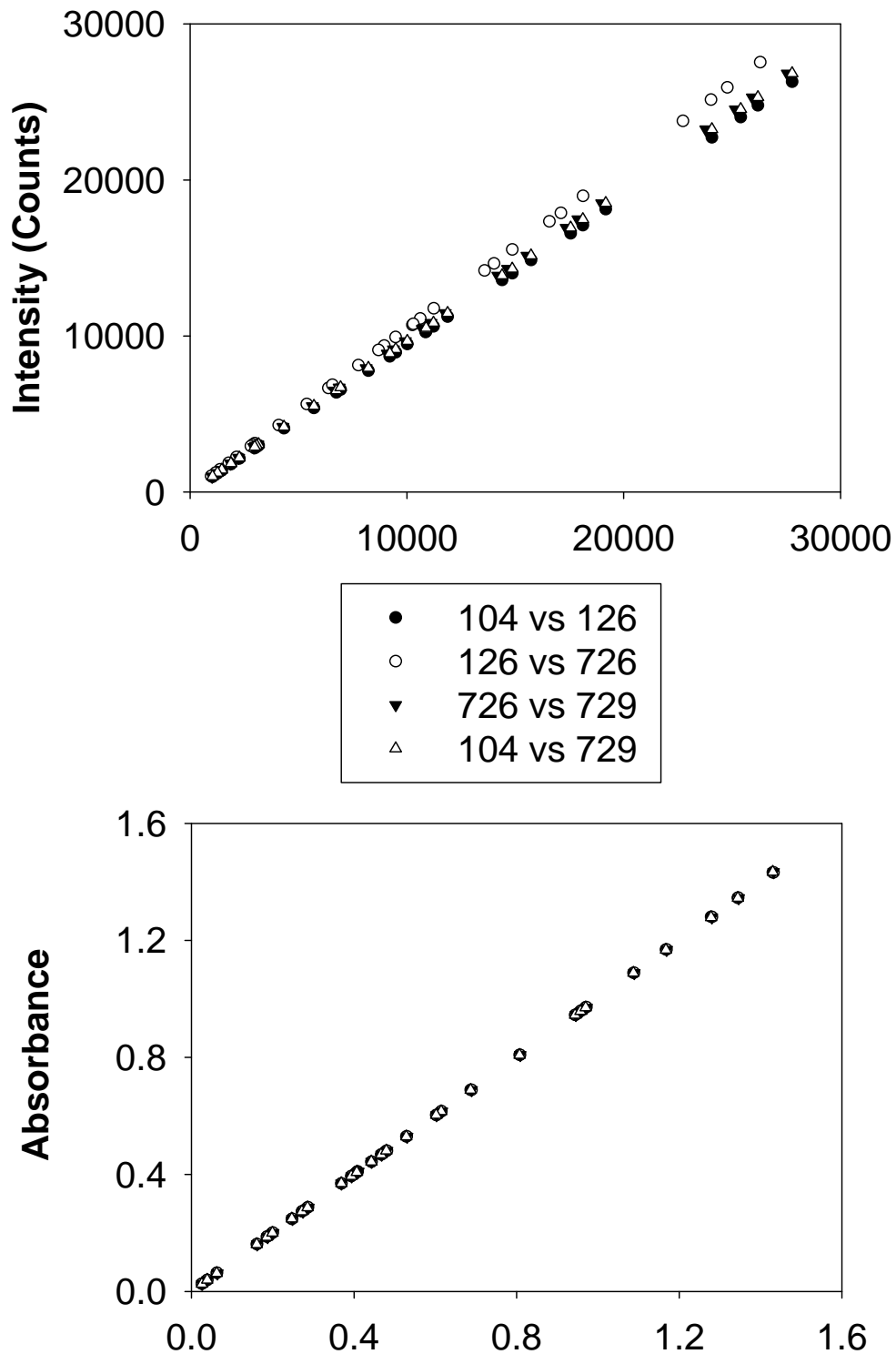


Figure 6.2. Graph of PDA photometric response of different pixels within the same MMS1 unit. Data from 023126 is shown, but was typical of all four units. The top panel represents raw sample analogue to digital conversion counts (ADCC), while in the bottom panel ADCC has been converted to absorbance.



**Figure 6.3.** Graph of PDA photometric response of the same wavelength from different MMS1 units. Data for 810 nm is shown, but was typical of other wavelengths. The top panel represents raw analogue to digital conversion counts (ADCC), while in the bottom panel ADCC has been converted to absorbance.

### **6.3.2 Exercise 2. Impact of wavelength accuracy on PLS prediction of fruit TSS**

The third order polynomial coefficients provided in the Zeiss test certificate for pixel to wavelength conversion across the whole spectrum showed an error of up to 3.214 nm, or up to 2.301 nm for the wavelength range used in the PLS regressions for TSS (e.g. for 301729, errors for HgAr peaks of 696.5431, 727.2936, 738.3980, 763.5106, 800.6157, 811.5311, 826.4522, 842.4648, 912.2967, 965.7786 and 1013.9760 were 1.1931, 1.0636, 1.2280, 1.0669, 1.1906, 2.0757, 2.3011, 1.6922, 2.1648, 0.9667, -0.1514 and -1.9440 nm respectively).

When fruit spectra were progressively shifted in 0.01 nm increments by up to 5 nm, both  $SEP_b$  and bias increased (Figure 6.4). Of course this bias represents the product of the model coefficient vector and the mean difference spectrum of wavelength shifted and original (derivative) spectra.

Of interest is the size of effect of small wavelength shifts on TSS model predictions. A difference of a sub pixel interval (i.e. less than 3.3 nm) in terms of wavelength accuracy between detectors was significant to the results of a PLS prediction, e.g. a shift of 1 nm resulted in an increase in  $SEP_b$  from 0.64 to 0.85, and a change in bias by -4.17 %TSS.

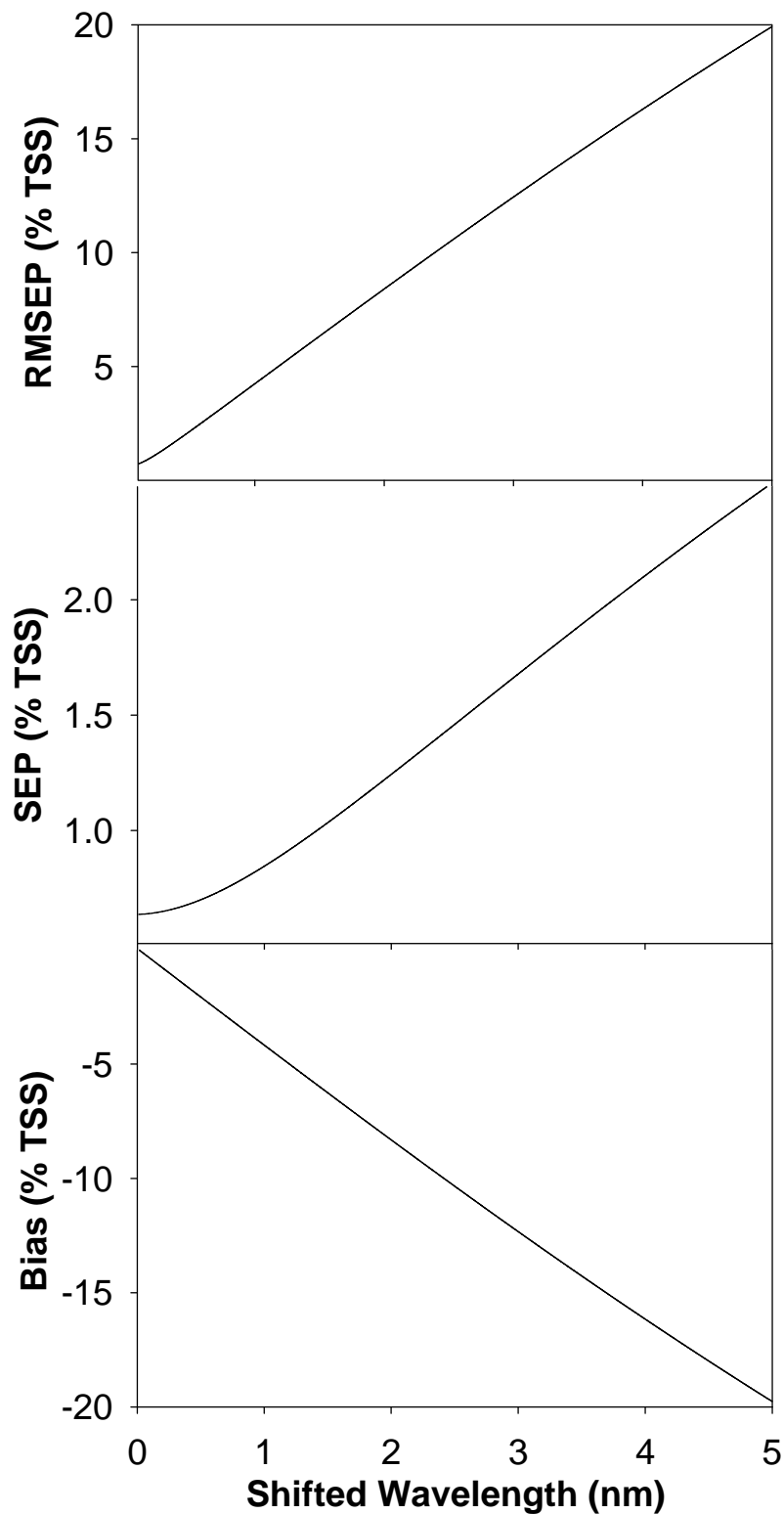


**Figure 6.4.** Effect of a shift in wavelength scale by up to 5 nm on (top) RMSEP, (middle) SEP and (bottom) Bias for a PLSR regression model of total soluble solids (%TSS) of peach fruit created on the same data set (and original wavelength assignments).

### 6.3.3 Exercise 3. Calibration transfer with on line unit

The performance of a TSS model from each unit in prediction of a validation set of spectra collected on the same unit was slightly improved with use of a 4<sup>th</sup> order polynomial over a restricted range for wavelength calibration (Table 6.1). Obviously simple assignment of wavelength values to pixels does not change the data set and thus model performance. Rather, the small change in model outcome must result from the change in data associated with interpolation (to 3 nm steps).

**Table 6.1. Apple total soluble solids (%TSS) for PLS regression model statistics for three different MMS1 units, for the manufacturer assigned wavelengths, new 4th order polynomial fit and a linear fit shown in the top, middle and bottom respectively.**

<b>MMS1</b>	<b>103</b>	<b>126</b>	<b>729</b>	<b>103</b>	<b>126</b>	<b>729</b>
	<b>Original Wavelengths</b>			<b>New 4th Order Fit Wavelengths</b>		
<b>PC</b>	4	4	5	4	4	5
	<b>Mean Centring</b>					
<b>r<sup>2</sup></b>	0.92	0.93	0.94	0.92	0.93	0.94
<b>SEP</b>	0.68	0.63	0.58	0.67	0.62	0.57
<b>BIAS</b>	-0.05	-0.01	-0.04	-0.05	-0.01	-0.04
	<b>Auto-scaling</b>					
<b>r<sup>2</sup></b>	0.93	0.94	0.96	0.93	0.94	0.96
<b>SEP</b>	0.64	0.61	0.49	0.64	0.60	0.49
<b>BIAS</b>	0.06	0.07	0.02	0.05	0.06	0.02

The autoscaling data pre-treatment improved results in every combination compared to MC, decreasing RMSEP values by as much as 0.09 for model validation (Table 6.1) and 0.11 %TSS in transferred models (not shown). SNV and MSC improved performance in some cases, but decreased in others (not shown).

The performance of a model created on one unit and used in prediction of spectra collected on another unit, with the same Hamamatsu detector type, was improved by use of the new wavelength assignments in terms of  $r^2$ , SEP and bias. For example, for the master 103 - slave 126 combination showed improvements in  $r^2$  from 0.93 to 0.94, SEP from 0.89 to 0.71%TSS and bias from -3.69 to -0.36 %TSS, for original and 4<sup>th</sup> order

polynomial modified wavelength assignments respectively, for the prediction of slave spectra with the master model (Table 6.2). The 4th order polynomial procedure slightly out performed a linear fit procedure (not shown). However, the performance between units with different detector type (e.g., master 726 to slaves 103 & 126) did not improve with the modified wavelength assignments alone, a result ascribed to the detector sensitivity difference.

Bias and SEP were improved with use of calibration transfer methods (PDS, MU & DSA), with PDS giving the best result of these methods (Table 6.2). In every case, the use of the new wavelength assignments and PDS was the optimal data treatment (in terms of RMSEP, SEP and bias), giving results comparable to that of models developed on the slave instruments (Table 6.1).

**Table 6.2. Apple total soluble solids (%TSS) prediction statistics for various master-slave combinations and transfer methods. Autoscaling was used. Units 103 and 126 are newer units containing the Hamamatsu S8381 detectors.**

Slave		Original Wavelengths							
		Direct	PDS	MU	Rep File	TOP	PDS + MU	DSA	DSA + MU
		Master 103							
126	$r^2$	0.93	0.94	0.93	0.91	0.87	0.94	0.93	0.93
	SEP	0.89	0.61	0.73	0.86	0.87	0.75	0.89	0.79
	BIAS	-3.69	-0.02	-0.19	0.80	-0.07	-0.08	-0.05	-0.06
729	$r^2$	0.93	0.93	0.92	0.90	0.86	0.94	0.93	0.94
	SEP	0.95	0.63	0.77	0.96	1.01	0.76	0.95	0.76
	BIAS	-1.64	0.11	-0.14	0.94	0.01	0.05	0.12	0.05
		Master 126							
103	$r^2$	0.88	0.92	0.90	0.90	0.86	0.92	0.88	0.90
	SEP	0.86	0.73	0.81	0.78	0.93	0.68	0.86	0.83
	BIAS	3.16	0.16	0.06	1.12	0.74	0.11	0.17	0.13
729	$r^2$	0.93	0.93	0.87	0.90	0.86	0.94	0.93	0.93
	SEP	0.68	0.62	0.85	0.77	0.90	0.64	0.68	0.62
	BIAS	1.96	0.20	0.30	1.22	0.15	0.07	0.21	0.12

		<b>Master 729</b>							
<b>103</b>	<b>r<sup>2</sup></b>	0.92	0.92	0.93	0.93	0.91	0.91	0.92	0.92
	<b>SEP</b>	0.77	0.74	0.72	0.76	0.79	0.70	0.77	0.75
	<b>BIAS</b>	1.19	0.11	-0.08	1.11	0.66	0.01	0.13	0.10
<b>126</b>	<b>r<sup>2</sup></b>	0.93	0.94	0.93	0.92	0.93	0.93	0.93	0.93
	<b>SEP</b>	0.63	0.59	0.64	0.68	0.61	0.66	0.63	0.61
	<b>BIAS</b>	-2.66	0.08	-0.29	0.87	0.09	-0.04	0.04	0.02
<b>Slave</b>		<b>New 4th order fit</b>							
		<b>Direct</b>	<b>PDS</b>	<b>MU</b>	<b>Rep File</b>	<b>TOP</b>	<b>PDS + MU</b>	<b>DSA</b>	<b>DSA + MU</b>
		<b>Master 103</b>							
<b>126</b>	<b>r<sup>2</sup></b>	0.94	0.94	0.94	0.92	0.91	0.94	0.94	0.94
	<b>SEP</b>	0.71	0.59	0.66	0.72	0.73	0.74	0.71	0.67
	<b>BIAS</b>	-0.36	-0.03	-0.11	0.97	0.32	-0.09	-0.06	-0.08
<b>729</b>	<b>r<sup>2</sup></b>	0.93	0.93	0.90	0.89	0.89	0.93	0.93	0.94
	<b>SEP</b>	0.78	0.61	0.77	0.83	0.88	0.77	0.78	0.64
	<b>BIAS</b>	3.55	0.11	0.09	1.29	0.37	0.06	0.11	0.06
		<b>Master 126</b>							
<b>103</b>	<b>r<sup>2</sup></b>	0.92	0.92	0.92	0.92	0.89	0.92	0.92	0.92
	<b>SEP</b>	0.68	0.72	0.71	0.72	0.82	0.67	0.68	0.70
	<b>BIAS</b>	0.32	0.15	0.14	1.10	0.10	0.11	0.14	0.12
<b>729</b>	<b>r<sup>2</sup></b>	0.92	0.93	0.88	0.86	0.88	0.94	0.92	0.93
	<b>SEP</b>	0.68	0.62	0.82	0.88	0.82	0.63	0.68	0.63
	<b>BIAS</b>	3.25	0.18	0.06	1.17	0.16	0.07	0.18	0.11
		<b>Master 729</b>							
<b>103</b>	<b>r<sup>2</sup></b>	0.91	0.92	0.91	0.88	0.92	0.91	0.91	0.91
	<b>SEP</b>	0.73	0.73	0.78	0.88	0.71	0.72	0.73	0.73
	<b>BIAS</b>	-2.49	0.10	0.08	1.18	0.19	0.01	0.10	0.10
<b>126</b>	<b>r<sup>2</sup></b>	0.92	0.94	0.93	0.92	0.94	0.93	0.92	0.93
	<b>SEP</b>	0.69	0.59	0.63	0.65	0.58	0.69	0.69	0.65
	<b>BIAS</b>	-3.80	0.07	-0.26	0.95	-0.06	-0.06	0.03	0.02

### 6.3.4 Exercise 4. Calibration transfer with handheld unit

The performance of each of four handheld spectrometers on their validation sets was improved when the 4<sup>th</sup> order polynomial wavelength calibration was used (Table 6.3). As for the in-line unit, the performance of a model created on one unit and used in prediction of spectra collected on another unit was improved in terms of  $r^2$  by use of the new wavelength assignments for both master and slave units, with the 4th order polynomial (Table 6.4) slightly outperforming the linear fit (not shown). Again, model bias could potentially be estimated and corrected for each instrument, ideally from assessment of non-fruit samples on master and slave. Alternatively, any of the calibration transfer strategies resulted in decreased bias.

The DSA method removed bias, and combined with new wavelengths and model updating, gave results comparable to the performance of the master instrument and to models directly developed on the slave instruments. Considering only 10 fruit were used, this is an easy method to transfer calibrations and allow for models to be easily updated for seasonal changes. PDS did perform marginally better in some cases, but DSA+MU is preferred due to ease of implementation.

Whilst the autoscaling pre-treatment performed slightly better on most model validation sets (Table 6.3), mean centring performed better on transferred models (not shown), in contrast to the result for the online units. This may be caused by the increased number of PCs used for the handheld units. On these units, MU outperformed PDS.

**Table 6.3. Apple total soluble solids (%TSS) model validation statistics for four handheld units, using pre-treatments of mean centring and autoscaling. Models are based on original wavelengths.**

MMS1	A	B	C	D
	<b>Mean Centre</b>			
$r^2$	0.95	0.93	0.95	0.92
SEP	0.46	0.53	0.50	0.58
BIAS	0.03	-0.01	0.12	0.03
	<b>Autoscale</b>			
$r^2$	0.96	0.95	0.95	0.91
SEP	0.44	0.46	0.46	0.60
BIAS	0.04	-0.07	-0.02	-0.09

**Table 6.4. Apple total soluble solids (%TSS) prediction statistics using unit A as the master, given use of several transfer methods.**

Slave		Original Wavelengths							
		Direct	PDS	MU	Rep File	TOP	PDS + MU	DSA	DSA + MU
B	$r^2$	0.88	0.84	0.86	0.89	0.75	0.93	0.88	0.94
	SEP	0.77	0.97	0.78	0.67	1.03	0.56	0.77	0.51
	BIAS	-12.95	0.02	-0.04	-2.95	-4.28	-0.02	0.03	0.04
C	$r^2$	0.91	0.91	0.95	0.95	0.90	0.95	0.91	0.94
	SEP	0.64	0.69	0.45	0.49	0.65	0.45	0.64	0.51
	BIAS	4.97	0.08	0.08	2.42	1.41	0.04	0.00	-0.02
D	$r^2$	0.88	0.91	0.95	0.94	0.73	0.95	0.88	0.95
	SEP	0.72	0.67	0.47	0.53	1.19	0.44	0.72	0.48
	BIAS	12.90	0.04	0.18	5.31	1.99	0.08	0.03	0.01
		New 4th order fit							
B	$r^2$	0.93	0.85	0.90	0.92	0.91	0.92	0.93	0.94
	SEP	0.54	0.94	0.64	0.58	0.64	0.57	0.54	0.50
	BIAS	-1.83	0.00	-0.16	-1.34	-0.21	-0.07	0.12	0.04
C	$r^2$	0.94	0.91	0.94	0.94	0.90	0.95	0.94	0.95
	SEP	0.52	0.69	0.53	0.49	0.66	0.46	0.52	0.47
	BIAS	-1.04	0.10	-0.05	-2.34	0.09	0.04	-0.03	-0.04
D	$r^2$	0.92	0.91	0.93	0.91	0.89	0.95	0.92	0.95
	SEP	0.59	0.68	0.57	0.62	0.70	0.45	0.59	0.47
	BIAS	-0.63	0.06	0.05	1.50	0.21	0.10	-0.09	-0.03

## 6.4 Conclusion

To match instrumentation, PDA photometric response and wavelength accuracy must be considered. The coefficients provided in the Zeiss MMS1 specification sheet for pixel to wavelength conversion across the whole spectrum produced assignment errors of up to 2.3 nm for the wavelength range used in the PLS regressions on TSS. Both SEP and bias were found to increase with inaccuracies in wavelength assignments. Improvement of wavelength assignment, particularly for the wavelength range used in the PLS regressions, was found to significantly decrease bias and SEP prediction values. Bias may be removed by a simple slope and bias correction. Ideally this bias could be calculated from assessment of non-fruit samples on master and slave, although further investigation

is required. For units of the same model PDA, DSA combined with new wavelengths and model updating gave results comparable to the performance of the master instrument and to models directly developed on the slave instruments. Considering only 10 fruit were used, this is an easy method to transfer calibrations and allows for models to be updated for seasonal changes in samples.

## **6.5 Acknowledgements**

The support of MAF P/L is acknowledged, as is funding from Horticulture Australia Ltd. We thank Mihail Mukarev for useful discussions, and the anonymous reviewers for their insightful comments. The authors acknowledge collaboration with Felix Instruments and MAF in the development of the F750 and InSight spectrometers.

## 7 Conclusion and future directions

Near infrared (NIR) spectroscopic systems have been successfully utilised in non-invasive analysis of internal attributes of fresh horticultural produce over the last 25 years. It was in the 1970s that NIRS was first used for agricultural food samples by Karl Norris to analyse wheat grain for protein and moisture<sup>146</sup>. The first horticultural use reported by Birth et al.<sup>147</sup> in 1984 for determination of dry matter in onions. This technique was extended by Kawano et al.<sup>148</sup> in the 1990s for the determination of total soluble sugar (TSS) in fruit. Many manufacturers have attempted to enter the fruit assessment industry with NIRS instrumentation, however few have survived and devices not been widely adopted, indicating the technology is not yet fully mature in this application. In considering or comparing instrumentation for the application of assessment of internal fruit attributes, the following issues are relevant:

- optical geometry (typically partial transmission)
- lamp type and output stability in terms of aging and environmental conditions
- detector wavelength range, signal to noise and stability to environmental conditions
- model transfer across instruments
- model robustness in terms of function in the face of varying temperature and ambient light levels .

This thesis investigated the characteristics of individual components of a spectroscopic system, in context of performance of PLS predictive models of fruit TSS. The effects of the environmental temperature on spectral variation in QTH lamp output and variation in readout of the front end electronics and spectrometer, as well as QTH temporal stability were assessed in terms of predictive model performance for TSS in intact fruit using a silicon PDA spectrometer based system. Spectral variation resulting from temperature changes of NIRS system components (lamp and FEE) affected output quantity rather than quality, and thus did not affect the predictive performance due to the second derivative absorbance pre-treatment. Some lamps displayed start-up output characteristics on their first use, which were not repeated in subsequent trials. This result indicates the need for a short lamp 'burn in' period (up to 2 h). Lamp output, once burnt in, was spectrally stable, for the purpose of predictive models based on second derivative of absorbance data,

within the time of the first measurement (10 s), even during the last hours of lamp life. The results showed that re-referencing was not required within the normal daily use period for an inline instrument, but change in white reference could be used as a diagnostic tool. Further work showed measurements were spectrally stable after only 350-400 ms, although total illumination was not stable until approximately 40 min from start-up.

Understanding of LED lamp behaviour is essential to support the use of these devices as illumination sources in NIR spectroscopy. The temporal stability and effects of the environmental temperature on spectral variation in LED output were also investigated, with a requirement for a short (<24 h in all cases) 'burn in' period to stabilise intensity described. Spectral intensity decreased exponentially over approximately 6 min from power up, a result ascribed to an increase in junction temperature as current is passed through the LED. As expected, increase in ambient temperature produced a logarithmic decrease in overall intensity of the LEDs and a linear shift to longer wavelength of the peak emission. This behaviour is consistent with the observed decrease in the  $I_{AD}$  Index ( $A_{670} - A_{720}$ ) with increased ambient temperature, as measured by an instrument based on LED illumination (DA Meter). Several measures could be implemented to mitigate such effects. Changes in peak wavelength and relative intensity are explicable in terms of forward current and temperature and thus predictable if current and temperature are known. Change in illumination intensity and spectral quality could thus be addressed by modelling, given knowledge of current and temperature, or photometric feedback.

The performance of a shadow probe interactance optical geometry was characterised at a range of probe to sample distances. At distances < 30 mm, the ratio of specular to diffuse radiation was < 3%, with slightly higher values noted for kiwifruit compared to apple. This result is consistent with an effect of kiwi skin hairs on light scattering. The specular component increased rapidly at greater distances due to loss of the shadowing effect. Designs with less collimation of the light source were associated with lamp converging rays impacting the shadow area, and thus a greater contribution of specular reflection to the detected signal. Effectively, the umbra size is proportional to lamp-probe distance and shadow probe diameter, and inversely proportional to the lamp diameter, and should be optimised for the application. If partial transmittance (cf. reflectance) is a requirement

of the application, then the contribution of specularly reflected light can be characterised using polarisers.

The ability to transfer calibration models between instruments is imperative for the adoption and widespread use of an NIR spectrometric system. The more spectral similarity is achieved in hardware, i.e. by matching the optical characteristics of the devices, the less chemometric correction is required. Pixel to wavelength assignments for a commercial Si diode array instrument showed errors of up to 2.3 nm. Improvement of wavelength assignment, particularly for the wavelength range used in the PLS regressions, was found to significantly decrease bias and SEP prediction values. Bias may be removed by a simple slope and bias correction. For units of the same model PDA, DSA combined with new wavelengths and model updating gave results comparable to the performance of the master instrument and to models directly developed on the slave instruments. Considering only 10 fruit were used, this is an easy method to transfer calibrations and allows for models to be updated for seasonal changes in samples.

Further work in the development of instrumentation is anticipated, particularly given the continued advances and reduced cost of LEDs and detectors. However, some instrumentation claims are 'ambitious'. Several claims for development of very low cost (<US\$1000) instruments have been made. For example, Tellspec (Food Sensor, Tellspec Inc., Ontario, Canada) claim development of a digital micromirror (MEMS) based device for wavelength selection that operates over the window 900 to 1700 nm with a single InGaAs detector, using two QTH lamps in a reflectance mode, packaged within a palm sized unit. The unit is claimed to be able to "identify calories, macronutrients, allergens, fiber, sugars, and also provide relevant nutritional information such as the glycemic index, with one simple scan." A similar product has been claimed by Consumer Physics (SCiO, Consumer Physics Inc., Israel). However, without an inbuilt system for referencing and with knowledge of the impact of factors such as ambient temperature on lamp and detector behaviours, the operational stability of these units is doubtful. Further, given the known limitations of NIRS, the claimed applications also appear doubtful. These units were successful with crowd sourced funding in 2014-5, but the claimed product release dates of late 2015 has been revised to August/September 2016.

Nonetheless, the excitement generated around these products is indicative of market interest. Another area of 'excitement' is the use of the ubiquitous low cost sensor

platform, the mobile phone, as a base for a spectroscopy system. Several systems are available that exploit the wavelength range of the phone camera CMOS detector (ca 400-1100 nm) by coupling a wavelength dispersive element before the camera lens. However, the 8 bit analogue to digital resolution of the typical phone camera represents a barrier to serious spectroscopic application. Perhaps more likely is the entry of low cost application specific instruments built around use of LEDs with interference filters.

Another area of continued development will be the use of wireless technology, e.g. to reduce instrument cost by using the screen of mobile devices rather than an inbuilt screen, and the use of cloud computing functions (in areas where wifi is adequate to the task). Cloud computing allows for the ability to update models with more data (samples), building a global calibration. This trend is presaged by the Foss networked feed and forage NIRS instruments (RINA, Remote Internet Analysis, FOSS Analytical A/S, Denmark) with use of neural network calibration. New sensor technologies and miniaturisation also show promise for use in fruit grading, including X-ray, magnetic resonance, Raman and Terahertz spectroscopy.

## 8 References

1. "Scopus", Elsevier B.V.: Amsterdam, Netherlands. (2016)
2. W. Herschel, "Experiments on the Refrangibility of the Invisible Rays of the Sun". *Philosophical Transactions of the Royal Society*, **90**, 184 (1800).
3. N. Sheppard, H.A. Willis and J.C. Rigg, "Names, symbols, definitions and units of quantities in optical spectroscopy (Recommendations 1984)", in *Pure and Applied Chemistry*. p. 105. (1985)
4. E.W. Ciurczak, "Principles of Near-Infrared Spectroscopy", in *Handbook of Near-Infrared Analysis*, D.A. Burns and E.W. Ciurczak, Editors., Marcel Dekker Inc: New York. p. 7. (2001)
5. R.M. Eisberg and R. Resnick, "Quantum physics of atoms, molecules, solids, nuclei, and particles". Wiley (1985)
6. F. Siebert and P. Hildebrandt, "Theory of Infrared Absorption and Raman Spectroscopy", in *Vibrational Spectroscopy in Life Science*. Wiley-VCH Verlag GmbH & Co. KGaA. p. 11. (2008)
7. D.N. Sathyanarayana, "Vibrational Spectroscopy: Theory and Applications". New Age International (P) Limited (2015)
8. B.G. Osborne, T. Fearn and P.H. Hindle, "Practical NIR Spectroscopy with Application in Food and Beverage Analysis". 2nd ed. Singapore: Longman Scientific & Technical (1993)
9. D.A. Burns. *NIR without overtone/combination bands?* in *6th International Conference on Near Infrared Spectroscopy NIR-94*. 1994. Lorne, Australia: NIR Spectroscopy Group.
10. C.V. Greensill, "Non-invasive assessment of fruit quality by near-infrared spectroscopy for fruit grading in an in-line setting". Unpublished Doctoral Thesis, *James Goldston Faculty of Engineering and Physical Systems*, (2000).
11. L.M. Harvey, B. McNeil and J.W. Hall, "Near-infrared spectroscopy". *Biopharm*, **Dec**, 38 (2001).
12. W. Kaye, "Near-infrared spectroscopy: I. Spectral identification and analytical applications". *Spectrochimica Acta*, **6**, 257 (1954).

13. "Metrohm Monograph". Metrohm AG: Herisay, Switzerland, [http://www.mep.net.au/wpmp/wp-content/uploads/2013/05/MEP\\_Monograph\\_NIRS\\_81085026EN.pdf](http://www.mep.net.au/wpmp/wp-content/uploads/2013/05/MEP_Monograph_NIRS_81085026EN.pdf) (2016),
14. C.R. Nave. *HyperPhysics*. Crossed Polarizers 2012 [accessed 21 August 2015]; Available from: <http://hyperphysics.phy-astr.gsu.edu/hbase/phyopt/polcross.html#c3>.
15. W. Kaye, C. Canon and R.G. Devaney, "Modification of a Beckman Model DU Spectrophotometer for Automatic Operation at 210–2700 m $\mu$ ". *Journal of the Optical Society of America*, **41**, 658 (1951).
16. F.L. Pedrotti and L.S. Pedrotti, "Introduction to Optics". 2nd ed. New Jersey: Prentice-Hall (1987)
17. M.W. Davidson. *Fundamentals of Light-Emitting Diodes (LEDs)*. Education in Microscopy and Digital Imaging [accessed 14 August 2015]; Available from: <http://zeiss-campus.magnet.fsu.edu/articles/lightsources/leds.html>.
18. *Product Data Sheet 64623HLX*. [Product Data Sheet] 2012 [accessed 24 September 2012]; Available from: [http://www.osram.com/osram\\_com/products/lamps/specialty-lamps/low-voltage-halogen-lamps/low-voltage-halogen-lamps-without-reflector/index.jsp?productId=ZMP\\_1006726](http://www.osram.com/osram_com/products/lamps/specialty-lamps/low-voltage-halogen-lamps/low-voltage-halogen-lamps-without-reflector/index.jsp?productId=ZMP_1006726).
19. C. Hayes, C. Greensill and K. Walsh, "Temporal and environmental sensitivity of a photodiode array spectrophometric system". *Journal of Near Infrared Spectroscopy*, **22**, 297 (2014).
20. V. Giovenzana, R. Civelli, R. Beghi, R. Oberti and R. Guidetti, "Testing of a simplified LED based vis/NIR system for rapid ripeness evaluation of white grape (*Vitis vinifera* L.) for Franciacorta wine". *Talanta*, **144**, 584 (2015).
21. E.F. Schubert and J.N. Miller, "Light-emitting diodes, devices". *Encyclopedia of Electrical & Electronics Engineering*, **11**, 326 (1999).
22. "High Power Top LED specifications", Ushio Epitex Inc.: Kyoto, Japan. (2015)
23. E.d.N. Gaião, et al., "An inexpensive, portable and microcontrolled near infrared LED-photometer for screening analysis of gasoline". *Talanta*, **75**, 792 (2008).
24. A. Fonseca and I.M. Raimundo Jr, "A multichannel photometer based on an array of light emitting diodes for use in multivariate calibration". *Analytica Chimica Acta*, **522**, 223 (2004).

25. G. Veras, et al., "A portable, inexpensive and microcontrolled spectrophotometer based on white LED as light source and CD media as diffraction grid". *Talanta*, **77**, 1155 (2009).
26. J.L. Taylor "Eliminating The Inherent Polarization Artifact Of UV/Vis/NIR Spectrometers". *PerkinElmer UV/Vis/NIR Spectroscopy Resource Page*. PerkinElmer Inc.: Waltham, Massachusetts, USA, [http://pe.taylorjl.net/PE\\_Blog/?p=231](http://pe.taylorjl.net/PE_Blog/?p=231) (2009),
27. *Blazed grating*. 2012 [accessed 23 March 2016]; Available from: [https://commons.wikimedia.org/wiki/File:Blazed\\_grating.svg](https://commons.wikimedia.org/wiki/File:Blazed_grating.svg).
28. "Gratings: Theory and Numeric Application", E. Popov, Editor, Aix Marseille Université: Marseille, France. (2014)
29. *Diffraction Efficiency & Relationship between Diffraction Efficiency and Polarization*. Shimadzu Diffraction Gratings 2016 [accessed 3 March 2016]; Available from: <http://www.shimadzu.com/opt/guide/diffraction/08.html>.
30. B.C. Smith, "Fundamentals of Fourier Transform Infrared Spectroscopy". Taylor & Francis (1995)
31. *Michelson Interferometer Operation*. Fourier Transform Infrared Spectroscopy [accessed 18 March 2016]; Available from: <http://blockeng.com/technology/ftirtechnology.html>.
32. P. Zhao, J.M. Mariotti, P. Léna, V.C.d. Foresto and G. Mazé, "Performance analyses of an infrared single-mode all-fiber-optic Fourier-transform spectrometer". *Applied Optics*, **34**, 4200 (1995).
33. S. Martin, T. Jürgen and F.R. John, "An all-fibre-optic Fourier transform spectrometer". *Measurement Science and Technology*, **7**, 1619 (1996).
34. P. Stchur, D. Cleveland, J. Zhou and R.G. Michel, "A review of recent applications of near infrared spectroscopy, and of the characteristics of a novel PbS CCD array-based near-infrared spectrometer". *Applied Spectroscopy Reviews*, **37**, 383 (2002).
35. C. McFee. *An introduction to CCD operation*. [accessed 10 March 2016]; Available from: [http://www.mssl.ucl.ac.uk/www\\_detector/ccdgroup/opttheory/ccdoperation.html](http://www.mssl.ucl.ac.uk/www_detector/ccdgroup/opttheory/ccdoperation.html).
36. *Monolithic Miniature Spectrometer (MMS)*. [Internet Document] 2016 [accessed 26 February 2016]; Available from:

- [http://www.zeiss.com/spectroscopy/en\\_de/products/spectrometer-modules/monolithic-miniature-spectrometer-mms.html#specification](http://www.zeiss.com/spectroscopy/en_de/products/spectrometer-modules/monolithic-miniature-spectrometer-mms.html#specification).
37. Zeiss. *MMS1 Monolithic Miniature-Spectrometer : Product Information*. [Internet Document] 2005 [accessed 16 October 2005]; Available from: <http://www.zeiss.de>.
  38. *USB2000+VIS-NIR-ES*. Modular Spectrometers 2016 [accessed 23 March 2016]; Available from: <http://oceanoptics.com/product/usb2000vis-nir-es/>.
  39. *MMS1 Monolithic Miniature-Spectrometer : Product Information*. [Internet Document] [accessed 16 October 2005]; Available from: <http://www.zeiss.de>.
  40. *Flame and USB Series Custom Configured Gratings and Wavelength Range*. [accessed 10 March 2016].
  41. B.A. Rock. *An Introduction to Chemometrics*. 1997 [accessed 5 February 2005]; Available from: [http://home.neo.rr.com/catbar/chemo/chem\\_txt.htm](http://home.neo.rr.com/catbar/chemo/chem_txt.htm).
  42. A. Savitzky and M.J.E. Golay, "Smoothing and Differentiation of Data by Simplified Least Squares Procedures". *Analytical Chemistry*, **36**, 1627 (1964).
  43. H. Martens and T. Næs, "Multivariate calibration". John Wiley & Sons (1992)
  44. T. Næs, T. Isaksson, T. Fearn and D. Davies, "A User-friendly Guide to Multivariate Calibration and Classification". Chichester, UK: NIR Publications (2002)
  45. "ASTM E1655-05", in *Standard Practices for Infrared Multivariate Quantitative Analysis*, ASTM International: West Conshohocken, PA, USA. (2005)
  46. R. De Maesschalck, D. Jouan-Rimbaud and D.L. Massart, "The Mahalanobis distance". *Chemometrics and Intelligent Laboratory Systems*, **50**, 1 (2000).
  47. H. Hotelling, "Analysis of a complex of statistical variables into principal components". *Journal of Educational Psychology*, **24**, 417 (1933).
  48. H. Hotelling, "The Generalization of Student's Ratio". 360 (1931).
  49. D. Jouan-Rimbaud, E. Bouveresse, D.L. Massart and O.E. de Noord, "Detection of prediction outliers and inliers in multivariate calibration". *Analytica Chimica Acta*, **388**, 283 (1999).
  50. R.D. Cook and S. Weisberg, "Residuals and influence in regression". (1982).
  51. E.-L. Bergman, H. Brage, M. Josefson, O. Svensson and A. Sparen, "Transfer of NIR calibrations for pharmaceutical formulations between different instruments". *Journal of Pharmaceutical and Biomedical Analysis*, **41**, 89 (2006).

52. T.B. Blank, S.T. Sum, S.D. Brown and S.L. Monfre, "Transfer of near-infrared multivariate calibrations without standards". *Analytical Chemistry*, **68**, 2987 (1996).
53. M. Blanco, J. Coello, H. Iturriaga, S. Maspoch and E. Rovira, "Wavelength calibration transfer between diode array uv-visible spectrophotometers". *Applied Spectroscopy*, **49**, 593 (1995).
54. E. Bouveresse, C. Casolino and C. de la Pezuela, "Application of standardisation methods to correct the spectral differences induced by a fibre optic probe used for the near-infrared analysis of pharmaceutical tablets". *Journal of Pharmaceutical & Biomedical Analysis*, **18**, 35 (1998).
55. E. Bouveresse, C. Hartmann, D.L. Massart, I.R. Last and K.A. Prebble, "Standardization of near-infrared spectrometric instruments". *Analytical Chemistry*, **68**, 982 (1996).
56. E. Bouveresse and D.L. Massart, "Improvement of the piecewise direct standardisation procedure for the transfer of NIR spectra for multivariate calibration". *Chemometrics and Intelligent Laboratory Systems*, **32**, 201 (1996).
57. E. Bouveresse, D.L. Massart and P. Dardenne, "Calibration transfer across near-infrared spectrometric instruments using shenks algorithm - effects of different standardisation samples". *Analytica Chimica Acta*, **297**, 405 (1994).
58. E. Bouveresse, D.L. Massart and P. Dardenne, "Modified algorithm for standardization of near-infrared spectrometric instruments". *Analytical Chemistry*, **67**, 1381 (1995).
59. O.E. de Noord, "Multivariate calibration standardization". *Chemometrics and Intelligent Laboratory Systems*, **25**, 85 (1994).
60. F. Despagne, D.L. Massart, M. Jansen and H. van Daalen, "Intersite transfer of industrial calibration models". *Analytica Chimica Acta*, **406**, 233 (2000).
61. F. Despagne, B. Walczak and D.L. Massart, "Transfer of calibrations of near-infrared spectra using neural networks". *Applied Spectroscopy*, **52**, 732 (1998).
62. E. Dreassi, G. Ceramelli, P.L. Perruccio and P. Corti, "Transfer of calibration in near-infrared reflectance spectrometry". *Analyst*, **123**, 1259 (1998).
63. L. Duponchel, C. Ruckebusch, J.P. Huvenne and P. Legrand, "Standardisation of near infrared spectrometers using artificial neural networks". *Journal of Near Infrared Spectroscopy*, **7**, 155 (1999).

64. T. Fearn, "Standardisation and calibration transfer for near infrared instruments: a review". *Journal of Near Infrared Spectroscopy*, **9**, 229 (2001).
65. T. Fearn, C. Eddison, R. Withey and I.A. Cowe, "A method for wavelength standardisation in filter instruments". *Journal of Near Infrared Spectroscopy*, **4**, 111 (1996).
66. P. Geladi, et al., "Calibration transfer for predicting lake-water pH from near infrared spectra of lake sediments". *Journal of Near Infrared Spectroscopy*, **7**, 251 (1999).
67. H. Leion, S. Folestad, M. Josefson and A. Sparen, "Evaluation of basic algorithms for transferring quantitative multivariate calibrations between scanning grating and FT NIR spectrometers". *Journal of Pharmaceutical and Biomedical Analysis*, **37**, 47 (2005).
68. D. Perez-Marin, A. Garrido-Varo and J.E. Guerrero-Ginel, "Remote near infrared instrument cloning and transfer of calibrations to predict ingredient percentages in intact compound feedstuffs". *Journal of Near Infrared Spectroscopy*, **14**, 81 (2006).
69. J.S. Shenk and M.O. Westerhaus, "New Standardization and Calibration Procedures for Nirs Analytical Systems". *SO - Crop Science*. 31(6). 1991. 1694-1696., (1991).
70. J.S. Shenk and M.O. Westerhaus. *Comparison of standardisation techniques*. in *7th International Conference on Near Infrared Spectroscopy*. 1995. Montreal: NIR Publications.
71. J. Sjöblom, O. Svensson, M. Josefson, H. Kullberg and S. Wold, "An evaluation of orthogonal signal correction applied to calibration transfer of near infrared spectra". *Chemometrics & Intelligent Laboratory Systems*, **44**, 229 (1998).
72. Q. Wang, S. Dejesus, J.P. Conzen, A. Schmidt and H. Weiler, "Calibration transfer for NIR analysis of liquids and solids". *Journal of Near-Infrared Spectroscopy*, **6**, A201 (1998).
73. Y. Wang and B.R. Kowalski, "Temperature-compensating calibration transfer for near-infrared filter instruments". *Analytical Chemistry*, **65**, 1301 (1993).
74. Y. Wang, M.J. Lysaght and B.R. Kowalski, "Improvement of multivariate calibration through instrument standardization". *Analytical Chemistry*, **64**, 562 (1992).

75. Y. Wang, K.J. Veltkamp and B.R. Kowalski, "Multivariate instrument standardisation". *Analytical Chemistry*, **63**, 2750 (1991).
76. Z.Y. Wang, T. Dean and B.R. Kowalski, "Additive background correction in multivariate instrument standardization". *Analytical Chemistry*, **67**, 2379 (1995).
77. C.V. Greensill, P.J. Wolfs, C.H. Spiegelman and K.B. Walsh, "Calibration transfer between PDA-based NIR spectrometers in the NIR assessment of melon soluble solids content". *Applied Spectroscopy*, **55**, 647 (2001).
78. B.G. Osborne and T. Fearn, "Collaborative evaluation of universal calibrations for the measurement of protein and moisture in flour by near infrared reflectance". *Journal of Food Technology*, **18**, 453 (1983).
79. J.A. Jones, I.R. Last, B.F. MacDonald and K.A. Prebble, "Development and transferability of near-infrared methods for determination of moisture in a freeze dried injection product". *Journal of Pharmaceutical & Biomedical Analysis*, **11**, 1227 (1993).
80. J.S. Shenk and M.O. Westerhaus, "Optical Instrument System Calibration": US. (1989)
81. B.M. Wise and N.B. Gallagher. *Double Window Piece-wise Direct Standardization*. in *Federation of Analytical Chemistry and Spectroscopy Societies*. 1998. Austin, Texas.
82. S. Wold, H. Antti, F. Lindgren and J. Ohman, "Orthogonal signal correction of near-infrared spectra". *Chemometrics and Intelligent Laboratory Systems*, **44**, 175 (1998).
83. S. Wold, H. Antti, F. Lindgren and J. Ohman, "Orthogonal signal correction of near-infrared spectra". *Chemometrics & Intelligent Laboratory Systems*, **44**, 175 (1998).
84. T. Fearn, "On orthogonal signal correction". *Chemometrics & Intelligent Laboratory Systems*, **50**, 47 (2000).
85. C.A. Andersson, "Direct orthogonalization". *Chemometrics and Intelligent Laboratory Systems*, **47**, 51 (1999).
86. J.A. Westerhuis, S. de Jong and A.K. Smilde, "Direct orthogonal signal correction". *Chemometrics and Intelligent Laboratory Systems*, **56**, 13 (2001).
87. J. Trygg and S. Wold, "Orthogonal projections to latent structures (O-PLS)". *Journal of Chemometrics*, **16**, 119 (2002).

88. B. Walczak, E. Bouveresse and D.L. Massart, "Standardization of near-infrared spectra in the wavelet domain". *Chemometrics & Intelligent Laboratory Systems*, **36**, 41 (1997).
89. S.G. Mallat, "A theory for multiresolution signal decomposition: the wavelet representation". *Pattern Analysis and Machine Intelligence, IEEE Transactions on*, **11**, 674 (1989).
90. S.J. Russell and P. Norvig, "Artificial Intelligence a modern approach". Second ed. Sydney: Pearson Educational Inc. (2003)
91. R. Goodacre, et al., "On mass spectrometer instrument standardization and interlaboratory calibration transfer using neural networks". *Analytica Chimica Acta*, **348**, 511 (1997).
92. K.B. Walsh, J.A. Guthrie and J. Burney, "Application of commercially available, low-cost, miniaturised NIR spectrometers to the assessment of the sugar content of intact fruit". *Australian Journal of Plant Physiology*, **27**, 1175 (2000).
93. S.T. Henderson and A.M. Marsden, "Lamps and Lighting". 2nd ed. London: Edward Arnold (Publishers) Ltd (1979)
94. H.D. Young and R.A. Freedman, "University Physics with Modern Physics". 10 ed. Sydney: Addison-Wesley Publishing Company (2000)
95. J. Wilson and J.F.B. Hawkes, "Optoelectronics : an introduction". 2 ed. New York, USA: Prentice-Hall Inc. (1989)
96. P. Martinsen, V.A. McGlone, R.B. Jordan and P. Gaastra, "Temporal sensitivity of the wavelength calibration of a photodiode array spectrometer". *Appl Spectrosc*, **64**, 1325 (2010).
97. C.V. Greensill and K.B. Walsh, "A remote acceptance probe and illumination configuration for spectral assessment of internal attributes of intact fruit". *Measurement Science & Technology*, **11**, 1674 (2000).
98. *Product Data Sheet 521995*. 2012 [accessed 24 February 2012]; Product Data]. Available from: <http://sla.net.au/content/521995>.
99. C.R. Nave. *HyperPhysics*. Heat and Thermodynamics [Internet site] 2014 [accessed 17/1/2014 2014]; Available from: <http://hyperphysics.phy-astr.gsu.edu/hbase/kinetic/relhum.html#c4>.
100. *Gas mixture spectra*. [accessed 17 February 2014 2014]; Available from: <http://hitran.iao.ru/gasmixture/spectr>.

101. W. Wang and J. Paliwal, "Near-infrared spectroscopy and imaging in food quality and safety". *Sensing and Instrumentation for Food Quality and Safety*, **1**, 193 (2007).
102. P. Butz, C. Hofmann and B. Tauscher, "Recent Developments in Noninvasive Techniques for Fresh Fruit and Vegetable Internal Quality Analysis". *Journal of Food Science*, **70**, R131 (2005).
103. P. Leisher, et al. *High-performance wavelength-locked diode lasers*. in *High-Power Diode Laser Technology and Applications VII*. 2009.
104. E.F. Schubert, "Light-Emitting Diodes". Cambridge University Press (2006)
105. Y.P. Varshni, "Temperature dependence of the energy gap in semiconductors". *Physica*, **34**, 149 (1967).
106. G. Yu, P. Kai-lin, R. Guo-tao, C. Shu-jing and Y. Fei. *Research on LED temperature characteristic and thermal analysis at low temperatures*. in *Electronic Packaging Technology and High Density Packaging (ICEPT-HDP), 2012 13th International Conference on*. 2012.
107. W. Guo, et al., "Characteristics of high power LEDs at high and low temperature". *Journal of Semiconductors*, **32**, 044007 (2011).
108. S. Chhajed, et al. *Junction temperature in light-emitting diodes assessed by different methods*. in *SPIE - Light-Emitting Diodes: Research, Manufacturing, and Applications IX*. 2005.
109. "LED Luminaire Lifetime: Recommendations for Testing and Reporting", U.S.D.o. Energy, Editor, U. S. Department of Energy. p. 30. (2011)
110. T. Nägele, "White Light LEDs – Importance of Accepted Measurement Standards", in *LED professional Review*, Luger Research e.U.: Dornbirn, Austria. p. 5. (2008)
111. Z.Z. Chen, et al., "Study on the stability of the high-brightness white LED". *physica status solidi (b)*, **241**, 2664 (2004).
112. N. Narendran and Y. Gu, "Life of LED-Based White Light Sources". *Journal of Display Technology*, **1**, 167 (2005).
113. G. Meneghesso, et al., "Failure Modes and Mechanisms of DC-Aged GaN LEDs". *physica status solidi (a)*, **194**, 389 (2002).
114. J. Malinen, M. Käsäkoski, R. Rikola and C.G. Eddison, "LED-based NIR spectrometer module for hand-held and process analyser applications". *Sensors and Actuators B: Chemical*, **51**, 220 (1998).

115. P.K. Dasgupta, I.-Y. Eom, K.J. Morris and J. Li, "Light emitting diode-based detectors: Absorbance, fluorescence and spectroelectrochemical measurements in a planar flow-through cell". *Analytica Chimica Acta*, **500**, 337 (2003).
116. G.S. Birth and K.H. Norris. *An instrument using light transmittance for nondestructive measurement of fruit maturity*. in *Eighteenth annual meeting of the institute of food technologists*. 1958. Chicago, Illinois.
117. S. Kawano, H. Watanabe and M. Iwamoto, "Determination of sugar content in intact peaches by near infrared spectroscopy with fibre optics in interactance mode". *Journal of the Japanese Society for Horticultural Science*, **61**, 445 (1992).
118. R. Long, K. Walsh and C. Greensill, "Sugar "imaging" of fruit using a low cost charge-coupled device camera". *Journal of Near Infrared Spectroscopy*, **13**, 177 (2005).
119. K. Shafie, R. Künnemeyer, A. McGlone, S. Talele and V. Vetrova, "An optimised six-wavelength model for predicting kiwifruit dry matter". *Journal of Near Infrared Spectroscopy*, **23**, 103 (2015).
120. *CP Data Sheet*. [accessed 9 February 2016]; Available from: <http://www.cp-info.de/datenblatt.htm>.
121. U. Praeger, M. Linke, R. Jedermann, A. Moehrke and M. Geye, "Effect of storage climate on green-life duration of bananas", in *5th International Workshop Cold Chain Management*, University of Bonn: Bonn. (2013)
122. B. Seifert, M. Pflanz and M. Zude, "Spectral shift as advanced index for fruit chlorophyll breakdown". *Food and Bioprocess Technology*, **7**, 2050 (2013).
123. K.P. Rutkowski, B. Michalczuk and P. Konopacki, "Nondestructive determination of 'Golden Delicious' apple quality and harvest maturity". *Journal of Fruit and Ornamental Plant Research*, **16**, 39 (2008).
124. V. Geraudie, et al. *A revolutionary device for predicting grape maturity based on NIR spectrometry*. in *FRUTIC 09, 8th Fruit Nut and Vegetable Production Engineering Symposium*. 2009. Concepcion, Chile.
125. V. Ziosi, et al., "A new index based on vis spectroscopy to characterize the progression of ripening in peach fruit". *Postharvest Biology and Technology*, **49**, 319 (2008).
126. *Discover the DA Meter*. 2016 [accessed 10 March 2016]; Available from: <http://www.trturo.com/en/content/8-da-meter>.

127. K. Walsh, M. Golic and C. Greensill, "Sorting of fruit using near infrared spectroscopy: application to a range of fruit and vegetables for soluble solids and dry matter content". *Journal of Near Infrared Spectroscopy*, **12**, 141 (2004).
128. M.R. Robinson, "Apparatus and method for determination of the adequacy of dialysis by non-invasive near-infrared spectroscopy", Google Patents: USA. (2003)
129. S. Upstone "Validating UV/Visible Spectrophotometers". *Technical Note*. PerkinElmer, Inc: Waltham, MA, USA 12, [https://www.perkinelmer.com/CMSResources/Images/44-136839TCH\\_Validating\\_UV\\_Visible.pdf](https://www.perkinelmer.com/CMSResources/Images/44-136839TCH_Validating_UV_Visible.pdf) (2012),
130. R.R. Alfano and S.G. Demos, "Imaging of objects based upon the polarization or depolarization of light", Google Patents: USA. (1998)
131. H. Yi, "Detecting semi-specular reflection component from a sequence of images", University of Maryland at College Park. p. 18. (2007)
132. V. Backman, et al., "Polarized light scattering spectroscopy for quantitative measurement of epithelial cellular structures in situ". *IEEE Journal of Selected Topics in Quantum Electronics*, **5**, 1019 (1999).
133. A. Andrew and T. Fearn, "Transfer by orthogonal projection: making near-infrared calibrations robust to between-instrument variation". *Chemometrics and Intelligent Laboratory Systems*, **72**, 51 (2004).
134. A. Soldado, T. Fearn, A. Martínez-Fernández and B. de la Roza-Delgado, "The transfer of NIR calibrations for undried grass silage from the laboratory to on-site instruments: Comparison of two approaches". *Talanta*, **105**, 8 (2013).
135. B. Igne, J.-M. Roger, S. Roussel, V. Bellon-Maurel and C.R. Hurburgh, "Improving the transfer of near infrared prediction models by orthogonal methods". *Chemometrics and Intelligent Laboratory Systems*, **99**, 57 (2009).
136. Y. Roggo, L. Duponchel, B. Noe and J.P. Huvenne, "Sucrose content determination of sugar beets by near infrared reflectance spectroscopy. Comparison of calibration methods and calibration transfer". *Journal of Near Infrared Spectroscopy*, **10**, 137 (2002).
137. M.C. Alamar, E. Bobelyn, J. Lammertyn, B.M. Nicolai and E. Molto, "Calibration transfer between NIR diode array and FT-NIR spectrophotometers for measuring the soluble solids contents of apple". *Postharvest Biology and Technology*, **45**, 38 (2007).

138. L. Salguero-Chaparro, B. Palagos, F. Peña-Rodríguez and J.M. Roger, "Calibration transfer of intact olive NIR spectra between a pre-dispersive instrument and a portable spectrometer". *Computers and Electronics in Agriculture*, **96**, 202 (2013).
139. M.O. Westerhaus, "Improving repeatability of NIR calibrations across instruments", in *Third international conference on Near Infrared Spectroscopy*, R. Biston and N. Bartiaux-Thill, Editors: Brussels, Belgium. p. 671. (1990)
140. S. Saranwong and S. Kawano, "A simple method of instrument standardisation for a near infrared sorting machine: the utilisation of average spectra as input vectors". *Journal of Near Infrared Spectroscopy*, **12**, 359 (2004).
141. C.V. Greensill and K.B. Walsh, "Calibration transfer between miniature photodiode array-based spectrometers in the near infrared assessment of mandarin soluble solids content". *Journal of Near Infrared Spectroscopy*, **10**, 27 (2002).
142. A.I.A. Measurements. *Brochure - MB FT-NIR laboratory Spectrometer*. 2013 [accessed 16/7/2015 2015]; Available from: <http://new.abb.com/products/measurement-products/analytical/ft-ir-and-ft-nir-analyzers/laboratory-spectrometers/mb3600>.
143. P.J. Brimmer and F.A. DeThomas, "Stability of NIR instrumentation: Control of critical parameters affecting analytical precision and transferability of NIR calibrations", in *Making Light Work: Advances in Near Infrared Spectroscopy*, I. Murry and I.A. Cowe, Editors., VCH Publishers: New York. p. 35. (1991)
144. Zeiss, "Test Certificate", Carl Zeiss Jena GmbH: Jena. (2002)
145. J.E. Sansonetti and W.C. Martin, "Handbook of Basic Atomic Spectroscopic Data", National Institute of Standards and Technology: Gaithersburg, MD, USA. (2009)
146. M. Blanco and I. Villarroya, "NIR spectroscopy: a rapid-response analytical tool". *TrAC Trends in Analytical Chemistry*, **21**, 240 (2002).
147. G.S. Birth, G.G. Dull, W.T. Renfroe and S.J. Kays, "Non-destructive spectrophotometric determination of dry matter in onions". *Journal of the American Society for Horticultural Science*, **110**, 297 (1985).
148. S. Kawano, T. Fujiwara and M. Iwamoto, "Nondestructive Determination of Sugar Content in Satsuma Mandarin using Near Infrared (NIR) Transmittance". *Journal of the Japanese Society for Horticultural Science*, **62**, 465 (1993).

## DECLARATION OF CO-AUTHORSHIP AND CONTRIBUTION

Title of Paper	The Impact of Lamp Environment on Prediction of Peach TSS Content
Full bibliographic reference for Journal/Book in which the Paper appears	C.J. Hayes, K.B. Walsh and C.V. Greensill. <i>The impact of lamp environment on prediction of peach TSS content.</i> in <i>XXIX International Horticultural Congress on Horticulture: Sustaining Lives, Livelihoods and Landscapes (IHC2014): International Symposia on Abscission Processes in Horticulture and Non-Destructive Assessment of Fruit Attributes.</i> 2016. Brisbane, Australia: International Society for Horticultural Science (ISHS), Leuven, Belgium.
Status	Published

Nature of Candidate's Contribution

All experimental work and analysis

Nature of Co-Authors' Contributions

Supervision

Candidate's Declaration

*I declare that the publication above meets the requirements to be included in the thesis as outlined in the Publication of Research Higher Degree Work for Inclusion in the Thesis Procedures*

*Signature*

*Date*

31 March 2016

## 9 Appendix A

### **The Impact of Lamp Environment on Prediction of Peach TSS Content<sup>5</sup>**

C.J. Hayes, K.B. Walsh and C.V. Greensill

#### **Abstract**

**The implementation of NIRS in horticulture involves translation of a laboratory technique to packhouse and field conditions. Reference measurements are often difficult and inconvenient, therefore taken periodically. The variation in halogen lamp output with change in ambient temperature and lamp age, the later both in the short term (from lamp power up) and long term (warm up time and longevity) is documented. The impact of such changes on predictive performance (RMSEP and bias of a PLS model) for estimation of Brix content in intact peaches is evaluated. Some lamps demonstrated an initial ‘burn in’ period from first initial use, differing in length from 40 to 220 min. Long term drifts in lamp output over an eight month period caused bias changes of as much as 5 Brix units in model predictions. The implications for practical use of this technology are discussed.**

#### **INTRODUCTION**

The stability of the light source and near infrared (NIR) detector system can be affected by several factors, including ambient temperature. This in turn can affect the precision of an NIR instrument. Typical protocols for near infrared spectrometric (NIRS) systems require halogen lamps 1-2 h to stabilise before use and white reference measurements to be acquired before each sample measurement. However, many in-line applications that employ NIRS systems involve scanning of numerous samples (fruit) each second, making reference measurements difficult and inconvenient. Most systems take references only periodically, often after extended periods. Portable instruments may require measurements to be taken quickly, to minimize measurement time and power use.

Ambient temperatures can vary by 50 °C or more, affecting light source intensity and quality, detector response (sensitivity), and electronic noise and readout of the front

---

<sup>5</sup> This appendix has been published under this title in the proceedings of The 29<sup>th</sup> International Horticultural Congress Symposia 2014, Brisbane. It extends the analysis in chapter 3 of QTH lamp stability during warm up, to sub second time frames during the first few seconds of power on.

end electronics (FEE) (Greensill, 2000; Walsh, et al., 2000; Zeiss, 2005). Such changes can have a detrimental effect on predictive model performance. A past reference measurement may no longer be representative of current conditions, thus guidelines on frequency of reference measurements need to be established to ensure and maintain optimal system performance.

Quartz tungsten halogen (QTH) lamps are employed by most dispersive and interferometric spectroscopic systems. A QTH lamp has a low pressure halogen gas and a tungsten filament within a quartz glass envelope. In operation, tungsten sublimates from the filament, combines with the halogen gas but is then deposited back on the filament. QTH lamp filaments typically operate at 2600 to 3200 °C (Henderson and Marsden, 1979). However, as the tungsten deposited back to the filament is crystalline and brittle and thus fragile. The expected life of a QTH lamp is 2000 - 3000 h, although instrument grade lamp life may exceed 10,000 h (Osborne, et al., 1993).

The objective of the current study was to model the spectral variation of QTH lamps with respect to elapsed time from power up and variation in environmental temperature.

## **MATERIALS AND METHODS**

### **Lamp Spectral Variation with Time and Environmental Temperature**

This study utilised 20 x 12 V 100 W GY6.35 QTH Lamps, with ten each of OSRAM HLX64623 (OSRAM A.G) and Sylvania 521995 (Sylvania Lighting Australasia Pty Ltd.). The QTH lamps were located at the focal point of a parabolic reflector to produce a collimated beam of light, and a detector optical probe located in the centre of this light beam, casting a shadow onto the sample (Greensill and Walsh, 2000) (see Fig1). A Zeiss MMS1 NIR Enhanced (Carl Zeiss GmbH, Jena, Germany) was used in acquisition of spectra of a white teflon tile.

With the light source, parabolic reflector, and Teflon tile housed in a Contherm 5200HS environmental chamber (Contherm Scientific Limited, Petone, New Zealand) at 30 °C and 50% RH, spectra were acquired at ten second intervals over 4 h from initial power up. The spectrometer was located outside the chamber, at  $22.5 \pm 1$  °C. In another exercise, with all components at  $22.5 \pm 3$  °C, measurements were acquired at 24 ms intervals over a period of 5 min after initial power up, and then at 10 min intervals over 8 months of continual use, or until lamp failure.

To assess the effect of environmental temperature on lamp spectra, the temperature of the lamp assembly was increased in 10 °C steps from 10 to 60 °C, with 1 h stabilisation between temperatures.

### **Assessment of Predictive Performance**

An assessment of the effect of lamp spectral variation was made using ‘actual’ predictive performance measures. Peach spectra (n=72) were collected using an ‘InSight’ (MAF Oceania) in-line unit, operating at 7 fruit per second in a commercial packhouse. This unit (see Fig. 1) uses the optical configuration described above. Fruit total soluble solids (TSS) was assessed of juice squeezed from a 2 cm diameter, 1 cm deep core of fruit taken at the point of spectral acquisition. PLS models for TSS were based on second derivative absorbance spectra, interpolated to 2 nm. Calibration statistics were: n=72, PC=4,  $\mu=13.6$   $\sigma=1.887$ ,  $R^2=0.966$ , RMSEC=0.347, RMSECV=0.423, SDR=5.441.

The effect of changing the white reference used in calculation of the peach absorbance spectra for those acquired at different times from lamp power up was explored. PLS models were redeveloped using the average of the last ten measurements over the 4 h period as the white reference (lamp output was considered stable at this extended time point). The data set was then iteratively reconstituted with the white tile measurements taken over the 4 h period, and the predictive performance of the model reassessed, simulating the taking of a white reference at the new time point.

This procedure was repeated for the measurements acquired at 10 min intervals over a period of 8 months or until failure (lamp lifetime), with the model developed using an averaged ten measurements at the 4 hour period. The procedure was also repeated for the measurements acquired at 24 ms intervals over a period of 5 min after initial power up, using single white measurements, in line with hand held (‘F-750’, Felix Instruments, Washington) design parameters.

The assessment of lamp spectral variation with temperature was performed similar to the above. The PLS predictive models were redeveloped using the new white reference acquired with the lamp ambient temperature of 10 °C, and used for prediction on spectra redeveloped using the white reference acquired with the lamp at a range of temperatures. As before, the average of ten measurements taken at each temperature setting was used.

## Chemometrics

PLS regression models were developed using MATLAB R2012b (MathWorks Inc., Natick, USA) with PLS toolbox 6.7 (Eigenvector Research Inc., Wenatchee, USA). The wavelength range used was 730-930 nm. Model performance was assessed in terms of calibration  $R^2$ , root mean square error of cross validation (RMSECV) based on full cross validation, and the ratio of SD to RMSECV (SDR). Prediction performance was assessed in terms of root mean square error of prediction (RMSEP) and bias corrected RMSEP (SEP-b).

$$\text{Bias can be calculated as: } \textit{bias} = \sqrt{\textit{RMSEP}^2 - \textit{SEP}_{-b}^2} \quad \text{Equation 1}$$

When the white reference used for calculation of absorbance for a set of spectra is changed, the effect on a PLS regression model prediction will be to change the bias of the model, with no effect on SEP-b. This bias could be calculated by multiplying the second derivative of the absorbance spectrum of the new white tile measurement (using the original white measurement as reference) by the coefficients of the model. However, RMSEP data is presented, with the minimum RMSEP in the plots being equivalent to that of the original model, to illustrate the importance of the error to the model prediction.

## RESULTS AND DISCUSSION

### Stonefruit TSS PLS regression models

The population (n=72) of fruit used had a mean TSS of 9.7 and SD 0.62 %TSS. The PLS regression models developed on the spectra as received from the in-line grading unit achieved a root mean square error of calibration (RMSEC) of 0.347, RMSECV of 0.423 %TSS and  $R_{cv}^2$  of 0.966.

### Lamp spectral variation with time

Initial examination of the spectral output of all lamps at 10 s increments over the 4 h period showed that generally, the lamp intensity stabilised after approximately 40 min (Fig. 2).

The predictive performances of the calibration models were assessed, as described above. Plots of RMSEPs as a function of times of the 60 trials showed two distinct lamp start-up behaviours:

- 4 lamps from Osram and 3 from Sylvania displayed improvements in RMSEP values from start up (an initial warm up period) - but only on their first trial (see Fig. 3). This result was interpreted as evidence of lamps requiring an initial “burn in” period from new and requires further investigation. The length of the warm up period was not consistent across the seven lamps, varying from 20 to 220 min.
- In general (all other trials), there was no improvement from the initial 10 s measurement following start up (see Fig. 3).

Analysis of the data showed that for nearly every trial (except those noted in the first dot point above), there was no statistical improvement past the first white reference measurement, made ten seconds after power up, for models using second derivative absorbance data.

The performance of each lamp and manufacturer was compared using the mean RMSEP and SDR of relative reconstructed prediction sets. All outcomes compared favourably with the RMSECV and SDR of the original model. One way ANOVA analyses of the mean RMSEP values showed no statistically significant difference between any trials or between the manufacturers at  $\alpha=0.01$

Spectra acquired every 24 ms during the initial power up plateaued in raw intensity at approximately 800 ms, followed by a gradual decrease (Fig. 2). However, the predictive performances (Fig. 4) of the calibration models plateau at approximately 350-400 ms. Thus, while peak spectral intensity may not have been reached in this time period, spectral quality has stabilised, such that there is no impact absorbance second derivative based models.

For measurements acquired over the lamp lifetime, lamp output was remarkably stable until filament breakage. Some lamps showed no ageing apparent in spectra through to filament breakage, while others demonstrated change in the last minutes to hours of lamp life (data not shown), with no effect on RMSEP values. Of the seven lamps trialled, one lamp lasted only for approximately 520 h, while all others outlasted the manufacturers' specifications of 1500 and 3000 h (Osram and Sylvania, respectively).

The effect of lamp age across 90 days (2000 h) on regression model prediction varied greatly across the 60 trials, demonstrating lamp individuality (Fig. 4). Some lamps were quite stable over the period, others showed instability. This instability could be due to imperfections or contaminants in the filament and/or halogen gas. The performance of

these lamps was still acceptable during the 4 hr trials, highlighting the need for regular referencing.

### **Lamp Spectral Variation with Environmental Temperature**

Initial examination of the spectral output of the QTH lamps showed that generally the spectral intensity of the lamps decreased with increasing temperature, but no spectral intensity variation over the wavelength range 720 - 930 nm (the range used in Brix PLS model) was observed.

No pattern was evident in any increase or decrease in RMSEP values with temperature. All RMSEP and SDR values were consistent with results from the lamp spectral variation with time. The result indicated that the spectral variation resulting from changes in lamp output with ambient temperature (Fig. 5) did not affect the predictive performance due to the second derivative absorbance pre-treatment.

### **CONCLUSIONS**

Lamp output was spectrally stable within 400 ms, although total illumination was not stable until approximately 40 min from start-up. Thus, performance of the predictive models based on second derivative of absorbance data was not impacted by lamp warm-up time. Noise on measurement (single white reference) accounted for a mean increase in RMSEP as high as 0.22 and individual increases high as 0.82, which may affect performance of models with a low SDR. However, using averages of white reference measurements significantly improved performance. When predictive models were developed using second derivative absorbance data and averaged (10) white references, there was no statistically significant impact in RMSEPs on time of lamp warm-up (after 10s), even during the last hours of lamp life.

Some lamps displayed start-up output characteristics on their first trial, which was not repeated in subsequent trials. This result indicates the need for a short lamp 'burn in' period of up to two hours, indicative of the need for quality assurance strategies being developed for processes which have tight performance requirements.

Spectral variation, resulting from ambient temperature changes on the lamp, also affected lamp output quantity rather than quality and thus did not affect the predictive performance due to the second derivative absorbance pre-treatment.

## ACKNOWLEDGEMENTS

We acknowledge funding support of our laboratory from Horticultural Australia Ltd. An expanded version of this work, including consideration of the effect of temperature on electronics and detector, will appear in the Journal of Near Infrared Spectroscopy.

## Literature Cited

- Greensill, C.V. (2000). Non-invasive assessment of fruit quality by near-infrared spectroscopy for fruit grading in an in-line setting Unpublished Doctoral Thesis, Central Queensland University.
- Walsh, K.B., et al. (2000). Application of commercially available, low-cost, miniaturised NIR spectrometers to the assessment of the sugar content of intact fruit. *Australian Journal of Plant Physiology* 27: 1175-1186.
- MMS1 Monolithic Miniature-Spectrometer : Product Information. Retrieved 16 October, 2005, from [http:// www.zeiss.de](http://www.zeiss.de).
- Henderson, S.T. and Marsden, A.M. (1979). *Lamps and Lighting*. London, Edward Arnold (Publishers) Ltd.
- Osborne, B.G., et al. (1993). *Practical NIR Spectroscopy with Application in Food and Beverage Analysis*. Singapore, Longman Scientific & Technical.
- Young, H.D. and Freedman, R.A. (2000). *University Physics with Modern Physics*. Sydney, Addison-Wesley Publishing Company.
- Pedrotti, F.L. and Pedrotti, L.S. (1987). *Introduction to Optics*. New Jersey, Prentice-Hall.
- Wilson, J. and Hawkes, J.F.B. (1989). *Optoelectronics : an introduction*. New York, USA, Prentice-Hall Inc.
- Greensill, C.V. and Walsh, K.B. (2000). A remote acceptance probe and illumination configuration for spectral assessment of internal attributes of intact fruit. *Measurement Science & Technology* 11(12): 1674-1684.

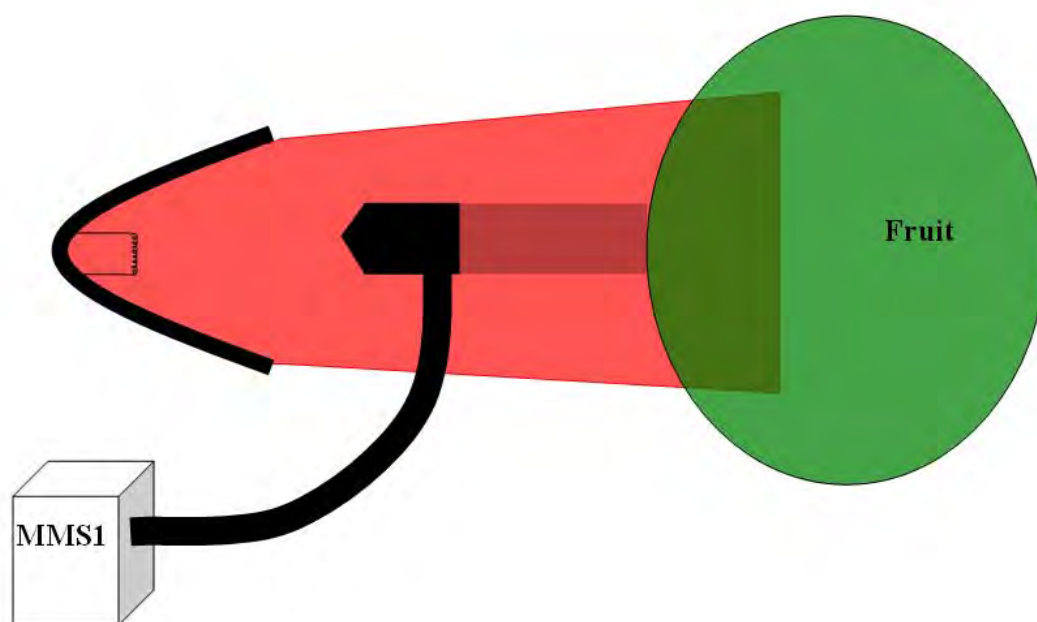
**Figures**

Fig. 1. “Insight” shadow probe configuration, consisting of a parabolic reflector with lamp, projecting light past an optical probe which casts a shadow onto the sample.

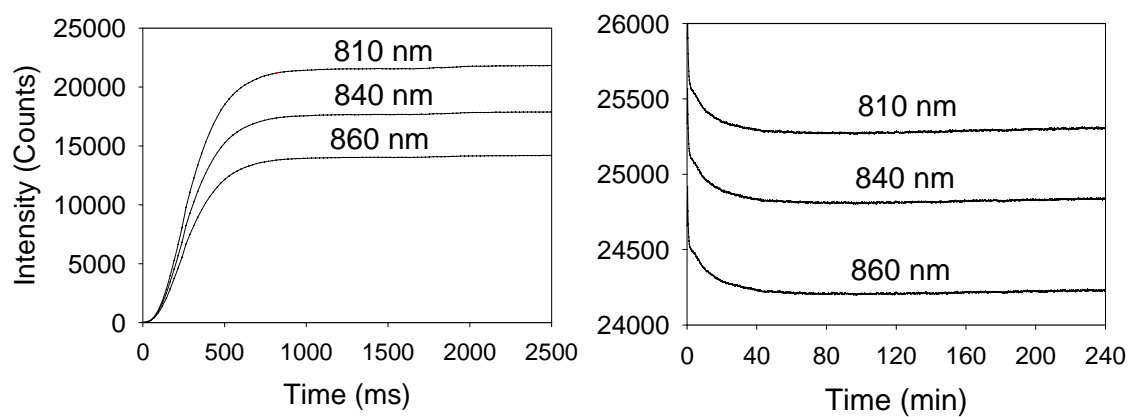


Fig. 2. Graphs of spectrometer output for three wavelengths (810, 840, 860 nm represented by upper, middle and lower lines, respectively) for a QTH lamp output over a four minute period from cold start-up (left) and over a four hour period from cold start-up (right)(data shown for an example lamp).

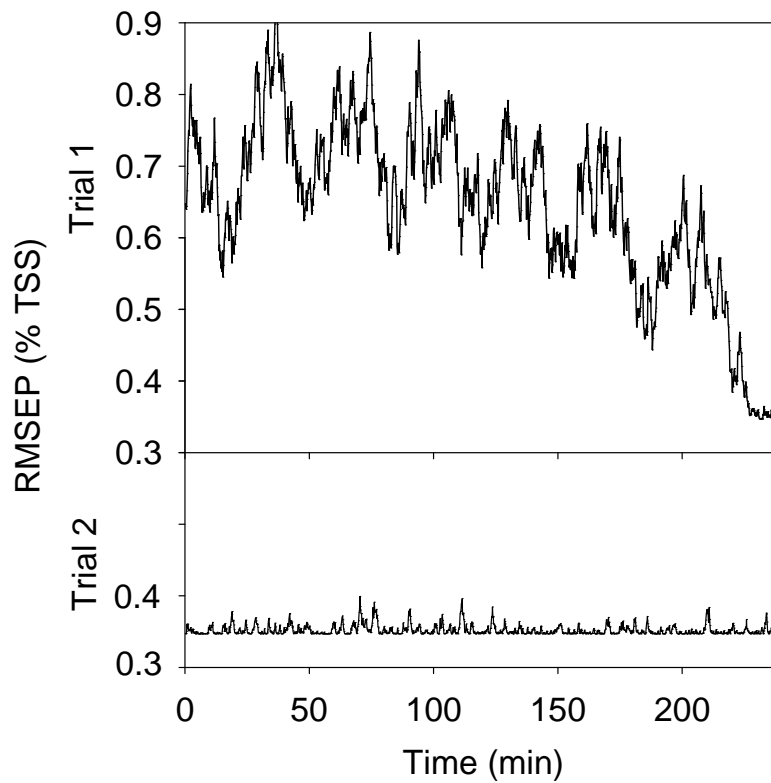


Fig. 3. PLS regression model prediction statistics (RMSEP, % TSS) based on use of (average of ten) spectra collected at various times over 4 h from lamp power-up as white reference data. Data from Sylvania lamp H is displayed. The top panel represents a 4 h period involving power up of the unused bulb, while the bottom panel represents a 4 h period after 4 h of lamp use.

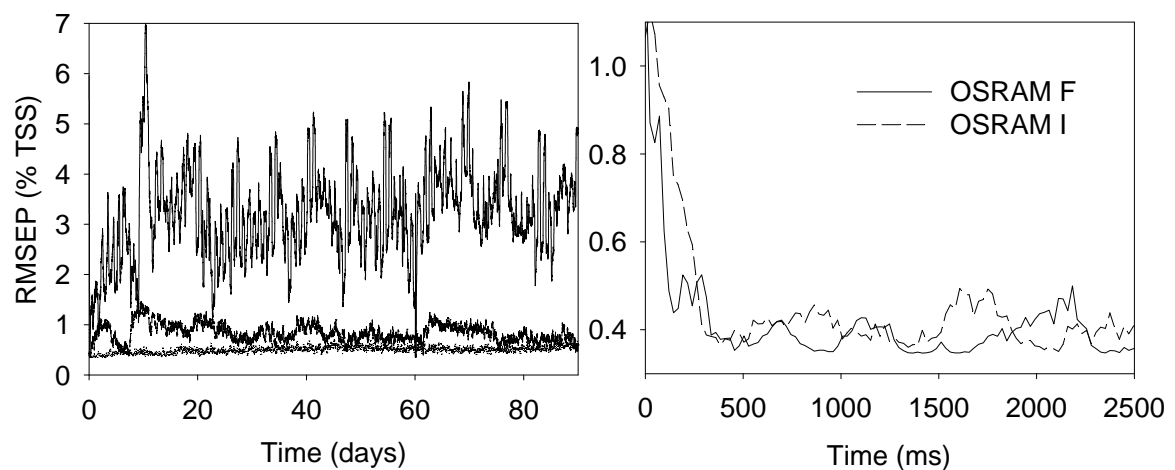


Fig. 4. Plots showing model performance (as RMSEP, % TSS) using white references taken (left) during lamp aging for Osram Lamp J (bottom) and G (top) and Sylvania Lamp A (middle), and (right) during intervals 24ms over 5 min from lamp power-up as white reference data.

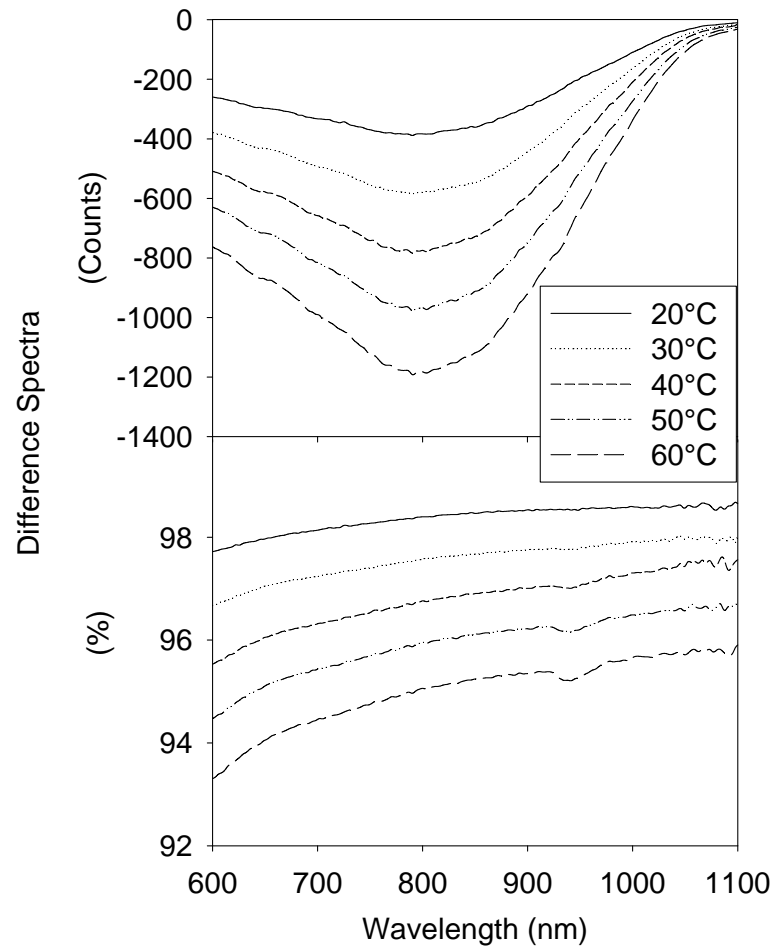


Fig. 5. Spectral intensity (ADC) recorded of a white tile, with increasing ambient temperature of the lamp, presented as a difference spectrum from spectra recorded at an ambient temperature of 10 °C (A) and as percentage of spectra recorded at an ambient temperature of 10 °C (B). Results are shown for a single lamp (Osram E), but were typical of 60 trials.

# 10 Appendix B

## Spectrophotometer Aging and Prediction of Fruit Attributes <sup>6</sup>

UK Acharya<sup>1,2</sup>, KB Walsh<sup>2</sup>, C Hayes<sup>2</sup>, PP Subedi<sup>2</sup>

Corresponding email: umeshach@gmail.com

1. Nepal Agricultural Research Council, Singhdurbar Plaza, Kathmandu, Nepal
2. Central Queensland University, Rockhampton, Australia

### Abstract

Deterioration of lamp output quality over time and degradation of detector signal to noise ratio are issues associated with aging of a spectrophotometer. To document the effect of instrument aging on SWNIRS based assessment of internal attributes of fruit quality prediction (e.g. Total soluble Solids, TSS, of juice), an assessment was conducted of several handheld PDA based spectrophotometers over several years, with repeated spectra of a reference PTFE (Teflon) tile and spectra of 20 apple fruit acquired at yearly intervals. The repeatability of each instrument was assessed as the standard deviation of absorbance of repeated measures of a reference, typically around 0.2 mAbs. Instrument changes were identified in performance and in PCA plots, but performance (apple TSS model) was not related to instrument repeatability. A piece-wise direct standardisation method is recommended to maintain multivariate calibration model across spectrometers.

**Keywords:** apple, repeatability, PDS, spectrometer, total soluble solid

---

<sup>6</sup> This appendix has been submitted to the Special Virtual Issue of Journal of Near Infrared Spectroscopy, January 2016

## 10.1 Introduction

There is a trend to take instrumentation from the laboratory to the field, e.g. spectrophotometers are commercially available for in field assessment of attributes of fruit on tree<sup>1</sup>. Recently use of a multiple crop (pear, apple and persimmon) calibration model for total soluble solids (TSS) content was reported<sup>3</sup>. Unfortunately, field users tend to place less emphasis on instrument maintenance, so understanding performance issues is important. Further, transferability of calibration models across instrument and commodities remains a practical impediment to uptake of the technology<sup>2</sup>.

The performance over time of a visible-shortwave near infrared spectrophotometer used in estimation of fruit attributes will depend on several factors, including aging of the light source, ambient temperature of lamp and detector system of spectrometer.<sup>14</sup> For example, Greensill et al.<sup>15</sup> demonstrated that for the application of assessment of sucrose concentration of aqueous solutions on cellulose fibre, model performance was decreased if wavelength resolution (FWHM) exceeds approximately 10 nm and repeatability decreased below approx. 0.1 mA (assessed as SD of repeated measures of a white reference, relative to that reference). By way of comparison, Foss recommends a noise of < 20  $\mu$ Abs for operation of its NIRSystems 6500 units (NIRSystems 6500 Operating Manual).

Change in either detector or lamp response will impact the output of a predictive model of fruit attributes, primarily in terms of bias.<sup>16, 18</sup> Change in ambient temperature is known to affect halogen lamp output, but in practice spectral quality is not affected sufficiently to impact TSS model predictions, and ageing of a halogen lamp is also not associated with changes in light quality, at least until near lamp failure.<sup>16, 17</sup> Increasing temperature also affects silicon photodiode photo-response (becoming more sensitive to longer wavelengths<sup>14</sup>), and also increases thermal noise.

Other instrument changes may also occur over time, affecting performance, e.g. probe alignment and wavelength<sup>19</sup>. The effect of small (sub nm) change in wavelength calibration of a diode array unit can be very dramatic in terms performance of a TSS model.<sup>17</sup> These authors reported that a drift of 0.03 nm over 150 days and 0.1 nm over a year period for Zeiss MMS1 diode array spectrometers. Instrument drift, as mentioned in

a white paper from the NIR instrument manufacturer Foss (<http://goo.gl/gwxa4C>), is a well-established performance issue for NIR spectrometers.<sup>20</sup>

There are a number of calibration transfer techniques available in literature, e.g. as documented by Feudale et al.<sup>4</sup> and Fearn<sup>5</sup>. There are three broad groups of methods<sup>6</sup>: (a) correction of calibration model before transfer (e.g. slope and bias correction); and (b) correction of spectra before calibration model development (e.g. orthogonal scatter correction (OSC), multiplicative scatter correction (MSC), standard normal variate (SNV), piecewise direct standardization (PDS), repeatability file (rep file)<sup>7</sup>, generalized least square weighting (GLSW)<sup>8</sup>, artificial neural network (ANN), wavelet transform-based standardization (WT), finite impulse transform (FIR) etc; (c) A 'global' model approach involving inclusion of all sample and instrument variability into the calibration set.

Transfer of calibration across network based on-line and bench top NIR systems<sup>9, 10</sup> is well established. Calibration transfer across instrument types has been demonstrated, including from bench top FTNIR to diode array based handheld NIR system<sup>2, 11</sup>. For example, Alamar et al.<sup>2</sup> reported transfer of an apple TSS PLSR calibration model from a FTNIR spectrometer (InfraProver, Norderstedt, Germany) to a diode array based spectrometer (MMS1, Carl Zeiss, Jena Germany, 380-2000 nm) using the PDS technique. Using a FTNIR as master, the prediction performance on two MMS1 units ( $R^2 > 0.70$ , RMSEP = 0.73% TSS) were only slightly inferior to the situation wherein a MMS1 unit was used as master with another MMS1 unit as slave ( $R^2 = 0.76$  and RMSEP = 0.56% SSC).

In general, however, there are very few reports dealing with calibration transfer across handheld NIR spectrometers, or in context of attributes of moist samples as compared to dry samples. Examples of the former case include rockmelon<sup>6</sup>, mandarin<sup>12</sup>, barley<sup>9</sup>, apple<sup>2</sup>, olive<sup>11</sup> and leaf chlorophyll.<sup>13</sup>

Multivariate standardization across instruments is generally carried out using spectra of same samples acquired with the instruments across which standardization is to be performed.<sup>21</sup> Ideally standardisation is performed using the sample type to be predicted in future. With hydrated biological samples (e.g. fruit), there is no possibility of retaining samples, thus all instruments need to be in one place at one time for standardisation.

For example, Wang et al.<sup>21</sup> noted that NIR spectrometer response may vary due to variation in wavelength calibration, detector instability, and electronic drift, necessitating re-calibration and multivariate instrument standardization. In their study, spectra of 52 gasoline samples were collected with each of two instruments (having different data points per nm), and instrument standardization was performed using  $d^2A$  data of the 850-1500 nm region. Direct, inverse model, classical model and piecewise direct standardization (PDS) methods were compared, with PDS recommended.

To assess the impact of SWNIR instrument aging on spectral quality and its implication to apple predictive model performance over year across instruments, a study was conducted over three to four years.

## **10.2 Materials and Methods**

### **10.2.1 Instrumentation and fruit**

Three Nirvana (Integrated Spectronics, Sydney; n.b. this company is no longer trading, but similar instrumentation is available from Felix Instruments, Camas, USA) handheld SWNIR spectrophotometers (Unit 05, 16 and 18) were used over a period of four years, following periods of intensive field use each year. These units utilise a Zeiss MMS1 spectrometer and a halogen lamp, configured in an interreflectance geometry (a shadow probe, as described by Greensill and Walsh).<sup>22</sup> In each of four years, spectra were repeatedly (n=20) collected of a Teflon (PTFE) tile to assess repeatability for at least three years while this work was extended to 7 years with unit 05 (year 2008-2014). Further, each year four fruit each from each of six apple varieties (Granny Smith, Red Delicious, Royal Gala, Pink Lady, Fuji and Jazz) were sourced from retail markets. Fruit were marked on opposite sides in the equatorial region. Spectra were collected twice at each marked spot, and then the fruit mesocarp at the marked spot was sampled with a 2 cm diameter corer to 1 cm depth and used to measure TSS. The TSS reading was taken of juice extracted from the same spot where spectra were collected, using a temperature compensated refractometer (Bellingham and Stanley RFM320).

## 10.2.2 Data processing and analysis

Apple and PTFE white tile spectra were manipulated to produce interpolated (to 3 nm steps) absorbance and second derivative (Savitsky-Golay, second order, 4 data points each side) ( $\text{id}^2\text{A}$ ) spectra.

The calibration transfer approaches of PDS (20 spectra chosen with Kennard stone method<sup>6</sup>, repeatability file (using 20 spectra from PDS)<sup>7</sup>, global model analysis and model update with sample replacement were trialled. These tasks were conducted using script written in Matlab2014a (Math Works, Inc) using PLS toolbox 7.5.1 (Eigenvector, USA). Principle component analysis was undertaken using the multivariate analysis software package, The Unscrambler (v10.3, Camo, Norway). Full cross validation method was used for PLSR model cross validation.

## 10.3 Results and Discussion

### 10.3.1 Instrument repeatability

The Nirvana unit uses an internal gold plated shutter as an internal reference with every sample measured, so the spectra of the PTFE tile presents an absorbance 'feature' in the visible region (gold is a good reflector on infrared wavelengths, but absorbs in the visible region) (Fig. 1). The apparent absorbance spectra of the PTFE (white) tile varied between instruments in the visible region (400-500 nm) (Fig. 1). This phenomenon is attributed to differences in the internal gold reference between units. The shape of the absorbance spectra of the PTFE tile did not visibly differ between years in two instruments (unit 16 and 18), while in unit 05, spectra collected in 2011 differed to other years (Fig. 1).

Repeatability was assessed as the SD ( $n = 20$ ) of absorbance spectra of a PTFE tile. Typical repeatability at wavelengths between 600 and 900 nm was less than 0.2 mAbs units (Fig. 2, Table 1). This compares favourably to the criterion (0.1 mAbs; above which model performance decreased) established for the Zeiss MMS1 module of for assessment of sucrose solutions on cellulose<sup>15</sup>. Instrument repeatability was generally consistent over time (Fig. 2, Table 1); however for unit 5, a poorer repeatability was recorded in 2010.

A principal component analysis plot of absorbance data of PTFE spectra from three instruments over three years demonstrated spread with a given instrument in PC1 (Fig. 3),

which was weighted to wavelengths below 500 nm (Fig. 4). With use of the second derivative, the spread in PC 2 between units was reduced, as expected for removal of baseline shifts in the absorbance spectra, except for unit 5. The wavelengths loading for PC2 also featured wavelengths <500 nm, consistent with the observed difference in the white reference spectra for this unit (Fig. 1). These differences between units and years are ascribed to differences in the gold coating of the reference shutter.

### 10.3.2 Apple TSS model performance

Apple model performance was comparable to other reports in the literature (e.g. typical RMSECV 0.6 % TSS). Performance varied between years; however this performance was neither correlated to unit repeatability nor was a trend with time apparent (Table 1 and Fig. 2). For example, in 2013 unit 16 recorded the poorest instrument repeatability (SD of 3.5 mA), but produced an apple TSS model superior to the other two units. Thus all units were operating with repeatability values (up to 3.5 mAbs) that were adequate to the task of apple TSS prediction.

Lu and McLure<sup>23</sup> reported that full spectrum calibration methods such as PLSR does surprisingly well in prediction of a three component mixture even with the presence of 99% noise (CV 0.17), while for PLSR of a natural product attribute (nicotine in tobacco); prediction error became poor only when noise was >30% (CV of 0.05). Thus while Signal to Noise Ratio is important, its impact must be investigated in context of an application. This conclusion is consistent with the observed poor relationship between white tile repeatability and apple model performance, at least for repeatability to 3.5 mAbs.

The cause of variation in apple model performance may be partly attributed to the change in apple population structure (between years), and partly attributable to shift in detector wavelength calibration. For example Martinsen et al.<sup>17</sup> reported that a 1 nm perturbation of a Zeiss MMS1 spectra used in a kiwifruit DM model resulted in a 7% bias error. Wavelength calibration was noted to be consistent to 0.1 nm over a year. When the fruit TSS was predicted from spectra of unit 05 in 2011 (for which reference spectra were notably different) using a model created using data from previous years, there was a large bias (Table 1), consistent with a consistent shift in spectra from that unit in that year (Fig. 1).

### 10.3.3 Calibration model maintenance and instrument standardization

PLSR model performance in TSS prediction over years, within and across instruments, were not consistent in terms of  $r^2_p$  and bias (Table 2). When a model was used from one instrument on other instruments for spectra collected of the same samples and the same time year),  $r^2$  was reasonable but bias was increased. When used to predict spectra collected from different instruments in a different year, bias was increased (Table 2). Modelling updating across two years in an attempt to capture variation associated with instrument ageing improved performance (decreased bias) for prediction of samples collected in another year (Table 2).

Among four methods trailed for model maintenance (Global, repeatability file, GLSW and PDS), PDS method gave the best result across instruments and year (Table 3). The PDS method solved the problem of prediction bias when the model calibrated on a given unit (for e.g. U05-2011) was validated with spectra collected with another units (U16-2013 and U18-2013) (Table 2 and 3). However, in another case with the same unit (U05-2011, validated with U16-2012 and U18-2012), prediction performance was not improved, because the value of the bias was already low before PDS treatment. The PDS treatment was more effective than other methods in reducing high prediction bias. The better performance of PDS method is in agreement with the work of Wang et al.<sup>21</sup> on instrument standardization with gasoline samples and melon fruit SSC work of Greensill et al.<sup>6</sup>

## 10.4 Conclusion

No evidence for a consistent decrease in apple TSS calibration performance was found, indicating instruments were stable over the period of experimentation, despite extensive field use under tropical conditions. White tile repeatability varied between instruments and years but it was not a good indicator of apple model performance. Instrument updating with spectra collected over years had a mixed effect- satisfactory prediction within same instrument but not across instruments. The variation in units was mostly at the visible region (Figure 4, score plot of two PCs), and attention should be given to stabilising the reference. The prediction bias across instruments can be attributed to small

differences in wavelength calibration between the units. The PDS approach worked well while the repeatability file and GLSW methods failed for calibration model maintenance across years and instruments.

## **10.5 Acknowledgements**

We acknowledge linkage with Felix Instruments and previously Integrated Spectronics in development of handheld instrumentation. UA acknowledges support of an Australian Aid Endeavour Award scholarship.

## 10.6 References

1. C.A.T.D. Santos, et al., "A review on the applications of portable near-infrared spectrometers in the agro-food industry". *Applied Spectroscopy OA*, **67**, 1215 (2013).
2. M.C. Alamar, et al., "Calibration transfer between NIR diode array and FT-NIR spectrophotometers for measuring the soluble solids contents of apple". *Postharvest Biology and Technology*, **45**(1), 38 (2007).
3. P. Jannok, Y. Kamitani and S. Kawano, "Development of a common calibration model for determining the Brix value of intact apple, pear and persimmon fruits by near infrared spectroscopy". *Journal of Near Infrared Spectroscopy* **22**, 367 (2014).
4. R.N. Feudale, et al., "Transfer of multivariate calibration models: a review". *Chem. and Intel. Lab. Sys.*, **64**, 18 (2002).
5. T. Fearn, "Standardisation and calibration transfer for near infrared instruments: a review". *Journal of Near Infrared Spectroscopy*, **9**, 229 (2001).
6. C. Greensill, et al., "Calibration transfer between PDA-based NIR spectrometers in the NIR assessment of melon soluble solids content". *Applied Spectroscopy*, **55**, 647 (2001).
7. M.O. Westerhaus, "Improving repeatability of NIR calibrations across instruments", in *Third international conference on Near Infrared Spectroscopy*, R. Biston and N. Bartiaux-Thill, Editors: Brussels, Belgium. p. 671. (1990)
8. B.M. Wise, J.M. Shaver and N.B. Gallagher, "Using clutter to improve pattern recognition, calibration and classification models", in *The Mediterranean Meeting (CMA4CH) Application of Multivariable Analysis and Chemometry to Cultural Heritage and Environment*: Taormina, Italy. (2010)
9. A. Andrew and T. Fearn, "Transfer by orthogonal projection: making near-infrared calibrations robust to between-instrument variation". *Chemometrics and Intelligent Laboratory Systems*, **72**(1), 51 (2004).
10. N.B. Buchmann, "The standardisation of Infracalc 1221 near infrared transmission instruments in the Danish network used for the determination of protein and moisture in grains". *Journal of Near Infrared Spectroscopy*, **3**, 35 (1995).
11. L. Salguero-Chaparro, et al., "Calibration transfer of intact olive NIR spectra between a pre-dispersive instrument and a portable spectrometer". *Computers and Electronics in Agriculture*, **96**(0), 202 (2013).
12. C.V. Greensill and K.B. Walsh, "Calibration transfer between miniature photodiode array-based spectrometers in the near infra-red assessment of mandarin soluble solids content". *Journal of Near Infrared Spectroscopy*, **10**, 27 (2002).
13. M. Wang, et al., "A robust Near Infrared calibration model for the determination of chlorophyll concentration in tree leaves with a calibration transfer method". *Analytical Letters*, **1** (2015).
14. K.B. Walsh, H.A. Guthrie and J.W. Burney, "Application of commercially available, low-cost, miniaturised NIR spectrometers to the assessment of the sugar content of intact fruit". *Australian Journal of Plant Physiology* **27**, 1175 (2000).
15. C. Greensill and K.B. Walsh, "Optimization of instrumentation precision and wavelength resolution for the performance of NIR calibrations of sucrose in a water-cellulose matrix". *Applied Spectroscopy*, **54**, 426 (2000).

16. C.J. Hayes, C.V. Greensill and K.B. Walsh, "Temporal and environmental sensitivity of a photodiode array spectrophometric system". *Journal of Near Infrared Spectroscopy*, **22** (2014).
17. P. Martinsen, et al., "Temporal sensitivit of the wavelength calibration of a photodiode array spectrometer". *Applied Spectroscopy*, **64**, 1325 (2010).
18. N.H. Sanchez, et al., "Robustness of models based on nir spectra for sugar content prediction in apples". *Journal of Near Infrared Spectroscopy*, **11**, 97 (2003).
19. P. Gujral, et al., "Framework for explicit drift correction in multivariate calibration models". *Journal of Chemometrics*, **24**(7-8), 534 (2010).
20. H.V. Andersen, H. Wedelsback and P.W. Hansen, "A white paper from FOSS-NIR spectrometer technology comparision": Denmark. p. 1. (2013)
21. Y. Wang, D.J. Veltkamp and B.R. Kowalski, "Multivariate instrument standardization". *Anal. Chem.*, **63**, 2750 (1991).
22. C. Greensill and K.B. Walsh, "A remote acceptance probe and illumination configuration for spectral assessment of internal attributes of intact fruit". *Measurement Science and Technology*, **11**, 1674 (2000).
23. J. Lu and W.F. McClure, "Effect of random noise on the performance of NIR calibrations". *Jounral of Near Infrared Spectroscopy*, **6**, 77 (1998).

## 10.7 Tables and Figures

**Table 1. Apple TSS model (based on id2A spectra over 729-975 nm) from three units over a time period of 3 years. Values in bold highlight the unit with best repeatability and apple model performance in each year. Apple TSS SD was 1.75, 1.53 and 1.51 in the years 2011, 2012 and 2013, respectively.**

Year	Unit	white	tilePCs	$R^2_{cv}$	RMSECV	SDR
2011	5	0.219	7	0.91	0.521	3.36
	16	0.613	7	0.87	0.625	2.80
	18	0.198	6	0.90	0.540	3.24
2012	5	0.185	9	0.79	0.713	2.15
	16	0.416	9	0.83	0.633	2.42
	18	0.256	8	0.84	0.608	2.52
2013	5	0.121	5	0.84	0.610	2.48
	16	3.523	5	0.82	0.640	2.36
	18	0.188	7	0.86	0.566	2.67
2011-12	5	-	8	0.85	0.636	2.59
	16	-	8	0.84	0.666	2.48
	18	-	8	0.88	0.564	2.93
2011	3 unit	Combined	9	0.89	0.571	3.05
		Rep-file	6	0.94	0.876	1.99
		GLSW	6	0.83	0.720	2.42

**Table.2. Prediction statistics based on models described in Table 1 (sample size=96, SD=1.51 %TSS). Populations used in calibration and prediction are described in terms of the unit used to acquire spectra (e.g. U05) and the year of acquisition (e.g. 2011-12 is combination of two sets).**

Calset	Predset	$r_p^2$	SEP	SDR	Bias
U05-2011	U05-2012	0.72	0.84	1.80	-0.096
U05-2011	U16-2012	0.75	0.83	1.82	0.323
U05-2011	U18-2012	0.77	0.81	1.86	0.455
U05-2011	U05-2013	0.70	0.84	1.80	0.053
U05-2011	U16-2013	0.73	0.78	1.94	1.39
U05-2011	U18-2013	0.61	0.95	1.59	-5.27
U05-2011-12	U05-2013	0.60	0.97	1.56	0.08
U05-2011-12	U16-2013	0.63	0.93	1.51	1.22
U05-2011-12	U18-2013	0.48	1.08	1.40	-5.05
U16-2011-12	U16-2013	0.61	0.96	1.57	0.44
U18-2011-12	U18-2013	0.71	0.82	1.84	0.09

**Table 3. Performance of calibration model maintenance methods in prediction (sample size=96, SD=1.51 %TSS)**

Calibration set	Prediction set	$r_p^2$	SEP	SDR	Bias
3 units-2011(Global)	U05-2013	0.38	1.65	0.92	1.10
3 units-2011 (Global)	U16-2013	0.42	1.53	0.99	1.42
3units-2011 (Global)	U18-2013	0.37	1.51	1.00	0.66
3 units-2011 (Rep file)	U05-2013	0.38	1.27	1.19	0.06
3 units-2011(Rep file)	U16-2013	0.52	1.05	1.44	0.78
3 units-2011 (Rep file)	U18-2013	0.47	1.11	1.37	-0.50
3 units-2011 (GLSW)	U05-2013	0.38	1.48	1.02	0.12
3 units-2011 (GLSW)	U16-2013	0.42	1.29	1.17	1.10
3 units-2011 (GLSW)	U18-2013	0.34	1.38	1.09	0.21
U05-2011 (PDS)	U16-2011	0.89	0.642	2.35	-0.03
U05-2011 (PDS)	U18-2011	0.91	0.574	2.63	-0.10
U05-2011 (PDS)	U16-2012	0.70	0.839	1.80	0.44
U05-2011 (PDS)	U18-2012	0.76	0.759	1.99	0.32
U05-2011 (PDS)	U16-2013	0.74	0.769	1.96	0.61
U05-2011 (PDS)	U16-2013	0.68	0.851	1.77	0.02

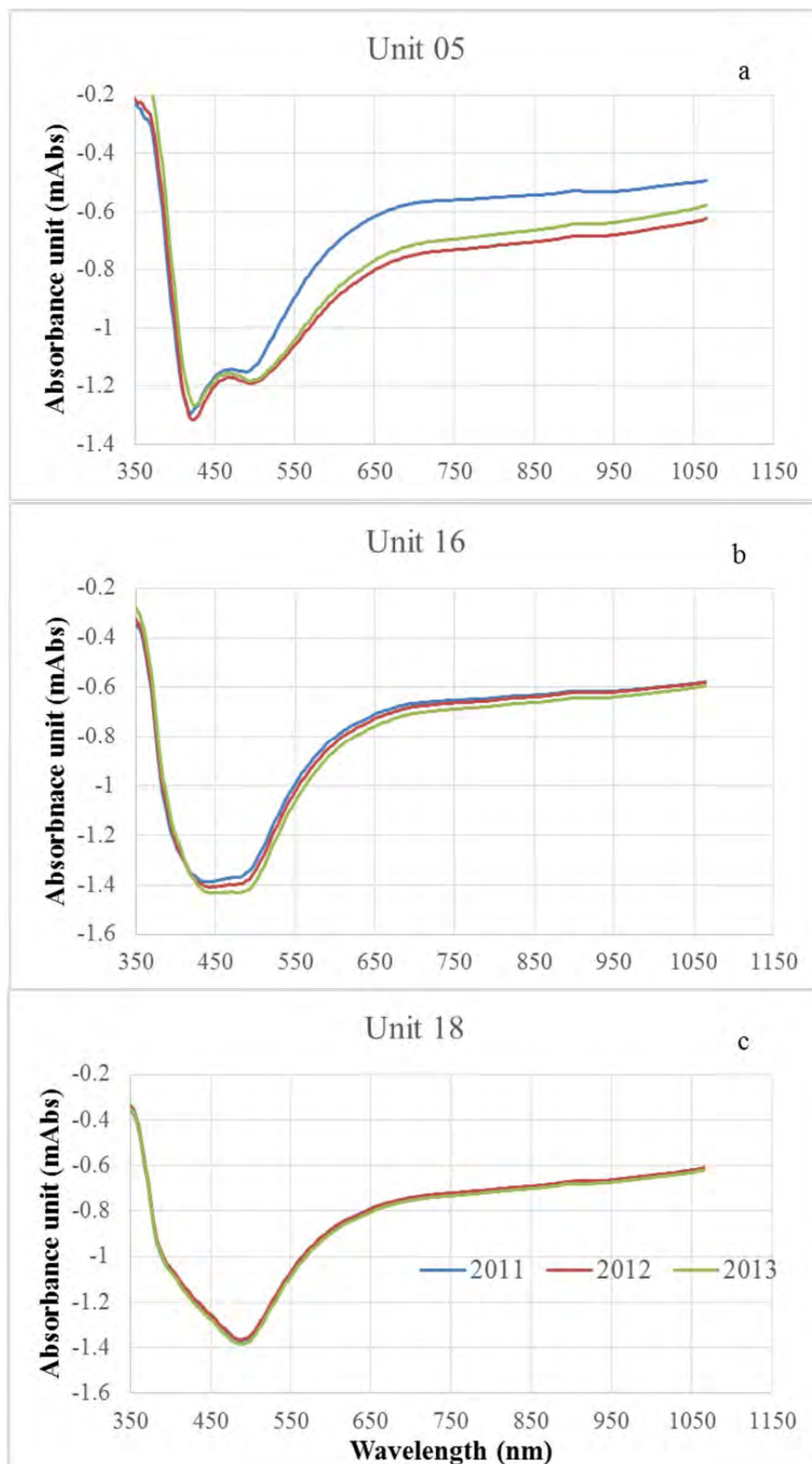


**Figure 1. Average PTFE white tile (Abs) spectra of three Nirvana units over three years period (n=20).**

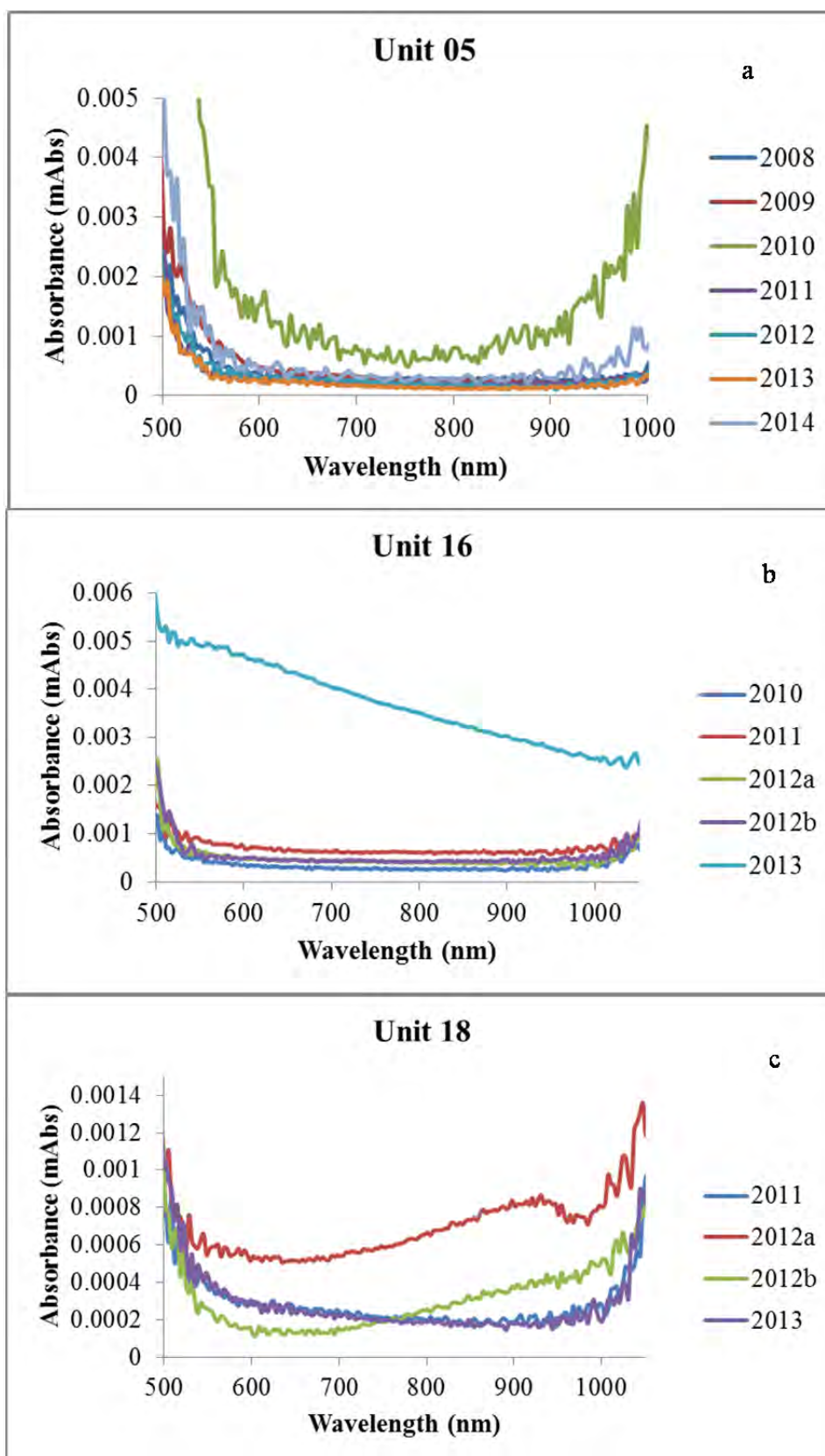


**Figure 2. Instrument repeatability, assessed as SD of 20 repeated PTFE tile spectra over several years**

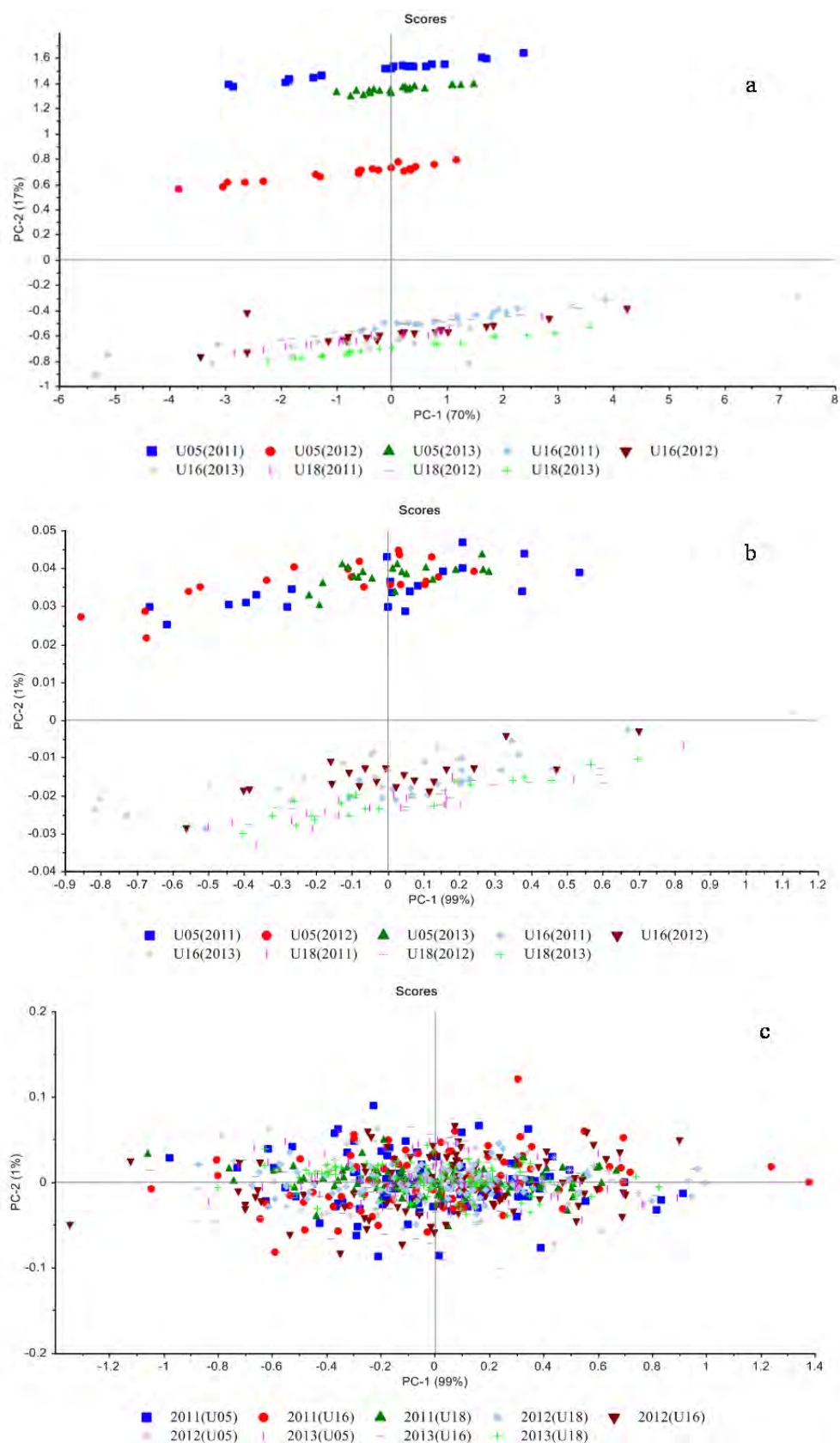


**Figure 3. PCA score plot of (a) Absorbance white tile spectra, (b) D<sup>2</sup>A white tile spectra and (c) D<sup>2</sup>A apple spectra from three instruments over three years**

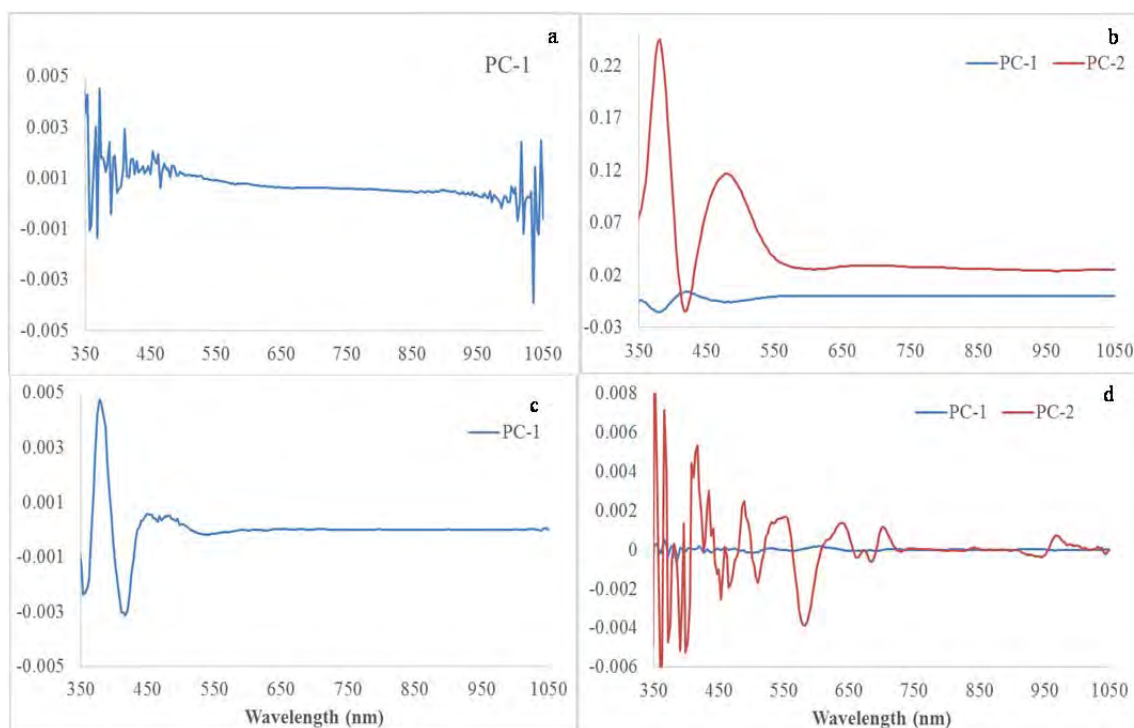


**Figure 4. Loading plot for PCs from (a) Abs white tile spectra (unit 18), (b) Abs white tile spectra (3 units), (c) D<sup>2</sup>A white tile (3 units) and (d) D<sup>2</sup>A apple spectra (3 units) from PCA analysis over 3 years**

# 11 Appendix C

## Assessment of internal flesh browning in intact apple using visible-short wave near infrared spectroscopy <sup>7</sup>

Bed P. Khatiwada, Phul P. Subedi, Clinton Hayes, Luis Carlos Cunha Junior<sup>1</sup> and Kerry B. Walsh

School of Medical and Applied Science, Central Queensland University, Australia

<sup>1</sup> current address: Escola de Agronomia, Universidade Federal de Goiás, Caixa Postal 131, Goiânia, Goiás, Brazil,

Corresponding author: Kerry B. Walsh: +61-74930-9707; email : [k.walsh@cqu.edu.au](mailto:k.walsh@cqu.edu.au)

### Abstract

Certain cultivars of apple are prone to an internal flesh browning defect following extended controlled atmosphere storage. A number of (destructive) reference methods were assessed for scoring the severity of this defect in a fruit, including visual assessment, image analysis (% cross section area affected), chromameter CIE Lab values and juice Abs<sub>420</sub>, of which visual scoring on a 5 point scale and a colour index based on CIE Lab were recommended. Non-invasive detection of this disorder using three instruments operating in the visible-shortwave NIR but varying in optical geometry (interactance, partial transmission and full transmission) was attempted. Quantitative prediction of defect level was best assessed using visible-shortwave NIRS in a transmission optical geometry, with a typical partial least squares (PLS) regression model  $R^2_p = 0.83$  and RMSEP = 0.63 (5 point defect score scale). The binary classification approaches of linear discriminant analysis (LDA), PLS discriminant analysis (PLS DA), support vector machine approach (SVM) and logistic regression were trialled for

---

<sup>7</sup> This appendix has been submitted under this title to the journal of Postharvest Biology and Technology, February 2016

separation of acceptable fruit, with the best result achieved using the PLS discriminant analysis (PLS-DA) method, followed by linear discriminant analysis and support vector machine classification. Classification accuracy  $[(TP+TN)/(P+N)]$  on an independent validation population of >95% and a false discovery rate  $[FP/(TP+FP)]$  of <2% was achieved.

**Keywords:** colour index, score, optical geometry, classification

## 11.1 Introduction

Several types of internal browning are recognised in apple (*Malus domestica* Borkh.) and other pome fruit, including radial, diffuse, bulge or internal breakdown (Bergman et al., 2012; James and Jobling, 2009). The browning symptom is considered to result from membrane disruption, with consequent oxidation of polyphenols otherwise localised to the vacuole of the brown compound, quinone, or its insoluble polymer, melanin (Hatoum et al., 2014a). The diffuse browning disorder developing during controlled atmosphere (CA) storage is suggested to be associated with varieties bred for increased crispness which also have lower intercellular space content (Herremans et al., 2014), although incidence severity is influenced by both pre and postharvest factors and their interaction (Lau, 1998; Castro et al., 2007; Franck et al., 2007; Castro et al., 2008; Benkeblia et al., 2011; Felicetti et al., 2011; Bergman et al., 2012; Wang and Sugar, 2013; Hatoum et al., 2014b). The incidence of the disorder can therefore be erratic (James and Jobling, 2009). Pre-harvest factors include nutrition (chiefly calcium and nitrogen), irrigation, harvest maturity, growing degree days and days after full bloom (Moggia et al., 2015). The main postharvest factor associated with diffuse internal browning is high carbon dioxide concentration, (Ferguson et al., 1999; Hatoum et al., 2014b), with probability of incidence increasing for fruit in controlled atmosphere storage beyond six months (Castro et al., 2007).

Internal browning is considered a ‘major defect’ by retailers, with consignments subject to rejection if more than 2% of fruit display the disorder (e.g. Woolworths, 2015). This market pressure creates demand for a technology capable of detection of the disorder in fruit, allowing for sorting to remove defect fruit. A range of technologies have potential for detection of this disorder, including visible-short wave near infrared spectroscopy (SWNIRS), acoustic, X-ray or nuclear magnetic imaging. For example, Gonzalez et al.

(2001) reported the use of MRI in detection of internal browning in 'Fuji' apples, with difference in longitudinal (T1) and transverse (T2) relaxation time and proton density between the normal, moderate and severe browning fruit. Indeed, Chayaprasert and Stroshine (2005) reported use of magnetic resonance imaging (MRI) for detection of browning in intact apple in an online sorting conveyor belt achieving classification accuracy  $[(TP+TN)/(P+N)]$  of 88%. However, conveyor speed was less than 150 mm/s, too slow for commercial application (typically 1000 mm/s). Visible SWNIRS shows more promise for adoption into online sorting.

(Norris, 1958) (reported in (Aulenbach et al., 1972) first reported on the measurement of transmittance of intact agricultural products for detection of internal defects. Birth and Olsen (1964) reported on the use of the difference in optical density at 760 and 810 nm of intact apple fruit as an index for water core, and this concept was expanded to the detection of both water core and internal browning by Francis et al. (1965). The topic was then left unreported for 30 years, until the work of Upchurch et al. (1997), Clark et al. (2003), and then McGlone et al. (2005) and then others. Francis et al. (1965) reported that the difference of absorbance at 840 and 740 nm was a useful index of the internal defect detection with 91% accuracy for separating normal fruit from defect in a population involving 50 fruit. Similarly, Upchurch et al. (1997) reported use of a ratio between transmittance at 720 and 810 nm as a classifier for discrimination between defective and good apples (the ratio decreased as the browning intensity increased, correlation coefficient of determination ( $R^2$ ) = 0.71). Error rates of 6.3% good apples misclassified as defect (false negative) and 12% defect fruit misclassified as good (false positive) were reported. The presence of bruises contributed to instances of false negatives. Clark et al. (2003) reported use of partial least squares regression using absorbance data over the wavelength region 697-861 nm for estimation of the degree of internal browning in Braeburn apple. Model statistics of correlation coefficient of determination for prediction  $[(R^2_p) = 0.91, \text{error of prediction (RMSEP)} = 7.9\%]$  were reported when using the average of spectra obtained from opposite sides of the fruit. Increased absorbance in the visible range is presumably by phenolics associated with the browning symptoms.

Given such positive results, the integration of SWNIR technology into on-line sorting is logical. McGlone et al. (2005) reported detection of brownheart disorder of Braeburn apples of moving fruit at speed of five fruit per second, using SWNIR transmittance

spectra over the range 650-950 nm range. Use of a 'large aperture spectrometer' was recommended for online measurement, with a partial least square regression (PLSR) model result of correlation coefficient of determination for prediction ( $R^2_p$ ) = 0.9, and standard error in prediction (RMSEP) = 4%.

Prediction of the level of disorder in fruit is, however, unnecessary as in practice separation to only two classes is required- accepted and non-acceptable. Han et al. (2006) reported use of a discriminant technique for detection of brown core in another member of the pome fruit family, pear (*Pyrus communis* L.), with spectra collected over the range 651-1282 nm with a transmission optical geometry. Using the absorbance difference between 713 and 743 nm as a classifier, 5.3% of good pears were incorrectly classified as defect, while only 4.3% of defect fruit were classified as good. Fu et al. (2007) reported the use of transmittance spectra over 400-1028 nm and also reported that defect fruit demonstrated a higher absorbance below 750 nm and a lower absorbance above 750 nm. In calibration, a discrimination accuracy of 89% was noted, while in validation, accuracy decreased to 81%. Discrimination based on data of spectral regions is also possible, using techniques such as soft independent modelling of class analogy (SIMCA), partial least square discriminant analysis (PLS-DA), k- nearest neighbourhood (k-NN) and linear discriminant analysis (LDA) (Moscetti et al., 2015; Pérez-Marín et al., 2011).

Recent publications have focussed on the application of novel techniques. Li (2011) reported assessment of internal browning in Fuji apples using Fourier Transform (FT) NIR in an interactance optical geometry, with the best PLSR model ( $R^2 = 0.87$ ) achieved at wavelength ranges of 950-1440 nm, 1480-1890 nm and 1960-2300 nm. Vanoli et al. (2014) reported the use of time resolved reflectance spectroscopy, with estimation of absorption and scattering coefficients at 780 nm used for separation of apple fruit with internal browning. They reported correct classification of 90% of good fruit and 71% of defect fruits.

Thus a number of reports indicate that non-invasive sorting of fruit on internal browning is possible. For the light transmission studies, published reports of detection of internal browning generally recommend a transmission geometry and the use of wavelengths in the vis-SWNIR region, but there is variation between the reports on the best wavelength range to use, and on the algorithm to use (PLSR, simple ratio, discriminant analysis etc.). One study has considered defect detection of moving fruit. The comparison of published

studies is difficult, as results depend on instrumentation, population distribution and the reference method used to assess level of defect. Further, all of the reports mentioned above are based on relatively small sample sizes, basically limited to a single population of fruit divided into training and validation sets, and thus fail to consider the range in variation of fruit optical properties occurring between populations (of different growing conditions etc.). The ‘reference’ method used in assessment of the internal browning defect varies across the published studies, from visual assessment to image analysis of the cut fruit surface or measure of browning of extracted juice. Perhaps it should not be a surprise then that commercial adoption of non-invasive technology for detection and sorting of this disorder is not widespread, an indication that application is not as straightforward as some of the scientific literature suggests. There are some commercial providers of instrumentation (e.g. as advertised by Compac, [www.compacsort.com](http://www.compacsort.com) Greefa, [www.greefa.nl](http://www.greefa.nl), MAF [www.maf.com](http://www.maf.com), and [www.sorter.eu](http://www.sorter.eu), among others), but there are no reports in the scientific literature on use of this equipment in context of detection of apple fruit with internal diffuse browning.

A specific issue not considered in previous reports is that of the effect of sample temperature. Fruit consist of approximately 80% water. The IR/NIR spectrum of water is affected by temperature due to an effect on the extent of hydrogen bonding, and this can impact prediction of soluble solids content (SSC) and dry matter (DM) in intact fruit using SWNIRS with the simplest accommodating measure being the inclusion of samples of a range of temperatures into the training sets (Acharya et al., 2014). Given that the spectral information relevant to internal browning may be restricted to the visible region, spectral based measures of internal browning may be free from interference associated with temperature change, however, this issue should be explicitly considered.

In the current exercise, results for detection of internal browning in apple are compared for spectra collected with instruments using an interactance, partial transmittance and full transmission geometries, including the instrumentation of a fruit grading equipment manufacturer, with consideration of reference method, wavelength region, algorithm and sample temperature, and the use of discriminant analysis with full spectral data. A preliminary report on this work was presented at IHC 2014.

## 11.2 Materials and Methods

### 11.2.1 Fruit

Apple (*Malus domestica* Borkh.) cv Pink Lady™ fruit were commercially harvested in Stanthorpe, south Queensland, Australia, in July 2013 and stored for six months in controlled atmosphere storage with 1-2% O<sub>2</sub> and 4-5% CO<sub>2</sub>. Fruit were sampled from each of four bins, being fruit from different harvest events, transported overnight to Rockhampton, Queensland at 25 °C, and then stored for another two months at 4 °C. Fruit were allowed to equilibrate to room temperature for 6 h before spectra were acquired.

The four independent lots (populations) of fruit contained a total of 296 fruit (93 good and 203 defect). Population 1, containing 69 fruit (22 good and 47 defect), was used for trials on chlorophyll fluorescence and absorbance at 420 nm of extracted juice. Population 2, consisting of 90 fruit (31 good and 59 defect), was used for SWNIR calibration model development. Population 3 and 4 contained 60 (12 good and 48 defect) and 77 (28 good and 49 defect) fruit, respectively, and were used as independent prediction sets for the SWNIR models. Population 2 and 3 (a total of 150 fruit) was further subset into five groups of 30 fruit (referred to as populations 5 to 9) for a study of the impact of fruit temperature on model prediction.

### 11.2.2 SWNIRS

Four spectra were acquired of each fruit (detector facing each of four equidistant locations around the equator of the fruit) using each of three instruments, involving different optical geometries and detectors:

- (i) a handheld instrument using an interactance optical geometry (Greensill and Walsh, 2000) with a 32 W halogen lamp and a MMS-1 photodiode array spectrometer (302-1150 nm); ('Nirvana', Integrated Spectronics, Sydney, Australia)
- (ii) an instrument developed 'in-house', employing a partial transmission optical geometry with a 300 W halogen lamp and a MMS1 photodiode array spectrometer (302-1150 nm) operated with an integration time of 1000 ms; (IDD0).

- (iii) a commercial online sorting instrument using a full transmission geometry with a 150 W halogen lamp and an Avantes spectrometer (600-973 nm) operated with an integration time of 9 ms; ('Insight-2', MAF Roda, Montabaun, France)

The IDD0, developed for this project was based on the Zeiss MMS-1 spectrometer, operated with a 16 bit analogue to digital converter (tec5, Germany). This unit has a mean pixel pitch of 3.3 nm, a wavelength resolution (FWHM) of approximately 10 nm, a repeatability of 1 milli-absorbance, a well depth of 1013 counts/Watt seconds and operates over the spectral range 310-1100 nm. Thus the unit has high signal to noise but modest sensitivity. To achieve a 180° geometry (lamp-fruit-detector angle) involving transmission of light through a whole fruit, a high intensity lamp (300 W Quartzline) and a long integration time were employed. The use of the 300 W lamp entailed heating problems of both fruit and lamp housing, so the unit was designed with a series of fans and a failsafe circuit to cut power if lamp holder temperature exceeded 100 °C. A shutter was incorporated to allow shielding of the fruit until measurement. Spectrometer analogue to digital conversion counts (ADCC) of over 67% of detector maximum were achieved for mandarin using this lighting, but for apple, similar detector ADCC and integration time was achieved only with a 90° illumination-sample-detector angle. Data acquisition and processing utilized LabView software developed in-house.

### **11.2.3 Other measurements**

The extent of the browning disorder within apple fruit was assessed using several reference methods:

- (i) Visual browning score

A panel of 6 members was trained in the assignment of a score for the severity of defect visible in a transverse equatorial cut of the fruit, using a 5 point scale, with scorers assisted by a reference pictorial chart (Fig. 1). The average value of all scorers was used. In the 5 point scale, score 1 is symptomless and score 2 is associated with an 'off white' colouration that can be considered acceptable to consumers, scores 3 to 5 are associated with increasingly distinct symptoms, all unacceptable to consumers (Fig. 1).



**Figure 1. Cut surfaces of apple with internal browning symptoms in order increasing order of browning intensity from left to right, with visual score ratings of 1 to 5, respectively.**

(ii) Area of defect

The cut apple (equatorial transverse cut), as used in visual scoring, was imaged using a Canon DS 126211 camera with a 17-85 mm lens at a fixed focal distance. Images were processed using ImageJ software, with conversion of the RGB colour image into grayscale and use of a threshold setting to differentiate defect tissues and masking of the core area (Fig. 2). Affected tissue area was expressed as a percentage of total fruit cross-sectional area, with subtraction of the core area.

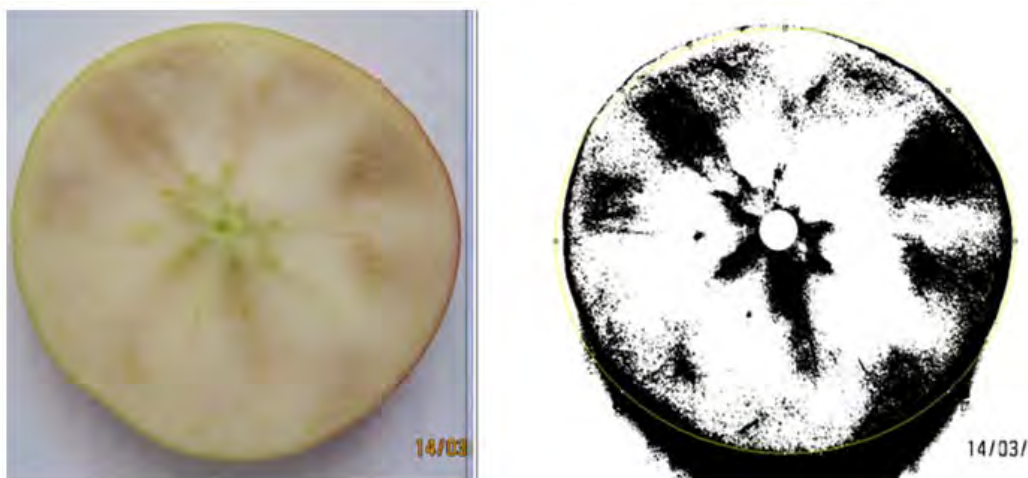


**Figure 2. Image processing using ImageJ software for quantification of affected area as a % of total cross-sectional area.**

(iii) Chlorophyll fluorescence and Abs<sub>420</sub>

Chlorophyll fluorescence ( $F_v/F_m$ ) was measured using an OptiSciences 30p (Bioscientific, Australia) at a modulation intensity of 4 following dark adaptation for 24 hours. One reading was taken per fruit.

The juice colour was assessed following the method of Song et al., (2007). Apple flesh (10 g fresh weight) was finely chopped and 12.5 mL of water added. The mixture was blended using an Ultraturrex and centrifuged for 5 min at 3000 rpm. An aliquot (5 mL) was mixed with 7.5 mL of 70% v/v ethanol and centrifuged again for 10 min at 3000 rpm and supernatant absorbance at 420 nm was measured using an UV-Visible spectrophotometer CARY 50 Bio (Labwrench, Ontario, Canada).

Population 1 was assessed for % area defect based on image analysis, Abs<sub>420</sub> of juice and chlorophyll fluorescence.

(iv) CIE colour space

The cut apple (equatorial transverse cut), as used in visual scoring, was also used for the measurement of surface colour (CIE Lab colour space) using a Chromameter CR 400 (Konica Minolta; 2 degree observer, D65 illuminant), with averaging of five randomly located measurements per fruit. CIE Lab values were used to calculate a Colour index (CI), as described by Magwaza et al. (2014):

Colour Index =  $(1000 \times a)/(L \times b)$ .

(v) Weight, SSC and DM

Following weighing of each fruit, a 20 mm diameter core was extracted to 10 mm depth from the point of spectral assessment. The core was halved radially, with one half used for dry matter (DM) and the other for soluble solids content (SSC) measurement. For DM assessment, tissue was dried in a fan forced oven at 65 °C for 48 h. For SSC, juice was extracted using a garlic press and measured using a refractometer (RFM 320, Bellingham and Stanley Ltd).

#### **11.2.4 Data analysis and Chemometrics**

Multivariate data analysis was undertaken using The Unscrambler software (version 10.3, Camo, Oslo, Norway) and MATLAB R2014a (Mathworks Inc., Natick, MA, USA) with PLS Toolbox (Eigenvector Research Inc., Wenatchee, WA, USA). IDD0 and Nirvana spectral data was collected in Absorbance units. InSight2 spectral data was output in units of % transmittance (T) and was converted to Absorbance ( $\log 1/T$ ). Absorbance data of all instruments was subject to a number of pre-treatments including mean centring,

standard normal variate (SNV), multiple scatter correction (MSC), and Savitzky Golay second derivatization using a window of 9 points (SG-9). Spectral data used for the analysis was restricted to 500-975 nm for IDD0 and Nirvana instrumentation while for the InSight2 unit the entire available range (600-973 nm) was used.

Predictive quantitative models developed partial least square regression (PLSR) were assessed using the criteria of correlation coefficient of determination ( $R^2_{cv}$ ), root mean square error of cross validation (RMSECV) and number of principal components (PCs), while predictive performance was assessed based on coefficient of determination of prediction ( $R^2_p$ ), root mean square error of prediction (RMSEP) and bias.

The binary classification algorithms of PLS–discriminant analysis (PLS-DA) based on two or multiple classes, linear discriminant analysis (LDA) based on linear or Mahalanobis distance (MD), PCA based discriminant analysis, support vector machine (SVM) classification, soft independent modelling of class analogy (SIMCA), and multiple logistic regression (MLoR) were assessed based on the true positive rate [(TPR = TP/(TP+FP)] true negative rate [TNR = TN/(TN+FN)] and accuracy [(TP+TN)/(P+N)] where TP = true positive (defect fruit), TN = true negative (sound fruit) in a population, FP = false positives (sound fruit identified as defect, and FN = defect fruit identified as sound.

## **11.3 Results and Discussion**

### **11.3.1 Population description**

Of the four populations assessed, population 3 had the highest mean visual (5 point) scores (Table 1). The mean CIE  $a^*$  and colour index values of the three populations was not proportionate to the mean visual scores (Table 1) consistent with a poor relationship between these variables (Table 2).

**Table 1. Mean and standard deviation of reference parameters for four populations – population 2 was used for model calibration and other sets were used as prediction sets. Score (5) refers to a 5 point scale visual score of the extent of browning. Values are presented as [Mean  $\pm$  standard deviation (SD)].**

Parameters	Pop 1	Pop 2	Pop 3	Pop 4
Number of fruit	69	90	60	77
Score (5)	2.8 $\pm$ 1.60	3.21 $\pm$ 1.53	3.81 $\pm$ 1.39	3.36 $\pm$ 1.75
Colour Index		0.37 $\pm$ 1.29	1.05 $\pm$ 1.4	1.38 $\pm$ 1.38

A further five sets of fruit were used in the exercise on assessment of influence of temperature on prediction performance (section 3.5). Each of these sets contained 30 fruit, with mean and SD (5 point visual score) of 2.96  $\pm$  1.49, 3.28  $\pm$  1.57, 3.14  $\pm$  1.48, 3.36  $\pm$  1.51 and 3.85  $\pm$  1.38, respectively.

**Table 2. Correlation coefficient of determination ( $R^2$ ) between various destructive measures of Pink Lady apple fruit (Populations 2 and 3; n= 150). Values above 0.75 are in bold.**

Parameters	Score	CIE L*	CIE a*	CIE b*	Colour	DM	SSC
Score (5)	1						
CIE L	0.68	1					
CIE a	<b>0.78</b>	<b>0.90</b>	1				
CIE b	0.40	0.56	0.52	1			
Colour Index	0.70	0.71	<b>0.77</b>	0.43	1		
DM	0.11	0.14	0.12	0.07	0.19	1	
SSC	0.23	0.30	0.28	0.18	0.38	0.61	1

### 11.3.2 Reference methodologies

Consumer assessment of the diffuse browning defect of apple involves subjective visual inspection of a cut surface of the fruit. However there are inaccuracies involved in classifying this disorder, e.g. how should a fruit with a diffuse overall browning be scored

compared to a fruit with a patchy but darker areas. In an attempt to quantify the visual assessment, five and ten point scoring systems were compared. For the 5 point scale, the average RMSED (root mean of squares of error of differences) of assessment of defect level in 125 cut fruit assessed by six different operators relative to that of the ‘average assessor’ was 0.54 (n=6), while for the 10 point scale it was 0.79 (adjusted to a 5 point scale). For a repeated assessment using the 5 point scale by one assessor only, the RMSED was 0.28. These errors are associated with the ability of a human observer to remember the descriptions of multiple levels. The 5 point scale is therefore recommended over the 10 point visual scale.

For population 1, the correlation ( $R^2$ ) between 1-5 visual score, 1-10 visual score, % area defect, Fv/Fm and Abs 420 nm was 0.85, 0.64, 0.2 and 0.02 respectively (data not shown). The indices of 1-10 visual score, % area defect, Fv/Fm and Abs 420 nm were not considered further.

In an exercise involving 150 fruit (Pop 2 and 3), a stronger linear correlation existed between the 5 point visual score and CIE a ( $R^2 = 0.78$ ) than L or the colour index, and score was poorly related to SSC or DM (Table 2). As visual score mimics a consumer assessment of the fruit, this method was adopted as the most relevant measure for this disorder, and as an easy to undertake, though destructive method.

McGlone et al. (2003) reported a correlation coefficient of determination ( $R^2$ ) of 0.93 between harvest time DM and post storage SSC for Royal Gala apple. Lower correlations were recorded in the current study suggesting that fruit were not fully ripened, with starch to sugar conversion yet to complete. Indeed, a poorer relationship between DM and SSC existed for defect fruit ( $R^2 = 0.47$ ) than sound fruit ( $R^2 = 0.76$ ) (data not shown), suggesting defect fruit were less ripened than control.

### **11.3.3 Visible – SWNIR spectral features**

Absorbance spectra of fruit were characterised by features associated with anthocyanin at around 550 nm, chlorophyll at around 665 nm and water at 730, 840 and 950 nm (Fig. 3).

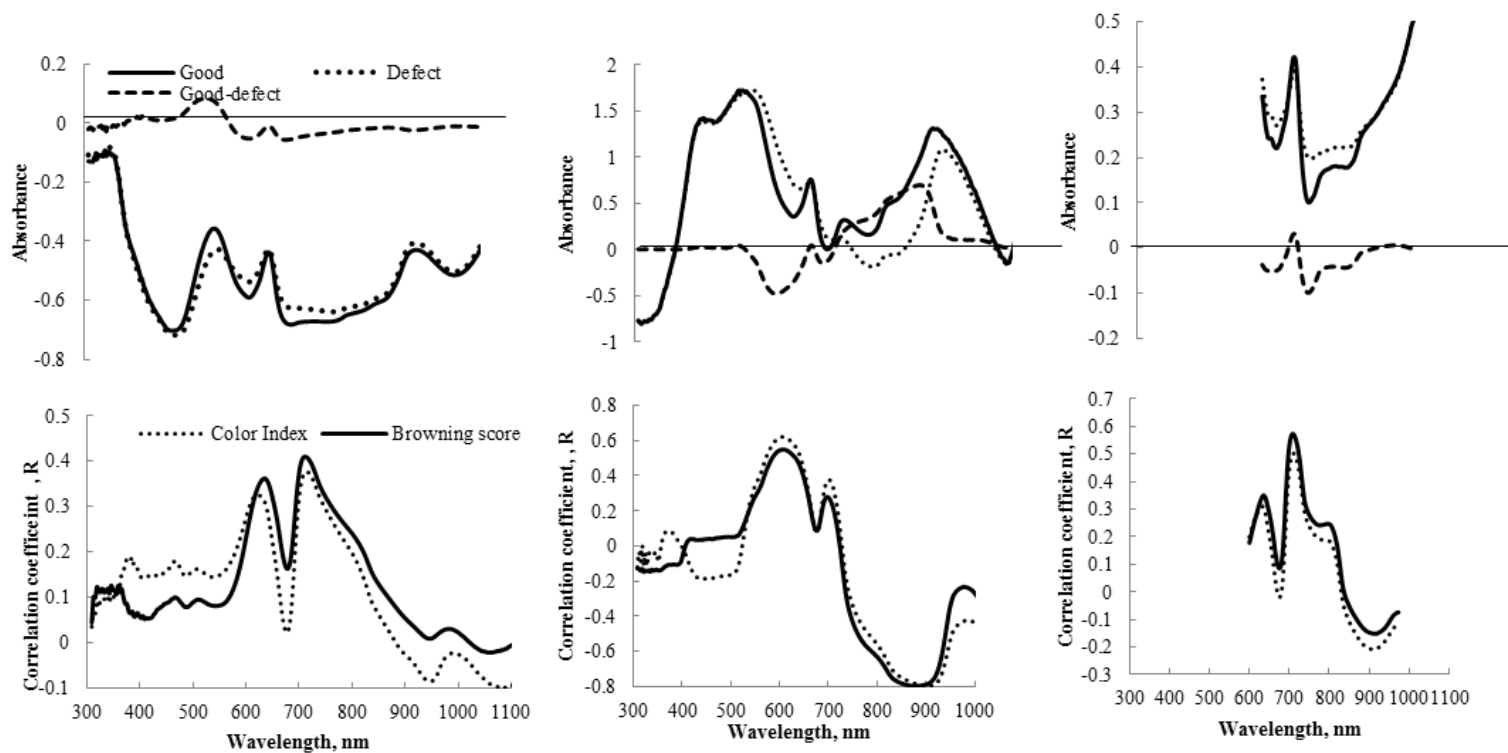


**Figure 3.** Mean absorbance spectra for good and defect fruit and their difference (score 1 and 5, respectively, from populations 2 and 3) and univariate correlation coefficient (R) of internal defect parameters (visual score and colour index) with absorbance at each wavelength using three instrumentations (Nirvana, left; IDD0, middle and Insight 2 right).

Average absorbance values were higher for defect relative to sound fruit at shorter wavelengths, specifically wavelengths less than 830 nm for the InSight2 spectra, and less than 730 nm for the IDD0 spectra, consistent with previous reports (Fig. 3). For example, Clark et al. (2003) reported higher absorbance for apple with internal browning over the range 600-750 nm, and lower absorbance at wavelengths beyond 850 nm. McGlone et al. (2005) noted higher absorbance in the red to near red region of spectrum. For pear, higher absorbance was noted over the range 640-860 nm for fruit with brown core (Han et al., 2006). The higher absorbance values in this region may represent absorption of light by the polyphenols associated with browning.

The strongest correlation between absorbance at a single wavelength and defect intensity was achieved at around 620 and 710 nm for the Nirvana and IDD0 / InSight2 instruments, respectively (Fig. 3).

#### **11.3.4 Partial Least Square Regression**

Partial least square regression (PLSR) models were developed using the reference values of visual score and Colour index (Table 3). Better calibration results were obtained using the Colour index than the visual score value, but the reverse held for prediction results (Table 3).

**Table 3. Partial least square regression results for spectra from three instruments, for raw absorbance spectra and for spectra treated with several pre-processing methods for Nirvana (interactance), IDD0 (partial transmission) and InSight2 (full transmission) instrumentation. Calibration set (pop2), prediction set 1 (pop3) and prediction set 2 (pop4) consist of 90, 60 and 77 fruit respectively. RMSEP and Bias have units of 5 scale color score and Color Index.**

### A. Nirvana

Pre treatments /Parameters	Calibration statistics (pop2)			Prediction statistics on pop3			Prediction statistics on pop4		
	$R^2_{cv}$	RMSECV	PCs	$R^2_p$	RMSEP	Bias	$R^2_p$	RMSEP	Bias
<b>Raw Abs</b>									
Score	0.79	0.7	14	0.57	1.01	-0.10	0.62	0.99	0.14
Colour Index	0.86	0.45	14	0.80	0.62	0.15	0.70	0.83	-0.12
<b>Abs. SNV</b>									
Score	0.77	0.71	14	0.52	0.40	-0.11	0.53	1.30	0.24
Colour Index	0.85	0.47	14	0.77	1.15	-0.48	0.71	0.82	-0.10
<b>Abs MSC</b>									
Score	0.76	0.73	11	0.53	1.08	-0.03	0.60	0.99	0.20
Colour Index	0.83	0.51	11	0.75	0.73	0.20	0.66	0.88	-0.10
<b>Abs d2A</b>									
Score	0.77	0.71	10	0.60	0.96	0.01	0.64	0.95	0.28
Colour Index	0.84	0.49	10	0.74	0.69	0.12	0.71	0.82	-0.11
<b>Abs. SNV d2A</b>									
Score	0.76	0.74	10	0.56	1.01	-0.08	0.59	1.00	0.20
Colour Index	0.83	0.52	10	0.71	0.71	0.02	0.66	0.90	-0.19

**B . IDD0**

Pre-treatments /parameters	Calibration statistics (pop2)			Prediction statistics on pop3			Prediction statistics on pop4		
	$R^2_{cv}$	RMSECV	PCs	$R^2_p$	RMSEP	Bias	$R^2_p$	RMSEP	Bias
<b>Raw Abs</b>									
Score	0.83	0.62	4	0.70	0.83	0.24	0.87	1.08	0.88
Colour Index	0.87	0.46	4	0.73	0.72	0.04	0.75	0.73	-0.16
<b>Abs. SNV</b>									
Score	0.78	0.71	4	0.76	0.7	0.16	0.89	0.82	0.56
Colour Index	0.87	0.46	3	0.71	0.75	0.03	0.77	0.61	-0.53
<b>Abs MSC</b>									
Score	0.77	0.73	3	0.75	0.71	0.13	0.89	0.9	0.66
Colour Index	0.88	0.45	3	0.74	0.71	0.03	0.77	0.68	-0.06
<b>Abs d2A</b>									
Score	0.75	0.75	3	0.73	0.73	0.06	0.84	0.8	0.02
Colour Index	0.86	0.49	4	0.68	0.79	-0.08	0.77	0.82	-0.47
<b>Abs. SNV d2A</b>									
Score	0.76	0.75	3	0.76	0.68	0.03	0.86	0.79	0.02
Colour Index	0.87	0.47	5	0.7	0.76	-0.06	0.77	0.67	-0.10

## C. InSight2

Pre-treatments /parameters	Calibration statistics (pop2)			Prediction results on pop3			Prediction results on pop4		
	$R^2_{cv}$	RMSECV	PCs	$R^2_p$	RMSEP	Bias	$R^2_p$	RMSEP	Bias
<b>Raw Abs</b>									
Score	0.83	0.63	7	0.75	0.81	0.26	0.84	1.12	0.87
Colour Index	0.85	0.50	7	0.68	0.81	0.11	0.65	0.89	0.23
<b>Abs. SNV</b>									
Score	0.84	0.61	6	0.72	0.88	0.25	0.82	1.18	0.86
Colour Index	0.84	0.52	6	0.68	0.82	0.13	0.64	0.99	-0.13
<b>Abs MSC</b>									
Score	0.83	0.62	5	0.73	0.84	0.23	0.79	1.49	1.10
Colour Index	0.84	0.51	5	0.68	0.82	0.12	0.70	0.92	-0.16
<b>Abs d2A</b>									
Score	0.78	0.71	5	0.75	0.69	-0.08	0.84	0.92	0.56
Colour Index	0.79	0.58	8	0.58	0.90	-0.10	0.61	1.08	-0.66
<b>Abs. SNV d2A</b>									
Score	0.80	0.68	7	0.74	0.72	-0.03	0.87	0.73	0.39
Colour Index	0.77	0.61	7	0.56	0.94	-0.18	0.69	1.02	-0.68

Initially, PLSR models were developed using the full wavelength range available from a given instrument. Smooth regression coefficients were obtained for the region 500-975 nm for the units based on a MMS 1 spectrometer (Nirvana and IDD0), and for the entire available range of 600-973 nm for Avantes spectrometer (InSight2 instrumentation) (Fig. 4), and these ranges were selected for further model development. For the IDD0 and InSight2 units, the PLSR models gave strong weighting to absorbance at 670, 710 and 900 nm, and 680, 710, 800 and 835 nm, respectively. For the reference parameter of visual score and spectra obtained using the IDD0 and InSight2 units, better calibration and prediction performance was obtained for models based on raw absorbance spectra, followed by use of SNV and MSC pre-treatments (Table 3). A correlation coefficient of determination ( $R^2$ ) of 0.89 was achieved for IDD0 SNV or MSC treated absorbance spectra. However, model predictive performance was higher for models developed using second derivative spectra. Poor predictive performance was obtained using spectra acquired with the Nirvana unit.

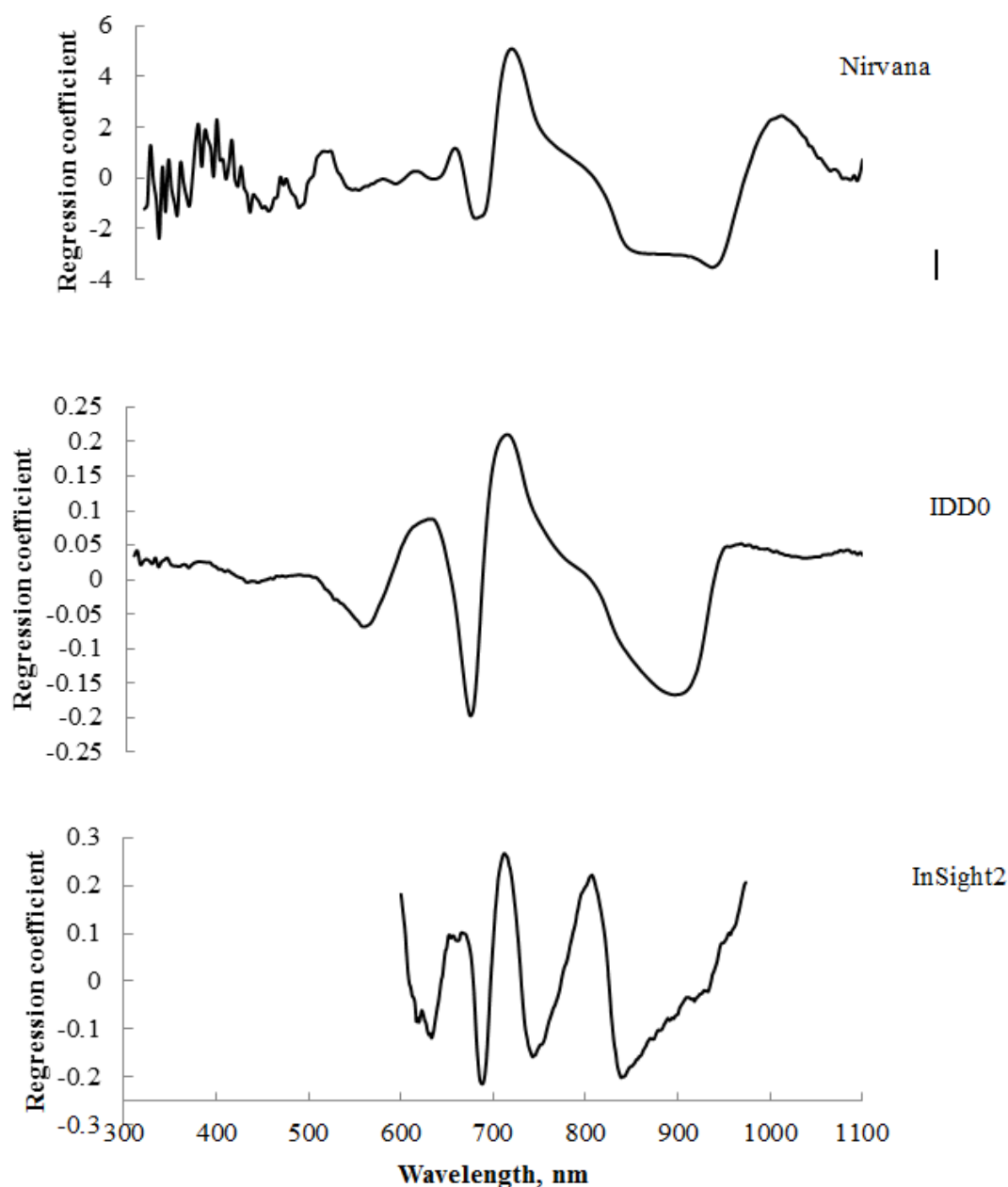


**Figure 4. PLS Regression coefficients for Nirvana (top), IDD0 (middle) and InSight2 (bottom) for visual score models based on absorbance data for a combined population involving 150 fruit (pop 2 and pop 3).**

Overall, of the three instruments, best prediction results were obtained using the IDD0 unit (e.g.  $R^2_{cv} = 0.83$ ,  $RMSECV = 0.62$ , for visual score model), with comparable results from the InSight2 unit but poorer results from the Nirvana unit (e.g.  $R^2_p = 0.62$ ,  $RMSEP = 0.99$ , visual score). The poorer performance of Nirvana unit is expected given its

interactance geometry, i.e. assessment of only a localised area of the fruit. IDD0 was operated in a 90° optical geometry, but scattering of light within the fruit apparently resulted in an adequate volume of fruit explored by detected light, supporting models comparable or superior to that achieved with the full transmission InSight2 system.

### **11.3.5 PLS model robustness to sample temperature**

The effect of sample temperature on prediction of apple diffuse browning was considered for the case of a PLSR model on diffuse browning developed using 120 absorbance spectra of 30 intact fruit (Pop 5) at 10 °C, with prediction undertaken for the same fruit at 25 and 35 °C, and for further lots of fruit at three temperatures. There was no bias associated with prediction of fruit at temperatures different to that of the calibration samples (Table 4), consistent with use of wavelength regions in the model (e.g. 570, 620, 670, 720, 900 nm) that were insensitive to temperature. Indeed, the b coefficients for the combined temperature model were similar to those models developed using fruit at a single temperature (Fig. 5).

**Table 4. Prediction performance for a PLSR model developed using raw averaged absorbance spectra for visual score (Pop5, 10 °C, calibration  $R^2_{cv} = 0.87$ , RMSECV = 0.53 %SSC, PCs = 4) developed using IDD0 absorbance spectra (500-975 nm) collected of intact fruit at 10 °C. Populations 5 to 9 are subsets of population 2 and 3, with 30 fruit in each population.**

<b>Populations</b>	<b>Temp (°C)</b>	<b>RMSEP (defect score)</b>	<b>Bias (defect score)</b>
Pop 5	25	0.58	0.14
SD* = 1.49	35	0.52	0.14
Pop 6	10	0.65	-0.09
SD = 1.57	25	0.59	0.07
	35	0.60	0.03
Pop 7	10	1.41	0.25
SD = 1.48	25	1.07	0.17
	35	1.28	0.27
Pop 8	10	1.18	0.04
SD = 1.51	25	0.99	0.06
	35	0.93	0.07
Pop 9	10	1.49	0.64
SD = 1.38	25	1.15	0.51
	35	0.98	0.47

\* Standard Deviation

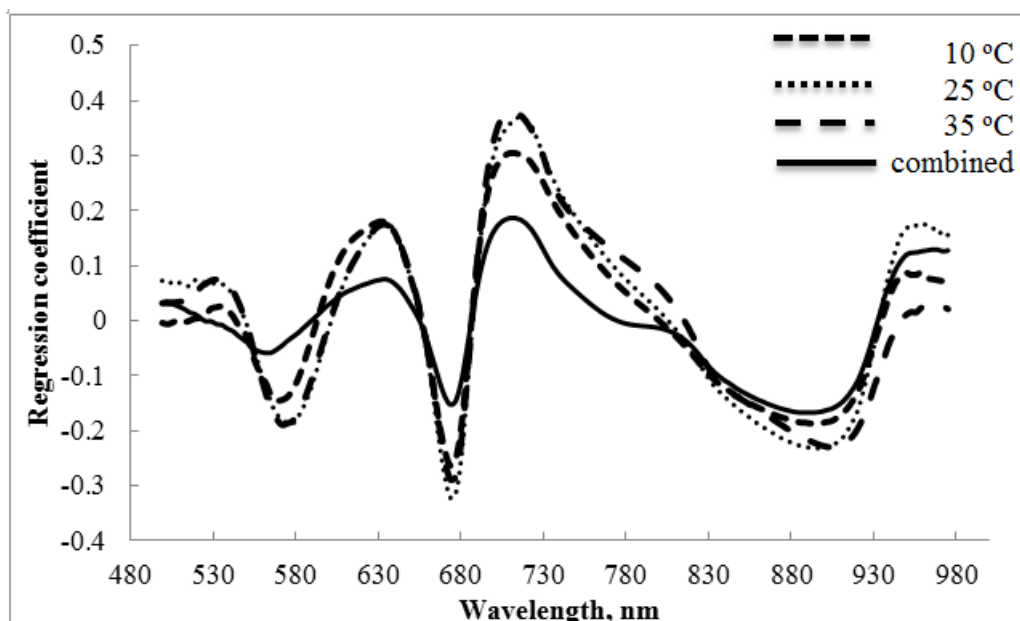


**Figure 5. PLSR b-coefficients for browning score models developed using spectra of fruit at three different temperatures (IDD0 instrumentation).**

### 11.3.6 Classification of sound and defect fruit

Given that practical application involves sorting of fruit to two grades rather than assessment of level of defect, attention was given to methods of discrimination. Principal component analysis (PCA) was undertaken using MSC treated absorbance data from the three instruments. A principal component plot using the first three PCs (explaining >95% of variation in the three cases) demonstrated separation of consumer acceptable fruit (visual score of 1 or 2) from defect fruit (visual score of 3 to 5 (Fig. 6).

Discrimination of sound fruit from defect based on spectra collected using the three instrumentations were attempted using several classification algorithms (Table 5). As relatively poor prediction results were achieved for the Nirvana instrument compared to that for the other two instruments for prediction set 1, the result for this instrument was not presented.

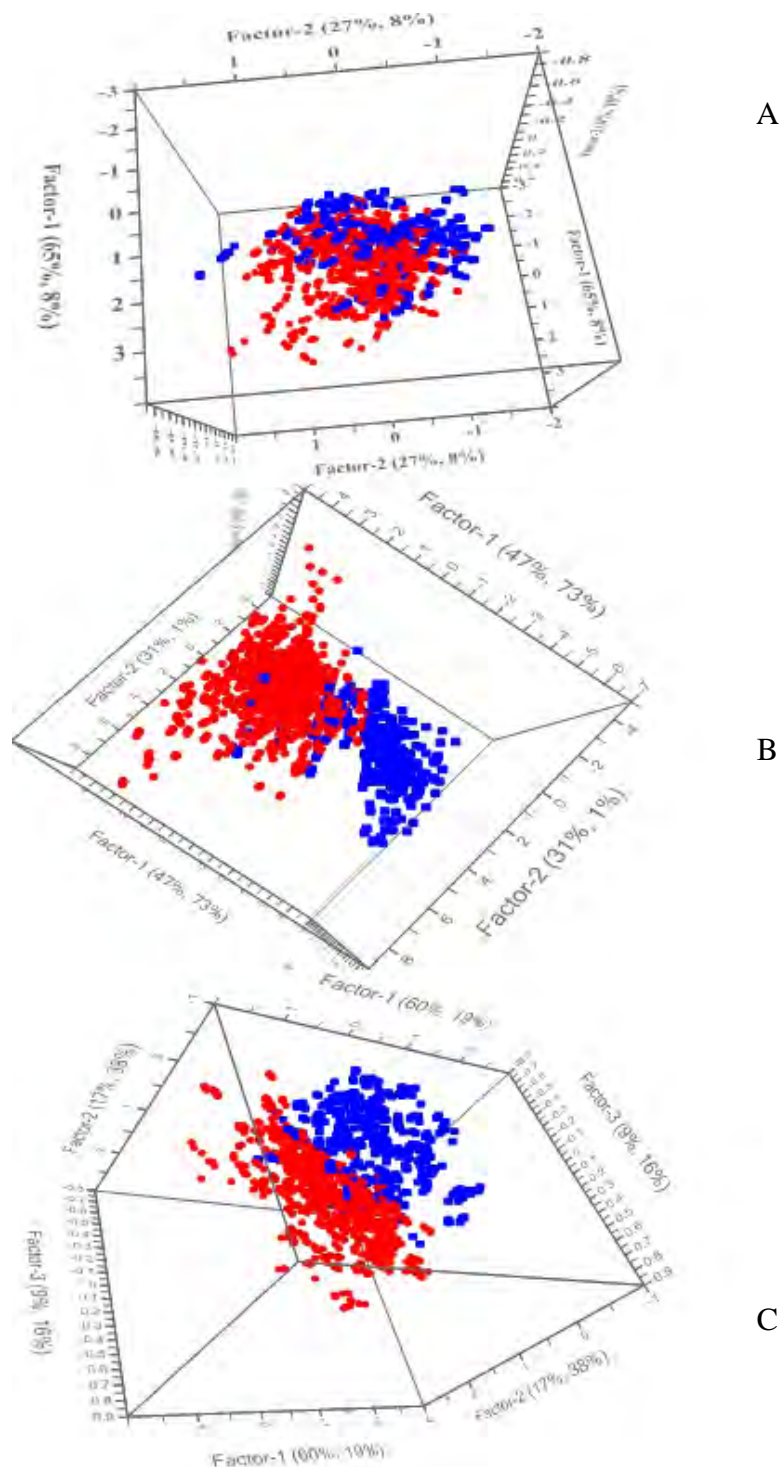


**Figure 6.** Score plots for principal components 1, 2 and 3 from a principal component analysis of MSC treated absorbance spectra (500-975 nm) using an interactance (Nirvana)(A), partial transmission (IDD0) (B) and full transmission (InSight2) (C) optical geometries for 150 fruit (populations 2 and 3). Values for defect fruit displayed as circular dots while those of good fruit is displayed as square dots.

**Table 5. Classification of good and defect fruit in calibration and in prediction of independent sets using 12 classification algorithms, using absorbance spectra from two instruments, and a reference assessment of visual score. TPR is true positive rate, TNR is true negative rate. Accuracy (Accu.) is mean of TPR and TNR, False discovery rate (FDR) is FP/(TP+FP). False discovery rates <2% associated with accuracy rate of >95% are shown in bold. Units are in percentage.**

**A. IDD0**

Algorithms	Calibration set (pop2)				Prediction set 1 (pop3)				Prediction set 2 (pop4)			
	TPR	TNR	Accu.	FDR	TPR	TNR	Accu.	FDR	TPR	TNR	Accu.	FDR
PLS DA(1-5) 6 PCs	76.3	98	87.2	2.6	89.6	96	92.8	4.3	97.3	91.84	94.6	7.7
PLS (1-5) 6 PCs	84.9	92.4	88.7	8.2	97.2	99.8	<b>98.5</b>	<b>0.2</b>	96.4	100	<b>98.2</b>	<b>0.0</b>
PLS DA (1-2) 6 PCs	79.8	94.2	87.0	6.8	97.9	97.9	97.9	2.1	100	82.7	91.4	14.7
PLS-DA	83.0	98.3	90.7	2.0	83.3	99.1	91.2	1.1	83.9	93.9	88.9	6.8
LDA (Linear)	87.6	98.6	93.1	1.6	80.5	99.5	90.0	0.6	91.0	86.7	88.9	12.8
LDA (MD)	95.2	97.6	96.4	2.5	76.3	98	87.2	2.6	92.9	93.9	93.4	6.2
PCA- LDA	78.5	97.2	87.9	3.4	98.6	97	97.8	3.0	98.2	83.7	91.0	14.2
PCA- LDA (MD)	85.5	93.9	89.7	6.7	89.6	99.5	94.6	0.6	96.4	95.9	96.2	4.1
k-NN	94.3	98.3	96.3	1.8	93	94.6	93.8	5.5	83.0	97.5	90.3	2.9
SIMCA	94.6	55.5	75.1	32.0	82.6	77.8	80.2	21.2	100	3.57	51.8	49.1
SVM, Linear	77.7	98.2	88.0	2.3	97.9	99.6	<b>98.8</b>	<b>0.4</b>	92.9	100	<b>96.5</b>	<b>0.0</b>
Logistic regression	86.8	94.2	90.5	6.3	99.3	100	<b>99.7</b>	<b>0.0</b>	70.5	100	85.3	0.0

**B. InSight2**

	Calibration set (pop2)				Prediction set 1 (pop3)				Prediction set 2 (pop4)			
	TPR	TNR	Accu.	FDR	TPR	TNR	Accu.	FDR	TPR	TNR	Accu.	FDR
PLS-DA (1-5) 6PCs	87.1	88.9	88	11.3	89.6	93.7	91.65	6.6	91.0	93.8	92.4	6.4
PLS (1-5) 6 PCs	90.0	95.6	92.8	4.7	82.6	99.3	90.95	0.8	86.6	100	93.3	0.0
PLS-DA (1-2) 6 PCs	88.2	96.6	92.4	7.0	85.4	99.5	92.45	0.6	91	100	<b>95.5</b>	<b>0.0</b>
PLS-DA	79.4	99.6	89.5	0.5	100.0	97.6	98.8	2.3	87.9	97.8	92.9	2.4
LDA (Linear)	91.6	99.1	95.4	1.0	80.5	98.8	89.7	1.5	91	98.5	94.8	1.6
LDA (MD)	99.2	100.0	99.6	0.0	33.3	100	66.7	0.0	0.0	100	50.0	0.0
PCA LDA (Linear)	82.2	97.7	89.9	2.7	85.2	99.8	92.5	0.2	89.3	100	94.7	0.0
PCA LDA (MD)	91.4	90.2	90.8	9.7	88.1	92.2	90.2	8.1	96.4	80.1	88.3	17.1
k-NN	96.5	98.0	97.3	2.0	73.6	92.8	83.2	8.9	77.7	95.4	86.6	5.6
SIMCA	98.4	43.5	70.9	36.5	95.1	59.0	77.1	30.1	96.4	84.2	90.3	14.1
SVM. Linear	99.2	99.8	99.5	0.2	84.7	95.6	90.2	4.9	75.9	100	88.0	0.0
Logistic regression	86.0	94.9	90.4	5.6	84.7	99.5	92.1	0.6	67.9	100	84.0	0.0

Comparable results were obtained with PLS DA, LDA and PCA LDA classification algorithms (Table 5). The PLS DA classification method yielded fairly consistent classification accuracy for all three instruments. Prediction set accuracy of more than 95% and false discovery rate of < 2% was achieved using IDD0 spectra with either SVM classification, logistic regression or PLS-DA using 4 PCs. With use of InSight2 spectra, these specifications were achieved using PLS-DA with 6 PCs (Table 5).

## 11.4 Conclusion

Internal diffuse browning in apple developing during controlled atmosphere storage is a significant industry problem. In line sorting to remove affected fruit, to meet retailer specifications of <2% affected fruit, is desirable to avoid rejection of whole consignments. Another possibility is monitoring of a number of 'sentinel' fruit within the controlled atmosphere storage to detect the onset of the disorder. Near infrared spectroscopy using partial or full transmission geometry over the wavelength range 500-975 nm is recommended for detection of the internal flesh browning using a discriminant analysis classification method such as PLS-DA. The method is noted to be independent of fruit temperature.

## 11.5 Acknowledgements

Authors acknowledge the support of farmers of Queensland, Australia for fruit samples, Mr. Larry Coleman for IDD0 instrumentation, MAF Roda for Insight 2 instrumentation support and to Central Queensland University for the provision of a scholarship to Bed Khatiwada.

## 11.6 References

Acharya, U.K., Walsh, K.B., Subedi, P.P., 2014. Robustness of partial least-squares models to change in sample temperature: II. Application to fruit attributes. *Journal of Near Infrared Spectroscopy* 22, 287-295.

Aulenbach, B.B., Yeatman, J.N., Worthington, J.T., 1972. Quality sorting of Red Delicious apples by light transmission, Marketing Research Report. United States Department of Agriculture, Washington, USA.

Benkeblia, N., Tennant, D.P.F., Jawandha, S.K., Gill, P.S., 2011. Preharvest and harvest factors influencing the postharvest quality of tropical and subtropical fruits, In: Yahia,

E.M. (Ed.), *Postharvest Biology and Technology of Tropical and Subtropical Fruits*. Woodhead Publishing, Cambridge, United Kingdom, pp. 112-142.

Bergman, H.E., Crouch, I., Crouch, M.J., Majoni, J., 2012. Update on the possible causes and management strategies of flesh browning disorders in 'Cripps Pink' apples. *South African Fruit Journal*, 56-59.

Castro, E., Barrett, D.M., Jobling, J., Mitcham, E.J., 2008. Biochemical factors associated with a CO<sub>2</sub>-induced flesh browning disorder of Pink Lady™ apples. *Postharvest Biology and Technology* 48, 182-191.

Castro, E.D., B. Biasi, E. Mitcham, S. Tustin, D. Tanner, Jobling J, 2007. Carbon dioxide induced flesh browning in Pink Lady™ apples. *Journal of American Society of Horticulture Science* 132 713-719.

Chayaprasert, W., Strohshine, R., 2005. Rapid sensing of internal browning in whole apples using a low-cost, low-field proton magnetic resonance sensor. *Postharvest Biology and Technology* 36, 291-301.

Clark, C.J., McGlone, V.A., Jordan, R.B., 2003. Detection of brownheart in 'Braeburn' apple by transmission NIR spectroscopy. *Postharvest Biology and Technology* 28, 87-96.

Ferguson, I., Volz, R., Woolf, A., 1999. Postharvest factors affecting physiological disorders of fruit. *Postharvest Biology and Technology* 13, 255-262.

Francis, F.J., Bramlage, W.J., Lord, W.J., 1965. Detection of watercore and internal breakdown in delicious apple by light transmittance. *Journal of American Society of Horticulture Science* 87 78-84.

Franck, C., Lammertyn, J., Ho, Q.T., Verboven, P., Verlinden, B., Nicolai, B.M., 2007. Browning disorders in pear fruit. *Postharvest Biology and Technology* 43, 1-13.

Fu, X., Ying, Y., Lu, H., Xu, H., 2007. Comparison of diffuse reflectance and transmission mode of visible-near infrared spectroscopy for detecting brown heart of pear. *Journal of Food Engineering* 83, 317-323.

Gonzalez, J.J., Valle, R.C., Bobroff, S., Biasi, W.V., Mitcham, E.J., McCarthy, M.J., 2001. Detection and monitoring of internal browning development in Fuji apples using MRI. *Postharvest Biology and Technology* 22, 179-188.

Greensill, C.V., Walsh, K.B., 2000. A remote acceptance probe and illumination configuration for spectral assessment of internal attributes of intact fruit. *Measurement of Science and Technology* 10 27-35.

Han, D., Tu, R., Lu, C., Liu, X., Wen, Z., 2006. Nondestructive detection of brown core in the Chinese pear 'Yali' by transmission visible-NIR spectroscopy. *Food Control* 17, 604-608.

Hatoum, D., Annaratone, C., Hertog, M.L.A.T.M., Geeraerd, A.H., Nicolai, B.M., 2014a. Targeted metabolomics study of 'Braeburn' apples during long-term storage. *Postharvest Biology and Technology* 96, 33-41.

- Hatoum, D., Buts, K., Hertog, M.L.A.T.M., Geeraerd, A.H., Schenk, A., Vercammen, J., Nicolai, B.M., 2014b. Effects of pre and postharvest factors on browning in Braeburn. *HortScience* 41, 19-26.
- Herremans, E., Verboven, P., Defraeye, T., Rogge, S., Ho, Q.T., Hertog, M.L.A.T.M., Verlinden, B.E., Bongaers, E., Wevers, M., Nicolai, B.M., 2014. X-ray CT for quantitative food microstructure engineering: The apple case. *Nuclear Instruments and Methods in Physics Research Section B: Beam Interactions with Materials and Atoms* 324, 88-94.
- James, H.J., Jobling, J.J., 2009. Contrasting the structure and morphology of the radial and diffuse flesh browning disorders and CO<sub>2</sub> injury of 'Cripps Pink' apples. *Postharvest Biology and Technology* 53, 36-42.
- Li, G., 2011. Nondestructive measurement model of apple internal browning based on FT-NIR spectroscopy. *Advanced Material Research* 304, 316-321.
- McGlone, V.A., Jordan, R.B., Seelye, R., Clark, C.J., 2003. Dry-matter-a better predictor of the post-storage soluble solids in apples? *Postharvest Biology and Technology* 28, 431-435.
- McGlone, V.A., Martinsen, P.J., Clark, C.J., Jordan, R.B., 2005. On-line detection of Brownheart in Braeburn apples using near infrared transmission measurements. *Postharvest Biology and Technology* 37, 142-151.
- Moggia, C., Pereira, M., Yuri, J.A., Torres, C.A., Hernández, O., Icaza, M.G., Lobos, G.A., 2015. Preharvest factors that affect the development of internal browning in apples cv. Cripp's Pink: Six-years compiled data. *Postharvest Biology and Technology* 101, 49-57.
- Moscetti, R., Haff, R.P., Stella, E., Contini, M., Monarca, D., Cecchini, M., Massantini, R., 2015. Feasibility of NIR spectroscopy to detect olive fruit infested by *Bactrocera oleae*. *Postharvest Biology and Technology* 99, 58-62.
- Norris, K., 1958. Measuring light transmittance properties of agricultural commodities. *Agriculture Engineering* 39, 640-643.
- Pérez-Marín, D., Sánchez, M.-T., Paz, P., González-Dugo, V., Soriano, M.-A., 2011. Postharvest shelf-life discrimination of nectarines produced under different irrigation strategies using NIR-spectroscopy. *LWT - Food Science and Technology* 44, 1405-1414.
- Upchurch, B.L., Throop, J.A., Aneshansley, D.J., 1997. Detecting internal breakdown in apples using interactance measurements. *Postharvest Biology and Technology* 10, 15-19.
- Vanoli, M., Rizzolo, A., Grassi, M., Spinelli, L., Verlinden, B.E., Torricelli, A., 2014. Studies on classification models to discriminate 'Braeburn' apples affected by internal browning using the optical properties measured by time-resolved reflectance spectroscopy. *Postharvest Biology and Technology* 91, 112-121.
- Wang, Y., Sugar, D., 2013. Internal browning disorder and fruit quality in modified atmosphere packaged 'Bartlett' pears during storage and transit. *Postharvest Biology and Technology* 83, 72-82.

Woolworths, 2015. Produce Specifications, Woolworths Australia. Data viewed on 15 March 2015, [www. Woolworths.com.au](http://www.Woolworths.com.au)